Strain partitioning during formation of oroclines and indentation

Implications for the Carpatho-Balkanides orogen

Deformatieverdeling tijdens oroclinevorming en indeuking: Implicaties voor de Karpaten-Balkaniden orogenese

(met een samenvatting in het Nederlands)

Расподела деформација током формирања ороклина и индентације: Импликације за Карпато-балкански ороген

(са резимеом на српском)

Proefschrift

ter verkrijging van de graad van doctor aan de
Universiteit Utrecht
op gezag van de
rector magnificus, prof.dr. H.R.B.M. Kummeling,
ingevolge het besluit van het college voor promoties
in het openbaar te verdedigen op

vrijdag 28 januari 2022 des middags te 12.15 uur

door

Nemanja Krstekanić

geboren op 4 september 1991
te Belgrado, Servië

Promotoren:

Prof. dr. L.C. Matenco
Prof. dr. M. Toljić

Copromotor:

Dr. E. Willingshofer

This study was financially supported by the Netherlands Research Centre for Integrated Solid Earth Science (ISES).

“Not all those who wander are lost.”
John Ronald Reuel Tolkien

Members of the Reading Committee:

Prof. Dr. Michele Cooke	University of Massachusetts Amherst, USA
Prof. Dr. Djordje Grujic	Dalhousie University, Canada
Prof. Dr. Magdalena Scheck-Wenderoth	GFZ Potsdam, Germany
Prof. Dr. Guido Schreurs	Universität Bern, Switzerland
Prof. Dr. Kamil Ustaszewski	Universität Jena, Germany

This is Utrecht studies in Earth Sciences volume 249

ISBN 978-90-6266-616-4

https://doi.org/10.33540/961

Printed in the Netherlands by Ipskamp Printing.

Cover: Landscape view of the Stara Planina (Old Mountain) at the transition between the Serbian Carpathians and the Balkanides.

Contents

Summary

Highly curved orogens form a large part of present-day and ancient convergent plate boundaries. Understanding their architecture and structural evolution is essential for understanding the variability of geodynamic processes occurring along zones of plate convergence. Arcuate orogens, or oroclines, often form by an interplay between subduction and indentation processes, but existing models do not provide clear mechanisms driving the strain partitioning during oroclinal bending associated with continental indentation.

The aim of this PhD thesis is to increase our understanding of the mechanisms controlling the strain partitioning during oroclinal bending around indenters. We constrain the effects of the interplay between indentation and lateral slab retreat on deformation transfer during the formation of oroclines. The thesis combines field structural observations in the southern Carpatho-Balkanides orocline of South-Eastern Europe (Chapters 2 and 4) and crustal-scale analogue modelling studies (Chapters 3 and 5) to build conceptual process-oriented hypotheses and validate them against several worldwide examples.

The introduction (Chapter 1) discusses aims to understand highly curved orogens that often demonstrate a complex poly-phase tectonic evolution and significant strain partitioning. While the oroclinal bending with convexity towards the outer arc is often driven by rapid slab roll-back processes, the mechanisms driving such bending with convexity towards the back-arc domain are less understood. Chapter 2 studies the kinematics of nappe stacking and the mechanics of oroclinal bending in the Serbian Carpathians segment of the Carpatho-Balkanides orocline, by the means of a field kinematic study correlated with available information in adjacent orogenic segments. Results demonstrate a poly-phase evolution, where the late Early Cretaceous nappe stacking was followed by Oligocene–middle Miocene ~40° of clockwise rotations. The superposition of Dinarides extension with the oroclinal bending in the Carpathians created overlapping stages of orogen-perpendicular extension and dextral strike-slip coupled with orogen-parallel extension, driven by the 100 km cumulated offset of the Cerna and Timok faults. The extension was associated with the formation of Oligocene–Miocene basins, providing critical timing constraints for the kinematic study. These deformations were followed by the late Miocene E-ward thrusting of the Upper Getic sub-unit, which was driven by a transfer of deformation in the orocline and around the Moesian Platform during the last stages of Carpathians collision. These results show that the mechanics of oroclinal bending is associated with the activation of strike-slip faults and strain partitioning by bi-modal extension, enhanced by the overlap between different geodynamic processes.

Chapter 3 investigates how shortening in front of indenters is transferred laterally to transpression, strike-slip and the formation of transtensional/extensional basins. For this purpose, a series of crustal-scale analogue models were performed in such a way that a deformable crust is moved around a stable and rigid indenter. The modelling demonstrates that the geometry of the indenter is the major controlling parameter driving strain partitioning and deformation transfer from thrusting and transpression to strike-

slip and transtension, whereas the rotation of the mobile plate controls the opening of triangular-shaped transtensional basins. The flow of the ductile crust leads to the distribution of deformation over a wider area, facilitating strike-slip splaying into transtension/extension behind the indenter. These results show a very good correlation with the Moesian indentation in the Carpatho-Balkanides system, where strain is partitioned around the dextral Cerna and Timok strike-slip faults and transferred to thrusting in the Balkanides part of the Moesian indenter and to transtension/extension in the neighbouring South Carpathians.

Chapter 4 focuses on the field kinematics to derive the mechanics of indentation and strain partitioning in the backarc-convex Carpatho-Balkanides orocline, where the kinematic evolution of the Serbian Carpathians is less understood. The results demonstrate that the overall deformation was accommodated by the Circum-Moesian Fault System surrounding the Moesian indenter, where the strain was partitioned in a complex network of coeval strike-slip, thrust and normal faults. This system represents one of the largest European intra-continental strike-slip deformation zones, with a cumulated 140 km dextral offset along previously known and newly found faults. These strike-slip faults transfer a significant part of their offset eastwards to thrusting in the Balkanides and westwards to orogen-parallel extension and the formation of intra-montane basins. The correlation with paleogeographic and geodynamic reconstructions demonstrates that the overall formation of the fault system is driven by subduction of the Carpathians embayment, resulting in laterally variable amounts of translation and rotation associated with indentation of the Moesian Platform. The onset of Carpathians slab retreat and backarc extension at 20 Ma has dramatically increased the rates of dextral deformation from ~3.5 mm/yr to ~2 cm/yr, facilitated by the pull exerted by the retreating slab.

Continental indentation is often affected by processes associated with other subduction zones, such as slab roll-back-driven back-arc extension. Chapter 5 uses crustal-scale analogue models to investigate the effects of a variably oriented extension direction on the strain partitioning and deformation transfer during indentation. The modelling results show that extension parallel to the strike-slip margin of the indenter creates subsidence distributed in several areas that may be ultimately connected in a large sedimentary basin behind the indenter. This basin narrows gradually towards the strike-slip margin of the indenter. In contrast, models with extension perpendicular to the strike-slip margin distributes transtensional deformation away from the indenter. Our results are in good correlation with the evolution of the Carpatho-Balkanides orocline, where the Circum-Moesian Fault System accommodates oroclinal bending during indentation against the Moesian Platform. In this area, the modelling explains the coeval and contrasting extensional features observed along the strike-slip margin and behind the indenter (i.e. the Morava Valley Corridor and the Getic Depression), driven by the roll-back of the Dinarides and Carpathian slabs.

Samenvatting

Sterk gekromde gebergteketens vormen een aanzienlijk deel van zowel de huidige als voormalige plaatgrenzen in continentale botsingszones. Inzicht in de architectuur en structurele evolutie van deze gebergteketens is essentieel om de verschillende geodynamische processen te kunnen duiden en begrijpen. Gekromde gebergteketens, ook wel oroclines genoemd, worden over het algemeen gevormd door het samenspel tussen subductie en indeuking (indentation). Hoewel de vorming van oroclines in verband wordt gebracht met indeuking van continentale platen, verschaffen bestaande tektonische modellen tot op heden nog geen duidelijkheid over de belangrijkste mechanismes die de deformatieverdeling in de plaat bepalen.

Het doel van dit proefschrift is om meer inzicht te krijgen in de mechanismes die de deformatieverdeling binnen botsende platen bepalen in de situatie waarbij de ene plaat de ander indeukt. Hiervoor zijn inschattingen gemaakt van de verschillende bijdrages van indeuking en zijdelingse plaatterugtrekking op de deformatieoverdracht tijdens orocline-vorming. In dit proefschrift worden veldobservaties in de zuidelijke Karpaten-Balkaniden orocline in Zuidoost-Europa (Hoofdstuk 2 en 4) gecombineerd met de resultaten van analoge aardkorstmodellen. Hiermee wordt een conceptuele en proces-georiënteerde hypothese opgesteld die wordt gevalideerd aan de hand van verschillende wereldwijde voorbeelden.

In de introductie (Hoofdstuk 1) worden de doelen beschreven om inzicht te krijgen in de vorming van sterk gekromde oroclines die vaak het product zijn van een complexe meerfase tektonische evolutie. Convexe oroclinale buiging in de richting van de buitenste boog wordt vaak veroorzaakt door het snelle terugrollen van de subducerende plaat. Het mechanisme verantwoordelijk voor convexe oroclinale buiging in de richting van het domein van de achterboog is echter minder goed begrepen. Hoofdstuk 2 bestudeert de deformatie gerelateerd aan dekbladoverschuivingen en de mechanica van oroclinale buiging in het Servische gedeelte van de Karpaten. Hierbij worden de resultaten van een veldstudie gecorreleerd aan beschikbare gegevens uit de aanliggende gebergtesegmenten. De resultaten tonen een meerfase ontwikkeling waarbij dekbladoverschuivingen tijdens het Laat-Krijt werden gevolgd door een kloksgewijze rotatie van ca. 40° tijdens het Oligoceen tot Midden-Mioceen. De fase van oroclinale buiging die de Karpatenboog heeft gevormd, werd gevolgd door een uitrekkingsfase in de Dinariden, gekenmerkt door meerdere overlappende fases van uitrekking loodrecht op de gebergteketen. Hierbij ontstonden ook dextrale zijschuivingsbreuken (Cerna- en Timok-breuken) met een cumulatief horizontaal verzet van ca. 100 km en daaraan gerelateerde uitrekking parallel aan de gebergteketen. Deze uitrekkingsfase wordt ook in verband gebracht met de bekkenvorming tijdens het Oligoceen-Mioceen. Hierbij helpt de tijdsbepaling van de deformatie aan de hand van de bekkeninvulling bij de interpretatie van de resultaten van de veldstudie. De uitrekkingsfase werd gevolgd door een oostwaartse opschuiving van de Boven-Getische subeenheid tijdens het Laat-Mioceen. Deze opschuiving werd veroorzaakt door de deformatieoverdracht van het gebergte naar de inkomende Moësische plaat tijdens de laatste fase van de botsing met de Karpaten. De resultaten laten zien dat oroclinale buiging vaak gepaard gaat met

activatie van zijschuivingsbreuken en deformatieverdeling door bimodale uitrekking, versterkt door de overlap van verschillende geodynamische processen.

In Hoofdstuk 3 wordt onderzocht hoe de inkorting aan de voorzijde van de inkomende plaat zich vertaalt in transpressie, zijschuivingsbreuken en vorming van transtensionele/uitrekkingsbekkens. Voor dit doeleinde is een serie analoge modellen op korstschaal uitgevoerd, waarbij een zwakke korstplaat zich om een stabiele en rigide inkomende korstplaat heen vervormt. De modellen laten zien dat de geometrie van de inkomende plaat een belangrijke parameter is bij de deformatieverdeling en -overdracht bij de overgang van overschuiving en transpressie naar zijschuiving en transtensie. Hierbij wordt de opening van driehoekige transtensionele bekkens gecontroleerd door de rotatie van de bewegende plaat. Stroming van de ductiele korst zorgt voor spreiding van deformatie over een groter gebied, waardoor zijschuivingsbreuken overgaan in transtensie/uitrekking achter de inkomende plaat. Deze resultaten laten een sterke correlatie zien met de indeuking van de Karpaten en Balkaniden door de Moësische plaat, waarbij de deformatie wordt verdeeld rondom de dextrale Cerna- en Timok-afschuivingsbreuken. In het Balkaniden-deel van de inkomende Moësische plaat gaan deze afschuivingsbreuken over in overschuivingen en in de naastgelegen Zuid-Karpaten in transtensie/uitrekking.

Hoofstuk 4 richt zich op veldobservaties om de mechanica van de indeuking en deformatieverdeling in de achterboog van de Karpaten-Balkaniden orocline te bestuderen, waar de ontstaansgeschiedenis van het Servische deel van de Karpaten minder goed is begrepen. De resultaten laten zien dat het grootste deel van de deformatie mogelijk werd gemaakt door het Circum-Moësische breuksysteem rondom de inkomende Moësische plaat. Daar werd de deformatie onderverdeeld over een complex netwerk van zijschuivings-, overschuivings- en afschuivingsbreuken die gelijktijdig actief waren. Dit zijschuivings breuksysteem vormt een van de grootste intracontinentale deformatiezones van Europa met in totaal 140 kilometer aan dextraal verzet langs de vele bekende en onbekende vertakkingen. Een groot deel van het verzet langs deze zijschuivingsbreuken vertaalt zich in oostwaartse richting naar overschuivingen in de Balkaniden. In westwaartse richting komt het verzet tot uiting in uitrekking parallel aan de gebergteketens, waardoor intra-montane bekkens zijn ontstaan. De correlatie met paleo-geografische en geodynamische reconstructies laat zien dat het ontstaan van het breuksysteem wordt gedreven door de subductie van de Karpatenbaai. Dit resulteert in een lateraal variabele hoeveelheid deformatie en in rotatie, geassocieerd met indeuking veroorzaakt door de inkomende Moësische plaat. De trekkrachten uitgeoefend door de terugtrekkende Karpatenplaat en achterboog-uitrekking 20 miljoen jaar geleden, hebben de dextrale deformatiesnelheid drastisch verhoogd van 3,5 millimeter per jaar naar 2 centimeter per jaar.

Continentale indeuking wordt vaak beïnvloed door processen gerelateerd aan subductiezones, zoals door plaatterugtrekking gedreven achterboog-uitrekking. Voor Hoofdstuk 5 zijn analoge modellen op korstschaal gebruikt om het effect te bestuderen van een variabele oriëntatie van de uitrekkingsrichting op de deformatieverdeling en -overdracht tijdens indeuking. De modelresultaten laten zien dat uitrekking parallel aan de zone met zijschuivingsbreuken aan de rand van de inkomende plaat, zorgt voor daling in verschillende gebieden die uiteindelijk leiden tot de vorming van een groot

sedimentair bekken achter de inkomende plaat. Dit bekken versmalt geleidelijk in de richting van de zone met zijschuivingsbreuken aan de rand van de inkomende plaat. Dit staat in contrast met de modellen waarbij uitrekking loodrecht plaatsvindt op de zone met zijschuivingsbreuken aan de rand van de inkomende plaat. In deze modellen verspreidt de deformatie zich door transtensie weg van de inkomende plaat. Deze modelresultaten zijn in overeenstemming met de evolutie van de Karpaten-Balkaniden orocline, waar het Circum-Moësische breuksysteem ruimte geeft aan oroclinale buiging tijdens indeuking door de inkomende Moësische plaat. In dat gebied verklaren de modellen de gelijktijdige en contrasterende vormen van uitrekking die kunnen worden geobserveerd langs de zone van zijschuivingsbreuken aan de plaatgrens en achter de inkomende plaat (i.e. de Morava Vallei Corridor en de Getische Depressie), gedreven door de terugrol van de Dinariden- en Karpatenplaat.

Резиме

Веома закривљени орогени чине значајан део како савремених, тако и некадашњих конвергентних граница тектонских плоча. Познавање њихове архитектуре и структурне еволуције је неопходно за разумевање баланса између различитих геодинамичких процеса који се одигравају дуж зона конвергенције плоча. Закривљени орогени, или ороклини, се често формирају заједничким утицајем субдукције и индентације. Међутим, постојећи модели не пружају јасна објашњења механизама који управљају расподелом деформација током ороклиног повијања асоцираног са континенталном индентацијом.

Циљ ове докторске тезе је да подигне ниво разумевања механизама који контролишу расподелу деформација током ороклиног повијања око индентера. У те сврхе утврђују се ефекти узајамног дејства индентације и бочног повлачења субдуковане плоче на трансфер деформација током формирања ороклина. У овој тези комбинују се теренски структурни подаци из јужног ороклина Карапто-балканида југоисточне Европе (поглавља 2 и 4) и аналогно моделовање у размери коре (поглавља 3 и 5). Добијени резултати се користе за формирање интегралне, процесно оријентисане хипотезе, која се проверава на више примера широм света.

У уводу (поглавље 1) разматрају се циљеви истраживања, усмерени на разумевање веома закривљених орогена који често показују сложену вишефазну тектонску еволуцију и значајну расподелу деформација. Док је убрзано повлачење субдуковане плоче најчешћи контролни механизам ороклиног повијања чија је конвексност оријентисана ка спољном луку, мање су познати механизми који управљају повијањем чија је конвексност ка изалучном домену. У поглављу 2 проучава се кинематика формирања навлака и механизми ороклиног повијања Српских Карпата, сегмента Карпато-балканског ороклина, коришћењем теренских кинематских истраживања у корелацији са доступним информацијама у суседним орогеним сегментима. Резултати показују вишефазну еволуцију код које је касно доњокредно формирање навлака праћено олигоценско – средњомиоценским ротацијама од ~40° у смеру казаљке на сату. Суперпозиција динаридске екстензије са ороклиним повијањем Карпата је створила преклапајуће етапе екстензије управне на ороген и десних транскурентних смицања удвојених са екстензијом паралелном орогену, изазваних кумулатним кретањима од 100 км дуж раседа Черна и Тимочког раседа. Екстензија је асоцирана са формирањем олиго-миоценских басена који пружају кључни временски оквир за проучаване деформација. Ове деформације су праћене касномиоценским навлачењем горњег гетикума ка истоку, које је контролисано трансфером деформација у ороклину и око Мезијске платформе током последњих етапа колизије Карпата. Ови разултати показују да је механизам ороклиног повијања асоциран са активацијом транскурентних раседа и расподелом деформација уз бимодалну екстензију, која је додатно наглашена преклапањем различитих геодинамичких процеса.

У поглављу 3 истражује се како сажимање испред индентера бочно прелази у транспресију, транскурентна смицања и формирање транстензионих/екстензионих басена. За те потребе, изведена је серија аналогних модела у размери коре тако

што је деформабилна кора кретана око стабилног и чврстог индентера. Моделовање показује да је геометрија индентера главни контролишући параметар који управља расподелом деформација, односно трансфером од навлачења и транспресије до транскурентних кретања и транстензије, док ротација покретне плоче контролише отварање транстензионих басена троугаоне геометрије. Течење дуктилне коре доводи до дистрибуције деформација на већем простору, што потпомаже гранање транскурентих раседа према транстензији/екстезији иза индентера. Ови резултати показују веома добру корелацију са мезијском индентацијом у карпато-балканском систему, где је деформација расподељена око десних Черна и Тимочког раседа, пренета у навлачење у Балканидима испред мезијског индентера и у транстензију/екстензију у суседним Јужним Карпатима.

Поглавље 4 је фокусирано на теренску кинематику за потребе дефинисања механизама индентације и расподеле деформација у изалучно-конвексном Карпато-балканском ороклину, где је кинематска еволуција Српских Карпата мање позната. Резултати показују да је укупна деформација акомодирана Циркум-мезијским раседним системом који окружује мезијски индентер и где су деформације расподељене у сложеној мрежи истовремених транскурентних, реверсних и нормалних раседа. Овај раседни систем представља једну од највећих европских интраконтиненталних транскурентних деформационих зона, са збирних 140 км десних смицања дуж претходно познатих и новооткривених раседа. Ови транскурентни раседи значајан део својих смицања преводе источно у навлачење у Балканидима и западно у екстензију паралелну орогену и формирање унутарпланинских басена. Корелација са палеогеографским и геодинамичким реконструкцијама показује да је формирање раседног система контролисано субдукцијом карпатског залива, што је довело до бочних варијација у количини транслације и ротације асоциране са индентацијом Мезијске платформе. Почетак повлачења субдуковане карпатске плоче и изалучна екстензија пре 20 милиона година су драстично повећали стопу десних смицања од ~3.5 мм/год to ~2 цм/год, што је олакшано истезањем изазваним повлачењем субдукујуће плоче.

Континентална индентација је често под утицајем процеса асоцираних са другим субдукционим зонама, као што је изалучна екстензија контролисана повлачењем субдукујуће плоче. У поглављу 5 користи се аналогно моделовање у размери коре за истраживање ефеката различито оријентисаних екстензија на расподелу и трансфер деформација током индентације. Резултати указују да екстензија паралелна транскурентним смицањима дуж маргине индентера ствара супсиденцију у неколико области које се касније могу повезати у велики седиментациони басен иза индентера. Овај басен се сужава поступно ка транскурентој маргини индентера. Супротно овоме, модели са екстензијом управном на транскурентну маргину распоређују транстензиону деформацију даље од индентера. Добијени резултати су у доброј корелацији са еволуцијом Карпато-балканида, где Циркум-Мезијски раседни систем акомодира ороклино повијање током индентације Мезијске платформе. Моделовање објашњава истовремене и контрастне екстензионе домене опсервиране дуж транскурентне маргине и иза индентера (тј., Великоморавски ров и Гетска депресија), који су контролисани повлачењем динаридске и карпатске субдуковане плоче.

Chapter 1. Introduction

1.1 Highly curved orogens

Subduction and subsequent continental collision processes along convergent plate boundaries led to the formation of most of the present-day and ancient fold and thrust belts and orogens such as the Alpine-Himalayan orogenic system, the North American Cordillera, the Andes, the Appalachian-Caledonian orogenic system, or the Variscan orogenic belt (Dewey and Bird 1970; Dewey, 1980; Platt, 1986; Royden 1993a; Moores and Twiss, 1995). Within these large orogenic systems, different segments can have a wide variety of map-view geometries, from relatively straight to highly arcuate. One type of arcuate orogens are primary or non-rotational arcs when the curvature is formed early during a collision and does not increase during progressive deformation (Fig. 1.1a; e.g., Marshak, 1988; Weil and Sussman, 2004; Johnston et al., 2013). No vertical axis rotations associated with later deformation phases occur and the curvature results from uniform (parallel) or radial slip with constant orientation and intensity throughout the entire deformation period (e.g., Yonkee and Weil, 2010). Other types of arcuate orogens form their curvature by bending an initially straight orogen with variable vertical axis rotations. These types of arcuate orogens create a horse-shoe or elbow geometry in map view and are termed "oroclines" since Carey (1955). This definition assumes that the entire oroclinal bending takes place after an initial structuration of a straight orogen. Other studies differentiate two further types of oroclines: progressive and secondary (Weil and Sussman, 2004; Cifelli et al., 2008; Yonkee and Weil, 2010; Johnston et al., 2013, and references therein). A progressive orocline achieves its curvature gradually by rotating its flanks during the main orogenic shortening (Fig. 1.1b). Such oroclines can form either by divergent emplacement, differential shortening or dragging along strike-slip faults during orogenic building. A secondary orocline is defined similarly to Carey (1955), in the sense that its bending fully post-dates the orogen-building stage and forms due to changing stress orientations (Fig. 1.1c).

The formation of arcuate orogens is associated with variable amounts and distribution of strain along the arc. In the case of oroclinal bending, the variability is a function of kinematics in the various segments of the orogen (Reis and Shackleton, 1976; Marshak, 1988; Yonkee and Weil, 2010). The strain distribution may include variable amounts of orogen-perpendicular or -parallel shortening in the inner (concave) part of the arc and/or orogen parallel extension in the outer (convex) segment of the orocline, strike-slip deformation with laterally variable offsets along the same fault, coupled with significant rotations, which create rather complex structural patterns (Fig. 1.1b, c; e.g., Lonergan and White, 1997; Platt et al., 2003, 2013; Glen, 2004; Hollingsworth et al., 2010; Yonkee and Weil, 2010; Pastor-Galán, 2011, 2015; Gutiérrez-Alonso et al., 2012; Li et al., 2018).

Both primary arcs and oroclines can be thin-skinned, affecting only shallow crustal levels above a sedimentary decollement, or can be thick-skinned by affecting in local situations the entire lithosphere, which creates significant buckling in the core of the orocline (Marshak, 1988; Gutiérrez-Alonso et al., 2012; Johnston et al., 2013). In both situations, the oroclinal bending can be driven by various processes, such as slab roll-back associated with trench retreat, slab-tearing, horizontal or vertical rheological heterogeneities, lithospheric folding, large-scale dragging along regional strike-slip

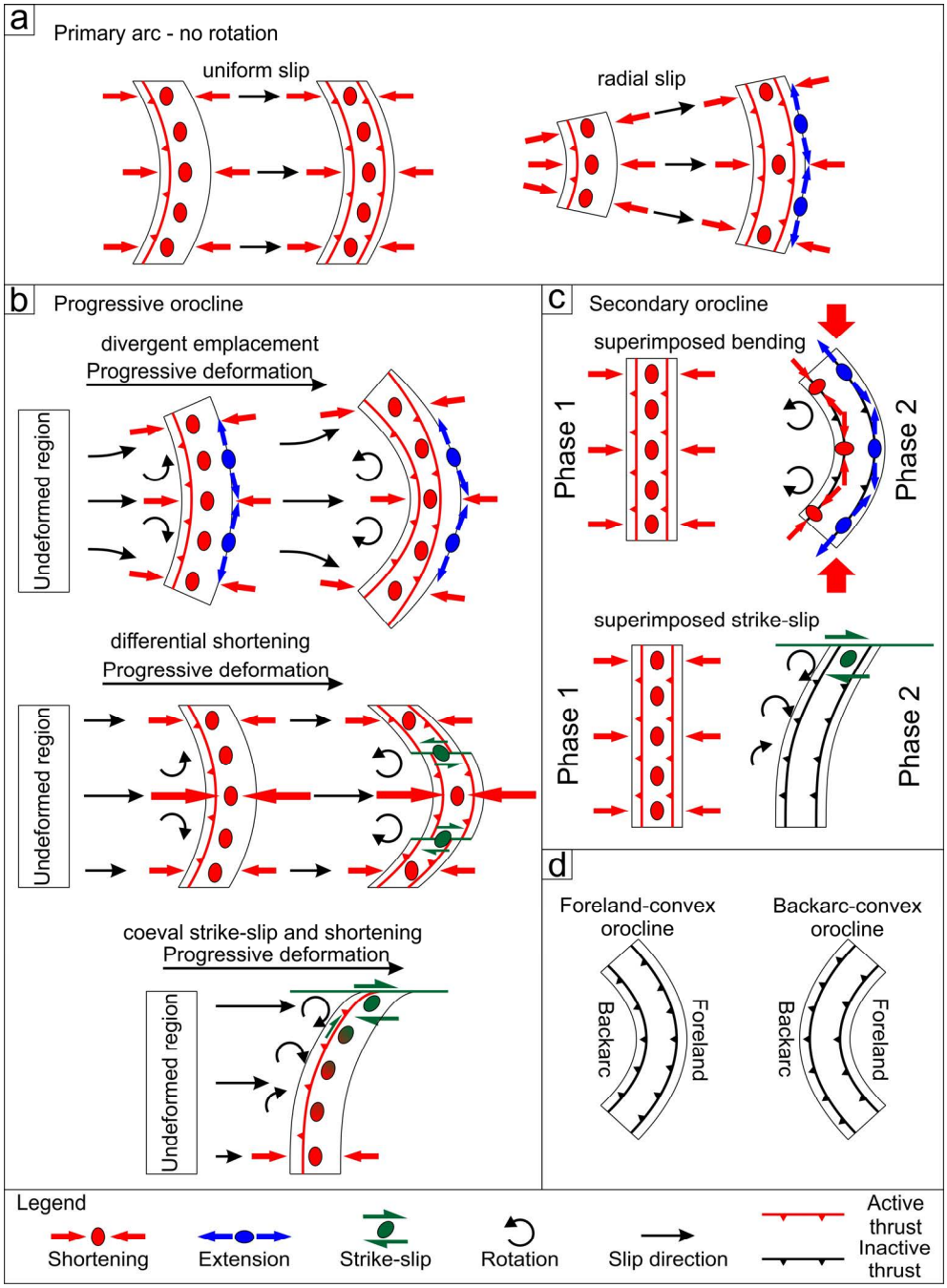

Figure 1.1 (previous page) - Simplified sketches of arcuate orogen formation models, inspired from Weil and Sussman (2004) and Yonkee and Weil (2010). a) Primary arcs

formed by uniform (parallel) or radial slip with constant slip direction and intensity, and without rotations; b) Progressive oroclines formed either by divergent emplacement, differential shortening or coeval drag along strike-slip faults and shortening at farther distances. The rotation increases gradually during orogenic shortening and, therefore, contractional structures gradually achieve their curvature. The progressive oroclinal bending can be associated with different second-order deformation styles, such as orogen-parallel extension during divergent emplacement, tear faulting that accommodates differential shortening or gradual change from strike-slip to shortening; c) Secondary oroclines formed by successive deformation stages. In the first stage, a linear orogen forms due to orogen-perpendicular shortening, which is subsequently continued by the formation of an oroclinal curvature by a differently oriented deformation. Such a secondary oroclinal bending can be driven either by orogen-parallel shortening leading to orogenic buckling or by superimposed strike-slip faulting that curves the linear orogen by dragging.

---

faults, irregular plate margins and indentation of continental fragments (e.g., Weil and Sussman, 2004; Gutiérrez-Alonso et al., 2012; Rosenbaum, 2014).

For simplicity, we separate oroclines into two categories: foreland-convex and backarc-convex (Fig. 1.1d). A foreland-convex orocline has the convex side oriented towards the foreland, meaning that the vergence of the main orogenic structure is away from its core. In contrast, the convex side of a backarc-convex orocline is oriented towards the backarc region and orogenic thrusting is towards the oroclinal core.

1.2 Indentation tectonics

The term indentation tectonics refers to processes related to the continental collision of two continents with different lithospheric strengths (e.g., Sokoutis et al., 2000; Willingshofer and Cloetingh, 2003; Regard et al., 2005; Sternai et al., 2016; van Gelder et al., 2017). A continent with relatively stronger rheology acts as a rigid block or "indenter" that deforms the weaker continent by significant shortening associated with orogenic uplift and/or lateral extrusion (Fig. 1.2a). The extrusion may be facilitated by other geodynamic processes, such as slab roll-back or opposite polarities subduction systems. A typical illustration is the indentation of the Indian continent into Eurasia by the creation of the Himalayan orogen and the lateral extrusion of Indochina, facilitated by the back-arc extension and retreat of the SE Asia subduction systems (Molnar and Tapponnier, 1975; Tapponnier et al., 1982, 1986; Davy and Cobbold 1988; Whipp, 2008; Jolivet et al., 2018). This concept was also widely applied to other situations of continental collision, especially across the Mediterranean, such as the indentation of Adria and lateral escape into the Pannonian Basin or the indentation of Arabia and lateral escape into Anatolia (e.g., Burke and Sengör, 1986; Ratschbacher et al., 1991a, b; Martinod et al., 2000; Regard et al., 2005; Mantovani et al., 2006).

Indentation tectonics is always associated with a significant variability in stress and strain distributions, which includes shortening and crustal/lithospheric thickening in front of the indenter, locally accompanied by vertical or lateral extrusion of weaker crustal or lithospheric material along regional strike-slip shear zones (Fig. 1.2a; e.g., Burke and Sengör, 1986; Peltzer and Tapponnier, 1988; Sokoutis et al., 2000; van Gelder et al., 2017). Lateral extrusion can also be accommodated by parallel extension that may be orthogonal to a coeval shortening direction (Fig. 1.2a), leading to orogenic collapse and formation of numerous normal faults (e.g., Tapponnier et al., 1986; Ratschbacher et al., 1991a, b; Wölfler et al., 2011). Furthermore, indentation induces vertical-axis rotations of continental fragments (Fig. 1.2; e.g., Sokoutis et al., 2000; Mantovani et al., 2006; Luth et al., 2013), leading to increased complexity in structural pattern and deformation partitioning around indenters that may lead to the formation of oroclines, facilitated by the coeval lateral activity of a roll-back subduction system (Fig. 1.2b).

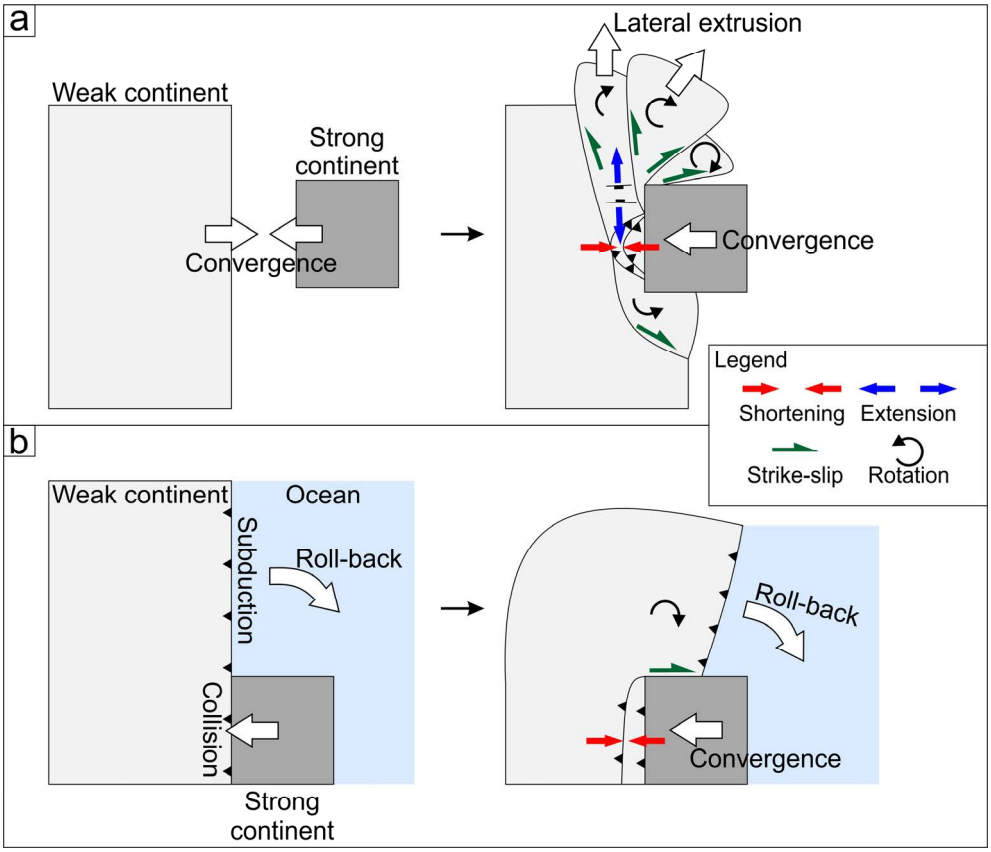

Figure 1.2 - a) Simplified sketch of an indentation process and associated structural and strain patterns, modified after Tapponnier et al. (1982), Tapponnier et al. (1986) and Davy and Cobbold (1988). b) Simplified sketch of indentation coupled with lateral slab retreat resulting in oroclinal bending of a weak continent around the indenter.

1.3 The Carpatho-Balkanides orogen in the framework of the Alpine-Mediterranean tectonic system

The Alpine-age orogens of the Mediterranean region formed during a complex long-lived convergence between the Eurasian and African continents and the numerous microplates defined near their contact during Mesozoic - Cenozoic times (Schmid et al., 2008, 2020; van Hinsbergen et al., 2020, and references therein). The evolution of this complex oroclinal region involved several subduction zones and their respective slab retreat systems (e.g., Royden, 1993b; Faccenna et al., 2004, 2014; Jolivet et al., 2013), continental collisions, indentation systems and lateral extrusions (e.g., McKenzie, 1972; Ratschbacher et al., 1991a, b; Martinod et al., 2000), and back-arc extensions (e.g., Matenco and Radivojević, 2012; Faccenna et al., 2014). This evolution has created the present-day geometry of the Alpine-Mediterranean orogenic system (Fig. 1.3) that includes numerous oroclines with various geometries, from Betics-Rif in the west to the Pontides and Taurides in the east (Rosenbaum, 2014), making it an exceptional natural laboratory for studying orocline formation and its driving processes.

One of these numerous Mediterranean oroclines is the Carpatho-Balkanides orogen of South-Eastern Europe. It formed during the evolution of a ~2000 km long northern branch of the Alpine orogenic system that spans from the Alps in the northwest to the Black Sea in the southeast. The Carpatho-Balkanides can be geographically defined to be composed of the West, East, South and Serbian Carpathians, as well as the Balkanides segments of the same orogenic system (shaded in Fig. 1.3). This double 180° orocline formed during the closure of the Neotethys and Alpine Tethys oceans and subsequent complex collision between the European continent and the Adria microplate, a continental fragment of the African continent (Csontos and Vörös, 2004; Schmid et al., 2008, 2020). The northern oroclinal part is composed of the West, East and South Carpathians (Fig. 1.3). Its foreland-convex curvature was achieved during Cenozoic times in response to the roll-back of the retreating Carpathians slab presently expressed in the Vrancea mantle anomaly and seismogenic zone, associated with opposite-sense rotations of its two upper tectonic plate continental mega-units (ALCAPA and Tisza-Dacia, Royden and Burchfiel, 1989; Csontos and Vörös, 2004). The southern, backarc-convex orocline is composed of the South and Serbian Carpathians and the Balkanides (Fig. 1.3) and formed during their translation and rotation around the Moesian Platform indenter, a promontory of the stable pre-Alpine European continent, which took place during the northward motion of the Adriatic micro-continent and the Carpathians slab retreat (Ratschbacher et al., 1993; Csontos and Vörös, 2004; Fügenschuh and Schmid, 2005; Ustaszewski et al., 2008).

Many previous studies have focused on the structure, kinematics and timing of deformations and rotations observed in the South Carpathians and Balkanides (e.g., Ratschbacher et al., 1993; Pătrașcu et al., 1994; Bojar et al., 1998; Schmid et al., 1998; Matenco and Schmid 1999; Willingshofer et al., 1999; Matenco et al., 2003; 2016; Dupont-Nivet et al., 2005; van Hinsbergen et al., 2008; Kounov et al., 2010, 2011, 2018; Panaiotu and Panaiotu, 2010; de Leeuw et al., 2013; Krézsek et al., 2013, Neubauer and Bojar, 2013; Vangelov et al., 2013; Burchfiel and Nakov, 2015, among others). A number of large-scale tectonic reconstructions have inferred the general large-scale

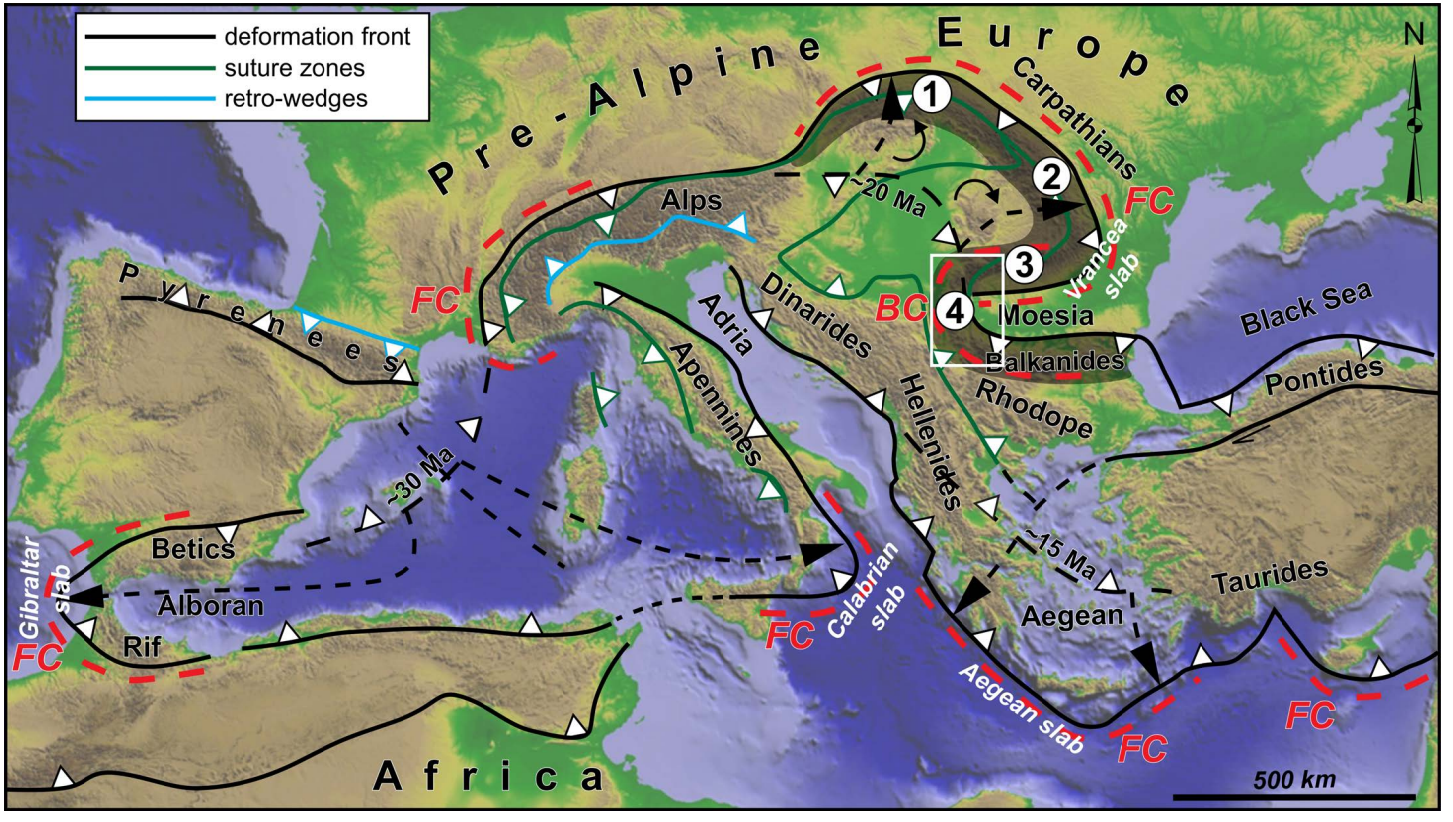

Figure 1.3 - The first-order Alpine-age structure of the Alpine-Mediterranean orogenic system. The shaded area is the Carpatho-Balkanides orocline. 1 – West Carpathians; 2 – East Carpathians; 3 – South Carpathians; 4 – Serbian Carpathians; FC – foreland-convex orocline; BC – backarc-convex orocline. The white rectangle indicates the position of the study area. Topography is based on SRTM data (Farr et al., 2007)

rotations and translations of large continental units (e.g., Csontos and Vörös, 2004; Fügenschuh and Schmid, 2005; Ustaszewski et al., 2008; van Hinsbergen et al., 2020). Other studies have observed dextral strike-slip offsets accumulating more than 100 km along several faults connecting these areas across the Serbian Carpathians, although their detailed timing and kinematics is largely unknown (the Cerna-Timok system, Berza and Drăgănescu, 1988; Kräutner and Krstić, 2002, 2003; Schmid et al., 2020). Such offsets may define one of the largest strike-slip systems observed in continental Europe. However, the detailed structural and kinematic evolution and the mechanisms of oroclinal formation during the indentation by the Moesian Platform are not understood because of a lack of systematic structural and kinematic studies in the critical segment of the Serbian Carpathians (Fig. 1.3). This segment is a key area where processes driving oroclinal bending during indentation and associated kinematic and strain partitioning effects can be studied in detail.

1.4 Scope of the thesis

This thesis aims to increase our understanding of the mechanisms driving strain partitioning during oroclinal bending associated with continental indentation. Existing indentation models differentiate between regions of shortening in front of indenters and lateral strike-slip deformation, but do not provide a clear understanding of how these distinct kinematic and structural domains connect and interact. We also aim to quantify the main controlling parameters of deformation transfer between the indenter margins and oroclinal bending rotations and their contribution to strain partitioning. Furthermore, we study the effect of lateral upper plate back-arc extension driven by a slab retreat on the evolution of indentation systems and oroclinal bending.

We apply and validate the process-oriented concepts of oroclinal bending to the evolution of the southern Carpatho-Balkanides orocline by an integrated structural and kinematic study in the area of the Serbian Carpathians, which connects all segments of the orocline. One structural peculiarity is the curved large-scale orogen-parallel strike-slip deformation observed in the hinge of the orocline. Such a structural feature is yet unexplained by existing models of strain partitioning in oroclines, as strike-slip was previously associated with deformation of the oroclinal flanks. In our research, we specifically make a distinction between the initial stage of orogen-building and the subsequent structures accommodating the observed oroclinal bending of the Carpatho-Balkanides during their indentation by the Moesian Platform.

1.5 Outline of the thesis

The research presented in this thesis uses field structural and kinematic observations to build process-oriented hypotheses (Chapters 2 and 4) that are validated by crustal-scale analogue modelling (Chapters 3 and 5).

Chapter 2 analyses the structural superposition of different deformation types associated with a variable paleostress field in the hinge area of the Carpatho-Balkanides

orocline along the Serbian Carpathians by the means of a field kinematic study coupled with observations of sedimentation in intra-montane basins. The results establish connections between nappe stacking, orogen-perpendicular and orogen-parallel extension associated with strike-slip deformation prior to and during the oroclinal bending in the area of the Serbian Carpathians. These novel results are correlated with existing studies in the neighbouring areas of the Dinarides, South Carpathians and Balkanides to constrain a new, process-oriented, conceptual model of strain partitioning during the oroclinal bending of the Carpatho-Balkanides.

In Chapter 3, an analogue modelling study focuses on understanding the partitioning of deformation in a curved strike-slip fault system around a rigid indenter during coeval indentation and rotations. Shortening in front of a rigid indenter is transferred laterally to transpression, strike-slip and the formation of transtensional/extensional basins. A series of crustal-scale analogue experiments bridge the gap in knowledge on how structurally distinct domains link kinematically and what are the controlling factors of deformation transfer around indenters during oroclinal bending. The modelling demonstrates that the geometry of the indenter is the major controlling parameter on strain partitioning and deformation transfer from thrusting and transpression to strike-slip and transtension, while deformation of the ductile crust controls the mode of strike-slip splaying into transtension/extension behind the indenter. These results are compared to the natural example of the Moesian indentation in the Carpatho-Balkanides and their coeval oroclinal bending, where strain is partitioned along large dextral fault system and transfer of strike-slip deformation from the Serbian Carpathians to thrusting in the Balkanides in front of the Moesian indenter and transtension/extension in the neighbouring South Carpathians.

Chapter 4 studies the driving mechanisms and kinematics in the large-scale fault system that accommodates oroclinal bending along the Moesian margins and its strain partitioning around the indenter corners. We analyse a new high-resolution structural kinematic dataset collected along one of the largest European intra-continental fault systems, the Circum-Moesian Fault System of the Carpatho-Balkanides, which cumulates 140 km of dextral offset while accommodating the oroclinal bending and indentation around the Moesian Platform. The results demonstrate that the analysed fault system accommodates the transfer of deformation during oroclinal formation from extension and transtension to large-scale strike-slip and ultimately to transpression and shortening. In more details, the strike-slip faults transfer a significant part of their offset eastwards to thrusting near the indenter and westwards to orogen-parallel extension and the formation of intra-montane basins at farther distances. Further correlations with existing studies in the neighbouring orogens and basins, as well as with paleogeographic and geodynamic reconstructions demonstrate that the formation of the fault system is driven by the Carpathians subduction resulting in laterally variable amounts of translation and rotation associated with Moesian indentation. This model of deformation transfer during oroclinal bending driven by slab retreat coupled with indentation can be applied to other similar systems worldwide.

Chapter 5 contributes to the understanding of the coupled effects of indentation and externally-driven extension on deformation transfer around rigid indenters. The areas located along a lateral indenter margin or behind an indenter are often affected by

extension driven by the slab-roll retreat. In such settings, indentation-driven deformation overlaps with this externally-driven extension. The presented analogue models test the influence of the extension direction during indentation in terms of kinematics, distribution of deformation and the coeval formation and evolution of sedimentary basins. The results demonstrate that the deformation transfer around rigid indenters can be significantly affected by a lateral extension driven by a different mechanism, which involves subsidence in newly formed basins, distribution of deformation away from indenter and increase in oblique kinematics along differently oriented faults. These results are in good agreement with the evolution of the Circum-Moesian Fault System during indentation and oroclinal bending of the Carpatho-Balkanides, where the retreat of the Carpathians and Dinarides slabs affected deformation transfer around the Moesian indenter.

Finally, Chapter 6 integrates the research presented in chapters 3 – 6 and provides the conclusions of the thesis. The mechanisms relevant for the oroclinal bending driven by an interplay of indentation and lateral subduction and the kinematics of a backarc-convex oroclinal bending are discussed. We also summarize the implications for the evolution of the Carpatho-Balkanides orogen and provide an outlook for future research.

Chapter 2. Understanding partitioning of deformation in highly arcuate orogenic systems: Inferences from the evolution of the Serbian Carpathians[1]

[1] This chapter is based on Krstekanić, N., Matenco, L., Toljić, M., Mandic, O., Stojadinovic, U., Willingshofer, E., 2020. Understanding partitioning of deformation in highly arcuate orogenic systems: Inferences from the evolution of the Serbian Carpathians. Global and Planetary Change 195, 103361. https://doi.org/10.1016/j.gloplacha.2020.103361

2.1 Introduction

The formation of highly arcuate orogenic systems has been documented in numerous worldwide studies, such as in the Altai and Alborz Mountains, New England Orogen, Dun Mountain Ophiolite Belt, South Andes, Ouachita Orogen, or the various mountain chains composing the Mediterranean area (e.g., Calignano et al., 2017; Edel et al., 2014; Li and Rosenbaum, 2014; Lonergan and White, 1997; Mattei et al., 2017; Meijers et al., 2010; Mortimer, 2014; Pastor-Galán et al., 2015; Rosenbaum, 2012, 2014; Torres Carbonell et al., 2016; Vergés and Fernàndez, 2012; Xiao et al., 2018). These studies have demonstrated that the formation of highly arcuate orogenic systems may be related to a number of processes influenced by inherited rheological heterogeneities, such as the variability of deformation in orogens influenced by slab roll-back or slab tearing mechanics, lithospheric folding or lateral variations in the geometry of plate boundaries and rigid indenters (e.g., Calignano et al., 2017; Hollingsworth et al., 2010; Pastor-Galán et al., 2012; Rosenbaum, 2014; Zweigel et al., 1998 and references therein). These highly curved orogens are sometimes referred to as oroclines, which acquired their curvature during and/or after the main orogenic process, or by subsequent bending of a primary arc (e.g., Carey, 1955; Cifelli et al., 2008; D'el-Rey Silva et al., 2011; Johnston et al., 2013; Platt et al., 2003; Rosenbaum, 2014). The term strain partitioning has been used in many different ways at different spatial scales (e.g., Carreras et al., 2013; Lister and Williams, 1983), from large strike-slip faults parallel to subduction zones accommodating oblique convergence (e.g., Fitch, 1972; Platt, 1993), coeval pure-shear and simple-shear strain that accommodate zone-perpendicular and zone-parallel deformation, respectively (Fossen et al., 1994; Jones and Tanner, 1995), or a multi-scale distribution of bulk strain to different genetic types of coeval structures that cannot be defined by a uniform stress field (e.g., Benesh et al., 2014; Cembrano et al., 2005; D'el-Rey Silva et al., 2011; De Vicente et al., 2009; Glen, 2004; Krézsek et al., 2013). We adopt the latter, more general meaning of strain partitioning to describe coeval structures of different genetic types associated with oroclinal bending.

In all situations, oroclinal bending is associated with large amounts of strain partitioning in various segments of the orocline, which makes it difficult to use standard field kinematic approaches based on the consistency of strain or paleostress directions along the orogenic strike (e.g., D'el-Rey Silva et al., 2011; Glen, 2004; Lacombe, 2012; Li et al., 2018; Pastor-Galán et al., 2011; Ries and Shackleton, 1976). Oroclinal bending towards the outer arc (the convex side oriented towards the foreland, i.e. herewith defined foreland-convex) displays significant strain partitioning during orogenic thrusting and backarc extension, being driven often by slab retreat, as commonly observed in the Apennines, Betics–Rif, Hellenides or Carpathians orogens of the Mediterranean system (Fig. 2.1a, e.g., Faccenna et al., 2004; Jolivet et al., 2013). The formation of such oroclines is also associated with orogen-parallel extension and the evolution of large-scale strike-slip systems (e.g., Gutiérrez-Alonso et al., 2015; Martínez-García et al., 2013; Roldán et al., 2014), which potentially compete with backarc, orogen-perpendicular extension driven by slab retreat and coeval shortening mechanics (e. g., Faccenna et al., 2014; Menant et al., 2016a, 2016b). However, the interplay between these processes is less understood due to their genetic separation in

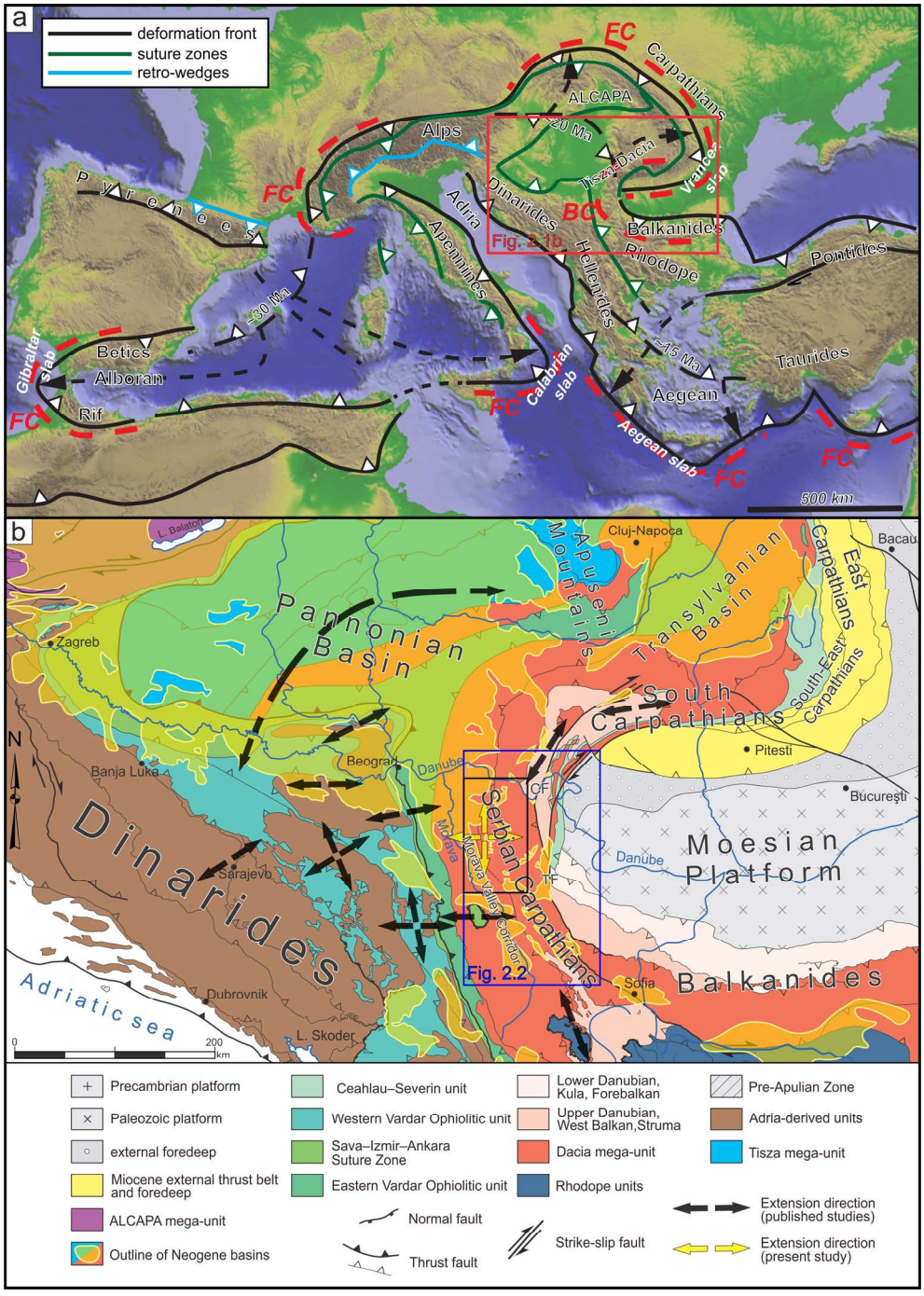
a
deformation front
suture zones
retro-wedges
FC
Carpathians
ALCAPA
~20 Ma
Alps
Tisza-Dacia
Vrancea slab
Pyrenees
FC
Dinarides
BC
Balkanides
Adria
Apennines
Fig. 2.1b
Rhodope
Pontides
Hellenides
~30 Ma
~15 Ma
Gibraltar slab
Betics
Alboran
Rif
FC
Calabrian slab
Aegean
Taurides
Aegean slab
FC
FC
500 km
b
L. Balaton
Cluj-Napoca
Bacau
Apuseni Mountains
Transylvanian Basin
East Carpathians
Pannonian Basin
Zagreb
South Carpathians
South-East Carpathians
Pitesti
N
Banja Luka
Beograd
Danube
CF
București
Moesian Platform
Morava
Morava Valley Corridor
TF
Danube
Serbian Carpathians
Dinarides
Sarajevo
Fig. 2.2
Sofia
Balkanides
Adriatic sea
Dubrovnik
L. Skoder
0
200
km
Precambrian platform
Paleozoic platform
external foredeep
Miocene external thrust belt and foredeep
ALCAPA mega-unit
Outline of Neogene basins
Ceahlau–Severin unit
Western Vardar Ophiolitic unit
Sava–Izmir–Ankara Suture Zone
Eastern Vardar Ophiolitic unit
Lower Danubian, Kula, Forebalkan
Upper Danubian, West Balkan,Struma
Dacia mega-unit
Rhodope units
Pre-Apulian Zone
Adria-derived units
Tisza mega-unit
Normal fault
Thrust fault
Strike-slip fault
Extension direction (published studies)
Extension direction (present study)

Figure 2.1 (previous page) - a) Simplified image of Mediterranean orogens formed during Mesozoic - Cenozoic times, displaying suture zones, orogenic fronts and retro-wedges (inspired from van Hinsbergen et al., 2020). Dashed red lines are oroclines. FC = foreland-convex orocline; BC - backarc-convex orocline; Red rectangle shows the location of Fig. 2.1b. b) Regional tectonic map of the area connecting the Dinarides and South Carpathians showing the main tectonic units (modified after Schmid et al., 2008, 2020). The blue rectangle shows the location of Fig. 2.2, the black rectangle indicates the locations of Figs. 2.5, 2.7, 2.8 and 2.10. Extension directions are plotted after Andrić et al. (2017), Erak et al. (2017), Fügenschuh and Schmid (2005), Kounov et al. (2011), Matenco and Radivojević (2012), Mladenović et al. (2015), Porkoláb et al. (2019); Schefer (2012), Stojadinovic et al. (2013, 2017) and Toljić et al. (2013). TF-Timok Fault; CF-Cerna Fault.

different locations across the strike of the orogen and the complexity of kinematics in oroclinal bending. This lack of knowledge is particularly valid in places where oroclinal bending takes place towards the backarc (Fig. 2.1a, the convex side towards the backarc, i.e. herewith defined backarc-convex).

One of the best examples of oroclinal bending in Mediterranean orogens is the double 180° arcuate loop of the Carpathians–Balkanides orogenic system. While the foreland-convex orocline segment composed of the West, East and South Carpathians formed in direct response to the Paleogene–Miocene slab retreat, the backarc-convex orocline segment composed of the Balkanides, Serbian and South Carpathians formed during coeval rotations and docking against the Moesian Platform (Fig. 2.1; e.g., Maţenco, 2017; Ratschbacher et al., 1993). The formation of this exceptional orocline was associated with opposite sense rotations of the two main continental blocks that make up the upper tectonic plate (i.e., ALCAPA and Tisza–Dacia mega-unit; Fig. 2.1a) during the gradual Cretaceous–Miocene closure of the external Carpathians embayment by subduction and collision (e.g., Csontos and Vörös, 2004; Horváth et al., 2015). The Cretaceous formation of the Carpathian thick-skinned nappe stack was followed by a gradual clockwise rotation and N-, NE- to E-ward translation of the Tisza–Dacia mega-unit (e.g., Balla, 1987; Csontos, 1995; Márton, 2000; Pătrasçu et al., 1994; Panaiotu and Panaiotu, 2010; Ustaszewski et al., 2008). In respect to the stable European units situated in the foreland of the Carpathians, this Tisza–Dacia mega-unit underwent up to 90° of clockwise rotations during the Cenozoic (Pătrasçu et al., 1990, 1992, 1993; Panaiotu and Panaiotu, 2010), of which 15°-30° was achieved during post-middle Miocene times (de Leeuw et al., 2013; Dupont-Nivet et al., 2005). The amount of clockwise rotation decreases southwards to no significant rotations in the Balkanides during the Cenozoic (van Hinsbergen et al., 2008). In the studied segment of the Serbian Carpathians, available paleomagnetic data suggest only ~25° clockwise rotation during the Cenozoic (Lesić et al., 2019 and references therein), while structural observations have inferred 10° clockwise rotation during post- Oligocene times (Marović et al., 2002). The neighbouring segment of the Dinarides orogen recorded 34°-46° clockwise rotations during post-early Miocene times (Lesić et al. (2019).

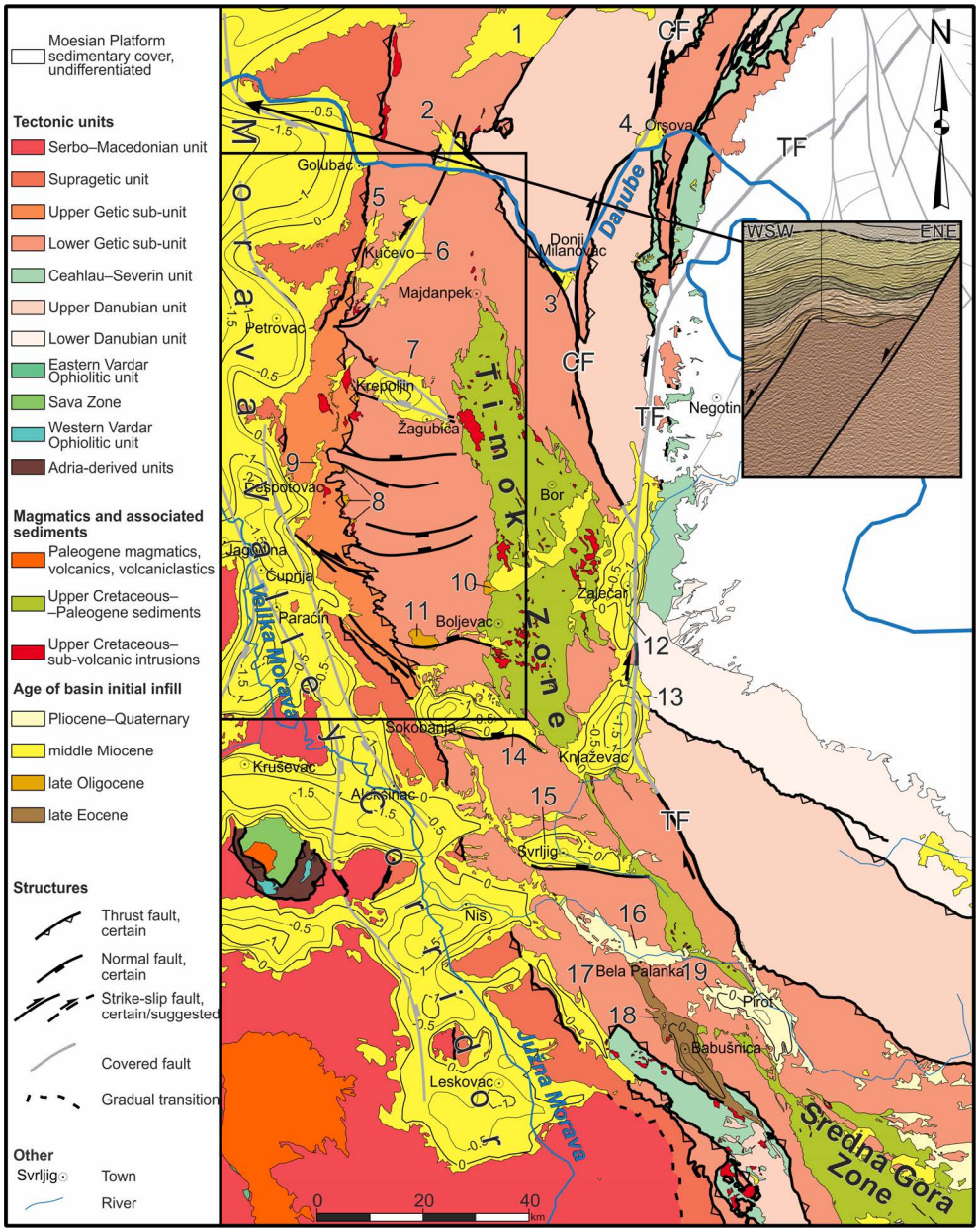

Figure 2.2 - Tectonic map of the Serbian Carpathians and adjacent areas of the South Carpathians and Balkanides showing the regional fault kinematics (compiled and modified after Basic geological map of former Yugoslavia, scale 1:100.000 and Maţenco, 2017). Isolines in Cenozoic basins indicate pre-Cenozoic basement structure (compiled after Balázs et al., 2016 and Matenco and Radivojević, 2012). Isoline numbers are in kilometres. The black rectangle indicates the position of Figs. 2.5, 2.7, 2.8 and 2.10. TF-Timok Fault; CF-Cerna Fault. Intramontane basins: 1-Bozovici Basin,

2-Sicheviţa Basin, 3-Donji Milanovac Basin, 4-Orşova Basin, 5-Rakova Bara Basin, 6-Kučevo Basin, 7-Žagubica Basin, 8-Senje–Resava Basin, 9-Panjevac Basin, 10-Bogovina Basin, 11-Krivi Vir Basin, 12-Timok Basin, 13-Knjaževac Basin, 14-Sokobanja Basin, 15-Svrljig Basin, 16-Bela Palanka Basin, 17-Zaplanje Basin, 18-Babušnica Basin, 19-Pirot Basin. Inset: Segment of a seismic cross-section of Matenco and Radivojević (2012), showing syn-sedimentary faults in the Morava Valley Corridor.

These rotations and translations were associated with Eocene–early Miocene orogen-parallel extension and ~ 100 km of dextral strike-slip offset along the curved Cerna–Jiu and Timok faults system in the South and Serbian Carpathians, and a gradual transtensive opening of basins in their foreland, which was accommodated by coeval shortening in the East Carpathians (Fig. 2.1b; Fügenschuh and Schmid, 2005; Krézsek et al., 2013; Matenco and Schmid, 1999; Schmid et al., 1998). All these large-scale movements were partly coeval with the Oligocene–Miocene orogen perpendicular back-arc extension recorded by the Tisza–Dacia part of the larger Pannonian Basin and its southern prolongation along the Morava Valley Corridor (e.g., Figs. 2.1b, 2.2; Balázs et al., 2016; Erak et al., 2017; Horváth et al., 2006; Toljić et al., 2013). This prolongation presently separates the orogenic structure of the Dinarides from the one of the Carpathians (Fig. 2.1b). The Pannonian Basin extension was followed by an overall N- to NE- ward indentation of the Adriatic continental microplate that inverted the southern part of the Pannonian Basin starting with the latest Miocene (e.g., Matenco and Radivojević, 2012; Pinter et al., 2005). This overall evolution infers the juxtaposition of orogen-perpendicular extension, orogen-parallel extension and strike-slip deformation in the area of the Morava Valley Corridor and the adjacent N-S oriented segment of the Serbian Carpathians (Figs. 2.1 and 2.2; e.g., Erak et al., 2017). Furthermore, this is the same area where orogenic extension driven by eduction or roll-back in the Dinarides system has been inferred (Andrić et al., 2018; Matenco and Radivojević, 2012). In this overall framework, the evolution of the Serbian Carpathians segment is still less constrained, although available structural and paleomagnetic studies indicate that its oroclinal bending connected with the Balkanides and the South Carpathians was largely achieved during the Oligocene–Miocene (e.g., Csontos et al., 1992; Márton, 2000; Márton et al., 2007; de Leeuw et al., 2013). More recent regional paleostress reconstructions indicate a stress field with variable orientations that formed during the gradual clockwise rotation around the Moesian Platform (Mladenović et al., 2019). However, how such a variable stress field is linked with the mechanics of regional and local deformation during the clockwise Carpathians rotation and the formation of extensional intra-montane and back-arc basins remains unclear.

We aim to understand the relationship between nappe stacking, orogen-perpendicular and orogen-parallel extension associated with strike-slip deformation during the backarc-convex oroclinal bending of the Carpathians–Balkanides Mountains. To this aim, we have performed a kinematic field study in the internal part of the Serbian Carpathians near their contact with the Dinarides, which is the key area of interference between the orogen-parallel and orogen-perpendicular extension. Our study is correlated with the evolution of Oligocene - Miocene basins, together with orogenic nappe stacking

kinematic and timing constraints available in more external areas of the Serbian Carpathians and the neighbouring areas of the Dinarides, Morava Valley Corridor, South Carpathians and Balkanides (Fig. 2.1). The results are discussed in the context of the regional evolution of Carpathians–Balkanides and Dinarides orogenic systems and in terms of strain partitioning during oroclinal bending.

2.2 Tectonic evolution of the Serbian Carpathians and associated sedimentary basins

The Serbian segment of the Carpathians–Balkanides forms part of the larger Europe-derived Dacia tectonic mega-unit (Fig. 2.1b). This segment is located in the area of interference between the nappe stacking recorded by two orogenic systems that formed during the closure of two oceanic realms, i.e. the Ceahlău–Severin branch of the Alpine Tethys Ocean and a northern branch of the Neotethys Ocean (e.g., Schmid et al., 2008, 2020).

2.2.1 The Cretaceous–Eocene tectono-stratigraphy and associated magmatism

The Ceahlău–Severin branch of the Alpine Tethys Ocean, whose remnants outcrop east and north of the studied area (Figs. 2.1 and 2.2), opened during the Middle Jurassic and was closed by Cretaceous subduction and collision, while its remnants were further deformed during Late Cretaceous–Miocene times (e.g., Maţenco, 2017; Schmid et al., 2008). To the east, the stable European foreland is made up of the Moesian Platform in the area adjacent to the South and Serbian Carpathians (Fig. 2.1, Săndulescu, 1988; Visarion et al., 1988). In this segment of the orogen, the Cretaceous closure by subduction and subsequent collision of the Ceahlău–Severin Ocean was associated with two main stages of shortening that created the presently observed nappe stack. The initial late Early Cretaceous thrusting (~100–110 Ma, 'Austrian' event in local literature, see Schmid et al., 2008 and references therein) of the Supragetic unit was followed by the latest Cretaceous thrusting (late Campanian–early Maastrichtian, ~75–67 Ma, 'Laramian' event in local literature, see Schmid et al., 2008 and references therein) of the Getic unit and the formation of a Danubian nappe stack derived from the margin of the Moesian Platform (e.g., Csontos and Vörös, 2004; Iancu et al., 2005a; Neubauer, 2015; Săndulescu, 1988; Seghedi et al., 2005). These events were coeval with significant exhumation of the entire nappe stack, well quantified by thermochronological studies in the South Carpathians (e.g., Bojar et al., 1998; Fügenschuh and Schmid, 2005; Neubauer and Bojar, 2013; Willingshofer et al., 1999).

The Supragetic unit exposes a metamorphic basement made up of a Neoproterozoic–Silurian volcano-sedimentary sequence metamorphosed dominantly in greenschist to sub-greenschist facies in the Serbian Carpathians and amphibolite to sub-greenschist facies in the South Carpathians during Variscan times (Figs. 2.3, 2.4; Iancu et al., 2005b; Kalenić et al., 1980). In the Serbian Carpathians, these rocks are overlain by a transgressive-regressive upper Carboniferous–Permian sequence containing conglomerates, sandstones and shales with coal seams that are replaced upwards in the

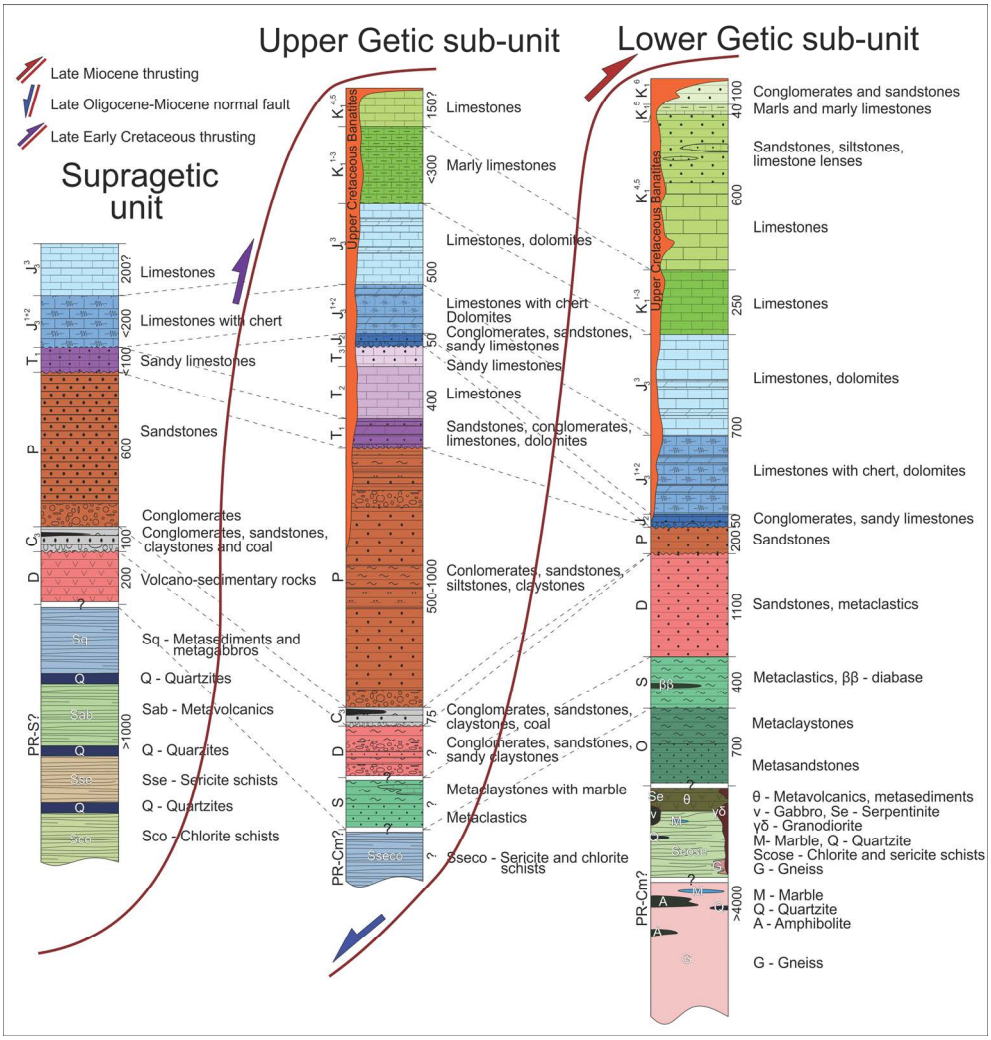

Figure 2.3 - Tectono-stratigraphic columns of Supragetic, Upper Getic and Lower Getic sub-units in the studied area (compiled and correlated after Basic geological map of former Yugoslavia, scale 1:100.000). The purple half arrow indicates the late Early Cretaceous shortening and nappe-stacking that created the Supragetic thrust, while blue and red half arrows illustrate Miocene normal faulting and thrusting, respectively, of the Upper Getic thrust. Stratigraphic age of the units is indicated by the symbols on the left side of each column (PR-Proterozoic; Cm-Cambrian; O-Ordovician; S-Silurian; D-Devonian; C3-Upper Carboniferous; P-Permian; T1-Lower Triassic; T2-Middle Triassic; T3-Upper Triassic; J2-Middle Jurassic; J31+2-Oxfordian-Kimmeridgian; J33 - Tithonian; K11-3-Berriasian-Hauterivian; K14,5-Barremian-Aptian; K15 -Aptian; K16 -Albian). Numbers on the right side of each column represent the maximal thickness of units in meters.

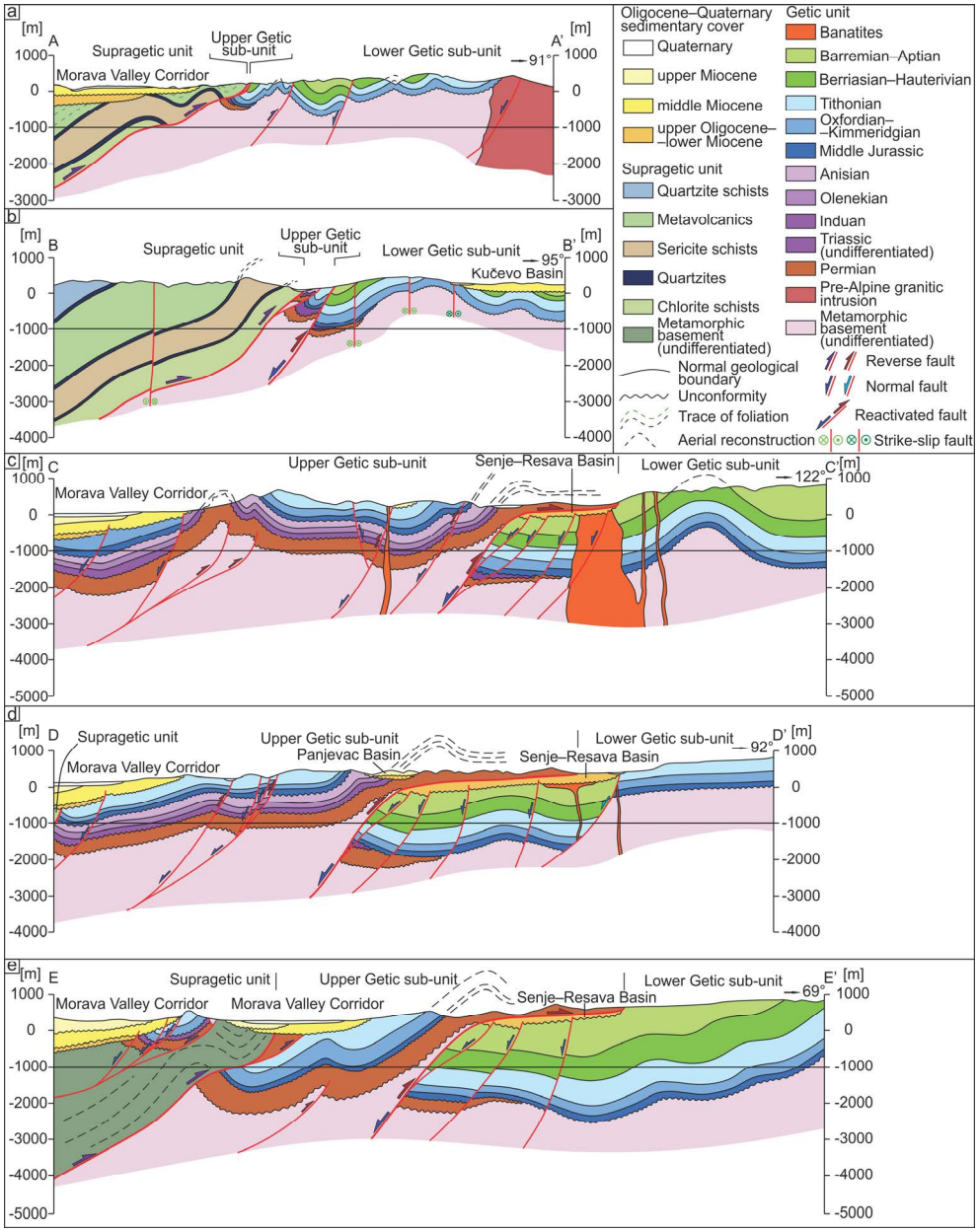

Figure 2.4 - Geological cross-sections across the studied area. Cross-sections are built following the field observations and results of this study. Surface to depth projection is based on the field kinematic data from this study and the Basic geological map of former Yugoslavia, scale 1:100.000. Colours of half-arrows indicating kinematics along faults are the same as respective structures in Figs. 2.5, 2.7 and 2.10. Sections a) and b) are modified after Krstekanić et al. (2017). The positions of the cross-sections are displayed

in Figs. 2.5, 2.7, 2.8 and 2.10. The strike of each cross-section is indicated in the upper right corner of the section. No vertical exaggeration.

---

stratigraphy by red alluvial sandstones (Fig. 2.3, Djordjević-Milutinović, 2010; Kalenić et al., 1980; Petković, 1975a). These sediments are overlain by a transgressive Triassic–Jurassic alluvial to shallow-water limestone sequence (Veselinović et al., 1970). The Getic unit is separated in the Serbian Carpathians into two sub-units (the Upper and Lower Getic, Figs. 2.2, 2.4) by a large offset thrust (Figs. 2.2, 2.4). Northwards, the late Early Cretaceous thrusting has created in the South Carpathians a narrow system of two nappes located in the upper part of the Getic unit that contain Triassic–Jurassic sediments and are found immediately beneath the main Supragetic thrust (the Sasca–Gornjac and Resita nappes, Iancu et al., 2005a). These nappes were interpreted to be the equivalent of the Upper Getic sub-unit emplaced during late Early Cretaceous times in a trailing imbricated fan sequence in the footwall of the main Supragetic thrust (e.g., Kräutner and Krstić, 2002; Săndulescu, 1984). The Upper and Lower Getic sub-units contain a similar Variscan greenschist to amphibolite facies metamorphosed basement that is intruded by plutons and overlain by an Upper Carboniferous to Cretaceous sedimentary cover (Figs. 2.3, 2.4; Iancu et al., 2005a, 2005b; Kräutner and Krstić, 2003). The Mesozoic cover reaches 2 km in thickness and is composed of a Permian - Lower Triassic transgressive alluvial clastic to shallow-water sequence (Fig. 2.3) that crops out on a larger area in the Lower Getic sub-unit, unconformably overlain by a sequence containing a mixed Middle Jurassic clastic carbonatic sequence, Upper Jurassic - Lower Cretaceous shallow-water limestones and dolomites, including a typical Urgonian reef facies, and Aptian–Cenomanian clastics (Fig. 2.3).

To the west and south of our studied area, the remnants of another ocean crop out, i.e. the northern branch of the Neotethys Ocean (or the Vardar Ocean, Fig. 2.1b). This ocean opened during the Middle Triassic times by separating the European from Adria-derived units, the latter being derived from the larger African domain (e.g., Pamić, 1984; Schmid et al., 2008; Stampfli and Borel, 2002). The Middle Jurassic onset of oceanic subduction led initially to obduction of ophiolites and genetically associated ophiolitic melanges over both the Adriatic- and European-derived continental margins (the Western and Eastern Vardar Ophiolitic units, respectively; Fig. 2.1b; Dimitrijević, 1997; Schmid et al., 2008). This obduction was followed by Cretaceous–Eocene shortening that peaked during the latest Cretaceous onset of collision and the subsequent formation of a suture zone at the contact between the two main continental units (i.e. the Sava Suture Zone; Pamić, 2002; Stojadinovic et al., 2017; Ustaszewski et al., 2009). The Late Cretaceous subduction of the Neotethys ocean was associated with the emplacement of a large volume of magmatism (~92–67 Ma) that is observed in the Apuseni–Banat–Timok–Sredna Gora Zone (ABTS) belt (e.g., Gallhofer et al., 2015; von Quadt et al., 2005). Alternatively, the emplacement of the ABTS magmatic belt has also been interpreted to be driven by subduction of the Ceahlău-Severin Ocean (Neubauer, 2015). East of the studied area in the Timok Zone (Fig. 2.2) and further to the SE in the Sredna Gora unit, these typical arc calc-alkaline magmas were emplaced as magmatic intrusions, volcanic lava flows and a volcanoclastic sequence in a number of extensional structures

that started at ~92–87 Ma, whereas the magmatism becomes progressively younger towards the hinterland (e.g., Gallhofer et al., 2015; Kolb et al., 2013). The onset of this extension was coeval with the formation of an extensional fore-arc basin overlying the European margin adjacent to the Sava Zone (Toljić et al., 2018). This Late Cretaceous extension has also possibly exhumed the high-grade metamorphosed Serbo–Macedonian unit from below the low-grade metamorphosed Supragetic unit along an extensional detachment (Antić et al., 2016a; Erak et al., 2017). However, the exact nature of this reactivated Paleozoic (Caledonian and Variscan) Serbo–Macedonian\Supragetic contact is poorly known, owing to its often burial beneath the Paleogene–Neogene sediments along the Morava Valley Corridor (Fig. 2.2; Antić et al., 2016b; Săndulescu, 1984). Other magmatic intrusions and volcanics are observed W to SSW of the studied area in three roughly parallel belts, emplaced during the latest Cretaceous, Eocene–Oligocene and Miocene times, which are thought to be related with an overall SW-ward migration and detachment of the Neotethys slab (Andrić et al., 2018 and references therein).

2.2.2 The Eocene–Miocene orogen-parallel and perpendicular extension associated with large scale transcurrent motions

The study area lies in the transition zone between orogen parallel and perpendicular extensions and strike-slip deformation that took place during the clockwise rotation of the Carpathians units (Fig. 2.1). In more details, an orogen-parallel extensional detachment formed during Paleocene–Eocene times in the South Carpathians by the reactivation of the inherited Getic unit thrust contact and the exhumation of Danubian nappe stack in its footwall (e.g., Fügenschuh and Schmid, 2005; Matenco and Schmid, 1999; Moser et al., 2005; Schmid et al., 1998). This orogen-parallel deformation continued by the activation of the late Oligocene Cerna and the early Miocene Timok faults system that retained 35 and 65 km offsets, respectively, in the South and Serbian Carpathians (Berza and Drăgănescu, 1988; Kräutner and Krstić, 2002). The activity along these strike-slip faults is partly coeval with the second, Miocene cooling event that was associated with a low magnitude of vertical movements (Moser et al., 2005). The onset of an E-W oriented extension (i.e. orogen-perpendicular for the study area) took place in or near the Morava Valley Corridor (Figs. 2.1 and 2.2) during Oligocene times (~29–27 Ma, based on thermochronological data of Erak et al., 2017), while the same basin was subsequently enlarged during the peak moments of extension that took place during the middle Miocene (~15–13 Ma), creating the well-observed syn-kinematic deposition (e.g., inset in Fig. 2.2, see also Matenco and Radivojević, 2012; Stojadinovic et al., 2013, 2017; Toljić et al., 2013). Large-offset early-middle Miocene normal faults and detachments accommodating a N-S to ENE-WSW oriented extension are observed in the neighbouring Dinarides (e.g., Andrić et al., 2017; Mladenović et al., 2015; Schefer, 2012; Ustaszewski et al., 2010). These structures and genetically associated basins were inverted starting with the latest Miocene, commonly interpreted to be driven by the indentation of the Adriatic microplate, which is still presently active (e.g., Andrić et al., 2017; Bada et al., 2007; Fodor et al., 2005).

The Oligocene - Miocene extension and strike-slip were associated with the formation of a significant number of extensional basins (Fig. 2.2). In the Morava Valley Corridor, the Oligocene–early Miocene normal faults and syn-kinematic sedimentation

are usually buried at depth beneath the largely outcropping post-kinematic deposition younger than 17 Ma (Fig. 2.2, Krstić et al., 2003; Matenco and Radivojević, 2012; Sant et al., 2018). Most of these post-kinematic shallow-water sediments are lacustrine and were deposited dominantly during and after the late Miocene endemic isolation of the Pannonian Basin (e.g., Kalenić et al., 1980; ter Borgh et al., 2013; Vujisić et al., 1981). The intra-montane basins of the Serbian Carpathians (Fig. 2.2) contain similar lacustrine facies that have a significant age variability. The oldest sediments are the middle to upper Eocene lacustrine turbidites observed at the base of the Babušnica Basin (de Bruijn et al., 2018; Marković et al., 2017). The late Oligocene–early Miocene Senje–Resava and Bogovina basins (including the Panjevac and Krivi Vir sub-basins, Fig. 2.2, Lihoreau et al., 2004; Mai, 1995; Maksimović, 1956; Obradović and Vasić, 2007; Pavlović, 1997; Žujović, 1886) are thrusted by Permian sandstones of the Upper Getic sub-unit (Fig. 2.4). Most of the other basins have an early middle Miocene initial infill, while being overlain by late Miocene–Pliocene sedimentation, such as the Sokobanja, Žagubica and Svrljig basins (Fig. 2.2; Kalenić et al., 1980; Lazarević and Milivojević, 2010; Marković, 2003; Obradović and Vasić, 2007; Sant et al., 2018). The sedimentation in the remaining basins (Bela Palanka and Pirot Basins, Fig. 2.2) is thought to have started only during Pliocene times (Anđelković et al., 1977; Vujisić et al., 1980).

2.3 Field structural observations and kinematic analysis

We have performed our fieldwork in the key area of interference between strike-slip, orogen-parallel and orogen-perpendicular extension, which is where the Supragetic and Getic units are in close proximity to the Morava Valley Corridor (Fig. 2.2). This area benefits from the high quality and full coverage of 1:100.000 scale geological maps (OGK former Yugoslavia). These maps were extensively used previously to define the timing and geometry of the Jurassic - Paleogene deformation by using the observed stratigraphic juxtaposition across faults combined with their overlying post-kinematic sedimentation (e.g., Dimitrijević, 1997; Schmid et al., 2008, 2020 and references therein).

We specifically focused the kinematic fieldwork to characterize the kinematics of large faults and shear zones, initially identified to have a large stratigraphic offset (vertical and/or horizontal) in geological maps, such as the thrust of the Supragetic and Upper Getic (sub-)units, large offset normal or strike-slip faults. We confirmed or re-interpreted these structures by measuring their kinematics and large offsets (from hundreds of metres to 20 km) along their strike across the entire studied area (coloured faults in Figs. 2.5, 2.7, 2.8 and 2.10). In the field, these major contacts are observed in the field by zones of intense deformation, such as meters-thick foliated fault gouges, intense faulting with large offset at outcrop scale, or tight folding. Similar zones of intense deformation with large outcrop-scale offsets have been observed also elsewhere, allowing the definition of new major tectonic contacts that are relevant at map scale. Furthermore, in order to understand the regional effects and superposition, we have also measured deformation at farther distances from major faults of shear zones (black faults in Figs. 2.5, 2.7, 2.8 and 2.10).

Deformation has a brittle character in most observed situations. The pre-Mesozoic basement contains ductile shearing and greenschist facies metamorphism in the Supragetic unit and greenschist to amphibolite facies metamorphism in the Getic unit. However, the Mesozoic sedimentary cover is generally not affected by this ductile deformation, with the exception of a low- to sub- greenschist metamorphic facies observed in the vicinity of the main Supragetic thrust. Field observations included measurements of foliations, fold axes and their geometry, brittle faults and shear zones, observations of tilting and rotations. The sense of shear along brittle faults and shear zones was derived from kinematic indicators such as slickensides (including calcite slickenfibres, grooves and other brittle lineations), Riedel shears and brittle shear bands, by taking into account confidence criteria and quality ranks (e.g., Angelier, 1994; Doblas, 1998; Sperner and Zweigel, 2010). Shear bands, sheared quartz aggregates and, less frequent, consistent asymmetry of folds (e.g., Simpson and Schmid, 1983) were used for inferring shear senses in ductile and brittle-ductile transitional fabrics. In few situations, a larger number of conjugate shears were measured in the main shear zone, which was particularly useful to derive the kinematics of foliated fault gouges. The fault-slip data was separated in the field by observations of consistency, superposition, reactivation of deformation, or using timing criteria. We paid particular attention to syn- and post-kinematic sedimentation, used as a key timing indicator for the observed deformation stages, the most important being related to the fault-controlled deposition observed in Oligocene–Neogene sediments (Fig. 2.2). Further timing indicators observed in the field are structural cross-cutting, tilting and truncation relationships, which aided to understand the structural superposition.

The analysis of the obtained kinematic dataset has resulted in the definition of five deformation types (Figs. 2.5, 2.7, 2.8 and 2.10), grouped by the interpretation of three tectonic events, which respect all timing and superposition criteria observed in the field or otherwise available in studies of the neighbouring Serbo–Macedonian, Dinarides, Pannonian Basin and Morava Valley Corridor units (e.g., Erak et al., 2017; Matenco and Radivojević, 2012; Stojadinovic et al., 2013, 2017). We furthermore focussed on understanding the partitioning of strain in observed major faults or shear zones, by assigning the kinematics observed in multiple outcrops along the fault strike to its specific expression at map scale. The lateral correlation between outcrops is based on the character of deformation in similar lithologies (e.g., brittle fault gouges versus individual fault planes or brittle shear bands) as well as on the compatibility of deformation and offsets observed in the field with the one at map scale. The lateral correlation has demonstrated that the thrusting observed at the Supragetic and Upper Getic nappe contacts has an overall curved geometry in map view and is associated with the coeval formation of a large number of tear faults (Figs. 2.5, 2.7, 2.10). We note that such tear-faults are perpendicular to and connect thrusting segments by accommodating their differential offsets in major shear zones. These tear faults are demonstrably different when compared with faults formed during the strike-slip deformation event (Fig. 2.8), which are widely observed outside major shear zones (see also Mladenović et al., 2019).

Our specific strain-based approach and the observed deformation are not entirely suitable to invert kinematic data to derive paleostress directions. Methodological

limitations come from the fact that measurements in large offset shear zones do not satisfy the Wallace-Bott criteria and the often observed strain partitioning during deformation (such as thrusting associated with wedge and tear faulting, regional and local vertical axis rotations observed along drag folds) are well-known limitations of the paleostress methodology (e.g., Célérier et al., 2012; De Vicente et al., 2009; Hippolyte et al., 2012; Jones and Tanner, 1995; Orife and Lisle, 2003; Sperner and Zweigel, 2010). Reconstructing paleostress for such strain partitioning requires a high-resolution data set that is beyond the regional scope of our study. Nevertheless, in order to test the consistency of deformation at regional scale, we have also inverted our data by calculating paleostress tensors for all deformation that does not display strain partitioning effects and are located in the vicinity of large-offset faults. This means, for instance, that tear faulting and faults observed in outcrops to be associated with drag-folding rotations were not included in calculations. We have used the WinTensor software (Delvaux and Sperner, 2003) to calculate and optimise reduced paleostress tensors (Figs. 2.A1, 2.A2 and Table 2.A1 of the Appendix) by following a standard inversion approach with confidence criterion (e.g., Angelier, 1994; Angelier and Goguel, 1979; Angelier and Mechler, 1977; Delvaux and Sperner, 2003 and references therein) and allowing a slip tolerance of ±26° (Lisle, 2013). Displacements along observed faults and calculated rotations are used as independent constraints to correlate with the paleostress tensors, which are interpreted to be part of the material response to imposed boundary conditions (e.g., Tikoff and Wojtal, 1999). Given the two approaches (strain and stress), we specifically use in interpretation a terminology that differentiates between stress calculations (compression-tension) and strain observations (contraction-extension).

Data were furthermore grouped and used in the construction of five regional cross-sections (Fig. 2.4), where the surface kinematics was projected at depth and correlated with other existing surface and depth constraints. The eastern part of these profiles has less structural control at depth and, therefore, our surface to depth projection has a higher degree of uncertainty.

Figure 2.5 (next page) - Lower hemisphere stereoplots of structures associated with Cretaceous shortening, plotted on the tectonic map of the studied area (complied after Kräutner and Krstić et al. (2003) and Basic geological map of former Yugoslavia, scale 1:100.000). Faults coloured in purple are thrusts active during this phase, light green faults are active strike-slip faults, while black faults are other major faults in the area. Suggested faults or faults covered by Neogene sediments are dashed. Dark green straight lines indicate positions of cross-sections in Fig. 2.4. Numbered structures in stereoplots are linked to map structures with the same number. Stereoplots legend: 1-thrust fault, 2-strike-slip fault, 3-normal fault, 4-fold axis. Note that plots Go2 D1 and Tu1 D1 show stretching lineations with a sense of shear.

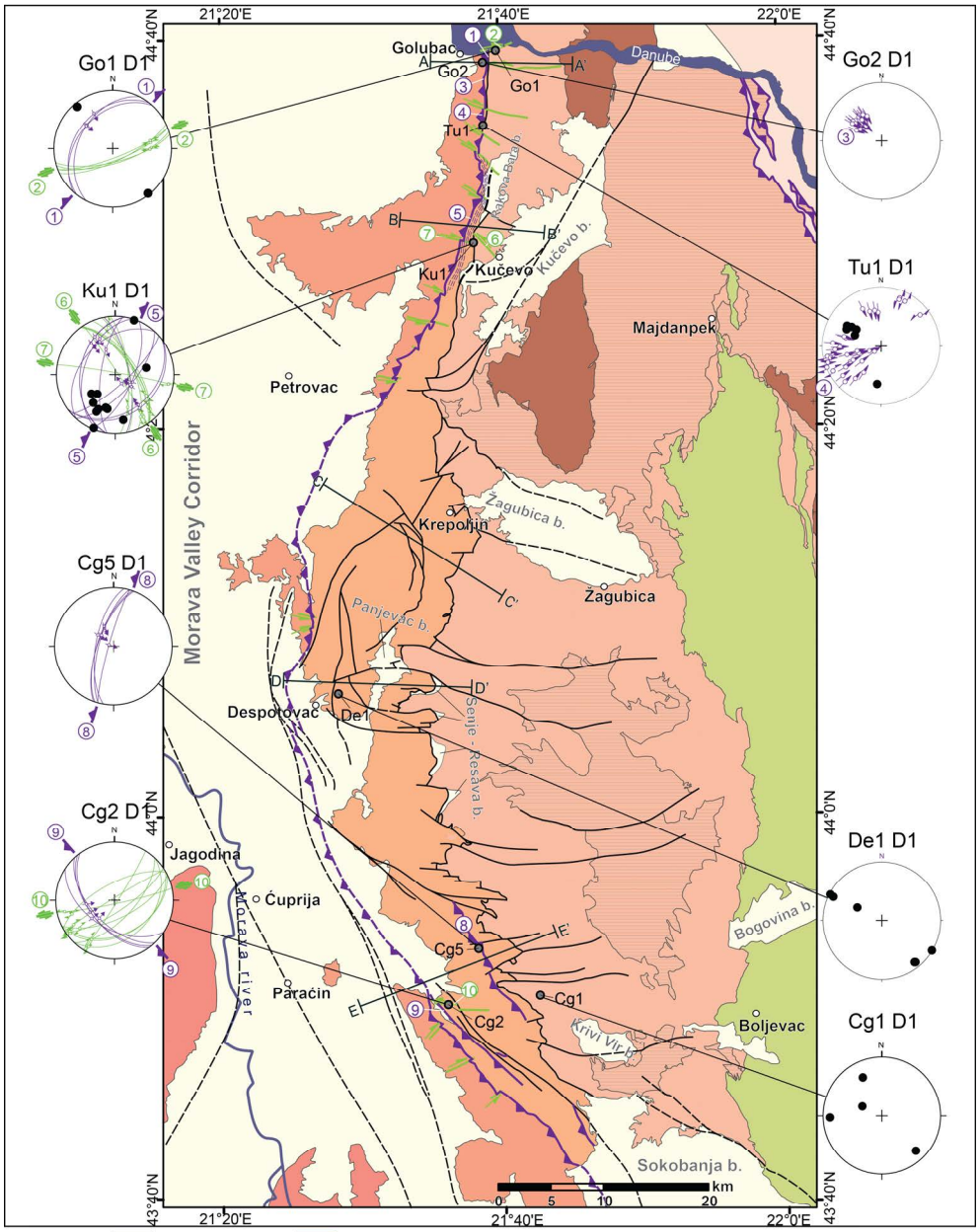
21°20'E
21°40'E
22°0'E
44°40'N
44°20'N
44°0'N
43°40'N
Golubac
Go2
Go1
Tu1
Danube
Rakovačka b.
Kučevo b.
Kučevo
Ku1
Majdanpek
Petrovac
Morava Valley Corridor
Žagubica b.
Krepoljin
Žagubica
Panjevac b.
Despotovac
De1
Senje - Resava b.
Jagodina
Ćuprija
Morava river
Paraćin
Cg5
Cg2
Cg1
Bogovina b.
Krivi Vir
Boljevac
Sokobanja b.
km
0 5 10 20
Go1 D1
Go2 D1
Ku1 D1
Tu1 D1
Cg5 D1
De1 D1
Cg2 D1
Cg1 D1
Cenozoic basin
Timok Zone
Serbo-Macedonian
Supragetic
Upper Getic
Lower Getic sediments
Pre-Alpine intrusions
Lower Getic basement
Danubian
Stereoplots
1
2
3
4
Thrust fault
Normal fault
Strike-slip fault
Wide shear zone
Studied site
Town

2.3.1 NW-SE to NE-SW oriented shortening in the vicinity of the Supragetic thrust

Although less extensive, the first set of structures are dominantly located along or in the vicinity of the Supragetic thrust and in all cases the observed faults and folds are buried beneath the sediments of the overlying upper Oligocene - Miocene basins and do not deform them (Fig. 2.5). These structures are more frequent in the northernmost and the southern segments of the studied area (near Golubac and Kučevo in the north and east of Paraćin in the south, Fig. 2.5), being truncated at outcrop and map scale by all other subsequent deformation. The Paleozoic basement of the Supragetic unit and the neighbouring Mesozoic limestones of the Upper Getic sub-unit are affected by a deformation characterized by moderate- to high-angle thrusts. These thrusts are oriented NE-SW in the northern part of the studied area and have a top to SE - E oriented tectonic transport (structures 1, 3, 4, 5 in Fig. 2.5) which changes to NW-SE and top to NE in the southern part (e.g., structure 9 in Fig. 2.5), although some local variability is recognized at farther distances from the Supragetic thrust (structure 8 in Fig. 2.5). These two different orientations of thrusts are not observed in the same location. Thrusting is associated with numerous sub-vertical strike-slip faults (structures 2, 6, 7, 10 in Fig. 2.5), whose orientation in outcrops and at map scale is generally perpendicular to the map-scale thrusts.

In more detail, deformation at or near the Supragetic thrust is more intense and indicates a different degree of burial of its hanging wall and footwall. An up to a few tens of meters thick low-grade metamorphic (low to very low greenschist facies) to cataclastic shear zone was observed in the Paleozoic metamorphics of the hanging wall. This hanging wall is affected by pervasive shearing, where a stretching lineation is observed to be associated with shear-bands and/or sigma clasts affecting oriented quartz aggregates (structures 3 and 4 in Fig. 2.5). For example, in the northern area near Golubac, such hanging-wall shearing in quartz aggregates is associated with a top to SE direction of tectonic transport (e.g., structure 3 in Fig. 2.5 and Fig. 2.6a). This shearing is sub-parallel with the dominantly W-dipping foliation of the Supragetic metamorphics. Often decimeters thick shear zones are observed affecting the Mesozoic limestones located in the immediate footwall of the Supragetic thrust (structure 5 in Fig. 2.5 and Fig. 2.6b). In the northern part of the studied area, deformation along these shear zones indicates thrusting with a dominant top-SE to E direction of tectonic transport, locally associated with NW-vergent backthrusts (structure 5 in Fig. 2.5), or with E-W to NW-SE oriented strike-slip faulting observed by conjugate Riedels in the main shear zone (site Ku1, structures 6 and 7 in Fig. 2.5). In the southern part of the studied area, the overall deformation changes to NW-SE oriented thrusts or shear-zones that have a dominant NE direction of tectonic transport (structure 9 in Fig. 2.5 and Fig. 2.6c) and are associated with NE-SW oriented strike-slip faults, cross-cut at map scale by subsequent strike-slip deformation (structure 10 in Fig. 2.5). The sense of shear along closely spaced thrusts truncating Tithonian limestones in the footwall of the Supragetic thrust is often derived from syn-kinematic growth of calcite fibers, grooves and centimeter-scale stylolites (an example is shown in Fig. 2.6c).

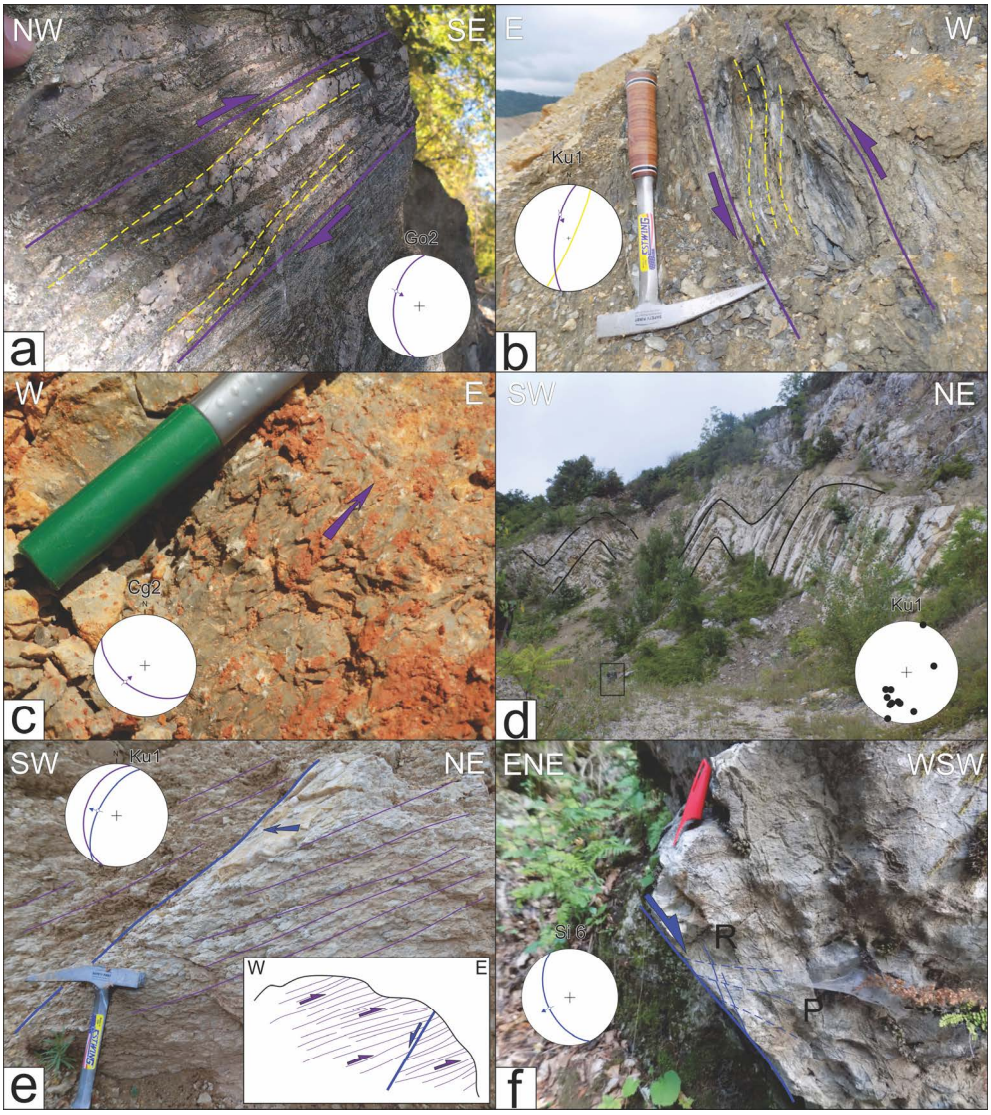

Figure 2.6 - Interpreted field photos of ductile to cataclastic structures associated with the late Early Cretaceous thrusting and subsequent Paleogene–Miocene orogen-perpendicular extension. The orientation of each photo is indicated in the upper right and upper left corners. Structures in the photos are plotted in stereoplots. Purple arrows and half arrows illustrate kinematics of interpreted structures related to the Cretaceous deformation, and blue ones indicate kinematics of subsequent extensional structures. a) Top to SE ductile thrusting in Supragetic unit metamorphic basement. Studied site Go2. b) Shear bands with a reverse sense of shear in Upper Getic sub-unit Tithonian limestones. These form a cataclastic C–S fabric. Studied site Ku1. c) Fault plane with stylolites as kinematic indicators demonstrating top to NE thrusting. Studied site Cg2. d)

Asymmetric decameter scale folds (see a standing man in the black rectangle for scale) in Tithonian limestones of the Upper Getic sub-unit in the footwall of the Supragetic thrust. Black lines represent bedding. Fold axes are plotted in lower hemisphere stereoplot. Vergence of the folds indicates top to SE thrusting. Studied site Ku1. e) Normal fault (blue arrow illustrates the relative hanging wall movement) truncating the cataclastic shear zone (purple lines) formed in Tithonian limestones in the footwall of the Supragetic thrust. Studied site Ku1. Inset: Outcrop-scale cross-section sketch of the relationship between thrusting-related foliation (purple lines and half arrows) and N-S oriented normal fault (blue half arrow). f) Normal fault with associated R and P Riedel shears, indicating NE-SW oriented orogen-perpendicular extension in Tithonian limestones at the studied site Si6.

The character of deformation changes at distance (few hundred meters) in the footwall of the Supragetic thrust, where the pervasive shearing is replaced by meter-scale, slightly asymmetric folds that are oriented NE-SW and have a SE vergence in the northern part of the studied area (e.g., site Ku1 in Fig. 2.5 and Fig. 2.6d). The asymmetric folds are oriented NW-SE with NE vergence in the southern part of the studied area, although the number of measurements is rather limited (e.g., site Cg1, Fig. 2.5). At kilometres distances, few high-angle reverse faults are observed in this footwall, which are truncated by subsequent normal faults in outcrops and map scale (structure 8 in Fig. 2.5 and structure 14 in Fig. 2.7).

2.3.2 Multi-geometry extension and strike-slip

Superposition criteria and truncation of the upper Oligocene – Miocene basins indicate that the Supragetic thrusting is followed in time by three types of structures. The first type of structures are N-S oriented, dominantly W-dipping normal faults, which are observed more frequently near the contact with the Morava Valley Corridor and in the vicinity of the Upper Getic thrust contact (dark blue in Fig. 2.7). These faults often truncate the previously described thrusts, as observed near Kučevo (site Ku1, structure 2 in Fig. 2.7). Here, the previously formed cataclastic foliation in the footwall of the Supragetic thrust is cross-cut in one example by a W-dipping normal fault (Fig. 2.6e). Outside main shear or fault zones, this deformation is observed along individual fault planes or Riedel shears by calcite slickenfibres, such as the top to SW normal faulting in Tithonian limestones of the Upper Getic sub-unit at site Si6 (Figs. 2.6f and 2.7). The strike of outcrop-scale normal faults and associated map-scale shear zones gradually changes southwards from N-S in the northern part of the studied area to NNW-SSE and NW-SE, with some local variations. This change follows the regional change in the strike of the main nappe contacts, while generally remaining (sub-)parallel to them, normal faults being observed both above and below the thrusts at outcrop scale. Map-scale normal faulting can be documented only in the vicinity of the Morava Valley Corridor and Upper Getic thrust contact, more frequent in the areas of Krepoljin and Despotovac (structures 4–7 and 9–10 in Fig. 2.7). The sense of shear is dominant top-W and top-E north of Despotovac and top- WSW to SW southwards, although the number of available

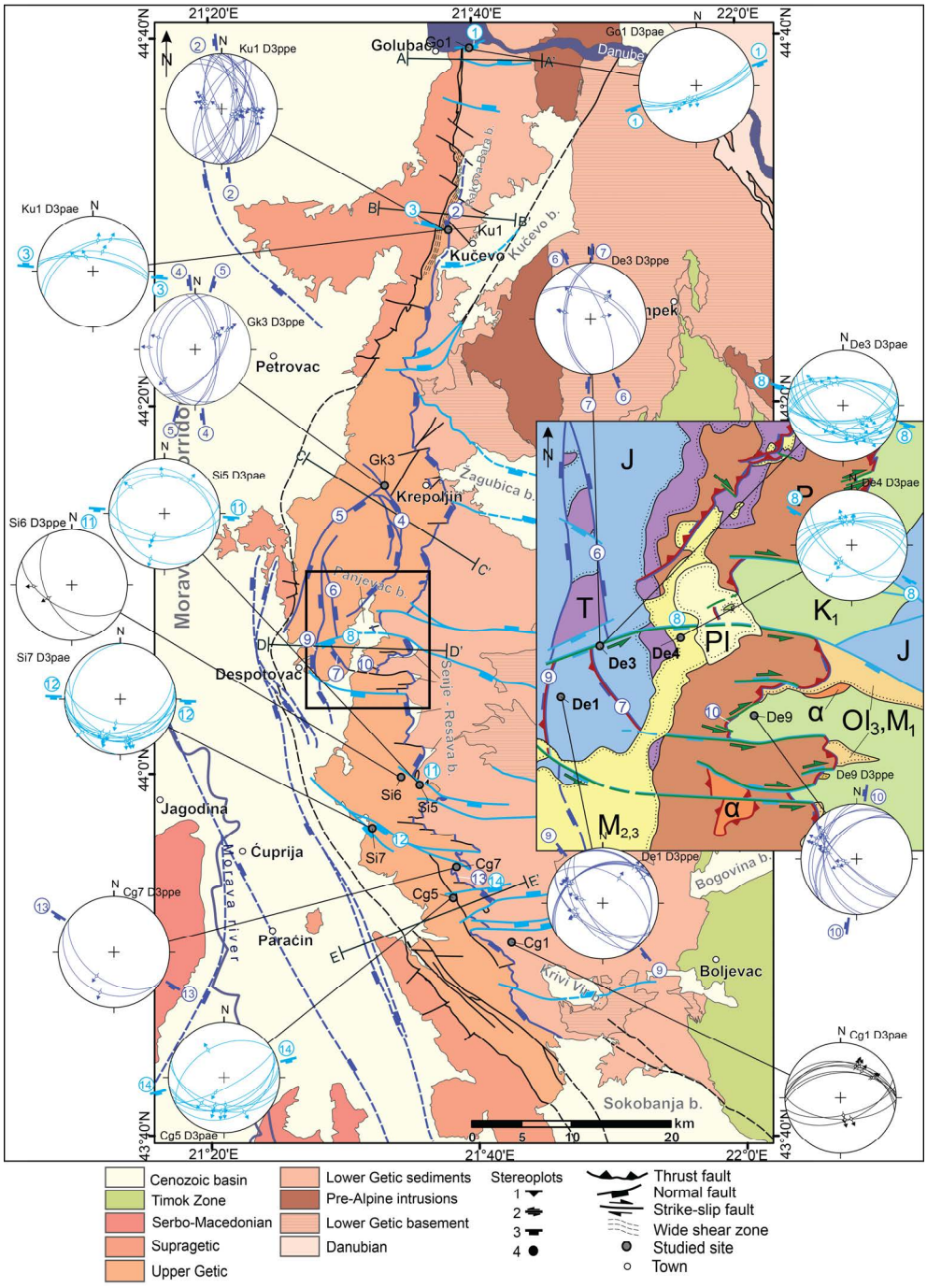
21°20'E
21°40'E
22°0'E
44°40'N
44°20'N
44°0'N
43°40'N
Golubac
Ku1 D3ppe
Gc1 D3pae
Danube
Ku1
Kučevo
Kučevo b.
Petrovac
Gk3 D3ppe
Gk3
Krepoljin
Žagubica b.
Si5 D3pae
Si6 D3ppe
Si7 D3pae
Despotovac
Panjevac b.
Senje - Resava b.
Si6
Si5
Si7
Jagodina
Ćuprija
Morava river
Paraćin
Cg7
Cg5
Cg1
Cg7 D3ppe
Cg5 D3pae
De3 D3ppe
De4 D3pae
De1 D3ppe
De9 D3ppe
Cg1 D3pae
Bogovina b.
Boljevac
Krivi Vir
Sokobanja b.
km
0 5 10 20
J
T
P
K1
Pl
De3
De4
De1
De9
α
Ol3,M1
M2,3
Cenozoic basin
Timok Zone
Serbo-Macedonian
Supragetic
Upper Getic
Lower Getic sediments
Pre-Alpine intrusions
Lower Getic basement
Danubian
Stereoplots
1
2
3
4
Thrust fault
Normal fault
Strike-slip fault
Wide shear zone
Studied site
Town

Figure 2.7 (previous page) - Map of the studied area (same conventions as in Fig. 2.5) with lower hemisphere stereoplots of structures associated to Oligocene–Miocene orogen-perpendicular and orogen-parallel extension. Faults coloured in dark and light blue are activated by these extensions, respectively. Black faults are other major faults in the area. Suggested faults or faults covered by Neogene sediments are dashed. The black rectangle shows the position of the inset in the right part of the figure. Inset: Simplified geological map of a segment of the Senje-Resava Basin thrusted by Permian sediments of Upper Getic sub-unit (simplified and modified after Basic geological map of former Yugoslavia, scale 1:100.000 and data from this study). P-Permian red clastics; T-Triassic clastics and limestones; J-Jurassic clastics and limestones; K1-Lower Cretaceous limestones and marls; α-Upper Cretaceous Banatites; Ol3,M1-upper Oligocene to lower Miocene sediments of Senje-Resava Basin; M2,3-middle to upper Miocene sediments of Morava Valley Corridor and adjacent basins; Pl-Pliocene conglomerates and travertine.

observations in the latter area is reduced. A higher density of such normal faults is observed near the Senje–Resava Basin, where they appear to control the Oligocene–early Miocene sedimentation (e.g., sites De9 and Cg7, structures 10 and 13 in Fig. 2.7) and are truncated by the subsequent Upper Getic thrusting, as explained below. The number and offset of such normal faults indicating orogen-perpendicular extension decrease eastwards, at farther distances from the Morava Valley Corridor and the Upper Getic thrust contact.

The second type of structures observed is made up of a large number of strike-slip faults (Fig. 2.8), which are distributed in the entire studied area and have variable kinematics from pure strike-slip to oblique-slip. This strike-slip deformation is dominantly dextral, with NNE-SSW to N-S oriented faults in the northern and central parts (Figs. 2.8, 2.9a,b) and further to NNW-SSE to NW-SE more southwards in the studied area (Figs. 2.8, 2.9c). Conjugate sinistral faults are commonly observed, varying in orientation from NE-SW to N-S oriented faults (Figs. 2.8, 2.9d). This change in orientation of outcrop-scale strike-slip faults also follows the general change in the strike of the main nappes contact from north to south, although local variations are also observed (Fig. 2.8). The character of this deformation is variable, from breccias and fault gouges in up to 50 cm wide shear zones to localized shearing along individual fault planes (e.g., Fig. 2.9a–d). These strike-slip faults were found locally to truncate or reactivate the older mylonitic to cataclastic foliation that formed at the Supragetic unit thrust contact. For example, in location Tu1 (structure 1 in Fig. 2.8) the reactivation is visible by dm-scale dextral shearing and mineral growth along individual fault planes (Fig. 2.9a) truncating the ductile to cataclastic foliation of the W-ward dipping high-

Figure 2.8 (next page) - Map of the studied area (same conventions as in Fig. 2.5, inset is same as in Fig. 2.7) with lower hemisphere stereoplots of structures associated with regional strike-slip deformation. Faults coloured in green are active during this phase. Black faults are other major faults in the area. Suggested faults or faults covered by Neogene sediments are dashed.

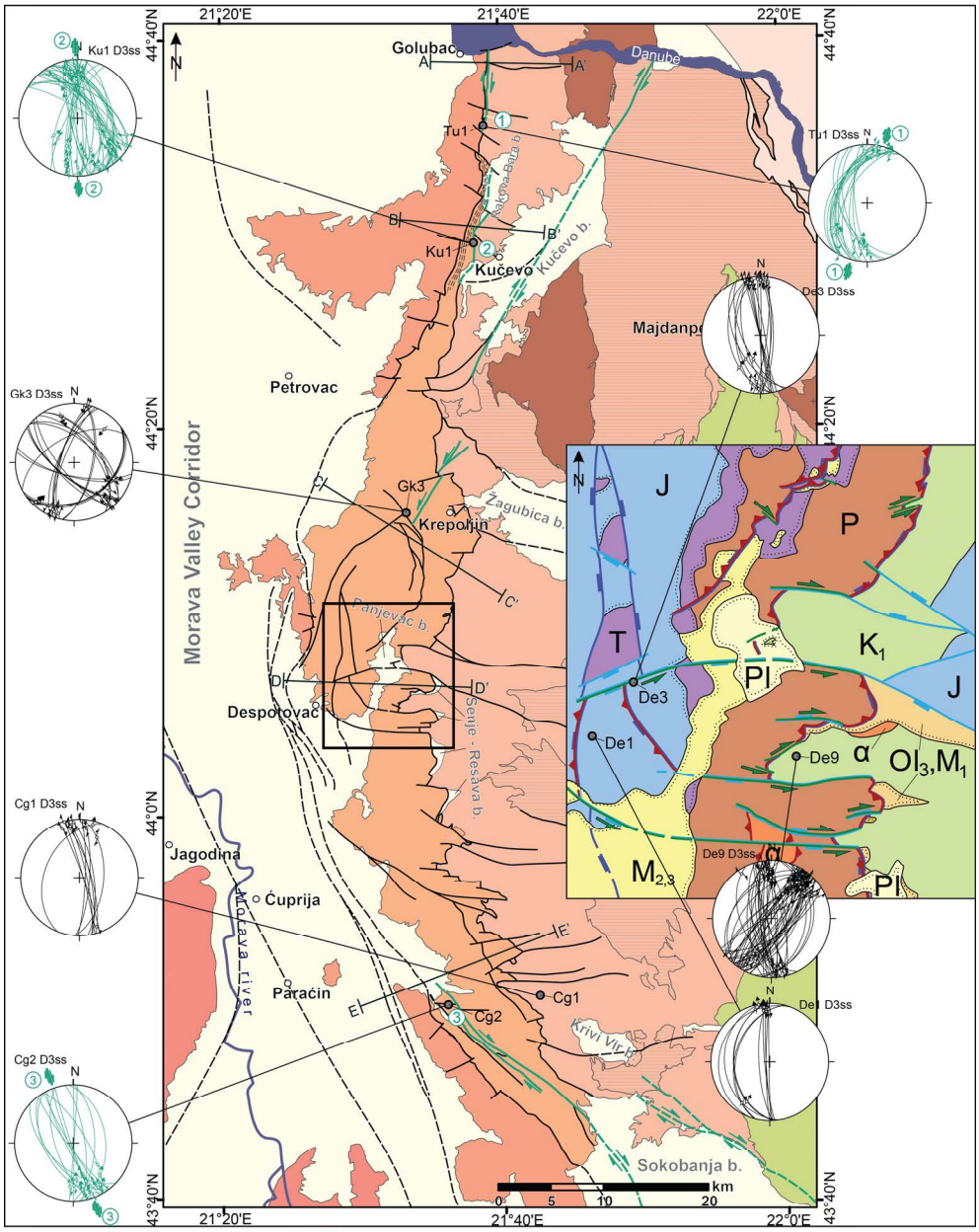
21°20'E
21°40'E
22°0'E
44°40'N
44°20'N
44°0'N
43°40'N
N
Golubac
A
A'
Danube
Tu1
Tu1 D3ss
Rakovačka b.
B
B'
Ku1
Kučevo
Kučevo b.
Majdanpe
De3 D3ss
Petrovac
Gk3 D3ss
Morava Valley Corridor
C
C'
Gk3
Krepoljin
Žagubica b.
Panjevac b.
D
D'
Despotovac
Senje - Resava b.
Cg1 D3ss
Jagodina
Ćuprija
Morava river
Paraćin
E
E'
Cg1
Cg2
Cg2 D3ss
Krivi Vir
Sokobanja b.
km
0 5 10 20
J
P
T
K1
Pl
De3
De1
De9
α
Ol3,M1
M2,3
De9 D3ss
Cenozoic basin
Timok Zone
Serbo-Macedonian
Supragetic
Upper Getic
Lower Getic sediments
Pre-Alpine intrusions
Lower Getic basement
Danubian
Stereoplots
1
2
3
4
Thrust fault
Normal fault
Strike-slip fault
Wide shear zone
Studied site
Town

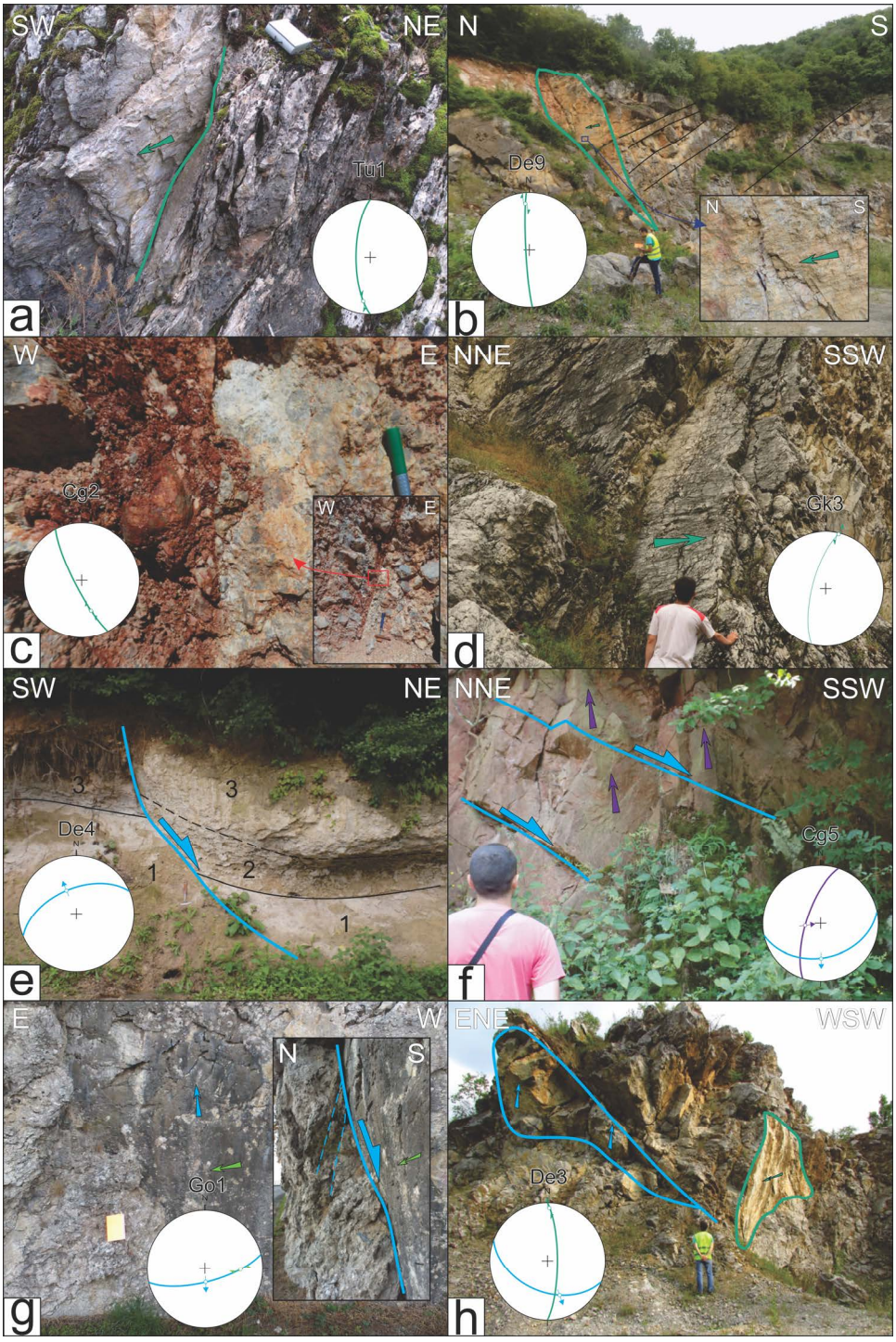
SW
NE
Tu1
a
N
S
De9
N
S
b
W
E
Cg2
W
E
c
NNE
SSW
Gk3
d
SW
NE
3
3
De4
N
1
2
1
e
NNE
SSW
Cg5
f
E
W
N
S
Go1
g
ENE
WSW
De3
h

Figure 2.9 (previous page) - Interpreted field photos of brittle structures related to Paleogene to Miocene deformation. The orientation of each photo is indicated in the upper right and upper left corners. Structures in the photos are plotted in stereoplots. a) Dextral, N-S oriented strike-slip fault (green arrow) truncating older thrusting related foliation in weakly metamorphosed Upper Jurassic limestones of the Upper Getic sub-unit. Studied site Tu1. b) Dextral, N-S oriented strike-slip fault offsetting tilted Lower Cretaceous limestones (black lines indicate bedding position) of the Lower Getic sub-unit at studied site De9. Inset illustrates the fault surface in detail with striations that indicate dextral shearing (green arrow shows the relative movement of the missing block). c) Fault breccia associated with NW-SE oriented dextral strike-slip fault zone at location Cg2. d) NNE-SSW oriented sinistral fault in Tithonian limestones. Studied site Gk3. e) Syn-kinematic sedimentation in the hanging wall of a normal fault during orogen-parallel extension (blue half arrow) in the middle to upper Miocene sediments (1-sandy siltstones, 2-conglomerates, 3-marls, the dashed line indicates a gradual transition from conglomerates to marls). Studied site De4. f) Outcrop of Permian sandstones of the Upper Getic sub-unit demonstrating normal faults activated by orogen-parallel extension (blue half arrows) truncating high angle reverse faults interpreted as a result of late Early Cretaceous thrusting (dipping towards the camera, purple arrows). Studied site Cg5. g) Dextral, ENE-WSW oriented strike-slip fault with weakly preserved striations (light green arrow indicates a relative movement of the footwall) that was reactivated by orogen-parallel extension as documented by Riedel shears in fault breccia (inset, blue half arrow). Studied site Go1. h) N-S oriented dextral fault (green arrow illustrates a relative movement of the missing block) and ESE-WNW oriented normal fault (blue arrow indicates a relative movement of the footwall). Interaction and superposition of faults are not clear. Studied site De3.

angle shear fabric of Tithonian limestones. However, most often such strike-slip deformation is observed along isolated faults that cannot be connected with regional structures and stratigraphic offsets, for instance in the vicinity of the Upper Getic thrust at site De9, where a decimetre to meter scale sub-vertical dextral fault deforms Lower Cretaceous limestones (Figs. 2.8 and 2.9b). Strike-slip kinematics is well visible in fault gouges, such as NW-SE oriented dextral strike-slip fault in Cg2 (Figs. 2.8 and 2.9c), or along thick slickensides or calcite slickenfibres, such as a NNE-SSW oriented sinistral fault observed in Tithonian limestones at site Gk3 (Figs. 2.8 and 2.9d). Despite the fact that outcrop kinematics is characterized often by a large number of isolated faults measured in the field, these are associated with only a few regional, map-scale dextral shear zones (Fig. 2.8). These shear zones are N-S to NNE-SSW oriented near Golubac and Kučevo in the north (structures 1 and 2 in Fig. 2.8) and NW-SE in the south, as observed SE of Paraćin (structure 3 in Fig. 2.8).

The third type of structures observed in the field consists of E-W oriented normal faults that are perpendicular to the orogenic strike and indicate orogen-parallel extension (light blue in Fig. 2.7). Conjugated N-and S- dipping normal faults were observed in outcrops and can be associated with regional, map-scale shear zones. In outcrops, this deformation is characterized by individual fault planes, or by fault breccias or meters

thick foliated fault gauges, when the observed offset is larger. These faults are associated with syn-kinematic sedimentation, such as observed in the middle–upper Miocene sediments of the Panjevac Basin (site De4, structure 8 in Fig. 2.7; see also Antonijević et al., 1970), where coarser wedge-shaped sediments were deposited only in the hanging-wall of E-W oriented normal faults that were overlain by deeper water sedimentation (Fig. 2.9e). These normal faults truncate earlier reverse faults, as observed in the Permian sandstones of the Upper Getic thrust (e.g., site Cg5, structure 14 in Fig. 2.7), where such truncation is observed along low-angle normal faults that indicate N-S extension (Fig. 2.9f). In other locations, these normal faults reactivate E-W oriented strike-slip faults formed by the first deformation event (e.g., structures 1 and 3 in Fig. 2.7), such as observed in Upper Jurassic limestones of the Lower Getic sub-unit (site Go1, structure 1 Figs. 2.7 and 2.9g). In this site, E-W oriented normal faults create a fault breccia that contains planes with inherited sub-horizontal dextral strike-slip slickensides. Interestingly, the E-W oriented normal faults and N-S oriented strike-slip faults overprint each other in outcrop kinematics, observed often in the vicinity of such normal fault with large, map scale offset (e. g., site De3, Figs. 2.7, 2.8 and 2.9h). Such an interplay between normal faulting and strike-slip infers that the two types of structures formed during the same tectonic event. In map view, regional E-W oriented normal faults border many of the Neogene basins, where they control the early middle Miocene sedimentation and are overlain by younger deposits (Figs. 2.2 and 2.7). These faults are also associated with tilting and exhumation of the metamorphosed Paleozoic sediments in their footwall (Fig. 2.7), suggesting a listric or block tilting geometry. These bordering normal faults decrease their offsets laterally along their strike, which imply increased amounts of extension in the centre of the Lower Getic sub-unit where the Paleozoic metamorphosed basement is more widely exposed (Fig. 2.7).

We note that these three sets of normal and strike-slip faults could have been formed during three successive deformation events, partly overlapping, or they can belong to the same event by distributing the strain along differently oriented structures. Available superposition timing criteria are not fully diagnostic.

2.3.3 Top-E thrusting of the Upper Getic sub-unit

Superposition criteria indicate that the youngest deformation type is associated with a large number of reverse faults with E-ward vergence that are associated with the thrusting of the Upper Getic sub-unit (commonly Permian red sandstones) over the Lower Getic sub-unit, commonly made up by Lower Cretaceous limestones and the upper Oligocene–lower Miocene sediments of the Senje–Resava Basin (Figs. 2.2 and 2.10). Two sets of structures were observed in the field in map-scale shear zones.

Figure 2.10 (next page) - Map of the studied area (same conventions as in Fig. 2.5, inset is same as in Fig. 2.7) with lower hemisphere stereoplots of structures associated with late Miocene shortening. Faults coloured in red are active thrusts during this contraction and green faults are active strike-slip faults. Black faults are other major faults in the area. Suggested faults or faults covered by Neogene sediments are dashed.

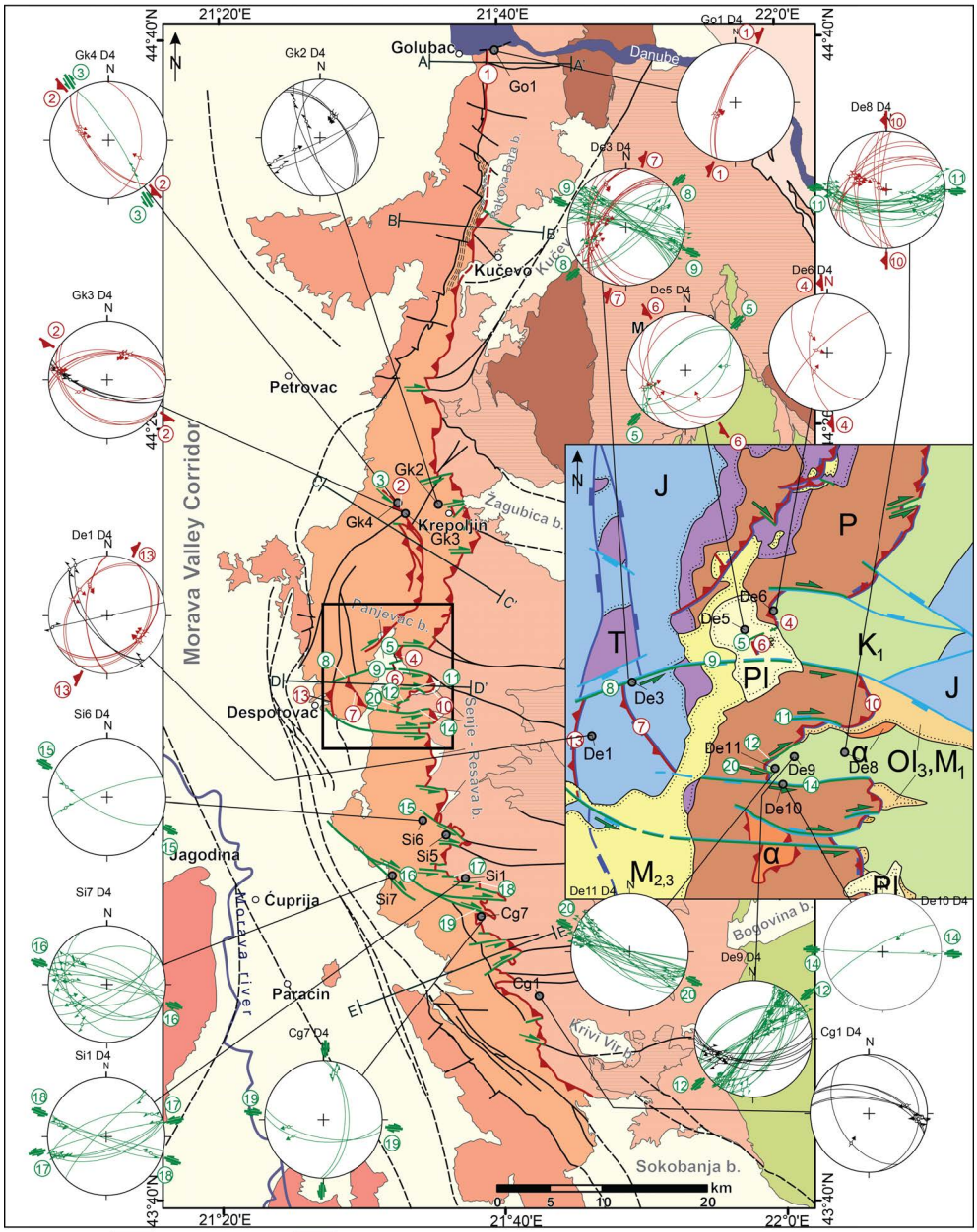
21°20'E
21°40'E
22°0'E
44°40'N
43°40'N
Golubac
Danube
Go1
Kučevo
Petrovac
Morava Valley Corridor
Krepoljin
Gk2
Gk4
Gk3
Despotovac
Jagodina
Ćuprija
Paračin
Morava river
Sokobanja b.
Žagubica b.
Panjevac b.
Senje - Resava b.
Bogovina b.
Krivi Vir
Kučevo b.
Beljanica - Bela b.
A
A'
B
B'
C
C'
D
D'
E
E'
M
J
P
T
K1
Pl
α
Ol3,M1
M2,3
0 5 10 20 km
Cenozoic basin
Timok Zone
Serbo-Macedonian
Supragetic
Upper Getic
Lower Getic sediments
Pre-Alpine intrusions
Lower Getic basement
Danubian
Stereoplots
1
2
3
4
Thrust fault
Normal fault
Strike-slip fault
Wide shear zone
Studied site
Town

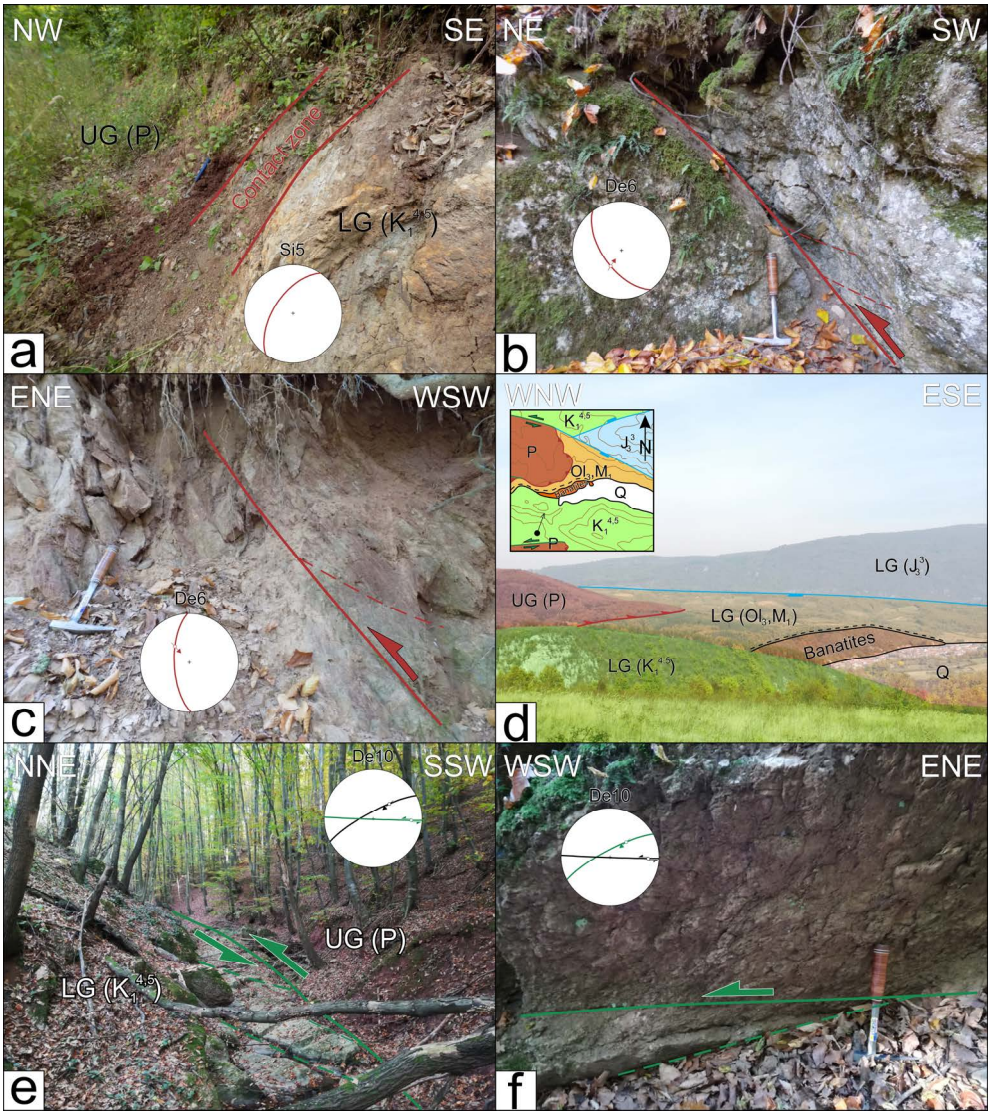

Figure 2.11 - Interpreted field photos of structures related to the Upper Getic thrust. The orientation of each photo is indicated in the upper right and upper left corners. Structures in the photos are plotted in stereoplots. UG-Upper Getic sub-unit; LG-Lower Getic sub-unit; P-Permian sandstones; J3 3 -Tithonian limestones; K14,5-Barremian–Aptian limestones; Banatites - Upper Cretaceous subvolcanic intrusion; Ol3,M1-upper Oligocene to lower Miocene sediments; Q-Quaternary sediments; a) Upper and Lower Getic sub-units in a high angle contact at studied site Si5. b) Lower Cretaceous limestones of the Lower Getic sub-unit in the footwall of the Upper Getic thrust, few meters away from UG/LG contact. Studied site De6. c) Permian sandstones of the Upper Getic sub-unit, few meters away from UG/LG contact in the hanging wall of the thrust. Studied site De6. d) Interpreted landscape view of the Upper Getic thrust. Note the low

angle geometry of the thrust with footwall represented by the early Miocene sedimentary sequence of the coal-bearing Senje–Resava Basin. Inset illustrates a simplified geological map of the area shown in the photo (modified after Basic geological map of former Yugoslavia, scale 1:100.000) with the position of the camera (black dot) and the azimuth of camera view (black arrow). e) Sub-vertical sinistral strike-slip fault (thick green line, green great circle in stereoplot) accommodating different offsets of the Upper Getic thrust segments north and south of the fault. Riedel shears are associated with this fault (dashed green lines, black great circle in stereoplot) and are defining a sense of shear along this major fault. Studied site De10. f) Sinistral strike-slip fault (green great circle in stereoplot) as one of the Riedel shears from Fig. 2.11e. Studied site De10.

The first set of structures is thrusts or oblique-reverse faults that are dominantly top-E and are observed along the Upper Getic thrust and its vicinity (e.g., structures 1, 2, 4, 6, 7, 10 and 13 in Fig. 2.10). This Upper Getic thrust is generally high angle where Permian sandstones are thrust over Lower Cretaceous limestones (e.g., site Si5, Figs. 2.10 and 2.11a). Although the thrust itself is rarely exposed, its kinematics is obvious in the immediately adjacent rocks affected by the wider shear zone (e.g. site De6, Figs. 2.10, 2.11b, c). The same structure is low angle when it is thrusted over the poorly consolidated upper Oligocene to lower Miocene sediments of the Senje–Resava Basin. These sediments do not create foliated fault gouges or other types of shear zones where kinematics can be measured. However, the kinematics of the contact can be measured in the Permian - Mesozoic rocks affected by the shear zone in the hanging wall or at farther distances in the footwall, while its geometry can be derived from the topographic expression (e.g., Fig. 2.11d). Interesting is that E-vergent thrusting over the upper Oligocene – Miocene sediments reactivate often earlier orogen-perpendicular normal faults (e.g., structure 2 in Fig. 2.10).

The second set of structures is observed in outcrops along numerous strike-slip faults (Fig. 2.10), where they are always associated with roughly E-W oriented map-scale shear-zones that connect various segments of the Upper Getic thrust and are both dextral and sinistral (structures 3, 5, 8, 9, 11, 12, 14–19 in Fig. 2.10). The orientation and sense of shear of the strike-slip faults measured in outcrops mirrors the ones of the E-W oriented map-scale faults, while often conjugates are observed (such as in the case of structures 12, 15 and 19 in Fig. 2.10). These strike-slip faults are generally perpendicular to the orientation of the Upper Getic thrust when offsetting this structure, while locally changing their strike towards NW-SE or NE-SW at farther distances. Typically, such strike-slip faults offset the Upper Getic thrust with 1–5 km (e.g., structure 14 in Fig. 2.10 and site De10, Fig. 2.11e), while outcrop kinematics is often derived from large Riedel shears (Figs. 2.11e, f).

Interestingly, measurements of bedding and the geometry of faults show vertical axis rotation in the vicinity of strike-slip faults due to local drag-folding, where differently oriented faults with the same kinematics are situated in the immediate vicinity. This situation is visible, for example, in site De9 (Fig. 2.10), where E-W oriented dextral strike-slip faults are rotated clockwise by dragging along a higher offset, NE-SW oriented dextral fault (structure 12, black and green respectively in plot De9 D4, Fig. 2.10).

2.4 Interpretation

The results of the kinematic study show a complex poly-phase tectonic evolution of the studied segment of Serbian Carpathians that reflects the formation of the highly bent Dacia Mega-Unit of the Carpatho–Balkanides overprinted by Dinarides orogenic processes. Although many structural elements are common with neighbouring segments of the South Carpathians and Balkanides, a number of deformation stages are specific to the studied area that relate in particular to multi-phase extension, strike-slip deformation and vertical axis rotations.

2.4.1 Cretaceous nappe emplacement

The oldest phase of contraction led to the nappe emplacement of the Supragetic unit that was associated with tear faulting (Fig. 2.5). Structures observed in this unit indicate that the onset of thrusting was associated with transitional ductile-brittle deformation that is cross-cut in later stages by brittle thrusts or tear faults. Such a succession of deformation during the same tectonic event indicates exhumation of the Supragetic unit during thrusting. This interpretation is in agreement with the observation of ductile structures at the Supragetic/Getic contact in the South Carpathians, dated at 120 Ma (Dallmeyer et al., 1996). Alternatively, one can interpret the ductile structures to be formed during an older Variscan event, while only the brittle ones formed during the Cretaceous thrusting. However, the ductile to brittle structures have the same kinematics, while the continuous exhumation is justified by the offset and geometry of Paleozoic-Mesozoic strata truncated by the Supragetic thrust (Fig. 2.4). Although the Cretaceous offset along the Supragetic thrust is difficult to estimate due to the absence of reliable markers, the transition from ductile to brittle deformation during thrusting indicates a minimum of 10–15 km offset. The youngest sediments affected by this thrusting are Lower Cretaceous limestones (Fig. 2.3), while the Supragetic thrust is truncated by all subsequent deformation and is often covered by Oligocene - Miocene sediments of the Morava Valley Corridor (Fig. 2.5).

Outcrops and regional cross-sections indicate that thrusting was associated with the formation of E-vergent folds and a wide shear zone at the Supragetic thrust that recorded splaying by the formation of trailing imbricated fans in the Upper Getic footwall (Fig. 2.4). The Supragetic thrusting has a flat-ramp geometry (e.g., Fig. 2.4a) that changes its offset along the orogenic strike (compare cross-sections in Figs. 2.4a, b, e). Changes in offset are accommodated by the formation of ~E-W oriented sub-vertical tear faults and lateral ramps (Fig. 2.5). A similar deformation style by the formation of ramp-folds, fault-propagation folds and asymmetric E-vergent folds is observed in the Upper Getic sub-unit. However, while the Supragetic thrust is covered by all Oligocene - Miocene sediments, the Upper Getic sub-unit thrusts with a large offset over these sediments (Figs. 2.4c–e) and has only a brittle character. This demonstrates that the thrusting of the two units took place during different deformation events, i.e. the Supragetic thrusting took place during the Cretaceous, while the Upper Getic thrusting took place during the late Miocene. However, it is also possible that the Upper Getic thrusting has been initiated during the Cretaceous by the low amount of offset observed in the north (Figs.

2.4a, b) by splaying in the footwall of the Supragetic thrust, while being reactivated during the late Miocene.

The overall transport direction of the Supragetic thrusting changes along the strike of the orogen from top-SE in the north to top-NE in the south, remaining always perpendicular to the present oroclinal geometry of the nappes. This wide variation in thrusting direction does not reflect two separate shortening events, but the observed change in contraction direction is the result of vertical-axis rotations post-dating the main Cretaceous thrusting event. This rotation agrees with a gradual increase in subsequent Paleogene–Miocene clockwise vertical axis rotation from negligible in the Balkanides to 90° in the South Carpathians (Csontos and Vörös, 2004; van Hinsbergen et al., 2008). These differences in contraction direction observed in the studied area suggest that ~40° of differential Paleogene–Miocene clockwise rotations have been taken up by the Serbian Carpathians after the Cretaceous thrusting (Fig. 2.5).

2.4.2 Paleogene to middle Miocene interplay between bi-directional extension and strike-slip

Although not directly apparent in the large-scale structure of the studied Serbian Carpathians, our detailed field observations infer that three of the observed deformation types are in fact different structural responses formed during a long-lived tectonic event that post-dated the Cretaceous nappe stacking.

The first type are normal faults that are oriented (sub-) parallel to nappe contacts and are clustered in the western part of the studied area near the Supragetic and Upper Getic thrusts (dark blue in Fig. 2.7). These normal faults have a dominant W-ward dipping direction and are associated with the initial Oligocene - early Miocene extension observed in the Morava Valley Corridor, together with Senje–Resava, Panjevac and Bogovina basins (e.g., Figs. 2.2 and 2.4c–e, Erak et al., 2017; Mai, 1995; Matenco and Radivojević, 2012; Obradović and Vasić, 2007; Pavlović, 1997; Žujović, 1886). The large number of N-S oriented and W-dipping normal faults clustered in the immediate vicinity of the Upper Getic/ Lower Getic contact indicates a larger amount of extension in the Morava Valley Corridor and the Senje–Resava Basin. It is likely that these two basins were initially continuous and part of a larger Morava Valley Corridor Oligocene - middle Miocene depositional area, being separated subsequently by the late Miocene thrusting of the Upper Getic sub-unit (Fig. 2.4c–e).

Based on all of these observations and correlations, we interpret that orogen-perpendicular extension has created the initial subsidence in the Morava Valley Corridor and the adjacent intramontane basins in the western part of the presently exposed Serbian Carpathians during Oligocene–early Miocene times. The change from E-W extension in the northern and central parts of the studied area to more NE-SW extension in the south follows the change in the orientation of main Supragetic and Getic units. Therefore, this change also indicates up to ~40° vertical-axis rotations largely post-dating the main extensional deformation.

The second type, strike-slip deformation has created NE-SW to NW-SE oriented dextral and sinistral faults that are distributed throughout the entire studied area at outcrop scale. The fact that only a few map-scale faults with low offset can be attributed to this deformation (Fig. 2.8) indicate a diffused and/or distributed character of

deformation, which is in agreement with previous observations (Mladenović et al., 2019). Outside the studied area, the kinematics and geometry of these outcrop-scale faults are compatible with the activation of the well-known and similarly 40°–80° curved large dextral strike-slip faults, the ~35 km offset late Oligocene Cerna Fault and ~ 65 km offset early Miocene – early middle Miocene Timok Fault (Fig. 2.2, Berza and Drăgănescu, 1988; Kräutner and Krstić, 2003). When compared with these large offset dextral faults, our kinematic observations indicate a similar change from NW-SE dextral in the south to more N-S dextral in the north associated with a compatible change in the direction of conjugate sinistral faults, although there is significant variability between these directions across the entire studied area (Fig. 2.8). The differences in strike-slip directions between the north and the south show ~40° of clockwise rotations, while the variability of deformation indicate that strike-slip deformation took place before or during rotation.

The third type, orogen-parallel extensional structures, is associated with numerous outcrop-scale E-W oriented normal faults that can be directly correlated with larger offset (<1 km) regional E-W oriented normal faults and shear zones (light blue in Fig. 2.7). These normal faults truncate the Paleozoic basement in the centre of the studied area, while northwards and southwards they control the onset of early middle Miocene deposition in the Žagubica and Krivi Vir Basins. Furthermore, similar E-W oriented normal faults control the early middle Miocene onset of deposition in large intramontane basins outside our studied area, such as Sokobanja and Svrljig Basins and also, possibly, in the Bela Palanka Basin (Fig. 2.2). These basins have asymmetric, half-graben geometry that shows increasing subsidence towards the main controlling fault located southwards (Marović et al., 2007). With the notable exception of the Žagubica Basin that shows a WNW-ESE orientation (i.e., 20–30° clockwise rotation), all other basins and genetically associated faults are E-W oriented along the entire curved geometry of the Serbian Carpathians (Fig. 2.2). This observation suggests that the N-S oriented orogen parallel extension took place dominantly after the ~40° clockwise rotation.

Although our study cannot fully discriminate a complete superposition of events, all these observations indicate that the three deformation types (orogen- perpendicular and parallel normal faulting combined with strike-slip) developed successively, but partly overlapped in time. The late Oligocene onset of orogen-perpendicular extension largely predates the ~40° of clockwise rotation, the latest Oligocene-early middle Miocene stage of strike-slip took place during the clockwise rotation and the early Miocene–early middle Miocene stage of orogen-parallel extension largely postdates the clockwise rotation. All these three deformation types can be actually grouped in a continuous late Oligocene–early middle Miocene tectonic event that took place during the overall clockwise rotation of the Serbian Carpathians, accommodated by the 100 km cumulated offset of the curved Cerna-Timok Fault system. One can obtain the previously reported variable strike-slip paleostress stress field for the Oligocene - middle Miocene rotation of the Serbian Carpathians (Mladenović et al., 2019) by cumulating all these three deformations together. However, our shear zone analysis correlated with the progression in ages and geometry of the intramontane basins shows a better separation in three successive, partly overlapping stages where the rotations create significant strain-partitioning between strike-slip and extension.

2.4.3 Late Miocene Upper Getic thrusting

The last deformation event observed in our studied area is the thrusting of the Upper Getic sub-unit, which took place likely by reactivating the orogen-perpendicular normal fault system inherited from the Oligocene - early Miocene deformation stage. The age of this event is constrained by the thrusted late Oligocene–early Miocene sediments of the Senje–Resava basin. Field kinematics and regional structures formed during this event truncate all previous ones, while the main thrust is covered by the upper part of Žagubica and Sokobanja Basins sedimentation, which is the latest Miocene–Pliocene in age (Fig. 2.10). Therefore, the age of this top-E thrusting of the Upper Getic sub-unit is late Miocene.

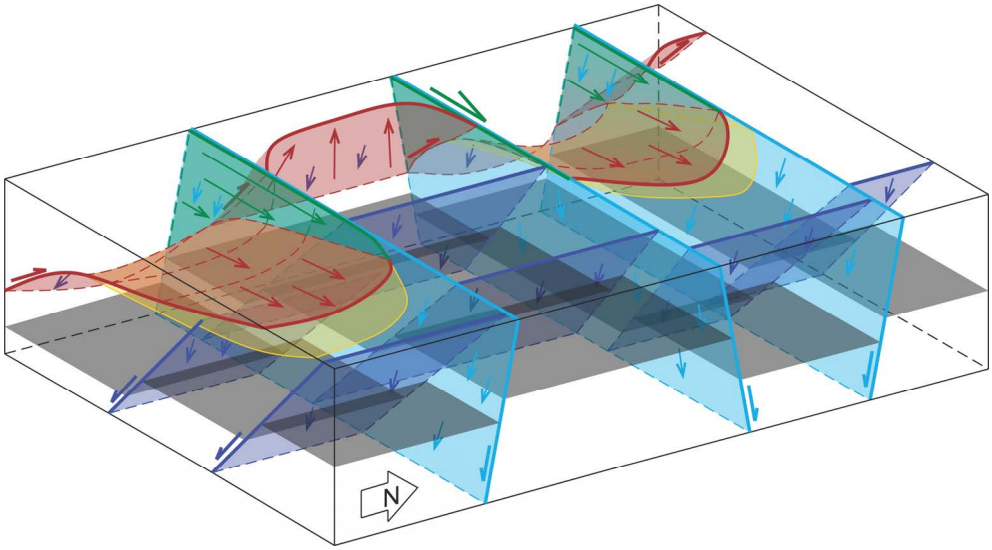

Figure 2.12 - 3D sketch of structural superposition and mechanics of Oligocene-Miocene extension and subsequent shortening in the vicinity of the Upper Getic thrust. Dark blue normal faults formed during orogen-perpendicular extension, light blue normal faults formed during orogen-parallel extension. These faults control the subsequent formation of thrusts (red) and strike-slip tear faults (green). Sediments of the Senje-Resava Basin are shown in yellow colour, while black horizons are drawn to illustrate offsets along normal faults. Arrows and half arrows show the relative movement of the hanging wall. When faults are re-activated, longer arrows indicate younger movement.

In the northern part of the studied area, the Upper Getic sub-unit is narrow, while the thrusting offset is in the order of 1 km (Figs. 2.4a, b, 2.10). Here, this unit formed as a fontal trailing imbricated fan of the Supragetic thrust where a possible Cretaceous offset cannot be clearly discriminated from the late Miocene one. Southwards in the studied

area, the total offset of the Upper Getic thrust gradually increases to more than 6 km (Fig. 2.4c–e). This Miocene thrusting forms a large ramp-anticline over the Oligocene–early Miocene sediments of the Senje–Resava Basin (Fig. 2.4c–e). More southwards, the offset along the Upper Getic thrust decreases rapidly towards the Sokobanja Basin, where this thrust is buried beneath younger sediments (Fig. 2.10). South of this basin and outside the study area, there is no equivalent of the Upper Getic thrust that can be observed at map scale (Fig. 2.2). The significant variability in thrusting along the Upper Getic strike also explains the formation of numerous E-W oriented strike-slip tear faults that laterally offset this structure (Fig. 2.10). Many of these tear faults are in fact lateral ramps that formed as normal faults during the orogen-parallel deformation stage (Fig. 2.12). These E-W normal faults have initially segmented the margin of the Senje–Resava Basin, preserving the late Oligocene-early Miocene sediments in their hanging walls. The lateral variability between late Oligocene-early Miocene sediments and Cretaceous limestones has created a rheologically heterogeneous footwall for the thrusting of the Upper Getic sub-unit (Fig. 2.12). The large scale tearing and the surface expression of the Upper Getic sub-unit demonstrate the thrusting was controlled by the inherited normal faulting associated with the formation of the Senje–Resava Basin.

2.5 Discussion

The Cretaceous thrusting of the Supragetic Unit is in agreement with the timing and geometry of the Sasca–Gornjac and Resita nappes defined northwards in the South Carpathians of Romania, emplaced during late Early Cretaceous times in the footwall of the main Supragetic thrust (e. g., Iancu et al., 2005a; Kräutner and Krstić, 2002; Săndulescu, 1984). However, no late Miocene thrusting of the equivalent Upper Getic thrust contact has been observed in the South Carpathians, which is in agreement with our interpretation that the late Miocene reactivation is reducing gradually its offset to zero northwards. It is likely that the Supragetic thrusting took place during the late Early Cretaceous, as observed in the South Carpathians (Fig. 2.13a). There are no indications that the latest Cretaceous Getic thrusting and the formation of the Danubian nappe stack (Fig. 2.13a) has also re-activated the Supragetic thrust only in the Serbian Carpathians prior to the subsequent activation of the CernTimok Fault system. However, we cannot completely exclude such a hypothesis due to the lack of further timing indicators, such as thermochronology or post-tectonic covers.

The orogen-perpendicular extension, strike-slip and orogen-parallel extension can be correlated with the formation of Oligocene-Neogene basins. The ~29–27 Ma onset observed in the Jastrebac area (Erak et al., 2017) is the earliest possible age of the orogen-perpendicular extension (Fig. 2.13b). An orogen-perpendicular back-arc extension driven by the roll-back of a Carpathians slab roll-back is not possible in the N-S Serbian segment adjacent to the fixed Moesian Platform (Fig. 2.1, see also Matenco and Radivojević, 2012). Therefore, the observed orogen-perpendicular extension must be related to processes active during the evolution of a Dinarides slab, such as slab-detachment or subsequent eduction (Andrić et al., 2018), which is compatible with the observed directions of extension (Figs. 2.1 and 2.13b).

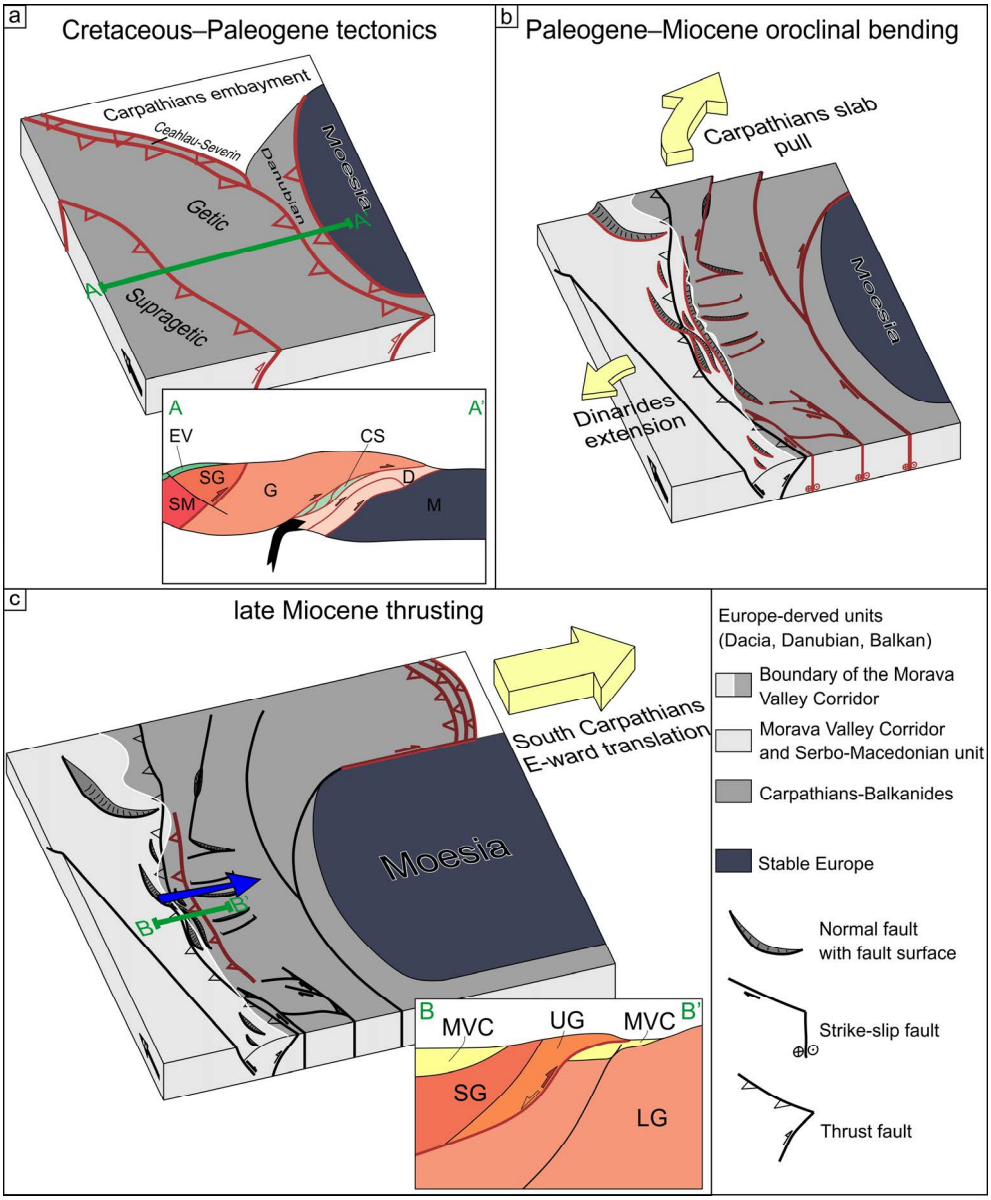

Figure 2.13 - a) 3D and cross-section sketches of main tectonic units and structures active during the Cretaceous–Paleogene shortening. EV-Eastern Vardar Ophiolitic unit, SM-Serbo-Macedonian unit, SG-Supragetic unit, UG-Upper Getic sub-unit, LG-Lower Getic sub-unit, CS-Ceahău-Severin unit, D-Danubian units, M-Moesian Platform. The 3D sketch is built after the map-view sketch of Fügenschuh and Schmid (2005). The position of the cross-section is indicated by the green line. b) 3D sketch of oroclinal bending mechanics with complex fault pattern that includes regional dextral strike-slip and orogen-parallel and perpendicular normal faults, mainly controlled by Carpathian

slab retreat to the north and north-east, the position of the rigid Moesian indenter and extension in the Dinarides to the west. c) 3D and cross-section sketches of the late Miocene reactivation of the Upper Getic thrust during the indentation by Moesian Platform (stable Europe). The direction of shortening in the Serbian Carpathians is indicated by the blue arrow. The cross-section sketch shows the Upper Getic thrusting over sediments of the Cenozoic basins. The position of the cross-section is indicated by the green line. MVC- Morava Valley Corridor sediments, SG-Supragetic unit, UG-Upper Getic sub-unit, LG-Lower Getic sub-unit.

2.5.1 Mechanisms of backarc-convex oroclinal bending

Our kinematic analysis correlated with paleomagnetic rotations measured in the South Carpathians indicates that ~40° of clockwise rotations took place during late Oligocene–middle Miocene times. The kinematics and timing are in agreement with the geometry and moments of activation of the large offset and curved late Oligocene Cerna and early Miocene Timok faults (Figs. 2.2 and 2.13b, e.g., Maţenco, 2017; Schmid et al., 2008). This kinematics indicates that oroclinal bending in the Serbian Carpathians has started with strike-slip deformation, which was gradually replaced in the later stages by the orogen-parallel extension (Fig. 2.13b). This overall mechanism is only partly compatible with observations by previous studies in the South Carpathians, where a longer and a more continuous coexistence of strike-slip and orogen-parallel extension has been inferred (Krézsek et al., 2013; Fügenschuh and Schmid, 2005; Matenco and Schmid, 1999). There, oroclinal bending triggered the formation of the Danubian detachment during the Paleocene-Eocene, which remained active until the early middle Miocene, overlapping in time with the activity of Cerna and Timok dextral strike-slip faults and the transtensional formation of the Getic Depression Basin (e.g., Dupont-Nivet et al., 2005; Fügenschuh and Schmid, 2005; Matenco and Schmid, 1999; Moser et al., 2005; Schmid et al., 1998). This basin was subsequently transpressionally inverted in middle-late Miocene times to form the South Carpathians foredeep (e.g., Matenco et al., 2003; Răbăgia et al., 2011). Furthermore, coeval transtension and orogen parallel extension in the South Carpathians has accommodated the observed shortening of the East Carpathians at their contact with the Moesian Platform by a gradual progression of deformation NE- and E- wards during Oligocene–middle Miocene times (Krézsek et al., 2013). In other words, while deformation started with orogen-parallel extension during Paleocene-Eocene and continued with coeval late Oligocene–middle Miocene strike-slip and orogen-parallel extension in the South Carpathians, the studied segment of the Serbian Carpathians indicates a progression from strike-slip to orogen-parallel extension during the latest Oligocene - middle Miocene.

Our studied case of the Serbian Carpathians is the one of a major intra-continental strike-slip fault system (i.e., Cerna–Timok) that formed coevally with oroclinal bending. Although deformation is distributed along a large number of small structures, we observe that oroclinal bending may be also associated with an orogen-perpendicular extension that evolves independently from the coupled strike-slip and orogen-parallel deformation. The former is driven by the interference with the geodynamic evolution of a different orogen (i.e. Dinarides). The latter is driven by the orogenic pull exerted by a slab-retreat

in a curved orogen, where orogen-parallel deformation starts closer to the slab (i.e., the South Carpathians) and develops progressively at farther distances (i.e., the Serbian Carpathians) in an orogen that gradually reorients itself perpendicular to the trench (i.e., the East Carpathians, Fig. 2.1).

Such observations are also known from other large-scale continental strike-slip faults, such as the San Andreas Fault, the Alpine Fault or the Dead Sea Fault, which show distributed deformation and strain partitioning in up to hundreds of kilometres wide zones (e.g., Dooley and Schreurs, 2012). Strike-slip shear zones often display oblique movements that create transpressive and/or transtensive deformation forming positive or negative flower structures, transpressional orogens and basins with highly variable geometries (Christie-Blick and Biddle, 1985; Dewey et al., 1998; Dooley and Schreurs, 2012; Leever et al., 2011; Smit et al., 2008, 2010). Furthermore, oblique or curved strike-slip zones show variable amounts of strain partitioning at releasing or restraining bends that show progressive evolution over time (e.g., Dewey et al., 1998; Fossen and Tikoff, 1998; Leever et al., 2011), associated with partitioning in normal or reverse faulting coeval with oroclinal bending (Allen et al., 2003; Hollingsworth et al., 2010; Mattei et al., 2017).

Foreland-convex oroclines dominate the Mediterranean region (Fig. 2.1a, e.g., Rosenbaum, 2014, and references therein) and are controlled by the retreat of subducting slabs (e.g., Faccenna et al., 2004; Jolivet et al., 2013; Johnston and Mazzoli, 2009; Lonergan and White, 1997). In our studied case of the Serbian Carpathians, the orogen-parallel extension took place during the formation of a back-arc-convex orocline (Fig. 2.1a and 2.13b). Such orogen-parallel extension has been observed or inferred during the formation of other backarc-convex oroclines, such as the Cantabrian arc of Ibero-Armorican orogen or Mongolian orocline (e.g., Pastor-Galán et al., 2012, 2015; Ries and Shackleton, 1976; Xiao et al., 2018). The formation of other backarc-convex oroclines has been controlled by an orogen-parallel compression induced by two converging cratons (e.g., Mongolian and Kazakhstan oroclines; Edel et al., 2014; Li et al., 2018), a collision between two or more rigid blocks with irregular margins (e.g., Alborz Mts., Brasília belt, central Pontides; D'el-Rey Silva et al., 2011; Mattei et al., 2017; Meijers et al., 2010) or an inherited initial curvature of the continental margin of the overriding plate (e.g., Bolivian and Cascadian oroclines; Finley et al., 2019; Isacks, 1988; Johnston et al., 2013; Weil and Sussman, 2004). These observations and correlations show that the type of orogen-parallel deformation is not relevant for the formation of a backarc-convex orocline. These oroclines are spatially controlled by the presence of a rigid, irregular continental block or craton that acts as an indenter during rotation. In the case of Serbian Carpathians orocline, the rigid Moesian promontory of the European continent controls the oroclinal geometry.

2.5.2 Late Miocene indentation of the Moesian Platform

Paleomagnetic studies have demonstrated that the large-scale clockwise rotation of the South and East Carpathians around the Moesian indenter has been achieved mostly until middle Miocene times and average ~ 15° afterwards, with a variability controlled by local rotations created by transpressional strike-slip structures (de Leeuw et al., 2013 and references therein; Lesić et al., 2019). The late Miocene thrusting of the Upper Getic

sub-unit observed in the Serbian Carpathians is coeval with the Adriatic indentation active in the Dinarides and, at the same time, is also coeval with the Carpathians docking against the Moesian Platform.

To the south and west, the indentation of the Adriatic promontory in the Dinarides inverted the Pannonian Basin and started during the latest Miocene. The effects of this indentation are more pronounced in the NW near the junction with the Southern Alps and in the SE near the other junction with the Albanides–Hellenides (e.g., Bennett et al., 2008; Pinter et al., 2005; Tomljenović et al., 2008). Close to the studied area, this Pannonian Basin inversion is expressed by E-W oriented thrusts and transpressional structures that recorded an uplift in the order of a few hundred meters (Matenco and Radivojević, 2012; Toljić et al., 2013). However, the N-S contraction direction of these structures is incompatible with the top-E direction of Upper Getic thrusting.

To the north and east, the dextral transpressional docking of the South Carpathians and the last phase of thin-skinned E-ward thrusting of the East Carpathians took place during the late middle–late Miocene times and ceased around 8 Ma, at the same time when the extension in the Pannonian Basin areas located north of the Morava Valley Corridor also ceased (e.g., Balázs et al., 2018; Maţenco, 2017). Because the main extension in the Morava Valley Corridor also ceased during middle Miocene times, it is likely that the late Miocene E-ward movement of the South and East Carpathians until 8 Ma was associated with E-ward thrusting reactivation of inherited normal fault between Upper and Lower Getic sub-units in the, by then, N-S oriented segment of the Serbian Carpathians (Figs. 2.12 and 2.13c, see also Ustaszewski et al., 2008 and references therein) during the late Miocene. The dextral movement of the E-W oriented South Carpathians in respect to the stable Moesian Platform was partly taken up by thrusting in the N-S oriented segment of the Serbian Carpathians. Such a mechanism would assume that the amount of thrusting gradually decreases as observed northwards in the Serbian Carpathians, while deformation being at the same time gradually transferred to dextral strike-slip north of the Moesian indenter (Fig. 2.13c), as observed in the South Carpathians (e.g., Matenco and Schmid, 1999). This mechanism should have been active only during late Miocene times, as the last phase of thin-skinned Pliocene–Quaternary deformation is localized only in the area of the SE Carpathians and was not observed in the intervening South Carpathians (e.g., Leever et al., 2006; Maţenco, 2017).

2.6 Conclusions

In order to understand the formation and evolution of the 180° of oroclinal bending recorded by the southern part of the Carpatho–Balkanides orogen, we have performed a kinematic study in the key area of the western Serbian Carpathians. The results demonstrate that this area was affected by a complex poly-phase kinematic evolution that recorded the geodynamic evolution of both the Carpathians and Dinarides orogen.

Following earlier Paleozoic and older deformation, the first shortening event that affected the studied part of the Serbian Carpathians was recorded by the late Early Cretaceous Supragetic thrusting, which is a peak deformation moment recorded during

the subduction of the Ceahlău-Severin Ocean and Carpathians continental collision. This thrusting largely pre-dates the oroclinal bending observed in the Serbian Carpathians.

Although not directly prominent in the large-scale orogenic structure, the second deformation event observed in the studied area was associated with a complex strain partitioning between partly overlapping stages of orogen-perpendicular extension, strike-slip and orogen parallel extension. This event took place mostly during the ~40° of oroclinal bending recorded by the studied segment of the Serbian Carpathians, derived from the variability of kinematic directions along the orogenic strike. The orogen-perpendicular extension is also compatible with the Oligocene onset of extension in the Morava Valley Corridor that is likely driven by the slab-detachment and eduction in the Dinarides. In contrast, the oroclinal bending in the studied part of the Serbian Carpathians was accommodated also by strike-slip deformation that was later gradually replaced by orogen parallel extension. This mechanism is compatible with the ~100 km of cumulated dextral strike-slip offset recorded along the curved fault geometry of the Cerna and Timok system located east of the studied area. These new insights on the rotational mechanisms of the Serbian Carpathians are somewhat different when compared with the neighbouring South Carpathians, which recorded first orogen-parallel extension followed by coupled strike-slip and orogen-parallel extension during Paleocene–middle Miocene times.

The last stage of deformation observed is the late Miocene thrusting of the Upper Getic sub-unit. Among all potential geodynamic mechanisms responsible for this thrusting, the one of transfer of deformation from dextral strike-slip at the northern margin of Moesian Platform in the South Carpathians to thrusting at the western margin of the same Moesian Platform in the Serbian Carpathians seems more likely. This deformation was coeval with the last moments of late Miocene thin-skinned thrusting until 8 Ma in the East and SE Carpathians and coeval extension in the Pannonian Basin.

Our study infers that the type of orogen-parallel deformation is not relevant for the formation of a backarc-convex orocline, such as the studied case of the Serbian Carpathians. These oroclines are spatially controlled by the presence of a rigid, irregular continental block or craton that acts like an indenter during rotation. In the case of Serbian Carpathians orocline, the rigid Moesian promontory of the European continent controls the oroclinal geometry. The study also shows the importance of a step-wise kinematic approach to reconstruct the tectonic evolution of highly curved orogens, such as the Carpathians–Balkanides, where strain partitioning is not apparent in their large-scale structure. Such reconstructions based on structural evidence must consider that strain partitioning overprints the inherited orogenic structure, in particular when differential rotations and translations are coeval. Understanding such structures must go beyond standard paleostress studies and must involve strain or shear-zone analysis and independent constraints, such as the coeval evolution of sedimentary basins.

2.7 Appendix

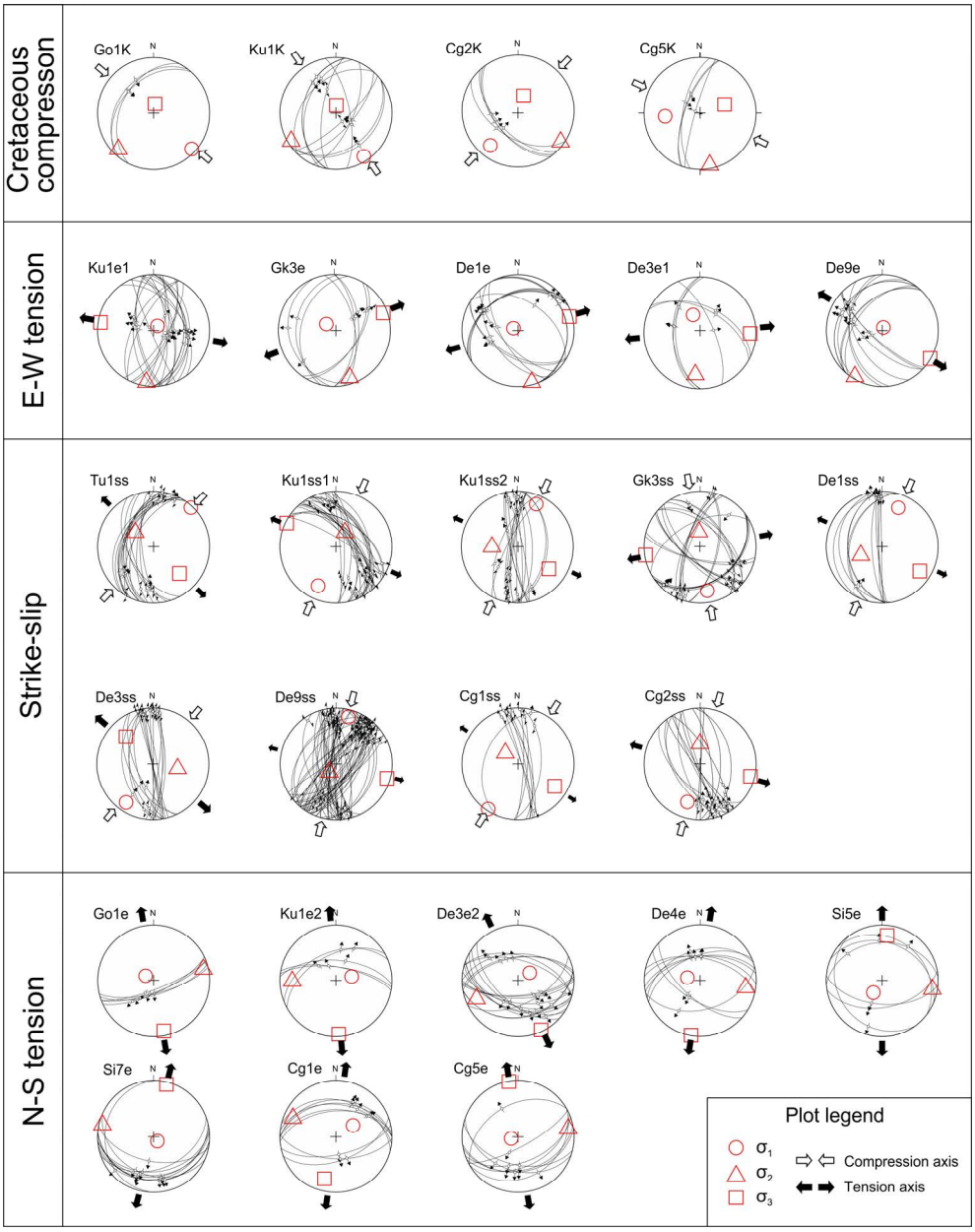

Figure 2.A1 - Stereoplots of calculated reduced paleostress tensors for Cretaceous compression, two tension and strike-slip regimes.

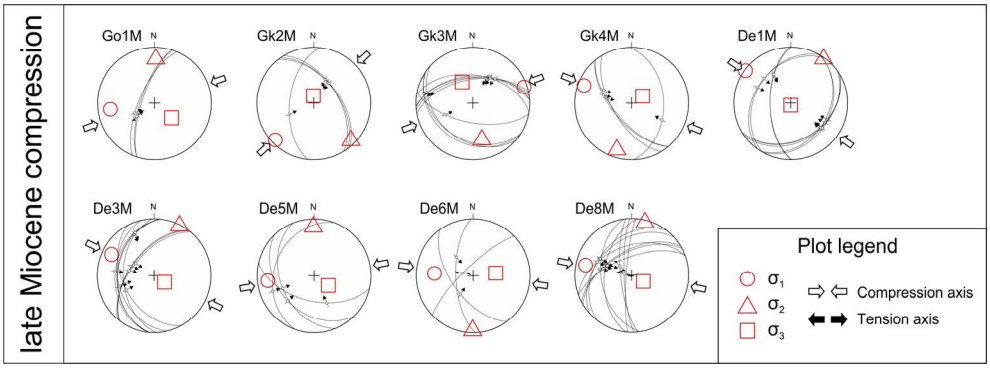

Figure 2.A2 - Stereoplots of calculated reduced paleostress tensors for late Miocene compression.

General regime	Tensor name	Longitude	Latitude	Tectonic unit	Rock stratigraphic age	σ_1	σ_2	σ_3	n	R	α	Tectonic regime
Cretaceous compression	Go1K	21°39'40"	44°39'28"	Lower Getic	Oxfordian-Hauterivian	133/08	225/11	009/76	3	0,5	8,5	compression
	Ku1K	21°38'08"	44°29'31"	Upper Getic	Upper Jurassic	147/09	238/06	003/79	11	0,6	8,3	compression
	Cg2K	21°35'57"	43°50'10"	Upper Getic	Tithonian	219/22	126/07	020/67	4	0,61	5,8	compression
	Cg5K	21°38'09"	43°53'00"	Upper Getic	Permian	265/37	169/07	071/52	4	0,6	4,7	compression
E-W tension	Ku1e1	21°38'08"	44°29'31"	Upper Getic	Upper Jurassic	041/81	188/07	279/05	21	0,35	10,6	extension
	Gk3e	21°33'19"	44°15'39"	Upper Getic	Tithonian	308/75	162/12	070/08	8	0,62	13,7	extension
	De1e	21°28'16"	44°06'12"	Upper Getic	Tithonian	297/83	165/05	075/05	14	0,39	5	extension
	De3e1	21°29'23"	44°07'15"	Upper Getic	Tithonian	339/62	186/11	091/11	6	0,38	7,8	extension
	De9e	21°33'15"	44°05'51"	Lower Getic	Barremian-Aptian	019/85	211/05	121/01	12	0,47	15,8	extension
Strike-slip	Tu1ss	21°38'50"	44°35'30"	Upper Getic	Upper Jurassic	043/04	308/56	136/34	18	0,3	14,6	strike-slip
	Ku1ss1	21°38'08"	44°29'31"	Upper Getic	Upper Jurassic	205/25	032/65	296/03	26	0,27	23,4	transpression
	Ku1ss2	21°38'08"	44°29'31"	Upper Getic	Upper Jurassic	024/17	269/53	125/32	18	0,21	23,3	transpression
	Gk3ss	21°33'19"	44°15'39"	Upper Getic	Tithonian	171/22	356/68	261/02	25	0,41	14,7	strike-slip
	De1ss	21°28'16"	44°06'12"	Upper Getic	Tithonian	022/25	248/56	123/21	11	0,22	10,9	transpression
	De3ss	21°29'23"	44°07'15"	Upper Getic	Tithonian	215/17	101/53	316/32	17	0,56	7,3	strike-slip
	De9ss	21°33'15"	44°05'51"	Lower Getic	Barremian-Aptian	014/14	220/75	106/06	66	0,13	15,2	transpression
	Cg1ss	21°42'30"	43°50'33"	Lower Getic	Barremian-Aptian	213/04	311/66	122/24	10	0,1	11,1	transpression
	Cg2ss	21°35'57"	43°50'10"	Upper Getic	Tithonian	198/29	000/60	104/08	24	0,35	14,1	strike-slip
N-S tension	Go1e	21°39'40"	44°39'28"	Lower Getic	Oxfordian-Hauterivian	301/76	077/10	169/09	5	0,61	8,7	extension
	Ku1e2	21°38'08"	44°29'31"	Upper Getic	Upper Jurassic	076/66	269/23	177/05	5	0,51	9,4	extension
	De3e2	21°29'23"	44°07'15"	Upper Getic	Tithonian	056/70	246/20	155/03	18	0,51	14,6	extension
	De4e	21°31'18"	44°07'20"	Neogene cover	middle-upper Miocene	282/71	099/19	189/01	9	0,39	8,5	extension
	Si5e	21°35'43"	43°59'17"	Upper Getic	Permian, Barremian-Aptian	216/68	100/10	006/19	6	0,43	6,2	extension
	Si7e	21°32'09"	43°56'54"	Upper Getic	Upper Jurassic	139/82	283/07	014/05	11	0,55	13,7	extension
	Cg1e	21°42'30"	43°50'33"	Lower Getic	Barremian-Aptian	056/60	293/17	195/24	9	0,56	4,3	extension
	Cg5e	21°38'09"	43°53'00"	Upper Getic	Permian	256/80	081/10	351/01	9	0,41	10,1	extension
late Miocene compression	Go1M	21°39'40"	44°39'28"	Lower Getic	Oxfordian-Hauterivian	262/23	002/23	131/57	3	0,55	0,8	compression
	Gk2M	21°35'40"	44°16'02"	Upper Getic	Banatites (Upper Cretaceous)	226/07	135/08	357/79	4	0,52	2,8	compression
	Gk3M	21°33'19"	44°15'39"	Upper Getic	Tithonian	072/06	166/34	333/56	9	0,59	6,4	compression
	Gk4M	21°32'41"	44°16'07"	Upper Getic	Upper Jurassic	291/11	198/15	057/71	4	0,4	4,1	compression
	De1M	21°28'16"	44°06'12"	Upper Getic	Tithonian	306/02	036/03	181/87	9	0,46	7,6	compression
	De3M	21°29'23"	44°07'15"	Upper Getic	Tithonian	296/18	027/02	123/72	9	0,36	16	compression
	De5M	21°32'07"	44°08'05"	Neogene cover	Pliocene	264/19	359/15	125/65	4	0,37	10,1	compression
	De6M	21°32'47"	44°08'29"	Upper Getic	Permian, Barremian-Aptian	273/32	180/04	084/57	3	0,47	9,6	compression
	De8M	21°34'34"	44°05'54"	Lower Getic	Barremian-Aptian	282/18	014/05	118/71	11	0,31	7,2	compression

Table 2.A1 – Results of the paleostress analysis for the studied area. σ1, σ2 and σ3 – dip direction/dip of the principal stress axis (σ1≥σ2 ≥σ3); n – number of faults in the set; R – stress ration (σ2- σ3)/(σ1- σ3); α – arithmetic mean of angles between measured and theoretical (calculated) slip direction

Chapter 3. Analogue modelling of strain partitioning along a curved strike-slip fault system during backarc-convex orocline formation: Implications for the Cerna-Timok fault system of the Carpatho-Balkanides[2]

[2] This chapter is based on Krstekanić, N., Willingshofer, E., Broerse, T., Matenco, L., Toljić, M., Stojadinovic, U., 2021. Analogue modelling of strain partitioning along a curved strike-slip fault system during backarc-convex orocline formation: Implications for the Cerna-Timok fault system of the Carpatho-Balkanides. Journal of Structural Geology 149, 104386. https://doi.org/10.1016/j.jsg.2021.104386

3.1 Introduction

Previous studies have shown that strike-slip deformation is often associated with segmentation of fold and thrust belts or mid-ocean ridges, with changes in polarity of subduction systems, as well as with lateral escape of continental lithosphere during indentation (e.g., Mann, 2007 and references therein). These studies have described complex deformation along numerous large-scale continental strike-slip faults, such as the San Andreas Fault (e.g., Anderson 1971.; Wallace, 1990), the Alpine Fault of New Zealand (e.g., Berryman et al., 1992), the North Anatolian Fault (e.g., Aramijo et al., 1999; Neugebauer, 1994), Dead Sea Fault system (e.g., Perinçek and Çemen, 1990; Smit et al., 2008), the Tibetan region and in Indochina (e.g., Chen et al., 2000; Morley, 2013), the Fagnano or the North Scotia Fault of South America (e.g., Lodolo et al., 2003), the Periadriatic Fault of the Alps, or the Mid-Hungarian Fault Zone of the Pannonian basin (e.g., Schmid et al., 2020). Many of these faults are associated with transpressional orogens or transtensive basins of various geometries and degrees of curvature in map view (e.g., Christie-Blick and Biddle, 1985; Dewey et al., 1998; Smit et al., 2008, 2010, among others). In these settings, the term strain partitioning has often been used in different ways and at different spatial scales to describe the large variability of observed deformation (e.g., Fitch, 1972; Lister and Williams, 1983; Platt, 1993; Carreras et al., 2013). Similar to other studies (Glen, 2004; Cembrano et al., 2005; De Vicente et al., 2009; D'el-Rey Silva et al., 2011; Krézsek et al., 2013; Benesh et al., 2014), we use the term "strain partitioning" to describe a multi-scale distribution of bulk strain into genetically different and coeval structures that cannot be explained by a uniform stress field.

Analogue and numerical modelling studies have demonstrated that the initiation and evolution of strike-slip corridors are always accompanied by significant strain partitioning, such as between Riedel shears and the main strike-slip fault (e.g. Leever et al., 2011; Dooley and Schreurs, 2012; Stefanov and Bakeev, 2014; Chemenda et al., 2016; Hatem et al., 2017; Iturrieta et al., 2017; Xiao et al., 2017). This strain partitioning is associated with significant local stress deviations and is more pronounced when either the movement is oblique to the main strike-slip fault, creating restraining and releasing bends with various geometries (e.g., Basile and Brun, 1999; McClay and Bonora, 2001; Smit et al., 2008; Leever et al., 2011; Dooley and Schreurs, 2012; González et al., 2012; Wang et al., 2017; Nabavi et al., 2018), or when the strike-slip fault has a curved geometry (e.g., Smit et al., 2010; Dufréchou et al., 2011). Furthermore, more complex systems of interacting thrusts and strike-slip faults have been observed or modelled (e.g., Duarte et al., 2011; Rosas et al., 2012, 2015; Fedorik et al., 2019). These studies have also shown that strain partitioning creates a gradual transfer of deformation from contraction to transpression and strike-slip. Other experimental studies have focused on deformation in front of an indenter (e.g., Marshak, 1988; Marshak et al., 1992; Zweigel, 1998 and references therein), where strike-slip deformation accommodates lateral extrusion (Tapponnier et al., 1982; Ratschbacher et al., 1991a, b; van Gelder et al., 2017). Often, strike-slip deformation links shortening in front of the indenter with deformation in another subduction system, such as observed in the Dinarides orogen connecting the shortening in the Alps with Aegean subduction (van Unen et al., 2019a), or the Sagaing

Fault linking the shortening in the Himalayas with the Sunda subduction zone (e.g., Tapponnier et al., 1986; Morley, 2002; Sternai et al., 2016). In such settings, the geometry and motion of the indenter influence significantly the deformation and structural response around the rigid indenter (Luth et al., 2013). However, the structural link (i.e., kinematics and geometry of major structures) between frontal, usually contractional, and lateral strike-slip deformation around the corner of an indenter is still not well understood.

One of the best examples of strain partitioning along curved strike-slip faults is the one of the Oligocene – middle Miocene Cerna-Timok fault system of the Carpatho-Balkanides orogen in South-Eastern Europe (Fig. 3.1). Previous studies have shown that this system has cumulated 100 km of dextral offset and links the deformation observed around the Moesian Platform (i.e., a rigid promontory in the prolongation of the East European Craton) along a 180° backarc-convex orocline connecting the South Carpathians, the Serbian Carpathians and the Balkanides (Fig. 3.1, e.g., Kräutner and Krstić, 2003; Schmid et al., 2020, and references therein). These studies have also shown that the same system transfers strike-slip deformation to thrusting and extension with variable offsets along its strike.

We aim to advance our understanding of the major parameters controlling strain partitioning and deformation transfer around indenters, with particular application to the Cerna-Timok fault system and associated deformation. To this aim, we performed a series of analogue experiments designed to analyse the deformational response to the shape of the rigid indenter (rounded or rectangular corners), the displacement (translation followed by rotation) along the margins of a rigid indenter and the rheological stratification of the deformable area. With respect to the latter, we analysed the influence of the flow in the ductile crust on the transfer and distribution of deformation. We use image correlation techniques for the detailed analysis of deformation around indenter corners in various experimental setups in order to qualitatively and quantitatively characterize the influence of their geometries on the deformation transfer. We compare the modelling results with the Cerna-Timok fault system of the Carpatho-Balkanides, which allows a detailed understanding of strain partitioning mechanisms during its Oligocene – middle Miocene evolution. We have chosen a strategy in the presentation of our results that involves first the description of a reference model with a simple analogue modelling setup, followed by a parametrical study of other models with a more complex initial geometry or composition. In a separate section, we show the relevance of a chosen best-fit model for understanding the evolution of the Cerna-Timok faults system and the associated Carpatho- Balkanides oroclinal bending. All modelling results are subsequently discussed in a process-oriented context.

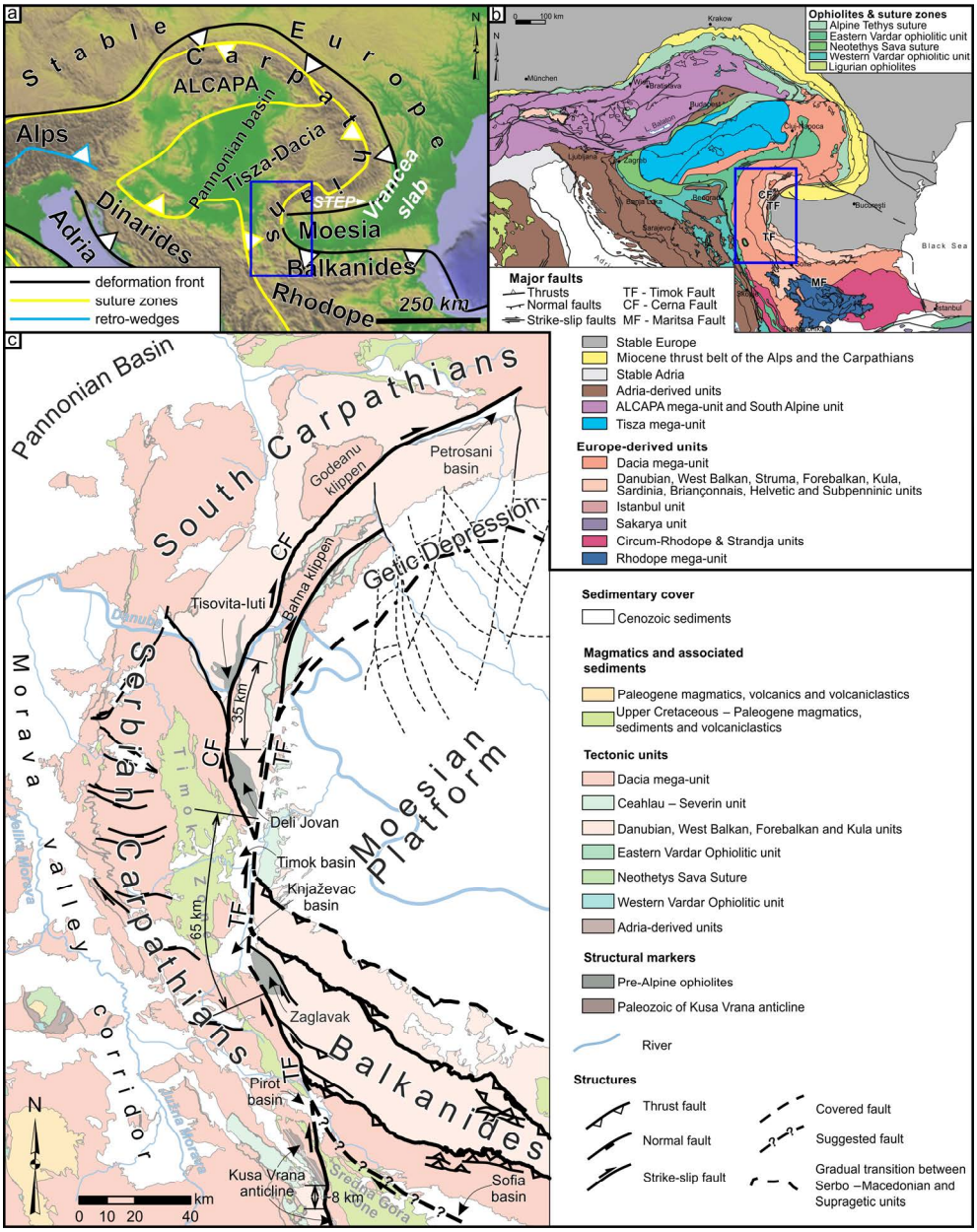

Figure 3.1 - a) Simplified topographic map of South-Eastern Europe overlain by the first-order structures (orogenic fronts, suture zones and retro-shears) of the Mediterranean Alpine-age orogens (modified from Krstekanić et al., 2020). The blue rectangle shows the location of Fig. 3.1c. STEP – Subduction-Transform Edge Propagator system in the South Carpathians. The white arrow indicates the direction of slab tearing. b) Regional tectonic map of south-east Europe (simplified after Schmid et al., 2020). The blue rectangle shows the location of Fig. 3.1c. c) Tectonic map of the

Cerna-Timok fault system in the South Carpathians-Serbian Carpathians-Balkanides orocline around the Moesian Platform. Black lines are faults that accommodate deformation related to oroclinal bending. CF – Cerna Fault; TF - Timok Fault. The map is compiled and modified after geological maps of Serbia, Romania and Bulgaria and Maţenco (2017). The structural pattern is modified after Maţenco (2017) and Krstekanić et al. (2020) while the suggested continuation of the Timok Fault below the Sofia basin is according to Schmid et al. (2020).

3.2 The Cerna-Timok fault system of the Carpatho-Balkanides orogen

The European area connecting the Carpathians and Balkanides orogenic system (Fig. 3.1a and b) shows a thick-skinned nappe-stack that was formed during two phases of Cretaceous shortening related to the closure of the Ceahlău-Severin branch of the Alpine Tethys Ocean and the subsequent collision between the Dacia mega-unit and the Moesian promontory of the stable European foreland (Săndulescu, 1988; Bojar et al., 1998; Csontos and Vörös, 2004; Iancu et al., 2005a; Schmid et al., 2008, 2020; Maţenco, 2017). The present-day geometry of the orogenic system shows two 180° curved loops, one in the north and east, and another in the south (Fig. 3.1a). This geometry was ultimately established during the Miocene slab retreat and gradual closure of the Carpathians embayment, consisting of oceanic crust and the continental passive margin of the Alpine Tethys Ocean (Fig. 3.1b, e g., Csontos and Vörös, 2004; Fügenschuh and Schmid, 2005). The southern 180° arc connects the South Carpathians, the Serbian Carpathians and the Balkanides by creating an orocline with a back-arc convex geometry bent around the Moesian Platform (Fig. 3.1a and b). The oroclinal bending formed by gradual clockwise rotation and N- to E-ward translation of the Dacia mega-unit during its movement into the Carpathians embayment. The post-Cretaceous rotation was significant (up to 90°) in the South Carpathians when compared to no significant rotation in the Balkanides (e. g., Balla, 1987; Pătraşcu et al., 1994; Márton, 2000; Ustaszewski et al., 2008; van Hinsbergen et al., 2008; Panaiotu and Panaiotu, 2010).

Previous studies have demonstrated that the clockwise rotation was first accommodated by Paleocene – Eocene orogen-parallel extension in the South Carpathians (Matenco and Schmid, 1999; Fügenschuh and Schmid, 2005; Schmid et al., 1998) and subsequently by the evolution of the late Oligocene – middle Miocene curved dextral Cerna and Timok faults system (Fig. 3.1c, Berza and Drăganescu, 1988; Ratschbacher et al., 1993; Kräutner and Krstić, 2002). Tectonic and lithological markers show that the Cerna Fault (CF) accommodates up to 35 km of dextral offset, as documented by the distance observed between the Godeanu and Bahna klippen, or between the Tisovita-Iuti and Deli Jovan ophiolites (Fig. 3.1c, Kräutner and Krstić, 2003). In comparison, the Timok Fault (TF) has up to 65 km dextral offset, inferred by the distance observed between the Deli Jovan and Zaglavak ophiolites (Fig. 3.1c, Kräutner and Krstić, 2003). These faults and their associated structures create a complex deformation system that was inferred to connect the strike-slip, thrusting and extensional

deformation around the western margin of Moesia from the Balkanides to the South Carpathians via the Serbian Carpathians (Fig. 3.1c, Schmid et al., 2020).

One interesting feature of the Cerna – Timok faults system is the formation of Oligocene – Miocene sedimentary basins observed along their strike, such as the Oligocene Petroşani, or the Miocene Timok - Knjaževac basins system (Fig. 3.1c). These triangular basins are syn-kinematic with respect to strike-slip deformation and formed during the gradual indentation and rotation around the Moesian indenter (e.g., Ratschbacher et al., 1993; Kräutner and Krstić, 2002; Schmid et al., 2020). The Timok - Knjaževac basins system reaches ~17 km in width southwards and is ~98 km in length. To the north, the Timok Fault connects with the late Oligocene - early Miocene transtensional opening of the South Carpathians foredeep (Fig. 3.1c, the Getic Depression of Răbăgia et al., 2011; Krézsek et al., 2013).

3.3 Methodology

3.3.1 Modelling approach

We present a series of 12 crustal scale analogue experiments that portray deformation of the upper to middle crust around a rigid indenter as a consequence of translation and rotation of the material surrounding it. Compared to previous indentation experiments where a rigid indenter is pushed into the model layers (e.g., Tapponnier et al., 1982; Davy and Cobbold, 1988; Ratschbacher et al., 1991a; Luth et al., 2013), our approach has a changed reference frame where the indenter is fixed, while the deformable material moves around it. As such, it allows direct investigation of the variability of deformation styles as a function of position relative to a fixed indenter (i.e., shortening dominated structures orthogonal to the indenter margin and strike-slip dominated structures parallel to the indenter margin) and, in a technical sense, provides more flexibility for implementing kinematic boundary conditions (see below) that are relevant for the comparison of modelling results with the natural case, the Carpatho-Balkanides (Fig. 3.1). Against the background of the natural example, the key parameters of this study include the shape of the indenter, the rheological stratification of the model crust and the addition of a rotational component of deformation to account for clockwise rotations of 5–10° in Oligocene-Miocene times (Marović et al., 2002).

3.3.2 Kinematic and geometric setup of the analogue models

All models contain a fixed rigid block, the indenter, with the upper width of 26 cm (Fig. 3.2a and b), which is scaled to the size (in the N–S direction) of the Moesian Platform in nature (Fig. 3.1). The indenter is surrounded by deformable layer(s) of brittle or brittle-viscous materials representing the upper to middle crust (Fig. 3.2). For the description of the modelling setup as well as the modelling results, a relative geographic reference frame with the north-oriented upwards is adopted (Fig. 3.2).

The model indenter is represented by a 2 cm thick stiff polyvinyl chloride (PVC) plate and has either rounded corners (Fig. 3.2a) or a rectangular geometry (Fig. 3.2b). The margins of either block have an inclination of 35° dipping towards the surrounding

deformable region (Fig. 3.2d). This inclination approximates the structure at the base of the Cretaceous nappes thrusted over the Moesian promontory (Fig. 3.1c); Matenco (2017) and references therein), representing an inherited feature in the model.

The deformable part of the model is underlain by two basal plastic plates/sheets (Fig. 3.2). The first, 1 mm thick plastic plate (green in Fig. 3.2), underlies the entire model (including the rigid block), is mobile and is attached to a motor (through a bar that is

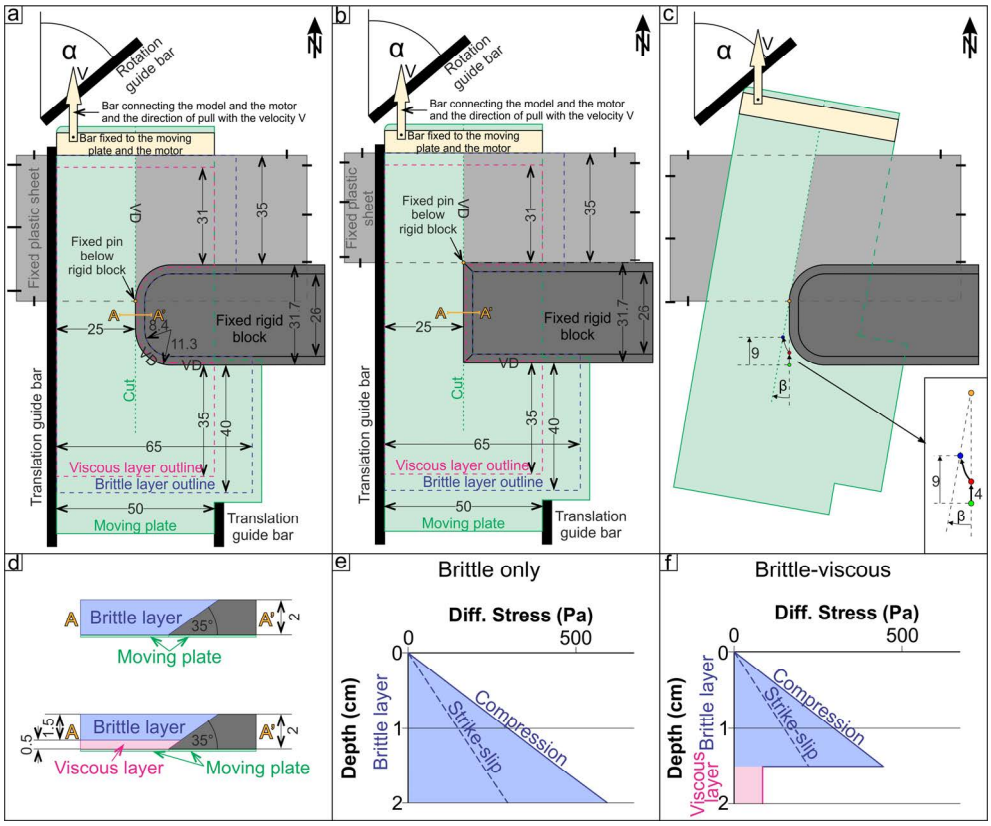

Figure 3.2 - Modelling setups. Adopted orientation is geographical with up being relative north. All numbers in Fig. 3.2a–d are in centimetres. a) Initial setup of experiments with rounded indenter's corners. b) Initial setup of experiments with rectangular indenter's corners. c) Configuration at the end of the experiment in Fig. 3.2a. Inset: Movements of the moving plate include the first phase of 4 cm of translation (green to red circle) and the second phase of combined translation/rotation kinematics (red to blue circle) that results in a total of 9 cm of northward translation and a final clockwise rotation angle β around the pole (yellow circle). In Fig. 3.2a–c the angle of the fixed rotation guide bar α equals to 0°, 30° and 50°, which corresponds to an induced rotation angle β of 0° (no rotation), 5° and 10° respectively. d) Setup cross-sections for brittle-only and brittle-viscous experiments in Fig. 3.2a and b. e) Strength profile for brittle-only experiments. f) Strength profile for brittle-viscous experiments.

connected to the model and motor by mechanical joints). The motor pulls it northward with a constant velocity of 10 cm/h or 2 cm/h for brittle only or brittle-viscous models, respectively. Depending on the specific model boundary conditions, this plastic plate is either only translated or translated and rotated. The rotation is achieved around a pole of rotation represented by a stationary pin protruding from below the indenter (fixed pin in Fig. 3.2). In our experiments, the fixed pin is located at the northern end of the straight segment of the rounded indenter's western margin or at the north-western corner of the rectangular-shaped indenter (Fig. 3.2a–c). The mobile plastic plate has a cut in the middle in the north-south direction (dashed green line in Fig. 3.2) to enable the sliding and rotation of the mobile plate along a stationary pin (Fig. 3.2). This construction allows for a combined translational-rotational movement of the mobile plate. The second, 0.1 mm thick plastic sheet (grey in Fig. 3.2), is fixed and overlies the moving plate north of the rigid block while underlying this moving plate to the northwest. This change takes place at the cut in the moving plate. We have chosen this configuration to prevent deformation north of the rigid block, where, otherwise, extension along the northern edge of the indenter would take place. At the same time, the area to the north-west of the rigid block is free to move. This setup predefines velocity discontinuities (VD) along the southern and western margins of the rigid block and along the contact between the moving plate and fixed plastic sheet (Fig. 3.2a–c). All experiments are confined laterally by either guiding bars or sand (Fig. 3.2a and b), which in the case of brittle-viscous experiments prevent the viscous layer to induce boundary effects by lateral flow outside the model area.

	Model number	Model type	Brittle layer thickness (cm)	Viscous layer thickness (cm)	Rigid block geometry	Engine pull velocity (cm/h)	Total translation (cm)	Total CW rotation (°)	Scaled thickness (km)
Group 1	**1**	b	2	-	Rounded corners	10	9	0	14
	2	b	2	-	Rounded corners	10	9	5	14
	3	b	2	-	Rounded corners	10	9	10	14
	4	b-v	1.5	0.5	Rounded corners	2	9	0	14
	5	b-v	1.5	0.5	Rounded corners	2	9	5	14
	6	b-v	1.5	0.5	Rounded corners	2	9	10	14
Group 2	**7**	b	2	-	90° corners	10	9	0	14
	8	b	2	-	90° corners	10	9	5	14
	9	b	2	-	90° corners	10	9	10	14
	10	b-v	1.5	0.5	90° corners	2	9	0	14
	11	b-v	1.5	0.5	90° corners	2	9	5	14
	12	b-v	1.5	0.5	90° corners	2	9	10	14

Table 3.1 - Model parameters. Model type: b - brittle only, b-v– brittle-viscous.

In experiments with no rotation (Table 3.1), the northward displacement of the mobile plate is 9 cm. For experiments with rotation (Table 3.1), we apply a stepwise approach by following previous experimental studies (Farangitakis et al., 2019, 2021). An initial 4 cm of northward translation is followed by a phase of combined translation and rotation. The purpose of these two phases of imposed kinematics is to create strike-slip deformation (in the first phase) and to study the influence of coupled rotation and translation (the second phase) on the pre-existing strike-slip faults. This complex movement of the mobile plate is guided by a fixed bar located in the north (Fig. 3.2a–c). During the experiment, when the mobile plate hits the rotation guide bar, we remove the

lateral translation guide bars to enable the combined rotational and translational movement (Fig. 3.2c). The total clockwise rotation reaches 5° and 10° in different models (Table 3.1). Similar to experiments with no rotation, the total northward displacement of the moving plate along the western margin of the rigid block is 9 cm (Fig. 3.2c).

The experiments presented in this study are subdivided into two groups. Group 1 (models 1–6) consists of experiments with rounded indenters whereas group 2 experiments (models 7–12) are characterized by rectangular indenters (Table 3.1). These distinct indenter geometries allow to quantitatively and qualitatively compare effects of corner geometry in cases where deformation is gradually transferred (rounded corners) and where the deformation transfer is more abrupt (90° corners). For each of these groups, we performed experiments with and without a rotational component applied to the deformable area surrounding the indenter as well as of brittle and brittle-viscous composition, respectively.

3.3.3 Model materials and scaling

In our models, the brittle layer consists of dry quartz sand with a bulk density of $\rho = 1500$ kg/m^3, a cohesion of 10–40 Pa and coefficients of friction of 0.63, 0.48 and 0.52, representing peak, dynamic and reactivation friction, respectively (Willingshofer et al., 2018). The sand has a grain-size spread of 100–300 μm and exhibits Mohr-Coulomb behaviour, which makes it a suitable analogue for natural brittle upper crust (Krantz, 1991; Dooley and Schreurs, 2012; Klinkmüller et al., 2016; Schellart and Strak, 2016). Thin marker horizons of coloured quartz sand were used as passive markers to show vertical offsets along faults in cross-sections, while horizontal offsets are tracked by passive maker lines of black and yellow quartz sand placed on the model upper surface.

The viscous layer in brittle-viscous models is the analogue of the ductile crust below the brittle-ductile transition. It consists of polydimethylsiloxane (PDMS silicon polymer) putty, mixed with iron powder and quartz sand as fillers in order to increase the density of pure PDMS (i.e., 970 kg/m^3) to a value close to the bulk density of the overlying quartz sand layer. This viscous mixture has a density of $\rho = 1470$ kg/m^3 and viscosity of $3.8 \cdot 10^4$ Pas at room temperature. The viscosity of the viscous mixture has been determined with a coni-cylindrical viscometer. An n-value of 1.2 indicates slightly non-Newtonian behaviour. We assume that for low stresses and low strain rates (i.e., similar to those used in analogue models) behaviour of the viscous mixture is essentially Newtonian (e.g., Broerse et al., 2019; Rudolf et al., 2016; Weijermars and Schmeling, 1986).

Scaling of all models follows the principles of geometrical, rheological and kinematical similarities between natural systems and models (Hubbert, 1937; Ramberg, 1981; Weijermars and Schmeling, 1986; Davy and Cobbold, 1991). Densities of our material of 1500 kg/m^3 represent natural upper to middle crust densities of 2750 kg/m^3, yielding a density-scale ratio ρ^* (ρmodel/ρnature) of 0.55. The length scale in our experiments is such that 1 cm in the model corresponds to 7 km in nature, yielding a length-scale ratio L* (Lmodel/Lnature) of $1.43 \cdot 10^{-6}$. We choose the length scale ratio such that the brittle-viscous transition in the models is at a depth of ~10 km when scaled to nature. This depth of the brittle-viscous transition is consistent with a change in

deformation behaviour of quartz-dominated lithologies from frictional sliding to creep (e.g., Kerrich et al., 1997; van der Pluijm and Marshak, 2004) for average continental geo-thermal gradients in the order of 30 °C/km (Turcotte and Schubert; 2014; Limberger et al., 2014, 2018) and the depth extent of weak seismicity documented in the South- and Serbian Carpathians (e.g., Dimitrijevic, 1994; Popa et al., 2018). At this depth the vertical stress (i.e., lithostatic stress, $\sigma = \rho \cdot g \cdot h$, where ρ is quartz sand density, g is the gravitational acceleration and h is the thickness of the overlying sand layer) in the experiments is 220 Pa, corresponding to 280 MPa in nature, which results in a stress-scale ratio of $7.87 \cdot 10^{-7}$. Strength profiles (Fig. 3.2e and f) are representative for the initial conditions and have been calculated following Brun (2002). To scale model velocity in brittle-viscous models, we use a time-scale ratio $t^* = 5.3 \cdot 10^{-11}$ calculated as (Hubbert, 1937):

$$t^* = \frac{1}{\dot{\gamma}^*} \quad (1)$$

while shear strain rate ratio $\dot{\gamma}^*$equals:

$$\dot{\gamma}^* = \frac{V^*}{L^*} \quad (2)$$

where velocity ratio $V^* = 2.7 \cdot 10^4$ means that 2 cm/h in models scales to 0.65 cm/yr in nature, which is consistent with the 60–65 km displacement along the Timok fault over a period of ~10 Myr (e.g., Kräutner and Krstić, 2003; Schmid et al., 2020). Note that the shear strain rate is calculated as velocity over the thickness of the viscous layer. For the calculated experimental velocities, the viscosity of the modelling material scales to natural viscosities of $\sim 10^{21}$ Pas, which is in the range of quartz dominated ductile crust below the brittle-ductile transition (e.g. Hirth et al., 2001).

3.3.4 Experimental procedures, recordings and PIV-derived strain analysis

Models are built and run in a normal gravity field and at room temperature (i.e., 19–20 °C). An electric motor imposes a constant velocity on the mobile plastic sheet. Depressions deeper than 1 mm are filled manually, using a funnel, with alternating layers of differently coloured sand, representing syn-kinematic sedimentation. At the end of each experiment, two post-kinematic layers of black and white sand are added on top of the entire model to preserve topography and water is sprinkled on the sand layers to increase cohesion within the sand and to allow for sectioning of the experiments to obtain information on the internal structures.

We monitor surface deformation by taking top-view photographs (by using Panasonic Lumix DC-G9 with 20.3 megapixels for models 1–6 and 10–12 and Canon EOS 700D with 18.0 Megapixels for models 7–9) at regular time intervals of 45 s for brittle only experiments and 3 min for brittle-viscous models, corresponding to 0.125 cm and 0.1 cm of translation displacement between two photographs, respectively. These top-view photographs are analysed using image correlation techniques (PIVlab, Thielicke and Stamhuis, 2014) in order to calculate incremental particle displacements. Subsequently, we remove very large displacements due to incorrect correlations by applying a magnitude threshold filter, followed by a visual inspection for remaining outliers and their manual removal and interpolation of displacements in basin areas for time frames when sedimentation is applied (i.e., only for a few time frames in a model). Displacements for these time frames are interpolated taking displacement values on the

margin of basins unaffected by sedimentation. The image correlation provides the displacement fields in a fixed spatial reference frame. However, model materials show large motions through this spatial frame. We therefore also track material by defining an initial regular grid that deforms at each time step using the interpolated, spatial displacement fields (i.e., Lagrangian summation, similar to Senatore et al., 2013; Stanier et al., 2016; Boutelier et al., 2019; Krýza et al., 2019). From the material displacements, the incremental deformation field is calculated (Appendix A, D). As the deformation is large, small strain definitions are no longer valid (Malvern, 1969). Therefore, we describe the finite deformation as a product of the stretch tensor (corresponding to the shape change), and a rotation tensor, using a polar decomposition of the finite deformation gradient tensor (Broerse et al., 2021). Note that the principal stretches (λ_i) relate to principal strains (ε_i) as $\lambda_i = 1 + \varepsilon_i$.

For small, incremental strains one can use the ratio of the largest to the smallest principal strain to determine a strain type in the horizontal plane: extension, strike-slip, shortening and their transitions (Kreemer et al., 2014). From Broerse et al. (2021) it follows that, for the mentioned types of strain, the logarithms of principal stretches for large deformation have the same ratios as incremental small strains. Therefore, we use the logarithmic principal stretches to determine the average strain type during model evolution (see Appendix B, E; see also Broerse et al., 2021). While in 3D, faulting always involves shear on fault planes, in horizontal view only strike-slip faulting is purely shear; thrust faulting will appear as shortening in 2D, while normal faults appear as extensional features. Our approach relies on the assumption that the surface deformation is not affected by subsequent phases of opposite deformation. If an inversion of deformation occurs, the analysis should be divided into separate periods. Finally, these results are combined with visual interpretations of cross-sections to infer 2D strain in the entire, 3D model.

3.3.5 Experimental limitations and simplification

The analogue models presented in this study do not account for isostasy, temperature gradients with depth (i.e., the viscosity of the viscous layer is constant, which is an acceptable approximation following Davy and Cobbold, 1991), surface erosion and sediment transport. Therefore, topographic heights are exaggerated in the contractional area in front of the indenter. Despite these limitations, we are confident that the modelling results are meaningful because we mostly focus on the area of the model where significant deformation is by strike-slip, which generally produces little thermal perturbations as well as low topography changes. Le Guerroué and Cobbold (2006) demonstrated that syn-kinematic erosion and/or sedimentation in a strike-slip setting only have minor effects on structural patterns, yet the results have been obtained at higher spatial resolution. As such, minor differences in structural patterns within strike-slip zones with or without syn-kinematic sedimentation are not significant on the scale of our models. Therefore, surface processes are in our view not among the controlling factors during the oroclinal bending of the Carpatho-Balkanides.

Compared to the natural case of the Serbian Carpathians and its Cretaceous inherited structures (Fig. 3.1c), our models do not have inherited topography and/or a wedge structure (i.e., and inherited mountainous fold and thrust belt) in the deformable part of

the model prior to deformation. This simplification is justified because the Cerna- Timok fault system offsets the inherited Cretaceous nappe stack and Paleocene-Eocene Danubian extensional dome in the Serbian and South Carpathians (e.g., Kräutner and Krstić, 2003; Fügenschuh and Schmid, 2005) and do not represent reactivated nappe contacts. Such simplification allows studying first-order structural responses to the varied parameters without complex overprinting interactions with earlier deformation.

3.4 The reference model and parametrical study

The results are described starting with a detailed analysis of a "reference model" (Model 1, Fig. 3.3), to which we compare the results of a parametric study (Figs. 3.4–3.7) and the best-fit model (Fig. 3.8). The latter serves to demonstrate the relevance of the modelling results for the evolution of the Cerna-Timok fault system and the associated Carpatho- Balkanides oroclinal bending. Note that the transpressional deformation in the northernmost segment of all models (i.e., at larger distances from the pole of rotation), results from the modelling setup (N–S oriented velocity discontinuity, Fig. 3.5) and is not relevant for the comparison with the natural case of the Carpatho-Balkanides.

Modelling results are described based on the structural interpretation of top-view photographs and cross-sections and results of digital image correlation methods documenting the variability of strain regimes in map-view (Figs. 3.3–3.5 and 3.8). Furthermore, we use time-lapse top-view videos of incremental strain components and cumulative strain type, available in Appendix A, B, D, E and temporal evolution of selected grid cells (Appendix C and F) to derive and explain detailed fault kinematics and their interplay during deformation.

3.4.1 Reference model: model 1

Model 1 consists of a rigid indenter with rounded corners, while the surrounding, deformable material is entirely brittle (Table 3.1, Fig. 3.2a, e). The deformation results only from northward translation of the model layers.

Model 1 (Fig. 3.3) documents the development of distinct strain regimes in time, which are characterized by predominantly strike-slip deformation along the N–S oriented flank of the indenter, transpression along the curved indenter segment and contraction at the E-W striking margin of the indenter. The partitioning into these deformation regimes takes place during the entire experiment, although structural complexity increases through time (Fig. 3.3; see also Appendix A and B that show the incremental 2D strain with time and the evolution of average strain type).

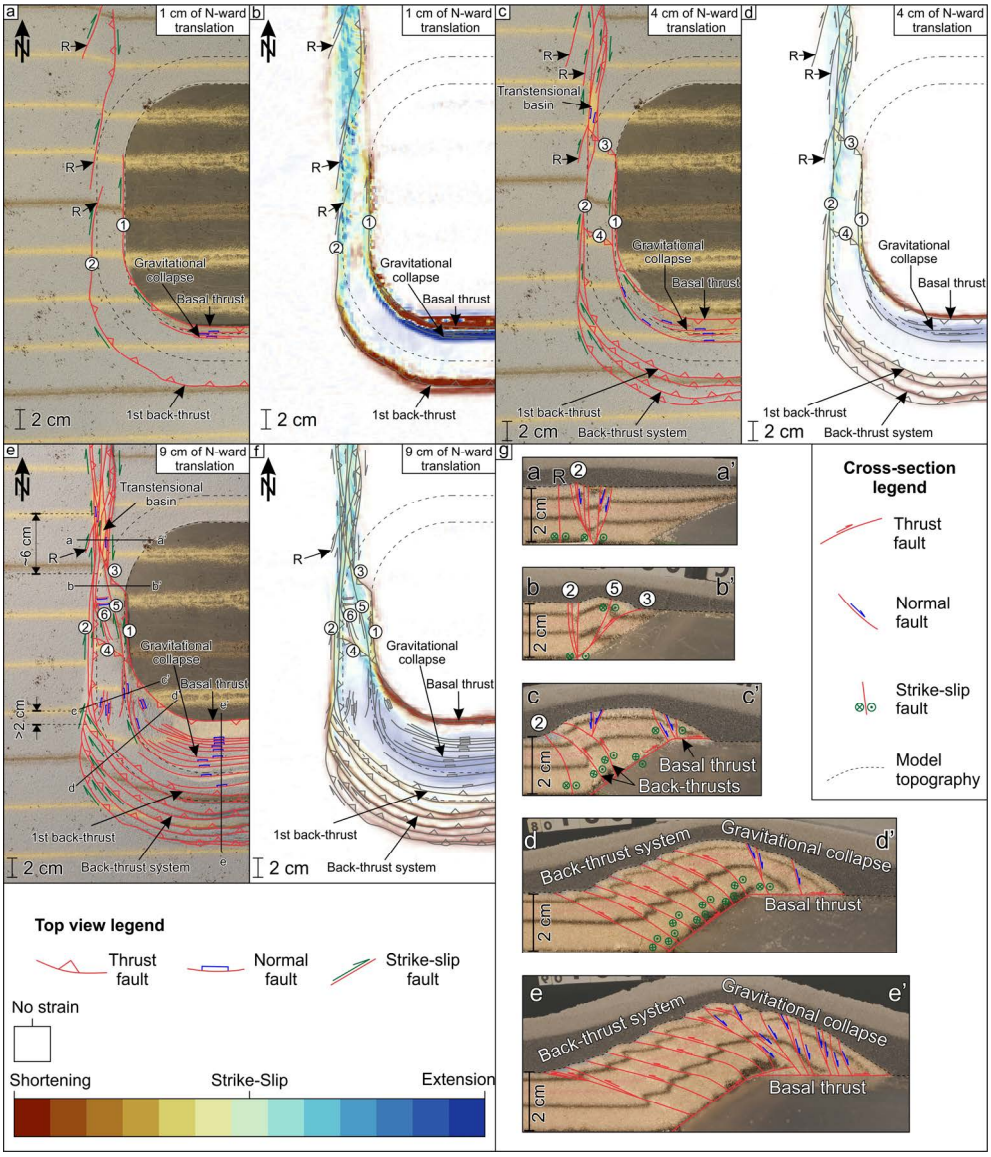

Figure 3.3 - Model 1 - reference model. Dashed black lines mark the upper and lower edges of the indenter. R – Riedel shear. a) Interpreted top-view photo after 1 cm of northward translation. b) Cumulative strain type map after 1 cm of northward translation. To suppress areas without significant deformation, the transparency of areas with a strain magnitude below the 95 percentile is increased. We define the strain magnitude as the maximum, absolute logarithmic principal stretch (i.e. maximum absolute Hencky strains). c) Interpreted top-view photo after 4 cm of northward translation. d) Cumulative strain type map after 4 cm of northward translation. e) Interpreted top-view photo at the end of the experiment. f) Cumulative strain type map at the end of the experiment. Strain plots in Fig. 3.3b, d and f are overlain with visually interpreted structures from Fig. 3.3a,

c and e (grey lines). Strain colour legend corresponds to Fig. 3.3b, d and f. g) Cross-sections of the reference model at the end of the experiment. The dashed line marks the model topography at the end of the experiment. The shaded area in the upper part of each cross-section marks the post-kinematic sand cover. Cross-section locations are shown in Fig. 3.3e.

3.4.1.1 Early stages

In the early stages of the experiment, deformation is localized along the western and southern margins of the indenter (Fig. 3.3a and b). In particular, strike-slip deformation localized along the western indenter margin interface, while being distributed above the VD (see Appendix A, B). This suggests that lower vertical stress levels above the ramp facilitate the onset of deformation at this location (structure 1 in Fig. 3.3a). However, a new strike-slip fault zone forms afterwards (structure 2 in Fig. 3.3a) above the lower edge of the indenter's inclined margin that coincides with the basal VD. NNE-SSW oriented Riedel shears (R in Fig. 3.3a) are related to the northward translation of the mobile sheet, suggesting early strain partitioning. As the shear zone in the north evolves, an area of transtensional strain (light blue shades in Fig. 3.3b), related to dilation during shearing is bounded by areas that underwent slight shortening and transpression (pale red, orange and yellow values in Fig. 3.3b). This shear zone develops into a positive flower structure in the north, with oblique-slip thrusts bounding the strike-slip corridor (Fig. 3.3c–f). Along the western margin of the rigid block, the deformation after 1 cm of displacement is mostly accommodated by the two early formed N–S oriented strike-slip faults (1 and 2 in Fig. 3.3a). In the early stages of deformation, these two faults are connected around the SW corner of the indenter to the E-W oriented shortening domain in the south. This connection is achieved through a basal thrust along the pre-existing indenter ramp and a back-thrusting system where the offset is initiated at the toe of the ramp (Fig. 3.3a, g). The overall system transfers N–S strike-slip into E-W oriented thrusts and back-thrusts (Fig. 3.3b).

3.4.1.2 Formation of the main N–S oriented strike-slip fault

After approximately 4 cm of displacement of the mobile sheet (Fig. 3.3c and d), all Riedel shears are connected and the main N–S oriented strike-slip fault (structure 2) represents a thoroughgoing strike-slip system. This structure is characterized by a change in fault dip angle, from sub-vertical in the north to steeply eastward-dipping in the south (e.g., compare cross-sections a-a', b-b' and c-c' in Fig. 3.3g), consistent with a southward increase of the reverse component of movement (Fig. 3.3g). Overall, the deformation zone gets wider southwards when approaching the rounded corner of the indenter (Fig. 3.3e), as the cumulated deformation is changing from strike-slip and transtension in the north to strike-slip and transpression in the south (Fig. 3.3f–g). Furthermore, the final dextral offset along the main strike-slip fault (structure 2) decreases towards the south from ~6 cm to <2 cm (see the offset in black and yellow marker lines in top view, Fig. 3.3e).

The initial strike-slip structure (1 in Fig. 3.3e and f) and the main strike-slip fault (2 in Fig. 3.3e and f) are connected by obliquely oriented thrusts in map view (3 and 4 in Fig. 3.3c–f, cross-section b-b' in Fig. 3.3g) and NNW-SSE oriented strike-slip faults (5 and 6 in Fig. 3.3e and f, cross-section b-b' in Fig. 3.3g). These thrusts develop on top of the inclined margin, adding to the complexity in the strain pattern in the central segment of the model (Fig. 3.3f), where strain is partitioned between top to N shortening (red along 3 and 4 in Fig. 3.3f), strike-slip (green) and transtension (light blue values) in the centre of the deformation zone (structures 5 and 6 in Fig. 3.3f), while bounded by transpressional deformation (orange values along 1 and 2 in Fig. 3.3f).

3.4.1.3 Transition between strike-slip and thrusting

The SW corner of the rigid block (Fig. 3.3e and f, cross-section d-d' in Fig. 3.3g) represents the area where strike-slip deformation transitions to thrusting with significant changes of fault orientations. The strike of major structures follows the predefined curvature of the rigid block resulting in curved geometries of the back-thrusts and the normal faults. Back-thrusting is transferred directly to the strike-slip deformation, demonstrating oblique dextral reverse slip in the bending zone (Fig. 3.3a–f). This connection evolves sequentially as the main strike-slip fault propagates farther to the south to connect with the newly formed back thrust (see Appendix A, B). N-dipping normal faults are linked with the main strike-slip fault (structure 2) through NNW-SSE oriented dextral faults (5 and 6 in Fig. 3.3e and f), while the basal thrust remains linked to the oblique strike-slip fault along the western edge of the indenter (1 in Fig. 3.3e and f). This gradual transfer is further marked by a decrease in contractional or extensional strain, characterizing an area of distributed deformation without clear faulting (decrease in red and blue intensity westward along the basal thrust, in the region of the gravitational collapse and back-thrust system in Fig. 3.3f). In this area the strain type changes from shortening and extension in the south (red and blue in Fig. 3.3f, respectively) to oblique-slip (orange, yellow, light blue values) and strike-slip (green) in the west. This change is associated with a decrease in vertical offset in the back-thrust system from 3.3 cm in the south (cross-section e-e' in Fig. 3.3g) to 1.9 cm in the SW corner area (cross-section d-d' in Fig. 3.3f). Minor E˜ and W- dipping normal faults in the bending region (Fig. 3.3e–g, cross-sections c-c' and d-d') display very small offsets, accommodating the topographic transition from elevated shortening dominated wedge south of the indenter to strike-slip dominated low-topography structures to the west of the indenter.

Directly south of the indenter, the displacement is perpendicular to the rigid block. In this part of the system, the inclined margin acts as a thrust ramp, along which material has been transported on top of the rigid block, resembling a flat-ramp-flat geometry (Fig. 3.3g, cross-section e-e') or Coulomb wedge model with fore- and retro-wedges (e.g., Davis et al., 1983; Dahlen et al., 1984; Del Castello et al., 2004). The final strain type map (Fig. 3.3f) demonstrates that most thrusting deformation is accommodated along the basal thrust (see also cross-sections d-d' and e-e' in Fig. 3.3g). The S-verging back-thrusts are partly re-activated as N-dipping normal faults to accommodate the change in geometry of the basal thrust from the ramp to the flat segment (Fig. 3.3e and f, cross-section e-e' in Fig. 3.3g; see also Appendix C).

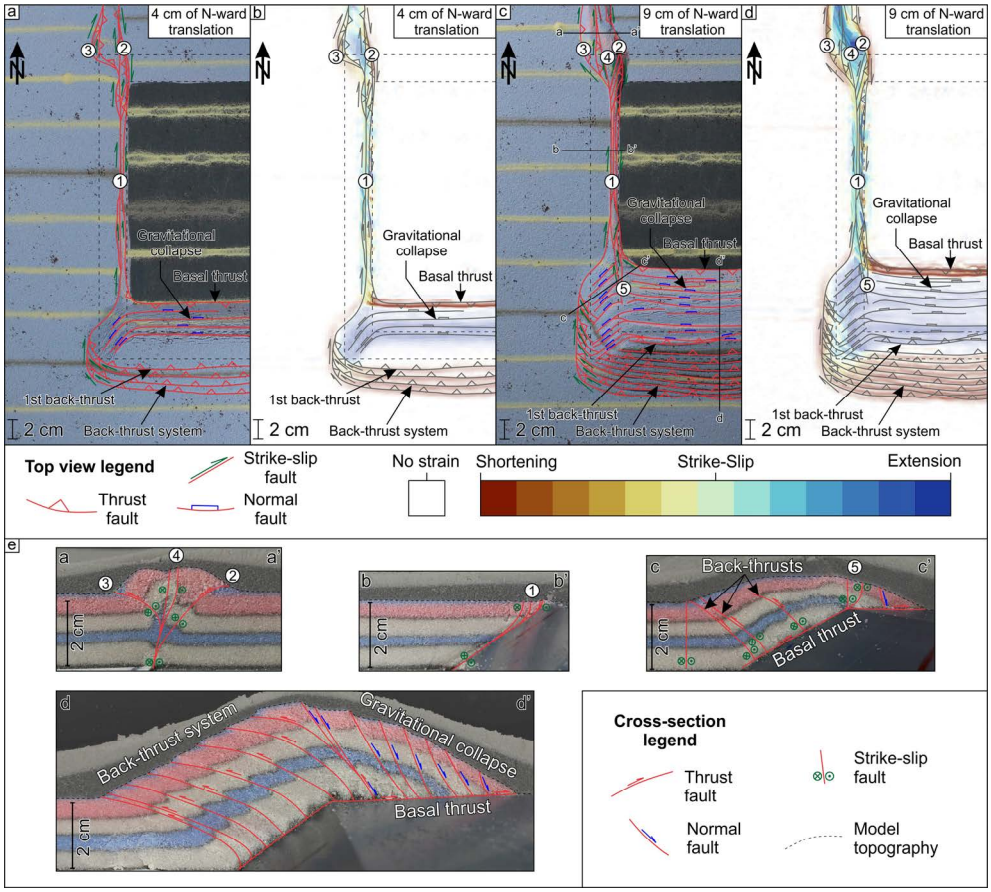

Figure 3.4 - Model 7 – brittle only model with rectangular indenter and no rotation. Dashed black lines mark the upper and lower edges of the indenter. a) Interpreted top-view photo after 4 cm of northward translation. b) Cumulative strain type map after 4 cm of northward translation. To suppress areas without significant deformation, the transparency of areas with a strain magnitude below the 95 percentile is increased. We define the strain magnitude as the maximum, absolute logarithmic principal stretch (i.e., maximum absolute Hencky strains). c) Interpreted top-view photo at the end of the experiment. d) Cumulative strain type map at the end of the experiment. Strain plots in Fig. 3.4b and d are overlain with visually interpreted structures from Fig. 3.4a and c (grey lines). Strain colour legend corresponds to Fig. 3.4b and d. e) Cross-sections of the model 7 at the end of the experiment. The dashed line marks the model topography at the end of the experiment. The shaded area in the upper part of each cross-section marks the post-kinematic sand cover. Cross-section locations are shown in Fig. 3.4c.

3.4.2 Parametrical study

In the following sections, we provide a concise overview of modelling results for the parameter space explored in this study. We start with highlighting similarities and differences of modelling results for different indenter geometries (Figs. 3.3–3.5) and the amount of rotation for set-ups where the crust consists of brittle material only (Fig. 3.5). Thereafter, we describe the results for models with brittle-ductile rheological stratification, for which we similarly vary the indenter shape and amount of rotation (Fig. 3.5). Next to displaying the modelling results as interpreted top-view images, cross-sections or strain maps (see also M1), histogram diagrams are used for the quantitative analysis of modelling results relating to the size (i.e., width, of strike-slip dominated shear zone, width, length and depth of basin, width and height of orogen) of structural features to the tested parameters (Figs. 3.6 and 3.7).

3.4.2.1 The influence of the indenter geometry

Our analysis of models with rounded (M1) and rectangular (M7) indenter corners subject to translational kinematic boundary conditions (Figs. 3.3, 3.4 and 3.5a, b) show that the indenter geometry significantly influences the geometry and kinematics of strike-slip zones and their transition to the E-W oriented thrust systems (compare Fig. 3.5a and b).

In the case of rounded indenter corners, the strike-slip system along the western margin is distributed over a wider area compared to models with rectangular corners (Figs. 3.3 and 3.4). In particular, the average width of the strike-slip zone is 4.6 cm in M1, while it is 1 cm in M7 (Figs. 3.5 and 3.6a). This difference is a consequence of how the strike-slip and thrust domains connect. For rounded indenters, it is the first back-thrust of the thrust domain that connects with the major strike-slip fault that develops at the VD along the western indenter margin (Fig. 3.3a and b), whereas it is the basal fore-thrust that connects with the strike-slip fault along the upper indenter-model boundary in the case of the rectangular indenter (Fig. 3.4a and b). The latter is probably an effect of stress concentration at indenter corners localizing deformation close to the sand-indenter boundary (Fig. 3.4). This difference in model evolution has major implications for the style and kinematics of deformation at the transition of the strike-slip to the thrusting domain where M1 shows a gradual change from thrusting to strike-slip deformation (Fig. 3.3e and f). In contrast, this transition is abrupt in M7 and defined by an array of small dextral faults with an important normal slip component (Fig. 3.4).

These faults link to displacement along the main strike-slip fault zone cutting the evolving thrust wedge (Fig. 3.4c and d). These first-order features are also observed when combining translation with rotation of the moving sheet (Fig. 3.5 e, f, i, j) and are less pronounced when adding a viscous layer at the bottom of the models (Fig. 3.5c, d, g, h, k, l).

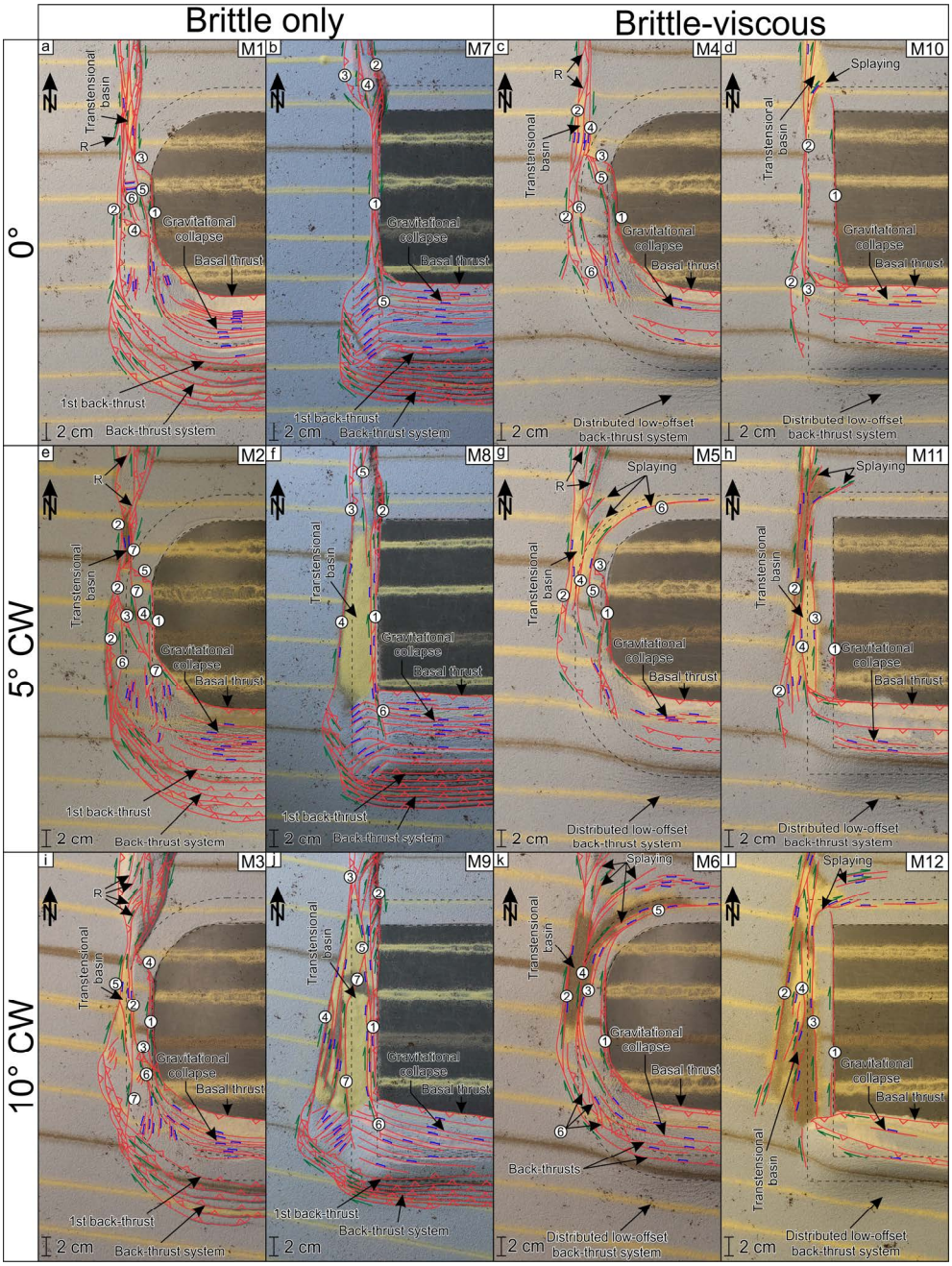

Figure 3.5 - Interpreted top-view photos taken at the end of all 12 experiments. Numbers indicate the sequence of major fault activation in the strike-slip zone. Dashed black lines mark the upper and lower edges of the indenter. Legend is the same as in Fig. 3.3.

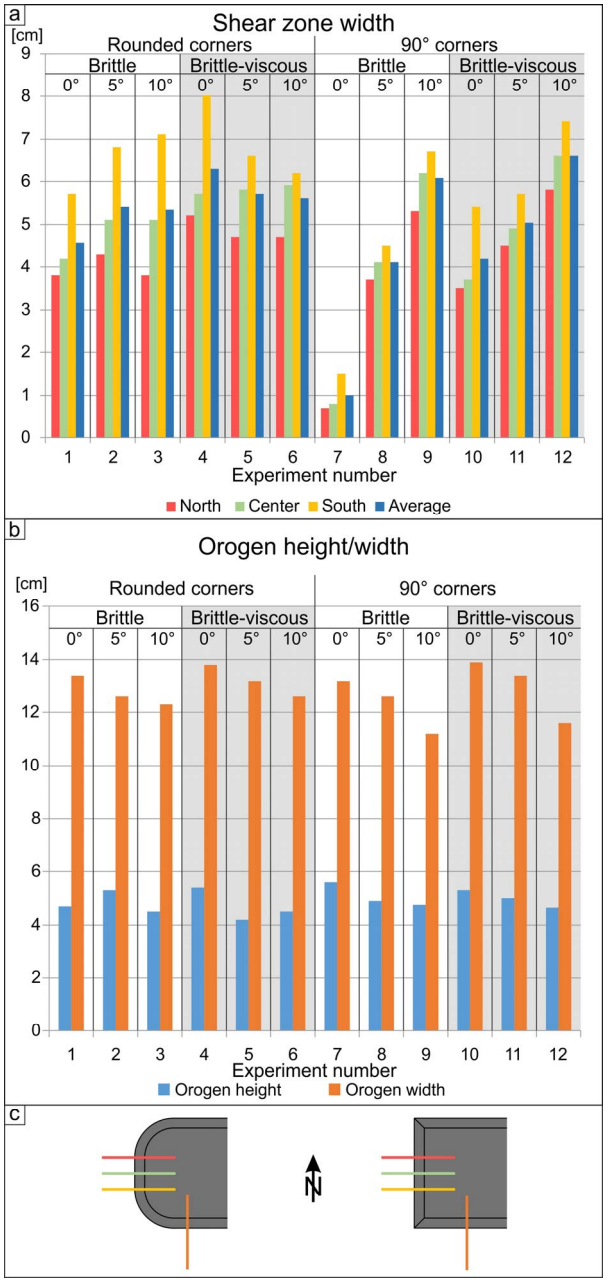

Figure 3.6 - a) Histogram of the strike-slip zone width perpendicular to the western indenter's margin in each experiment measured in the north, centre and the south of the zone, and their average. All measurements are done visually on the top-view photographs at the end of the experiment. We define the strike-slip zone width as the distance between two bounding faults with a visually observable offset. b) Chart of orogen (thrusting wedge) height and width. Orogen height is measured in cross-sections and orogen width in top-view photographs at the end of the experiment, perpendicular to the southern margin of the indenter. We define the orogen width as the distance between two bounding faults with visually observable offset. c) Top-view locations of the sections along which we determine the strike-slip zone and orogen widths.

3.4.2.2 The influence of imposed rotation

Including rotation leads to a systematic widening of the deformed area, particularly of the strike-slip dominated domain (Fig. 3.5). This effect is more pronounced when indenter corners are rectangular. For example, when comparing models with rectangular corners (Fig. 3.5b, f, j), the average strike-slip zone width in models with no rotation is as low as 1 cm (model 7), ~4 cm for 5° of rotation (M8) and ~6 cm for models with 10° rotation (M9; Fig. 3.6a). These differences are related to the scissor-style opening of, in map-view, triangular-shaped transtensional basins above the basal velocity discontinuity (Figs. 3.5 and 3.7). As such these basins are narrower and shallower in the north but wider and deeper in the south where the extensional component is largest (M8 and M9, Figs. 3.6 and 3.7). Progressive rotation also induces the formation of new strike-slip

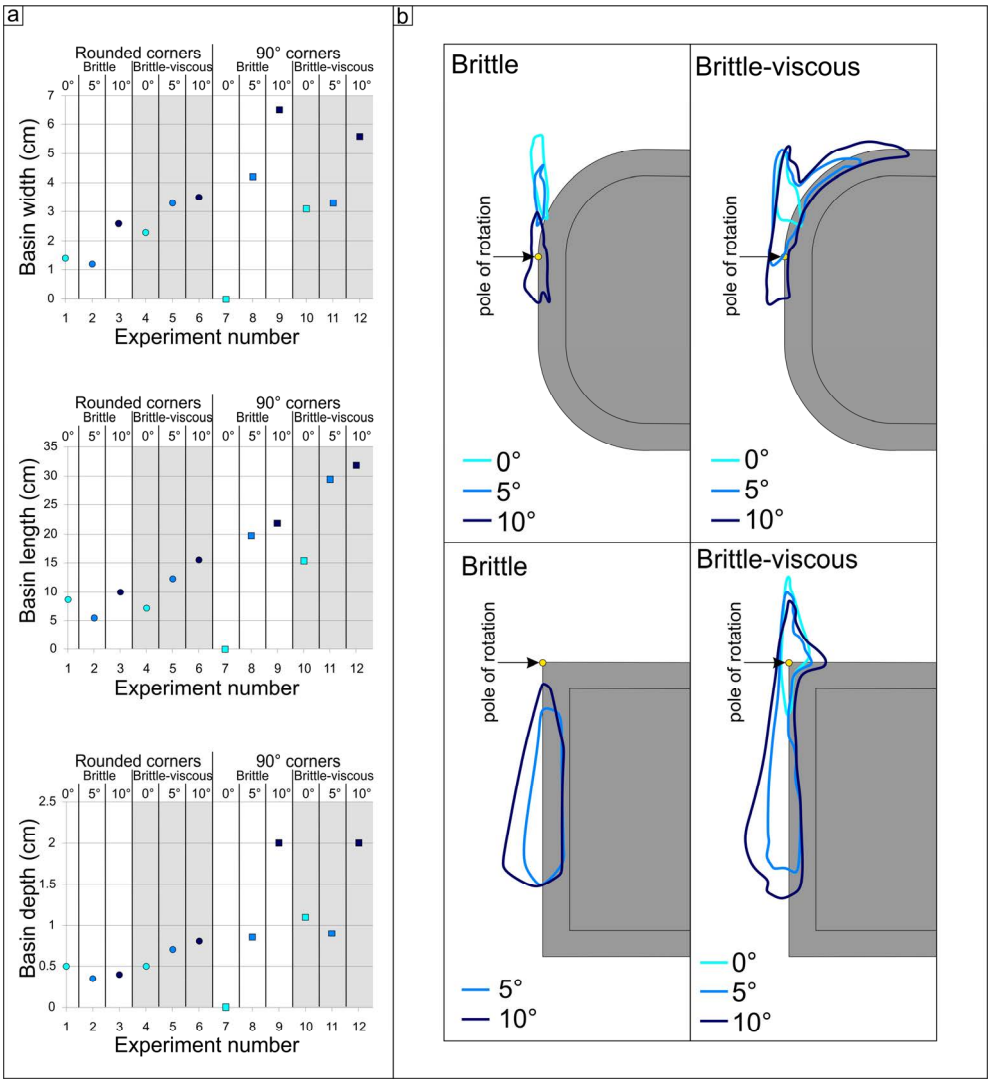

Figure 3.7 (previous page)- Basin geometry parameters and top-view shape and position. a) Charts of basin width, length and depth in each experiment. Basins' widths and lengths are measured in the final top-view photos in the E-W and N–S direction. Basin depths are obtained from the cross-sections. b) Top-view basin location and geometry at the end of each experiment relative to the indenter, taken as the outline of the syn-kinematic sediments in the final top-view photograph.

faults with the normal component of slip (e.g., fault 7 in Fig. 3.5j) within the evolving sedimentary basin, which cut into the orogenic wedge at the transition zone. Furthermore, the orogenic wedge gets lower and less wide with the increasing amount of rotation for both, models with rounded and rectangular indenter corners (Fig. 3.6b).

Models with curved indenter also show widening of the deformation zone away from the rotation pole, which is, however, less pronounced compared to models with rectangular corners (compare M2 and M3 with M8 and M9, Fig. 3.5). Consequently, these transtensional basins are smaller and less deep (width: 1.2–2.6 cm, length: 5.0–10.0 cm, depth: 0.3–0.4 cm; Fig. 3.7). Similar to models with rectangular corners, widening of the strike-slip deformation zone is also associated with the formation of new faults that link this zone to the thrust wedge (e.g., fault 4 in Fig. 3.5k).

3.4.2.3 The influence of rheology: brittle-only vs. brittle-viscous rheology

In models with a viscous layer, deformation is distributed over a wider area but a smaller number of discrete structures is formed that accommodate the motion of the underlying plate (Figs. 3.5 and 3.6). The evolution of first-order structural patterns is similar in brittle and brittle-viscous experiments, especially along the western margin of the indenter. The influence of the viscous crust is particularly obvious at the southern and northern margins of the indenter, where the transfer of deformation is more gradual. Also, notably fewer structures accommodate shortening south of the indenter, while north of the indenter new structures (i.e., splaying off of the main strike-slip zone; Fig. 3.5) form that do not exist in brittle-only models. Comparing M7 with M10 shows that main the dextral shear zone evolves on top of the velocity discontinuity in M10 and thus at a distance from the boundary between the rigid indenter and the sand layers. This suggests that flow in the viscous layer has a de-localizing effect.

The viscous layer does not have a significant influence on the width of the transtensional basins along the western margin of the indenter, although the basins are slightly larger (especially longer) (Fig. 3.7a). The viscous layer controls the geometry of the basin (Fig. 3.7b), allowing the transfer of deformation around the NW corner of the indenter creating oblique-slip normal faults (splaying in Fig. 3.5d, g, h, k, l, 3.7b). These oblique-slip faults control the subsidence in this NE-SW to E-W oriented basin north of the indenter, which is connected to the main N–S oriented basin along the western margin (Figs. 3.5 and 3.7b).

The orogenic wedge at the southern margin of the indenter is systematically wider but is not systematically different in height for models with viscous rheology (Fig. 3.6b). The associated faulting patterns are characterized by a few discrete structures (on

average 1–2 fore-thrusts and up to 2 back-thrusts) additional to a multitude of low offset structures appearing as "wrinkles" on the model surface (Fig. 3.5).

3.5 The best-fit model for the Cerna-Timok system and associated Carpatho-Balkanides oroclinal bending

Among all modelling scenarios (Fig. 3.5), the one that simulates most closely the evolution and geometry of the Cerna-Timok fault system and the associated oroclinal bending is model 6, hereafter referred to as the "best-fit" model. This model consists of a rigid block with rounded corners and brittle-viscous rheology (Table 3.1, Fig. 3.2a, c, f), where kinematic boundary conditions are applied in two stages. After four centimetres of northward translation (i.e., the first stage), a total 10° clockwise rotation is applied simultaneously with continued northward translation (i.e., the second stage). This setup creates a combination of constant translation and rotation of the moving basal plastic sheet (Fig. 3.2c).

Similar to the previously described ones (Fig. 3.5), the best-fit model transfers strike-slip and transtension in the west into thrusting in the south via a transpressional region at the SW corner of the indenter (Fig. 3.8). The viscous layer distributes deformation over a larger area when compared to the reference model, with similar geometry to the one of the Cerna-Timok faults system (compare Figs. 3.1c and 3.8).

The initial translation stage (Fig. 3.8a and b) forms NNE-SSW oriented en-echelon Riedel shears oblique to the basal VD in the north (R in Fig. 3.8a) and two main strike-slip faults along the western margin (structures 1 and 2 in Fig. 3.8a and b), similar to other models (Fig. 3.5). These strike-slip faults simulate an original onset of the Timok and Cerna as separate faults, which were linked to the main southern thrusting area via the curved SW indenter's corner, in a similar way to the transfer to an initial Cerna-Timok dextral offset to the Balkanides (compare with thrusting in Fig. 3.1c). This geometry also implies that the present-day truncation of the Cerna by the Timok Fault is a later, early Miocene feature, by a splay connecting the southern Cerna with the northern Timok. The southern area shows distributed low offset back-thrusts (Fig. 3.8a), while north dipping normal faults accommodate the collapse of the gravitationally unstable thrust wedge in the hinterland of the main thrust front (blue in Fig. 3.8b).

3.5.1 Transtensional basin geometry and structure

The transfer of deformation around the NW indenter corner from strike-slip/transtension (green and light blue values in Fig. 3.8b) along the western margin into transtensional (light blue and pale blue values in Fig. 3.8b) deformation in the north of the indenter takes place already during the initial translation stage (Fig. 3.8a and b). Such a transfer mechanism has already been inferred for the general splaying of the strike-slip system towards the South Carpathians, around the rigid indenter's NW corner, where the slip changes from strike-slip into oblique normal-slip and even normal-slip deformation, resulting in the early Miocene transtensional opening of the Getic Depression (Fig. 3.1c, Matenco et al., 2003; Krézsek et al., 2013).

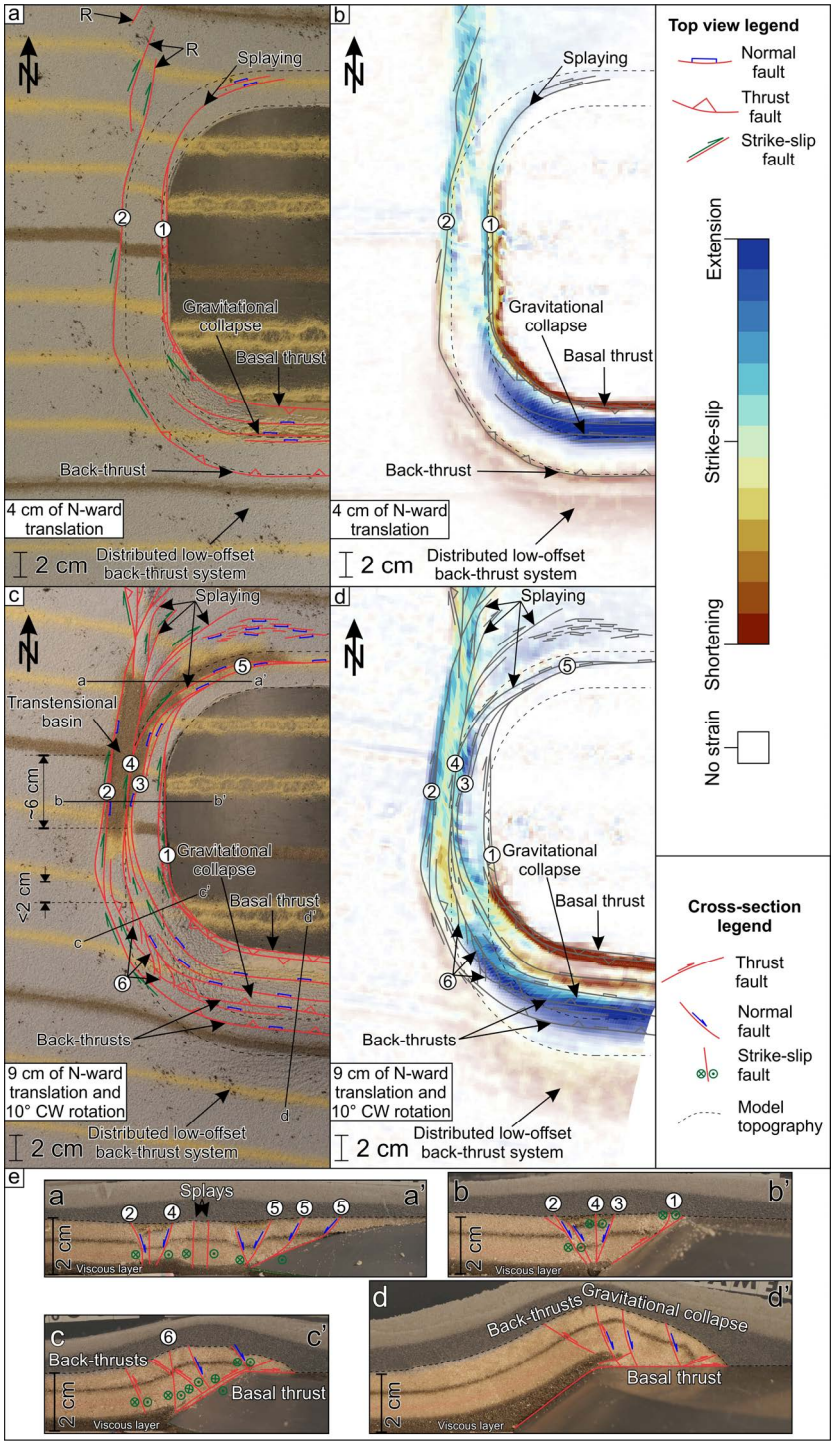
a
R
R
Splaying
Gravitational collapse
Basal thrust
Back-thrust
4 cm of N-ward translation
2 cm
Distributed low-offset back-thrust system
b
Splaying
Gravitational collapse
Basal thrust
Back-thrust
4 cm of N-ward translation
2 cm
Distributed low-offset back-thrust system
Top view legend
Normal fault
Thrust fault
Strike-slip fault
Extension
Strike-slip
Shortening
No strain
c
Splaying
Transtensional basin
~6 cm
<2 cm
Gravitational collapse
Basal thrust
Back-thrusts
9 cm of N-ward translation and 10° CW rotation
2 cm
Distributed low-offset back-thrust system
d
Splaying
Gravitational collapse
Basal thrust
Back-thrusts
9 cm of N-ward translation and 10° CW rotation
2 cm
Distributed low-offset back-thrust system
Cross-section legend
Thrust fault
Normal fault
Strike-slip fault
Model topography
e
Splays
Viscous layer
Back-thrusts
Gravitational collapse
Basal thrust

Figure 3.8 (previous page) - Model 6 – best-fit model. Dashed black lines mark the upper and lower edges of the indenter. R – Riedel shear. a) Interpreted top-view photo at the end of translation phase. b) Cumulative strain type map at the end of the translation-only phase. To suppress areas without significant deformation, the transparency of areas with a strain magnitude below the 95 percentile is increased. We define the strain magnitude as the maximum, absolute logarithmic principal stretch (i.e., maximum absolute Hencky strains). c) Interpreted top-view photo at the end of the experiment. d) Cumulative strain type map at the end of the experiment, where the deformation is analysed starting in the second phase, without the initial 4 cm of translation (i.e., there is no overprint of the previous strain). Strain plots in Fig. 3.8b, d are overlain with visually interpreted structures from Fig. 3.8a, c (grey lines). Strain colour legend corresponds to both Fig. 3.8b, d. e) Cross-sections of the best-fit model. The dashed line marks the model topography at the end of the experiment. The shaded area in the upper part of each cross-section marks post-kinematic sand cover. Cross-section locations are shown in Fig. 3.8c.

The subsequent rotation in the best-fit model has comparable scaled dimensions and is controlled by 10° of total clockwise rotation along the western margin of the indenter (Fig. 3.8c), an amount that was reported for the Serbian Carpathians for Oligocene – Miocene times (Marović et al., 2002). In the same area, the model shows the formation of transtensional basins along the western margin of the indenter that are very similar to the ones observed in the natural case (Fig. 3.1c). The similarity also insinuates that the subsurface SW and NW corner geometry of the Moesian indenter had a similar curvature to the one presently observed. In models with rectangular indenters and 10° CW rotation, basins are much larger than the ones observed in the Serbian and South Carpathians (compare Figs. 3.1c, 3.5 and 3.7). The subsequent rotation in the best-fit model complicates the structural pattern by distributing deformation over additional structures. For instance, new faults (e.g., 3 and 4 in Fig. 3.8c) form in the area between previously formed structures (1 and 2, Fig. 3.8c and d), similarly to other models with rotation (Fig. 3.5). Furthermore, rotation increases oblique movements along all structures (intercalating light blue and yellow – orange colours in Fig. 3.8d).

In more details, the transtensional basin at the western margin of the indenter displays a more complex geometry than the one in the reference model because of the combined influence of the rotation and viscous layer at the bottom. In M6 it consists of two interconnected basins (Fig. 3.8c) which gradually enlarge and connect in later stages of deformation. The larger basin (Figs. 3.7b and 3.8c) is elongated in roughly N–S direction and is opened along the western margin of the rigid block. The smaller one is located to the north with a curvature controlled by the NW corner of the indenter.

The geometry of the larger basin is controlled by the position with respect to the pole of rotation (fixed pin in Fig. 3.2a, c). Initially, a triangular transtensional basin opens due to the oblique normal slip along Riedel shears (similar to M4, M5, M7-10 in Fig. 3.5), which gradually widens southwards with subsequent deformation and rotation (i. e., in the direction away from the pole of rotation). Transtensional (dextral-normal) faults control the subsidence and bound the basin to the west and east (structures 2 and 3 in Fig. 3.8c). Structure 2 accommodates a larger amount of deformation (Fig. 3.8e, cross-

sections a-a', b-b'). Its associated sedimentary infill is affected by subsequent dextral strike-slip faulting (structure 4) that cuts through the basin and transfers most offset from structure 2 (Fig. 3.8c). These modelling geometries are fairly similar to the triangular geometry and differential subsidence observed in the Timok - Knjaževac basins system (Fig. 3.1c, Marović et al., 2007).

The smaller basin opens along the northern margin and NW curved corner of the indenter. In this area, the transtensional dextral slip is transferred into dominantly NNW- to N-dipping normal faults (structure 5 in Fig. 3.8c and d and cross-section a-a' in Fig. 3.8e) that control sedimentation in the basin. The offsets along these faults are significantly smaller than along faults controlling the N–S oriented basin and, therefore, the curved basin in the north is shallower (e.g., cross-section a-a' in Fig. 3.8e). These transtensional faults form towards the end of the experiment and have eastward decreasing offsets (structure 5 in Fig. 3.8c and d). These patterns are in agreement with observations in the Getic Depression (Fig. 3.1c), where the Timok Fault splays in multiple branches with gradually decreasing offset (e.g., Răbăgia et al., 2011 and references therein). However, the basin that opens along the NW corner and northern margin of the rigid block in the best-fit model is much shallower compared to up to 3 km subsidence generated in the Getic Depression (Matenco et al., 2003). This observation indicates that dragging along the Cerna-Timok faults system may be responsible for the ultimate connection between the Timok basin and the Getic Depression but is not the main mechanism controlling the subsidence in the latter. This is in agreement with the interpretation of the transtensional Getic Depression opening mechanism (e.g., Krézsek et al., 2013; Maţenco, 2017) in response to the Carpathians slab pull (presently remaining only as the Vrancea slab, Fig. 3.1a) and its associated tearing along an E-W oriented Subduction-Transform Edge Propagator (STEP) system in the South Carpathians (Fig. 3.1a; Govers and Wortel, 2005; Maţenco, 2017). Our modelling does not account for such more advanced geodynamic effects.

3.5.2 Transition between strike-slip/transtension and thrusting

South of the N–S oriented basin along the western indenter's margin, the strike-slip deformation is distributed over numerous vertical to high-angle faults (Fig. 3.8c, e, cross-section c-c'). These faults have a normal slip component that decreases southwards and is replaced with oblique reverse slip as the deformation is gradually transferred around the SW corner of the indenter (Fig. 3.8c and d) and further to thrusting south of the indenter (Fig. 3.8c and d, cross-section d-d' in Fig. 3.8e). The thrusting in the south and associated normal faulting due to the gravitational instability of the built-up wedge (Fig. 3.8c and d) are similar as in the reference model. The only difference is that back-thrusts and normal faults have smaller offsets in the best-fit model (Fig. 3.8c and d, cross-section d-d' in Fig. 3.8e). An interesting feature is that the area of gravitational collapse during translation (blue in Fig. 3.8b) gets shortened during the subsequent rotation (red and orange area in the hanging wall of the basal thrust in Fig. 3.8d; see also Appendix F). Both, thrusts and normal faults have a curved map-view geometry because they are linked with the strike-slip corridor in the west (Fig. 3.8c).

The transfer of strike-slip deformation into thrusting simulates very well and is compatible with the transfer of deformation observed from the Cerna-Timok fault system

into the western Balkanides thrust wedge (e.g., Schmid et al., 2020). The thrusts in the Balkanides also have a curved geometry due to the dextral drag along the Timok Fault during the transfer of deformation (Fig. 3.1b and c, see Schmid et al., 2020). Minor back-thrusting is also observed in the Balkanides nappes north of the Sofia basin (Fig. 3.1c).

The offset along the strike-slip system at the western margin of the rigid block decreases southwards in the best-fit model (from ~6 cm to <2 cm, see the offset of black and yellow marker lines in the top view of Fig. 3.8c). Notably, the southern propagation of the strike-slip faults offset earlier shortening structures (structure 6 in Fig. 3.8c, e, cross-section c-c'). Such propagation of strike-slip faults and truncation of older structures in the south are common features in other models as well (e.g., fault 6 in M2, 6 and 7 in M3, 6 in M4, southern prolongation of 4 and 5 in M5, 5 in M7, 6 in M8, 6 and 7 in M9, 3 in M10, southern prolongation of 4 in M11 and M12, Fig. 3.5). The decrease in offset in models explains well the observed significant decrease in Timok Fault dextral offset from 65 km in the north to around 5–10 km south of the Pirot Basin (Fig. 3.1c). A large part of the Timok dextral offset is taken up by thrusting in the Balkanides (Schmid et al., 2020), while the remainder in the southward prolongation is less constrained. One interpretation assumes that the Timok Fault is an inherited feature that was connected with the Cretaceous strike-slip deformation in the northern Rhodope (Fig. 3.1a and b, dashed line in Fig. 3.1c, the connection with the NW-SE oriented Maritsa Fault of Schmid et al., 2020, see also Naydenov et al., 2009, 2013; Henry et al., 2012; Vangelov et al., 2016). Another interpretation suggests that the Timok Fault continues south of the Pirot basin, offsetting the Kusa Vrana anticline (Fig. 3.1c, Kräutner and Krstić, 2003; Vangelov et al., 2016; van Hinsbergen et al., 2020). By comparing the geometries and overall evolution (Figs. 3.1c, 3.5 and 3.8), including the observed geometry of strike-slip deformation, our models are more compatible with the second solution.

3.6 Deformation transfer and oroclinal bending around indenters

In this section, we will discuss and compare our modelling results, summarized in Fig. 3.9, with previous studies.

3.6.1 Effects of the rigid indenter geometry on the strain partitioning

Our results show that deformation around a rigid indenter with either round or angular corners leads to curved fault systems where thrusting in the shortening domain transitions to strike-slip deformation through a system of oblique-slip faults (Fig. 3.9). This transitional area coincides with the maximum curvature of the fault system. This curvature is gradual in cases of rounded indenter corners, but abrupt in cases of rectangular comers, indicating that stress concentrations at indenter dips control the locus and geometry of deformation. Similar effects have been shown by Luth et al. (2013), where new faults nucleate at indenter dips. Overall, our results are in line with previous

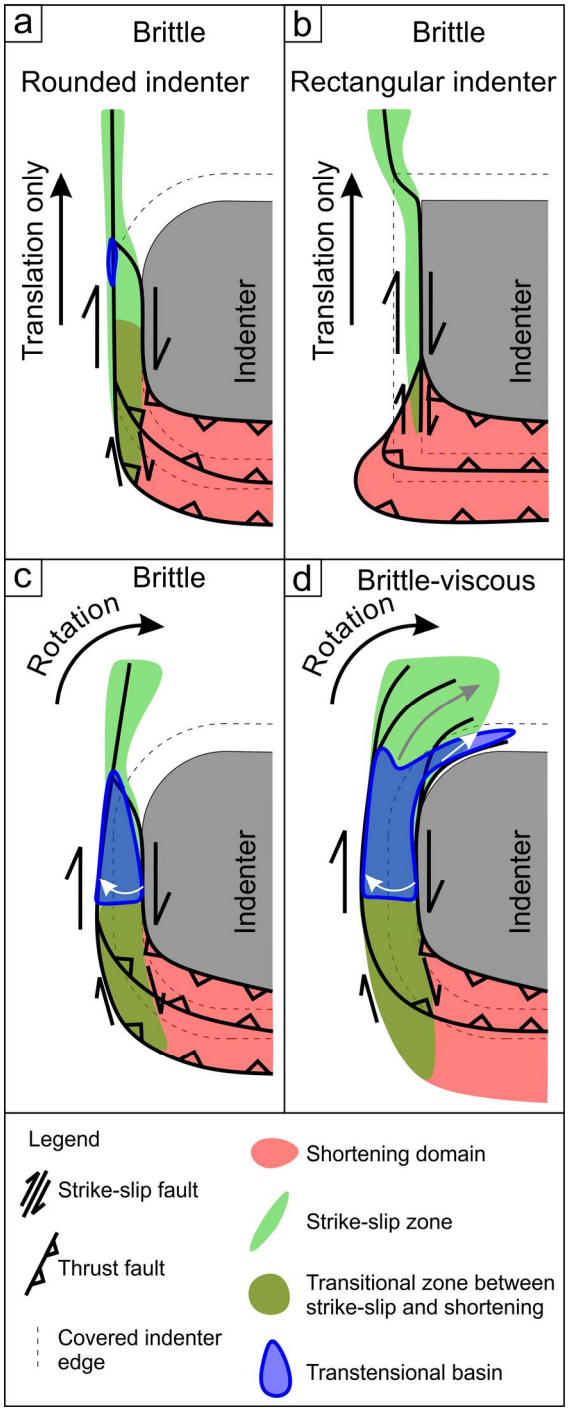

Figure 3.9 - Influence of various parameters on the structural evolution and deformation transfer around the indenter. a) and b) Comparison of effects of different indenter geometries (rounded vs rectangular, respectively) on the transfer of deformation between different indenter margins. c) Effects of rotation on widening the deformation zone and opening of triangular basins. The white arrow indicates the direction of the basin opening. d) Added effects of flow in the viscous layer compared to brittle only rheology as in Fig. 3.9c. The viscous layer distributes deformation in a larger area and facilitates the transfer of deformation around indenters corners. The grey arrow indicates the direction of flow in the viscous layer. The white arrow indicates the direction of the basin opening.

analogue modelling studies where the curvature of fold and thrust belts in front of an indenter are controlled by the indenter geometry (Marshak, 1988; Marshak et al., 1992; Zweigel et al., 1998; Costa and Speranza, 2003; Crespo-Blanc and González-Sánchez, 2005; Luth et al., 2013; Jiménez-Bonilla et al., 2020). Similar to our results, these studies exhibit a narrowing of the deformed area when deformation is transferred from the frontal to the lateral indenter margin (e.g., Marshak, 1988; Crespo-Blanc and González-Sánchez, 2005; Luth et al., 2013). The change in deformation regime around the indenter is also associated with a decrease in topography from the contractional to the strike-slip domain, which is gradual in the case of a rounded indenter (Fig. 3.9a) because northward translational component of displacement continuously transfers deformation to the strike-slip domain. This material transfer results in a higher topography farther northward and limits the formation of a wide and deep basin. In contrast, when the corner is rectangular (Fig. 3.9b), the wedge topography rapidly decreases northwards along a series of normal faults leading to a narrow transition zone (Fig. 3.9b).

The structure of the thrust wedge that forms south of the indenter is largely independent of the indenter geometry. The top to north basal thrust has a flat-ramp-flat geometry and the south-verging back-thrust system accommodates deformation in the hanging wall during thrusting (Fig. 3.5, see also cross-sections e-e' in Fig. 3.3g and d-d' in Fig. 3.4e). N-dipping normal faults, which reactivate previously formed back-thrusts, are interpreted as an expression of gravitational instability on top of the upper flat segment (Fig. 3.3g, cross-section e-e', Fig. 3.4e, cross-section d-d' and Fig. 3.8e, cross-section d-d'; see also Appendix C, F). These key features are consistent with previous modelling studies (Bonini et al., 2000; Rosas et al., 2017 and references therein; Fedorik et al., 2019).

3.6.2 Rotational control on the coupled basin-orogen evolution

In our models, morphologic depressions with limited lateral extent evolve along the strike-slip shear zone (Fig. 3.5) and probably reflect early dilatancy during shear zone development. All major sedimentary basins open in response to rotation of the mobile plate (Fig. 3.9c). During rotation, the tangential extension (i.e., the pole of rotation coincides with the pole of extensional opening) will create basins with a triangular map-view geometry (Fig. 3.9c), which is narrowing towards the pole of rotation, as observed in many natural examples including the Aegean (eg. Brun et al., 2016) or the southern Ethiopian segment of the East African rift system (Philippon et al., 2014a), and modelling studies (Zwaan et al., 2020 and references therein).

Although basins in our models are triangular and overall become narrower northwards (Figs. 3.5 and 3.7b), the combination of rotation and translation creates significant dextral shearing within the basin and partitions deformation between normal, oblique-normal and strike-slip faults as also described by Farangitakis et al. (2019; 2021). This is different to rotational extensional settings without coeval translation, where the size of the basin and its propagation towards the pole of rotation is solely controlled by the amount of rotation (Zwaan et al., 2020). The dextral component of shearing inside the basin creates major high angle faults, which are similar to the previous results of transtensional strike-slip experiments invoking a curved velocity discontinuity at the base of the model (Smit et al., 2010).

Shearing along the oblique-slip dextral faults transfers northern parts of the basin beyond the pole of rotation (Fig. 3.7b), which would otherwise be an area of transpression (see Zwaan et al., 2020). This effect is enhanced when invoking a ductile crust (see section 6.3). We furthermore note that the geometry of rotational triangular basins can also be controlled by inherited structural patterns or rheological heterogeneities (e.g., Molnar et al., 2017; 2019; Zwaan and Schreurs, 2020). However, as these aspects are not the focus of this study, they will not be discussed further.

3.6.3 Influence of the viscous layer on structural patterns

The presence of a viscous layer distributes deformation over larger areas with a lower number of high offset structures (Figs. 3.5–3.7, 3.9d). The reduced number of faults in these models and a more gradual transition of deformation along the indenter's margins results in a less well-developed structural pattern. These features have also been observed in previous studies (e.g., Casas et al., 2001; Leever et al., 2011; Luth et al., 2013; Jiménez-Bonilla et al., 2020 and references therein).

A novel aspect of our study is related to the transfer of deformation around the north-western indenter corners, where we interpret the development of splay faults in the brittle layer as an expression of flow in the underlying viscous layer that also affects areas on the adjacent fixed sheet (see Figs. 3.2c, 3.7 and 3.9c). We suggest that this flow generates a transtensional deformation regime leading to minor thinning of the viscous layer and subsidence within a local basin. The geometry of the (sub-)basin is controlled by the geometry of the NW corner (curved basin vs. more angular basin connection, Fig. 3.7b). South of the indenter, where the viscous layer is involved in thrusting over the ramp, most of the shortening is accommodated by the main basal thrust with well-distributed hanging wall shortening (e.g., Fig. 3.8e, cross-section d-d'), which is also observed in models by Bonini et al. (2000).

3.7 Conclusions

We present a series of crustal scale analogue experiments studying strain partitioning around an overall rectangular, rigid indenter with inclined margins. The investigated parameters include the shape of the indenter corners, the kinematic boundary conditions and the rheological stratification of the model crust.

Our models show that the shape of the indenter corners (rounded versus rectangular) has a major control on the style and geometry of deformation in the vicinity of the indenter. Styles of deformation include thrusts striking parallel to the indenter margin in the contractional domain, strike-slip fault systems parallel to the overall transport direction and oblique-slip fault systems accommodating the deformation transfer from the contractional to the strike-slip domain. Together these structures define an orocline whose curvature, the width of deformed area and along strike topographic gradient are largely controlled by the indenter corners. Models with rounded corners result in a gradual transition from thrusting to strike-slip deformation affecting a relatively wide area. This transition is abrupt in the case of rectangular indenter corners and deformation

is concentrated in the strike-slip domain within a narrow zone close to the indenter-model interface. These differences are the consequence of stress concentrations at indenter tips.

The modelling results furthermore demonstrate that 10o clockwise rotation of the model layers relative to the stationary indenter is critical for the opening of syn-tectonic sedimentary basins with triangular geometry along indenter margin(s). Overall, this area is characterized by transtensional strain where new, steeply dipping strike-slip faults with the normal component of shear form in the centre of the basin accommodating its rotational opening. Implementation of a viscous layer leads to distribution deformation over a wider area, which is, however, accommodated by fewer large offset structures. Most importantly, the flow of the viscous layer around the indenter corner allows for the transfer of deformation from the mobile to the stationary plate and the formation of curved transtensional basins.

Based on these models, we propose that oroclinal bending of the Carpatho-Balkanides is not only accommodated by the Cerna and Timok strike-slip faults, but involves the transfer of strain from the Balkanides where simultaneous contraction lead to the formation of a fold and thrust belt. Deformation is partitioned along numerous structures that control the northward translation and coeval opening of the transtensional basins (such as Timok and Knjaževac basins) along the Timok Fault, while the dextral splay faults around the NW Moesian corner, link up with deformation in the Getic Depression. Furthermore, we suggest that the southward decrease in dextral offset along the Timok Fault is a result of deformation transfer into thrusting in front of Moesia, which gradually reduces the amount of strike-slip deformation southwards along this fault.

In general, our modelling results show that oroclinal bending around rigid indenters is inevitably associated with the partitioning of deformation involving the coeval displacement of linked thrust, oblique-slip and strike-slip fault systems to accommodate translational and rotational plate movements.

3.8 Appendix

Appendices A-G to this chapter can be found online at https://doi.org/10.1016/j.jsg.2021.104386.

Chapter 4. Strain partitioning in a large intracontinental strike-slip system accommodating backarc-convex orocline formation: the Circum-Moesian Fault System of the Carpatho-Balkanides[3]

[3] This chapter is based on Krstekanić, N., Matenco, L., Stojadinovic, U., Willingshofer, E., Toljić, M., Tamminga, D., 2022. Strain partitioning in a large intracontinental strike-slip system accommodating backarc-convex orocline formation: the Circum-Moesian Fault System of the Carpatho-Balkanides. Global and Planetary Change 208, 103714. https://doi.org/10.1016/j.gloplacha.2021.103714

4.1 Introduction

The indentation of continental fragments is commonly used to explain orogenic shortening and crustal/lithospheric thickening accompanied by lateral extrusion, which is often associated with opposite polarity subduction systems (Davy and Cobbold, 1988; Doglioni et al., 2007; Faccenna et al., 2014; Johnson, 2002; Jolivet et al., 2018; Molnar and Tapponier, 1975; Regard et al., 2005). Indentation tectonics is observed in many orogenic systems (e.g., Argand, 1924; McKenzie, 1972; Ratschbacher et al., 1991a, b). For instance, the indentation of the Indian indenter is accommodated by shortening and uplift of the Himalayas and Tibet, and lateral extrusion towards SE Asia (Chen et al., 2000; Molnar and Tapponier, 1975; Searle et al., 2011; Shen et al., 2001; Sternai et al., 2016; Tapponier et al., 1986), shortening in front of the Arabian indenter is accompanied by Anatolian extrusion towards the Aegean (Kaymakci et al., 2010; Mantovani et al., 2006; Martinod et al., 2000; Regard et al., 2005), or the post-Oligocene shortening in the Eastern Alps is accompanied by extrusion towards the Pannonian-Carpathians region (Frisch et al., 1998; Neubauer et al., 2000; Ratschbacher et al., 1991b; Rosenberg et al., 2018; van Gelder et al, 2020, Wölfler et al., 2011). The lateral transfer of collisional shortening to other subduction systems is often facilitated by a complex strike-slip and transpressional/transtensional deformation associated with significant strain partitioning (e.g., Jolivet et al., 2018; van Hinsbergen et al., 2020; van Unen et al., 2019a). Similar to many other studies (e.g., Benesh et al., 2014; Cembrano et al., 2005; D'el-Rey Silva et al., 2011; De Vicente et al., 2009; Glen, 2004; Krézsek et al., 2013), we use the term strain partitioning in its general meaning of a multi-scale distribution of the total strain in different types of coeval structures whose kinematics cannot be explained by a homogenous stress field. Such cases of strain partitioning and deformation transfer during indentation include the Dinarides orogen that transfers the deformation from the Alps to the Aegean subduction (van Unen et al., 2019a), the East Anatolian and the Dead Sea faults that accommodate deformation along the lateral margin of the Arabian indenter (Lyberis et al., 1992; Perinçek and Çemen, 1990; Smit et al., 2010) or the Sagaing Fault of Indochina that connects India/Eurasia collision with the Sunda subduction system (Morley, 2002, 2013; Morley and Arboit, 2019; Vigny et al., 2003). Although kinematics along individual faults is well studied, the mechanisms of deformation transfer from shortening in front of an indenter to strike-slip along its lateral margins and the effects of indenter's geometry on strain partitioning are still not fully understood.

One remarkable example of deformation transfer from frontal shortening to lateral strike-slip along the margins of an indenter is the Carpatho-Balkanides orocline of south-eastern Europe. This double 180° curved orogenic system is comprised of a foreland-convex segment in the north and east, and a backarc-convex segment in the south and west (Fig. 4.1a). In our definition, a foreland-convex orocline has the convex side oriented towards the foreland (i.e., the vergence of the main orogenic structure is away from its core), while a backarc-convex orocline has the convex side oriented towards the backarc region (i.e., the orogenic thrusting is towards the oroclinal core, see also Krstekanić et al., 2020). The foreland- and backarc- convex oroclines are geometrically

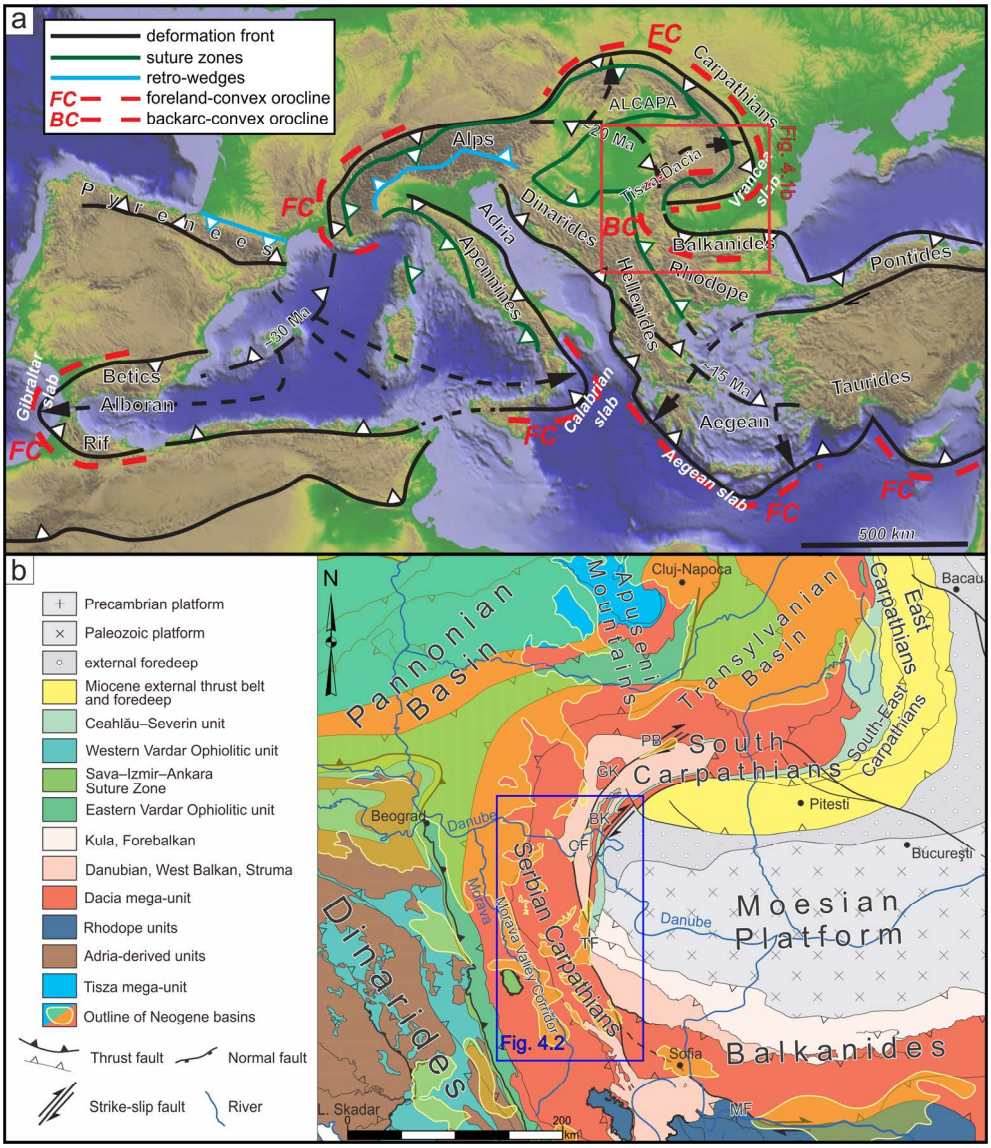

Figure 4.1 - a) Simplified European topographic map overlain by tectonic key elements (orogenic fronts, suture zones and retro-shears) of the Mediterranean Alpine-age orogens (modified from Krstekanić et al., 2020). The red rectangle shows the location of Fig. 4.1b. b) Regional tectonic map of the Carpatho-Balkanides orocline (modified after Schmid et al., 2020). The blue rectangle indicates the location of Fig. 4.2. BK - Bahna Klippe; CF - Cerna Fault; GK - Godeanu Klippe; MF - Maritsa Fault; PB - Petroşani Basin; TF - Timok Fault.

similar to a pair of salient – recess geometries (e.g., Marshak 1988; Miser 1932; Weil and Sussman, 2004). The later terms are used to describe the curvature of a single thrust front or a fold-and-thrust belt that is often related to thin-skinned thrusting and controlled by the footwall basin geometry and rheological variability (e.g., Livani et al., 2018; Marshak, 1988; Yonkee and Weil, 2010). In contrast, we use foreland- and backarc-convex oroclines to describe the geometry of larger scale curvatures that include rotations during orogenic build-up (i.e., oroclinal bending).

The overall formation of the Carpatho-Balkanides backarc-convex orocline was associated with the late Oligocene – middle Miocene formation of one of the largest strike-slip systems known in continental Europe, which accumulated more than 100 km of dextral offset along the curved Cerna and Timok faults system (Fig. 4.1b, Berza and Drăgănescu, 1988; Kräutner and Krstić, 2002, 2003; Ratschbacher et al., 1993). The Serbian Carpathians were coevally affected by orogen-parallel and orogen-perpendicular extension that formed numerous Oligocene-Miocene intra-montane basins and the prolongation of the Pannonian Basin along the Morava Valley Corridor (Figs. 4.1b, 4.2; Erak et al., 2017; Krstekanić et al., 2020; Matenco and Radivojević, 2012). The connected and neighbouring structures of the western Balkanides recorded contraction during their thrusting over the Moesian Platform (Figs. 4.1b, 4.2; Schmid et al., 2020).

All these deformations associated with the ultimate formation of the Carpatho-Balkanides backarc-convex oroclinal bending created a large fault system where contrasting types of deformation affected the orogenic system and are connected around the southern, western and northern margins of the Moesian Platform (Fig. 4.1b). We herewith define this deformation associated with large-scale strain partitioning as the Circum-Moesian Fault System (CMFS), which is made up of a complex network of coeval strike-slip, thrust and normal faults. The mechanics and kinematics of this fault system and its strain partitioning along the Moesian margins are not understood. To advance this understanding, we have performed a field kinematic and structural study, focused on quantifying the CMFS deformation in the less understood area of the Serbian Carpathians, which links the deformation in the South Carpathians in the northeast to deformation in the Balkanides in the southeast. We correlate our results with previously published studies from the neighbouring East Carpathians, Rhodope, Dinarides, Pannonian Basin and Morava Valley Corridor (Fig. 4.1b, e.g., Brun and Sokoutis, 2007; Ellouz et al., 1994; Erak et al., 2017; Krstekanić et al., 2020; Matenco and Radivojević, 2012; Necea et al., 2021; Stojadinovic et al., 2013, 2017) to infer the relative importance of deformation in these regions on strain partitioning in our study area and to discuss potential mechanisms driving the formation of the backarc-convex Carpatho-Balkanides orocline. Because the formation of this backarc-convex orocline is rather unique during the Alpine evolution of the entire Mediterranean area (see Fig. 4.1), the results are shortly discussed in a larger regional and process-oriented context.

4.2 Tectonic evolution of the Carpatho-Balkanides during oroclinal bending and Moesian indentation

Previous studies have shown that most of the South and Serbian Carpathians and Balkanides mountains are made up of the large Europe-derived, Dacia continental mega-unit (Fig. 4.1b) that split-off during the Middle Jurassic opening of the Ceahlău–Severin branch of the Alpine Tethys Ocean, while to the west and south-west this mega-unit was separated from the Adria microcontinent by a northern branch of the Neotethys Ocean, which started to open during Middle Triassic times (Schmid et al., 2008, 2020; van Hinsbergen et al., 2020 and references therein). The Carpatho-Balkanides orogen (Fig. 4.1a) formed during the Cretaceous – Miocene closure of the Alpine Tethys Ocean (Csontos and Vörös, 2004; Horváth et al., 2015; Maţenco, 2017). The initial late Early Cretaceous partial closure of the Ceahlău–Severin branch in the South and Serbian Carpathians and Balkanides segments of the orogen created a thick-skinned nappe-stack and was facilitated by the collision with Moesian Platform, a promontory of the stable European continent, which acted as indenter during the collision (Fig. 4.1b, Csontos and Vörös, 2004; Săndulescu, 1988; Schmid et al., 2020). Shortening of the Dacia mega-unit created two main thick-skinned units, i.e., the Supragetic and Getic nappes of the South and Serbian Carpathians (see also Kräutner and Krstić, 2002). The nappe-stacking was followed by Late Cretaceous extension and calc-alkaline magmatism (in the Apuseni-Banat-Timok-Sredna Gora belt, see Gallhofer et. al., 2015; von Quadt et al., 2005) and a latest Cretaceous overthrusting of the Dacia mega-unit over the Ceahlău–Severin nappe and Moesia that created a Danubian nappe-stack derived from the Moesian margin (Fig. 4.1b, Csontos and Vörös, 2004; Săndulescu, 1988; Seghedi et al., 2005). These Cretaceous events were followed by the continuation of oceanic subduction and Miocene slab retreat in the Western and Eastern Carpathians, which facilitated the creation of the southern backarc-convex orocline during 90 degrees of clockwise rotation and docking of the South Carpathians against the Moesian indenter (Fig. 4.1, Balla, 1984, 1986; Csontos et al., 1992; Krstekanić et al., 2020; Márton, 2000; Panaiotu and Panaiotu, 2010; Pătraşcu et al., 1994; Ratschbacher et al., 1993; van Hinsbergen et al., 2020). The oroclinal bending was associated with a Paleocene-Eocene orogen-parallel extension that exhumed the Danubian nappes of the South Carpathians (Fig. 4.1b; Fügenschuh and Schmid, 2005; Matenco and Schmid, 1999; Schmid et al., 1998) and the late Oligocene – middle Miocene creation of the curved Cerna and Timok faults system (Fig. 4.1b).

4.2.1 The Cretaceous multi-phase nappe structure, extension and associated magmatism

The remnants of the Ceahlău–Severin Ocean are thought to outcrop in two regions within our studied area (Figs. 4.2 and 4.3, see also Schmid et al., 2020). In the north-eastern region situated in the vicinity of the Danube River, these remnants are composed of the uppermost Jurassic – Lower Cretaceous clastic to calcareous, locally ophiolite-bearing, turbiditic sequences (Bogdanović and Rakić, 1980; Kalenić et al., 1976; Melinte-Dobrinescu and Jipa, 2007; Săndulescu, 1984; Savu et al., 1985; Veselinović et al., 1975). In the southern part of the studied area west of the Kusa Vrana anticline (Fig. 4.2),

Tithonian – Lower Cretaceous clastic to calcareous turbidites overlie the Danubian units and are thrusted by the Getic nappe of the Dacia-mega unit (Anđelković et al., 1977; Petrović et al., 1973; Vujisić et al., 1980).

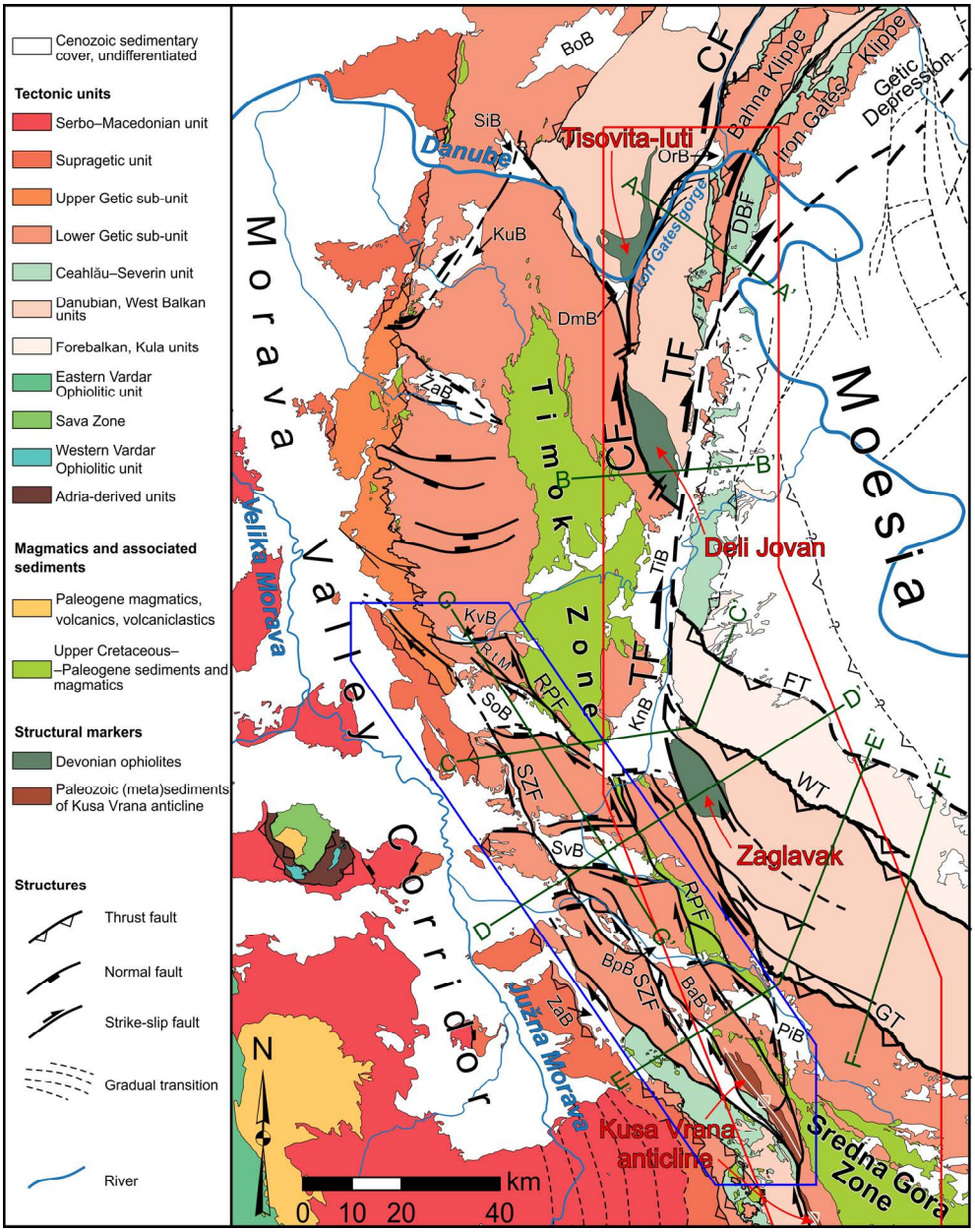

Figure 4.2 - Tectonic and structural map of the Serbian Carpathians and adjacent areas showing the regional fault kinematics of the Circum-Moesian Fault System (CMFS, compiled and modified after Basic geologic map of former Yugoslavia, scale 1:100.000,

Maţenco, 2017, Krstekanić et al., 2020, following the terminology of Schmid et al. 2020 and the results of this study). Red polygon is the location of Fig. 4.4, blue polygon marks the location of Figs. 4. 6 and 4.8. Dark green lines show positions of cross-sections in Fig. 4.3. BaB – Babušnica Basin; BoB – Bozovici Basin; BpB – Bela Palanka Basin; CF - Cerna Fault; DBF - Dževrin-Balta Fault; DmB – Donji Milanovac Basin; FT - Forebalkan Thrust; GT - Getic Thrust; KnB – Knjaževac Basin; KuB – Kučevo Basin; KvB – Krivi Vir Basin; OrB – Orşova Basin; PiB – Pirot Basin; RPF - Rtanj-Pirot Fault; RtM – Rtanj Mountains; SiB – Sicheviţa Basin; SoB – Sokobanja Basin; SvB – Svrljig Basin; SZF - Sokobanja-Zvonce Fault; TF - Timok Fault; TiB – Timok Basin; WT - West Balkan Thrust; ZaB – Zapljanje Basin; ŽaB – Žagubica Basin.

The late Early Cretaceous (~100–110 Ma) thrusting of the Supragetic over the Getic units was top to ~E in the present-day geometry of the Serbian Carpathians (Figs. 4.2 and 4.3, Krstekanić et al., 2020, and references therein). The Supragetic basement is made up of Variscan mostly greenschist to sub-greenschist facies metamorphic rocks (e.g., Iancu et al., 2005b), overlain by passive margin continental late Carboniferous – Permian clastics and, locally, thin Triassic – Jurassic shallow-water limestone sequences (Kalenić et al., 1980; Petković, 1975a; Veselinović et al., 1970). The Getic unit is locally separated in Upper and Lower Getic sub-units along a large, but variable offset, thrust (Fig. 4.2; Krstekanić et al., 2020). Both sub-units have a similar greenschist to amphibolitic metamorphic basement, intruded by syn- to post-collisional Variscan granitoids (~325–290 Ma; Iancu et al., 2005a, b; Jovanović et al., 2019; Kräutner and Krstić, 2002). The sedimentary cover is composed of Permian alluvial red clastics and transgressive Lower – Middle Triassic shallow-water sediments overlain by Middle Jurassic transgressive clastics and carbonates, Upper Jurassic – Lower Cretaceous deep water to reef limestones and dolomites (Fig. 4.3, e.g., Antonijević et al., 1970; Grădinaru et al., 2016; Krstić et al., 1976; Petković, 1975b; Veselinović et al., 1970; Vujisić et al., 1980). The total thickness of the Getic sedimentary cover reaches ~2 km.

The Carpatho-Balkanides recorded a Late Cretaceous phase of calc-alkaline magmatism, genetically interpreted to be related to the roll-back of the Neotethys subducting slab, or alternatively by the variability of the subduction in the Ceahlau-Severin Ocean, which created the so-called Apuseni–Banat–Timok–Sredna Gora (ABTS) magmatic belt (Andrić et al., 2018; Balla, 1984, 1988; Berza et al., 1998; Gallhofer et al., 2015; Kolb et al., 2013.; Neubauer, 2015; Toljić et al., 2018; von Quadt et al., 2005). In the study area, this magmatism is observed in the Timok and Sredna Gora zones (Figs. 4.2 and 4.3), where the Upper Cretaceous – Paleogene intrusives, volcanics and volcaniclastics are associated with coeval normal faulting (Banješević, 2006; Kalenić et al., 1976; Knaak et al. 2016; Kräutner and Krstić, 2003; Petković, 1975b; Veselinović et al., 1975). To the west, this extension is thought to have exhumed the amphibolite facies metamorphics of the Serbo-Macedonian unit (peak metamorphism of Variscan age, ~480-330 Ma; Antić et al., 2016a) from below the Supragetic unit in the footwall of detachments (Fig. 4.2; Antić et al., 2016a, b; Erak et al., 2017). The Serbo-Macedonian unit is also part of the Dacia mega-unit and, together

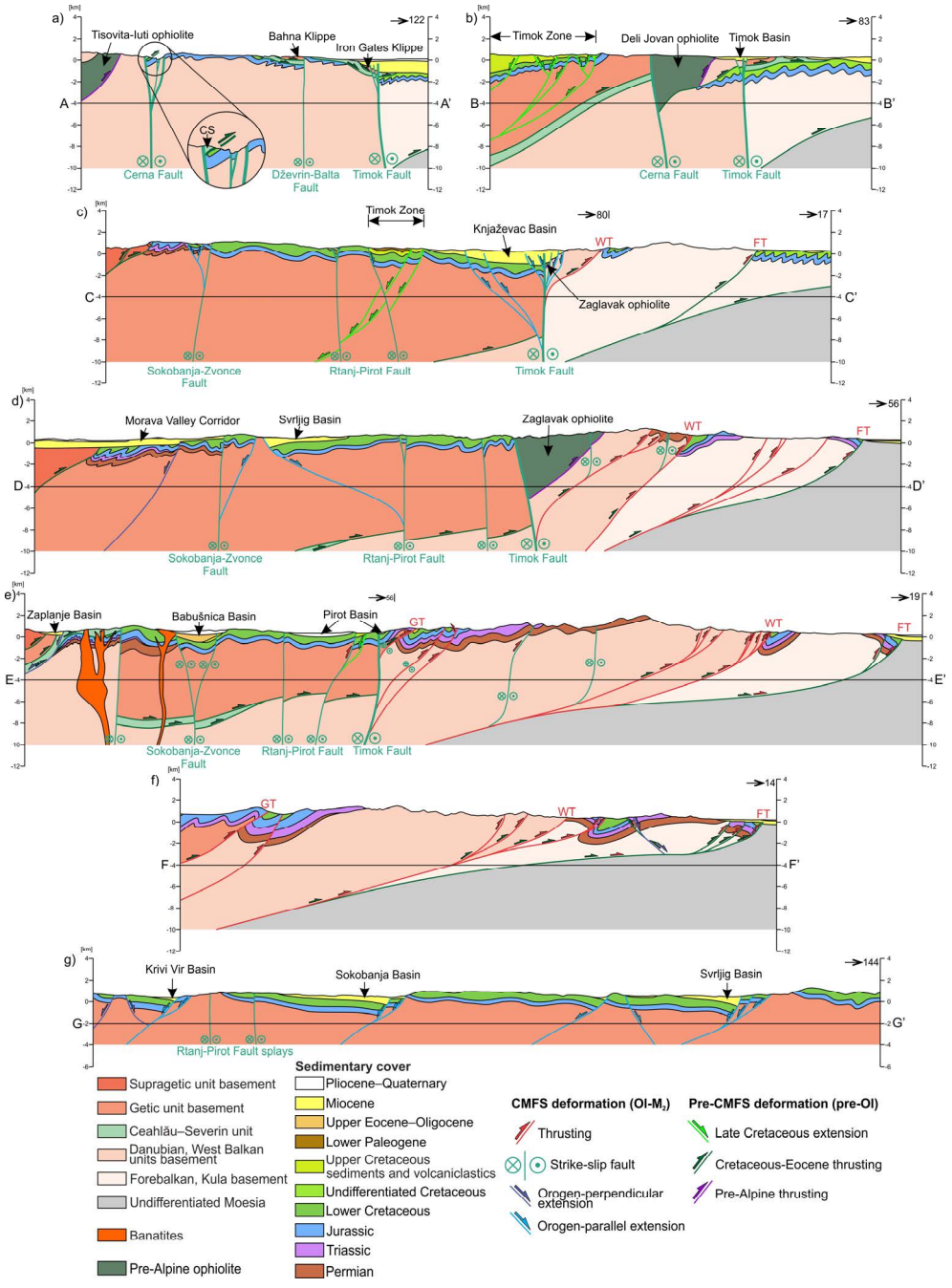

Figure 4.3 - Geologic cross-sections in the studied area. Surface to depth projection is based on the field kinematic data from this study and the Basic geologic map of former Yugoslavia, scale 1:100.000. The locations of the cross-sections are displayed in Fig.

4.2. The strike of each cross-section is indicated in the upper right corner of the section. No vertical exaggeration has been applied. FT - Forebalkan Thrust; GT - Getic Thrust; WT - West Balkan Thrust.

---

with the obducted Eastern Vardar Ophiolitic unit, forms the upper plate in respect to the Neotethys subduction along the Sava suture zone of the Dinarides (Figs. 4.1, 4.2; Pamić, 2002; Stojadinovic et al., 2017; Schmid et al., 2008; Ustaszewski et al., 2010).

Renewed shortening took place during the latest Cretaceous (~75–67 Ma), postdating the extension and magmatism in the ABTS belt (Iancu et al., 2005a; Neubauer and Bojar, 2013; Schmid et al., 2008), which created the Supragetic-Getic-Danubian nappe stack (Figs. 4.2 and 4.3, Ciulavu et al., 2008; Csontos and Vörös, 2004; Berza et al., 1983; Maţenco, 2017; Săndulescu, 1984). The basement of Danubian units has recorded several deformation events and poly-phase metamorphism and is built of high-grade Neoproterozoic Pan-African and low-grade Caledonian to Variscan metamorphic rocks with a weak Alpine metamorphic overprint (Dallmeyer et al., 1998; Iancu et al., 2005a, 2005b; Kräutner and Krstić, 2002; Ratschbacher et al., 1993; Seghedi et al., 2005). This metamorphic basement includes also the pre-Alpine granitic intrusions and Devonian Tisovita-Iuti – Deli Jovan – Zaglavak ophiolitic complex (Iancu et al., 2005b; Kalenić et al., 1976; Kräutner and Krstić, 2002; Krstić et al., 1976; Plissart et al., 2017; Seghedi et al., 2005, Zakariadze et al., 2012), whose location is important for restoring the below described post-Eocene oroclinal deformation (Figs. 4.2 and 4.3). The Danubian metamorphic basement is overlain by continental to shallow-water lacustrine Permian clastics, lower Triassic clastics and Middle to Upper Triassic carbonates, a Lower to Middle Jurassic clastic succession, Middle Jurassic to late Early Cretaceous carbonates and locally Late Cretaceous fine-grained sediments (Fig. 4.3, Anđelković et al., 1977; Bogdanović and Rakić, 1980; Iancu et al., 2005a; Kalenić et al., 1976; Krstić et al., 1976; Veselinović et al., 1975).

4.2.2 The Eocene–Miocene oroclinal bending

Following the Cretaceous orogeny, subduction of the Carpathian embayment lithosphere and continental collision continued in the Western and Eastern Carpathians during Paleogene-Miocene times. The nature of the subducted slab is still debated and could have had oceanic or highly extended continental character (e.g., Bokelmann and Rodler, 2014; Necea et al., 2021). The N-, NE- and E-ward Miocene roll-back and closure of the Carpathian embayment have created ultimately the two oroclines observed in the double Carpatho-Balkanides loop (Fig. 4.1a; Ustaszewski et al., 2008). While the South Carpathians segment underwent a coeval gradual clockwise rotation of up to 90° (e.g., Balla, 1984, 1986, 1987; de Leeuw et al., 2013; Dupont-Nivet et al, 2005; Pătraşcu et al., 1990, 1992, 1993; Panaiotu and Panaiotu, 2010), this rotation decreases to 25°-30° in the Serbian Carpathians segment and becomes negligible in the Balkanides (Lesić et al., 2019; van Hinsbergen et al., 2008).

The Paleocene – Eocene orogen-parallel extension reactivated the inherited basal thrust of the Getic unit in the South Carpathians and exhumed the Danubian nappe-stack along an extensional detachment, forming the Danubian window (Figs. 4.1b, 4.2;

Fügenschuh and Schmid, 2005; Matenco and Schmid, 1999; Moser et al., 2005; Schmid et al., 1998). During the late extensional exhumation of the Danubian nappes, the main Eocene nappe stacking of the Balkanides took place, which truncated or partly reactivated the late Early Cretaceous thrusts and was followed likely by renewed thrusting in the West Balkans unit (Burchfiel and Nakov, 2015; Schmid et al., 2020; Vangelov et al., 2013). The orogen-parallel extension was followed by the formation of late Oligocene – early middle Miocene high offset curved strike-slip dextral Cerna and Timok faults (Figs. 4.1b, 4.2 and 4.3; Berza and Drăgănescu, 1988; Kräutner and Krstić, 2002; Ratschbacher et al., 1993). The 35 km late Oligocene offset of the Cerna Fault and 65 km late Oligocene – early Miocene offset along the Timok Fault are documented by displaced Devonian ophiolites in the Danubian/West Balkan units basement (Tisovita-Iuti, Deli Jovan and Zaglavak, see Fig. 4.2) or by displaced South Carpathians nappe stack and intramontane basins (Berza and Drăgănescu, 1988; Kräutner and Krstić, 2002; Ratschbacher et al., 1993). The Timok Fault is thought to have transferred its offset to thrusting southwards in the Balkanides (e.g., Schmid et al., 2020, and references therein) and to transtension and extension in the frontal part of the South Carpathians (e.g., Rabăgia and Maţenco, 1999). Further away from the Moesian Platform, in the hinge of the backarc-convex orocline (i.e., the internal Serbian Carpathians), the strike-slip deformation was more distributed, previous studies being unable so far to identify regional-scale structures that may have accommodated significant strike-slip offsets (Mladenović et al., 2019; Krstekanić et al., 2020).

Dextral strike-slip displacement of the Cerna and Timok faults was largely coeval with the Oligocene-Miocene orogen-perpendicular extension in the Pannonian Basin and its southern Morava Valley Corridor prolongation (Figs. 4.1b, 4.2 and 4.3), thought to have been driven by the coupled effect of the roll-back of Carpathian and Dinaridic slabs (Andrić et al., 2018; Balázs et al., 2016; Erak et al., 2017; Horváth et al., 2006; Matenco and Radivojević, 2012; Stojadinovic et al., 2013, 2017; Toljić et al., 2013). The E-W oriented extension in the Morava Valley Corridor started during the Oligocene (~29–27 Ma) and lasted until the middle Miocene (Erak et al., 2017; Matenco and Radivojević, 2012; Sant et al., 2018), affecting the internal segments (i.e., the hinge of the orocline) of the Serbian Carpathians (Krstekanić et al., 2020). Several lacustrine intramontane basins overlie the Cretaceous orogenic fold-and-thrust structure of the Serbian and South Carpathians (Figs. 4.2 and 4.3, Table 4.1). Among these, the oldest sediments are middle to upper Eocene lacustrine turbidites observed at the base of the Babušnica Basin (Fig. 4.3e, Table 4.1; de Bruijn et al., 2018; Marković et al., 2017). Most of the other basins are filled with lower middle Miocene – Pliocene sediments, such as the Sokobanja, Žagubica and Svrljig basins (Figs. 4.2, 4.3d, g, Table 4.1; Kalenić et al., 1980; Lazarević and Milivojević, 2010; Marković, 2003; Obradović and Vasić, 2007; Sant et al., 2018). The sedimentation in the Bela Palanka and Pirot basins is thought to have started only during Pliocene times (Table 4.1; Anđelković et al., 1977; Vujisić et al., 1980). Other basins are observed along the Cerna and Timok faults, some connected with the coeval marine sedimentation overlying the Moesian Platform (Figs. 4.2, 4.3a-c). The middle Miocene Donji Milanovac and Orşova basins opened along the Cerna Fault (Fig. 4.2,

Basin	Sedimentary infill age	References
Babušnica	Initial infill: middle – upper Eocene (38-34 Ma) Middle stage: Oligocene (33-30 Ma) Final infill: Pliocene (~5 Ma)	de Bruijn et al. (2018); Marković et al. (2017); Vujisić et al. (1980)
Bozovici	Initial infill: lower Miocene? (~17-15 Ma) Main infill: lower middle Miocene (15-13 Ma)	Codrea (2001); Hír et al. (2016)
Bela Palanka	early Pliocene (~5 Ma)	Vujisić et al. (1980)
Donji Milanovac	lower middle Miocene	Bogdanović and Rakić (1980)
Knjaževac	Initial infill: lower Miocene (~17 Ma) Main infill (marine ingression): lower middle Miocene (15-13 Ma) Final infill: upper middle Miocene	Djurović and Živković (2013); Krstić et al. (1976); Rundić et al. (2019); Veselinović et al. (1975)
Kučevo	Initial infill: lower middle Miocene (15-13 Ma) Final infill: upper middle Miocene	Kalenić et al. (1980); Lazarević and Milivojević (2010)
Krivi Vir	Initial infill: late Oligocene (~24.5-23 Ma) Main and final infill: lower to upper Miocene?	Mai (1995); Veselinović et al. (1970); Žujović (1886)
Orşova	lower middle Miocene to upper middle Miocene	Geological map of Romania
Pirot	early Pliocene (~5 Ma)	Anđelković et al. (1977)
Sicheviţa	middle Miocene	Geological map of Romania
Sokobanja	Initial and main infill: lower middle Miocene (15-13 Ma) Final infill: upper Miocene? – Pliocene?	Krstić et al. (2012); Sant et al. (2018); Veselinović et al. (1970)
Svrljig	Initial and main infill: lower middle Miocene (15-13 Ma) Final infill: upper Miocene? – Pliocene?	Krstić et al. (1976); Krstić et al. (2012); Sant et al. (2018)
Timok	Initial infill: lower Miocene (~17 Ma) Main infill (marine ingression): lower middle Miocene (15-13 Ma) Final infill: upper middle Miocene	Djurović and Živković (2013); Krstić et al. (1976); Rundić et al. (2019); Veselinović et al. (1975)
Zaplanje	Initial and main infill: lower middle Miocene (15-13 Ma) Final infill: upper Miocene? – Pliocene?	Obradović and Vasić (2007); Sant et al. (2018); Vujisić et al. (1980)
Žagubica	Initial and main infill: lower middle Miocene (15-13 Ma) Final infill: upper Miocene? – Pliocene?	Antonijević et al. (1970); Lazarević and Milivojević (2010); Sant et al. (2018)

Table 4.1 - Summarized ages of the intramontane basins in the South and Serbian Carpathians in Fig. 4.2. Ages are based on the correlations of geologic maps of former Yugoslavia and Romania, publications cited in the table and basins age synthesis in Krstekanić et al. (2020).

Table 4.1; Bogdanović and Rakić, 1980; Kräutner and Krstić, 2003), while the lower-middle Miocene sediments of the Timok and Knjaževac basins (Krstić et al., 1976; Rundić et al., 2019; Veselinović et al., 1975) are truncated by and overlie the Timok Fault (Figs. 4.2, 4.3b, c). Previous studies have shown that some of the E-W trending basins (e.g., Žagubica, Krivi Vir, Sokobanja and Svrljig, Fig. 4.2 and 4.3g) were formed during a middle Miocene period of orogen-parallel extension, controlling their lacustrine deposition (Fig. 4.2; Krstekanić et al., 2020).

4.3 Methodology

4.3.1 The structural mapping approach

We have performed a field structural and kinematic analysis in the Serbian Carpathians and their transition to the Balkanides (Fig. 4.2). First, we identified the major faults or fault zones by using the existing 1:100.000 scale geologic maps (Basic geologic map of former Yugoslavia). These maps were also used for identifying other major regional structures (such as km-scale folds or uplifted and exhumed basement), correlations with neighbouring areas and for defining the timing of post-Cretaceous tectonic events by combining observations of stratigraphic offsets along faults and sealing post-kinematic deposits (see also Dimitrijević, 1997; Kräutner and Krstić, 2003; Schmid et al., 2008; 2020; Krstekanić et al., 2020 and references therein). The studied major structures include the curved dextral strike-slip Cerna and Timok faults, two sub-parallel narrow (i.e., up to a few hundreds of meters wide) NNW-SSE oriented corridors of Paleogene to Miocene sediments and fault zones (the Sokobanja-Zvonce and Rtanj-Pirot faults zones) and several E-W oriented normal faults bounding Miocene intramontane basins (Fig. 4.2). During fieldwork, we focussed on mapping the kinematics of large-offset faults and fault zones within post-Cretaceous sediments that are pre- to syn-kinematic to the observed faulting. Subsequently, we documented kinematics and the faulting superposition (by observing cross-cutting relationships, tilting, rotations and truncation) along the strike of these structures in the ophiolites, pre-Alpine granitoids and basement and the Mesozoic cover of the Getic and Danubian units (Fig. 4.2). We also investigated the middle Miocene intramontane basins, where we focused our mapping on the kinematics of the basin-controlling E-W oriented faults and their interaction with the connecting NNW-SSE oriented fault zones (Fig. 4.2). Furthermore, we mapped and analysed the kinematics of reactivated nappe contacts in the western Balkanides segment of the orocline (east and in the vicinity of the Timok Fault in Fig. 4.2).

All observed deformation has a brittle character. Field measurements include orientations of faults and fault zones, foliations within fault gouge and cataclasite, faulting-related cleavage and observations of tilting and rotations. Slickenside kinematic indicators (including calcite slickenfibres, grooves and other brittle indicators), Riedel shears and brittle shear bands in fault gouge and foliated cataclasite were used to derive the sense of shear along faults and fault zones by considering confidence criteria and quality ranks (e.g., Angelier, 1994; Doblas, 1998; Sperner and Zweigel, 2010). The fault-slip data was separated by superposition, timing criteria and consistency of slip direction

and sense of slip. Data collected in outcrops (Supplementary Appendix A, B) located in proximity and along the same map-scale structure are analysed together. We grouped the analysed data into structures (circled numbers and points in Figs. 4.4, 4.6 and 4.8) that combine multiple observation points.

4.3.2 Deformation analysis

We focussed only on the post-Cretaceous and pre- late Miocene deformation related to the Cerna and Timok faults system and their associated structures. The older pre-Cenozoic structures are discriminated by mapping in the major post-Cretaceous fault zones, observed superposition criteria and their comparison with the previously studied Cretaceous tectonic events, such as orogen-perpendicular shortening(s) that created the Carpatho-Balkanides nappe-stack or Late Cretaceous backarc extension (e.g., Schmid et al., 2008; Gallhofer et al., 2015; Mladenovic et al., 2018; Krstekanić et al., 2020). The Oligocene – middle Miocene orogen-perpendicular extension is observed in the Morava Valley Corridor in the convex side of the orocline to decrease eastwards (Erak et al., 2017; Stojadinovic et al., 2013, 2017; Toljić et al., 2013), which is coeval with the activity of Cerna and Timok faults (Mladenović et al., 2019; Krstekanić et al., 2020. This observation enabled a separation of kinematics of these different coeval expressions of strain partitioning during the oroclinal formation (see also Krstekanić et al., 2020). It is important to note that in most situations of cross-cutting, structures showing different kinematics (e.g., strike-slip and normal faults) or orientations (e.g., two sets of dextral strike-slip faults) mutually truncate each other in outcrops. In such cases, we associate these structures to the same tectonic event.

The post-Cretaceous kinematics observed in multiple outcrops along strike of the major faults is assigned to its specific expression at map scale, which enabled an analysis of strain partitioning observed along major faults or fault zones. The lateral correlation between outcrops is based on the character of deformation in similar lithologies (e.g., fault gouges versus individual fault planes or brittle shear bands) as well as on the compatibility of deformation and offsets observed in the field with the one at the map scale. We present the mapped fault-slip data as being the result of a single large tectonic event because the observed cross-cutting relationships of reported structures with significantly different kinematics (normal, strike-slip and reverse faults) do not allow their separation to different events. These relationships demonstrate that structures of different kinematics formed coevally in the same area, which is a typical indication for strain partitioning.

The type of strain partitioning often observed in our dataset is related to local vertical axis rotations of earlier segments of faults in the same fault zone, restraining and releasing bends, horse-tail geometries, step-overs, thrusting associated with tear-faulting, or drag folding. We provide solutions for the type of observed strain partitioning based on kinematic effects, such as folds or strata rotations observed in outcrops by connecting field data and carefully following the same structure along its strike. Further information on this strain-based approach is available in published kinematic studies (e.g., Krstekanić et al., 2020; van Gelder et al., 2015; van Unen et al., 2019a, b).

The observed strain partitioning is not suitable for deriving paleostress directions by kinematic data stress inversion. Paleostress inversion methods require that fault-slip

measurements are taken along faults that do not have large offsets (i.e., kilometres to tens of kilometres) that are comparable with the fault size (e.g., Twiss and Unruh, 1998), which contrasts with the measured kinematics along faults that have offsets reaching tens of kilometres. Kinematic measurements taken within wide, large offset fault zones do not satisfy the Wallace-Bott criteria (Yamayi, 2003, and references therein) and are often associated with strain partitioning during deformation. Furthermore, one of the assumptions of the paleostress inversion methods is that fault kinematic data is derived from independently slipping faults and that there is no fault interaction (Angelier, 1979, 1989), which contrasts with the observed fault system. In addition, lithological contrasts between rocks with contrasting strength, such as limestones and volcaniclastics are often activated by large-offset faults. All these paleostress methodology limitations are otherwise well-known (e.g., Célérier et al., 2012; De Vicente et al., 2009; Hippolyte et al., 2012; Jones and Tanner, 1995; Lacombe, 2012; Orife and Lisle, 2003; Sperner and Zweigel, 2010).

4.4 Kinematic observations

Our dataset is presented in relationship with the major (i.e. large offset) structures, which are the Cerna and Timok faults (Figs. 4.4, 4.5), the NNW-SSE oriented Sokobanja-Zvonce and Rtanj-Pirot faults (Figs. 4.6, 4.7a-g) and the E-W oriented normal faults controlling the formation of Miocene basins (Figs. 4.7g, h and 4.8). The kinematics of regional faults was used to construct seven regional cross-sections (Fig. 4.3), which are both perpendicular and parallel to the main orogenic structures. The structure at depth is constructed only from surface kinematic projections by following the definition of the main tectonic units and the observed lateral variability of stratigraphy. Therefore, the degree of uncertainty of these cross-sections increases with depth.

4.4.1 Connecting the Cerna and Timok strike-slip with the Balkanides thrusting

The curved Cerna and Timok faults system offsets the Cretaceous nappe-stack, the late Cretaceous basin(s) and the Eocene extensional Danubian window (Figs. 4.2, 4.4). The strike of these faults changes from NE-SW in the north, N-S in the centre, to NW-SE in the south. All observed deformation related to these faults is dominantly associated with (sub-)vertical strike-slip faults (Fig. 4.4). In the main fault zones, we commonly observed numerous closely-spaced (i.e., at tens of centimetres distance) sub-vertical faults with fault gouges and similar kinematics (e.g., Figs. 4.5a, d), decametre-scale, corrugated and striated fault surfaces (e.g., Fig. 4.5b), or several metres thick fault gouge zones that often display foliation (Figs. 4.5c, f).

Deformation along the Cerna and Timok faults is often partitioned along multiple (sub-)parallel strands (e.g., structures S1, S5 and S13 in Fig. 4.4) that accommodate variable offsets. High-angle to vertical dextral strike-slip faults that are parallel to the map-view orientation of the Cerna or Timok faults are observed in all locations (colour 1 in Fig. 4.4). Numerous secondary structures oriented obliquely to the strike of the

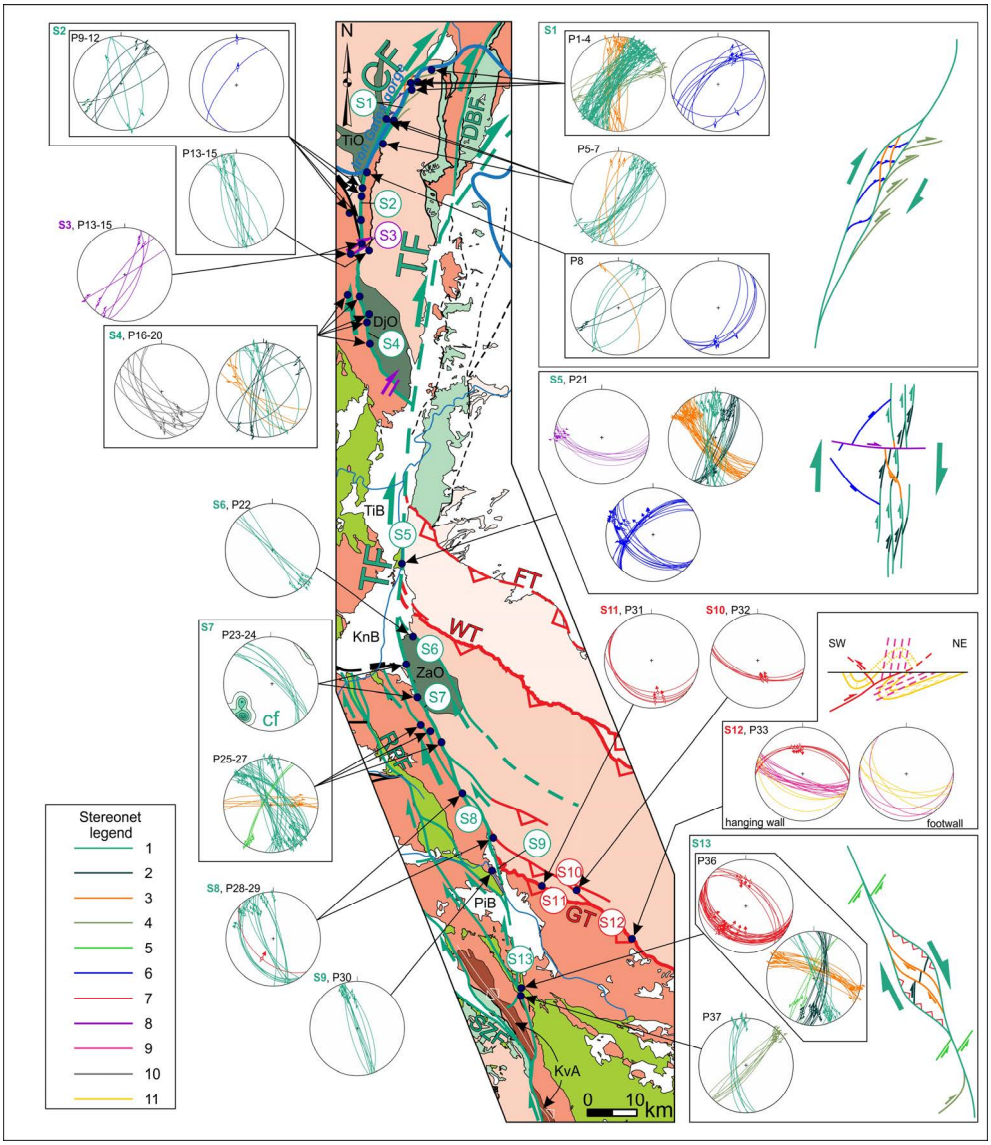

Figure 4.4 - Structural map of the Cerna and Timok faults and neighbouring Balkanides thrusting areas with lower hemisphere stereographic projections of measured faults and foliations within fault gouge. The location of the map is displayed in Fig. 4.2. Faults covered by Neogene sediments or faults with unclear prolongation are dashed. Numbered structures in stereonets correspond to map-scale structures with the same number. Each structure may combine multiple observation points. S - structure; P - observation point; fault planes without a sense of shear are measured foliations within fault gouge; cf - density plot of the poles of foliation in fault gouge. Faults measured in outcrops are located within or correlated with faults at map-scale with the same kinematics. Their genetic interpretation follows the stereonet legend: 1 - faults parallel

with the main map-scale dextral strike-slip fault, 2 - clockwise rotated dextral strike-slip faults within the main fault zone, 3 - faults connecting main fault strands, generally corresponding to the orientation of P- shears, 4 - dextral strike-slip faults splaying from the main fault zone, generally corresponding to the orientation of R-Riedel shears, 5 - conjugated sinistral strike-slip fault, 6 - normal fault with an oblique-slip component, 7 - thrusts and reverse faults with an oblique-slip component, 8 - late-stage NE-SW to E-W oriented dextral faults offsetting the main fault zones, 9 - cleavage, 10 - unclear structures, 11 - bedding. CF - Cerna Fault; DBF - Dževrin-Balta Fault; DjO - Deli Jovan ophiolite; FT - Forebalkan Thrust; GT - Getic Thrust; KnB - Knjaževac Basin; KvA - Kusa Vrana anticline; PiB - Pirot Basin; RPF - Rtanj-Pirot Fault; SZF - Sokobanja-Zvonce Fault; TF - Timok Fault; TiB - Timok Basin; TiO - Tisovita-Iuti ophiolite; WT - West Balkan Thrust; ZaO - Zaglavak ophiolite.

Cerna or Timok faults are also observed (Fig. 4.4), which demonstrate the presence of associated structures with different kinematics and/or local strain partitioning by different styles of branching or splaying, local rotations and up to kilometre-scale negative or positive flower structures (e.g., S1 and S13 in Fig. 4.4).

The segment of the Cerna Fault running through the Iron Gates gorge of the Danube River and its flanks (Figs. 4.2, 4.4) offsets the Danubian basement to the NW from its Mesozoic sedimentary cover to the SE and has at least two major strands (S1, Fig. 4.4). The main strand is outcropping along the NW bank of the Danube, exposing a high-density dextral strike-slip zone (Fig. 4.5a) or decametre-scale fault surfaces visible over the gorge walls (Fig. 4.5b). Furthermore, this strand is associated with up to several meters thick, weakly foliated fault gouge often observed in granites (the Variscan Ogradena granite, Fig. 4.5c). In the same gorge area to the southeast, the SE Cerna Fault strand (S1, Fig. 4.4) shows a more distributed deformation without distinct high-strain fault gouge formation. Outcropping between these two strands, a narrow sliver of highly deformed uppermost Jurassic – Lower Cretaceous sediments of the Ceahlău–Severin unit is tectonically overlying the uppermost Danubian sedimentary cover (see zoom-in of Fig. 4.3a; see also Kräutner and Krstić, 2003). The overall map and cross-section geometry shows a dextral negative flower structure. Between the two main strands deformation is accommodated by connecting oblique normal faults or connecting P-shears (S1 in Fig. 4.4), while R-Riedel shears show splaying towards the NE (S1 in Fig. 4.4). Southwards, outcrop-scale faults follow the change in orientation of the Cerna Fault, which becomes more N-S oriented (S2, Fig. 4.4). Within the main fault zone, Cerna-parallel faults truncate earlier dextral faults rotated clockwise and are associated with few normal faults (S2, Fig. 4.4). Furthermore, the main N-S oriented Cerna Fault segment is offset by few hundred meters along a later NE-SW oriented dextral fault (S3, Fig. 4.4). Further south, the Cerna Fault changes its orientation to NW-SE and separates by dextral strike-slip the basement of the Getic unit to the west from the Danubian basement to the east. Along this segment, besides the Cerna-parallel, rotated faults or P-shears, all with a dextral sense of shear, a kinematically unclear type of likely sinistral normal faults have been observed outside and at farther distances from the main Cerna Fault zone (S4, Fig. 4.4).

Figure 4.5 - Interpreted field photos of structures (and their stereographic projections) associated with the Cerna and Timok fault zones. Locations of photos are displayed in Fig. 4.4. The legend of fault colours is the same as in Fig. 4.4. a) Cerna Fault deformation zone along the flanks of the Iron Gates gorge in the NW fault strand at studied point P1. The fault zone affected Lower Cretaceous limestones by the formation of a pervasive high-angle to vertical foliation in fault gouge that displays often brittle senses of shear, plotted as fault planes with a sense of shear in the stereonet. b) Decametre scale fault plane with large scale striations and corrugations affecting Upper Jurassic limestones in the Cerna Fault zone along the flanks of the Iron Gates gorge in the NW at studied point P1. For the scale, note the two standing men in the black rectangle. c) Metres-thick fault gouge and foliation and zoomed detail in the Variscan Ogradena granite in the Cerna Fault zone along the NW flanks of the Iron Gates gorge at studied point P5. The position of the zoom-in photograph is indicated by the black rectangle. d) High-density fault system in Tithonian limestones along the Timok Fault zone at the eastern margin of the Timok and Knjaževac basins at studied point P21. Deformation is characterized by

decametre-scale N-S oriented faults (green) parallel to the Timok Fault, associated P-shears (orange) and transtensional normal faults (blue). e) Oblique normal faults in Tithonian limestones within the Timok Fault deformation zone along the eastern margin of the Timok and Knjaževac basins at studied point P21. f) Fault gouge with sub-vertical foliation in the Devonian Zaglavak ophiolite (sheared and serpentinised gabbro) in the Timok Fault deformation zone at studied point P23. g) Oblique thrust in Tithonian limestones at studied point P29. h) Transfer of strike-slip deformation into thrusting in Jurassic limestones of the West Balkan unit at studied point P32. i) Overturned fold limb associated with low-angle pervasive axial plane cleavage in Lower Cretaceous marls in the footwall of the Getic Thrust at studied point P33. j) Sub-vertical and pervasive axial plane cleavage in Upper Jurassic limestones in hanging-wall of the Getic Thrust at studied point P33. k) Entrance to the Jerma gorge at studied point P36. Lower Cretaceous limestones building the flanks of the gorge are affected by strike-slip and thrust faulting in a large positive flower structure along the southern prolongation of the Timok Fault. l) WNW-ESE oriented dextral splay connecting two strands of the Timok Fault in the positive flower structure of the Jerma gorge at studied point P36.

Unlike the Cerna Fault, the Timok Fault is generally buried in its northern and central segments by the middle Miocene sediments of the Getic Depression and Timok and Knjaževac basins. This is where the 65 km offset along this fault has been constrained by the distance between the truncated Deli Jovan and Zaglavak ophiolites (Fig. 4.4, see also Kräutner and Krstić, 2002). In this area, the Timok Fault crops out in one outlier at the transition between the Timok and Knjaževac basins (S5, Fig. 4.4), where the N-S oriented Timok Fault separates the Forebalkan cover (Tithonian limestones) to the east from the Timok zone of the Getic unit (Turonian clastics) to the west. These Tithonian limestones are intensely deformed (Fig. 4.5d) by sub-vertical N-S oriented dextral strike-slip faults grouped in at least 3 closely spaced main strands that display decametre-scale fault surfaces. These strands are connected by splays and often truncate earlier, clockwise rotated, dextral faults, while the main fault zone is offset by late-stage E-W oriented dextral faults (S5, Fig. 4.4). The same area shows oblique, top to W or NW normal faults that are both truncated and truncate dextral faults (S5 in Fig. 4.4, see also Figs. 4.5d, e). The character of deformation remains similar south of the Knjaževac Basin until the Pirot Basin, but all structures are rotated to become parallel with the NNW-SSE Timok Fault main orientation. In this area, dextral strike-slip separates the Getic unit (Lower Cretaceous limestones) to the west from the West Balkan unit (the Zaglavak ophiolite, basement and Permian cover) to the east (Fig. 4.4). The deformation is distributed to discrete striated fault surfaces and rare foliated fault gouges (e.g., Fig. 4.5f). Most dextral faults and fault gauge foliations have the NNW-SSE Timok Fault orientation (S7-9, S13, Fig. 4.4), associated with obliquely oriented, clockwise rotated dextral faults, splays or conjugated sinistral faults (S7 and S13, Fig. 4.4). Further south, deformation associated with the Timok Fault is partitioned in two areas, associated with different sets of structures.

The first area is located immediately north of the Pirot Basin (Fig. 4.4), where structures document a gradual transfer from the top- N to NNW Srednogorie/Getic thrust

(S10-12) to multiple splays changing gradually their kinematics westwards to reverse faults with a dextral component, which are ultimately connected to the NNW-SSE oriented Timok Fault (S8-9). For instance, this transfer can be observed by NW-SE dextral transpressive faults (Fig. 4.5g) that gradually change their orientation and get connected with top-NNW thrust faults in Jurassic limestones of the West Balkan unit to the SW (Fig. 4.5h), or by a pervasive cleavage associated with the same thrusting. The dip of this cleavage (high- versus low-angle) reflects a different degree of drag-folding in the footwall (Fig. 4.5i) versus the hanging-wall (Fig. 4.5j), as a function of different lithologies (shales versus limestones, respectively), associated locally with oblique S- to SSE-ward backthrusting (structure S12 in Fig. 4.4). Overall, the system of faults observed in this area documents a transfer of the top- N to NNW thrusting observed at the Getic/West Balkan contact (i.e., the Getic Thrust, Figs. 4.2-4.4) to the NNW-SSE oriented dextral offset along the Timok Fault.

South of the Pirot Basin, Timok-type deformation is observed in the Jerma river gorge in Tithonian to Lower Cretaceous limestones (S13, Fig. 4.4). Here, two main NNW-SSE oriented strands of the Timok Fault (Fig. 4.5k) are connected and change their orientation to NW-SE and kinematics to dextral transpressive to define a positive flower structure. The flower structure is associated with thrusts (Fig. 4.5k), connecting splays (Fig. 4.5l), conjugated sinistral faults and truncated, clockwise rotated, earlier dextral faults (S13, Fig. 4.4). In this area, the Timok Fault offsets the Kusa Vrana anticline axis by ~8 km (Fig. 4.4). This implies that only a small part of the 65 km Timok Fault offset measured north of the Pirot Basin can still be recognized southwards.

4.4.2 Strike-slip deformation along the Rtanj-Pirot and Sokobanja-Zvonce faults

West and southwest of the Timok Fault, large, kilometres-sized offsets along dextral strike-slip faults are for the first time observed in our study along a larger array of ~NNW-SSE oriented structures. Among these structures, two have larger offsets and are herewith named the Rtanj-Pirot Fault and the Sokobanja-Zvonce Fault (RPF and SZF in Figs. 4.2, 4.6). Within these fault zones, deformation is transferred or partitioned along multiple strands and splays. Similar to the Cerna and Timok faults, the character and type of deformation along these faults changes along their strike, often as a function of lithology, from tens of metres thick foliated fault gouges, pervasive (sub-) vertical faulting with similar kinematics to individual fault surfaces with striations (Fig. 4.7).
The most frequent structures are NNW-SSE oriented dextral faults, parallel to the map-scale orientation of the RPF and SZF (Fig. 4.6). These faults often truncate Upper Cretaceous or Paleogene strata (Fig. 4.7a, b) or tilt them to (sub-)vertical position (Fig. 4.7c). These dextral faults often display flower structure geometry (Fig. 4.7b). Similar to the Cerna and Timok faults, these structures are associated with conjugated sinistral faults, earlier formed and clockwise-rotated dextral faults during the same dextral deformation, splays and dextral faults connecting different strands, as well as oblique thrusts and normal faults (Fig. 4.6). Earlier formed dextral faults are locally folded by

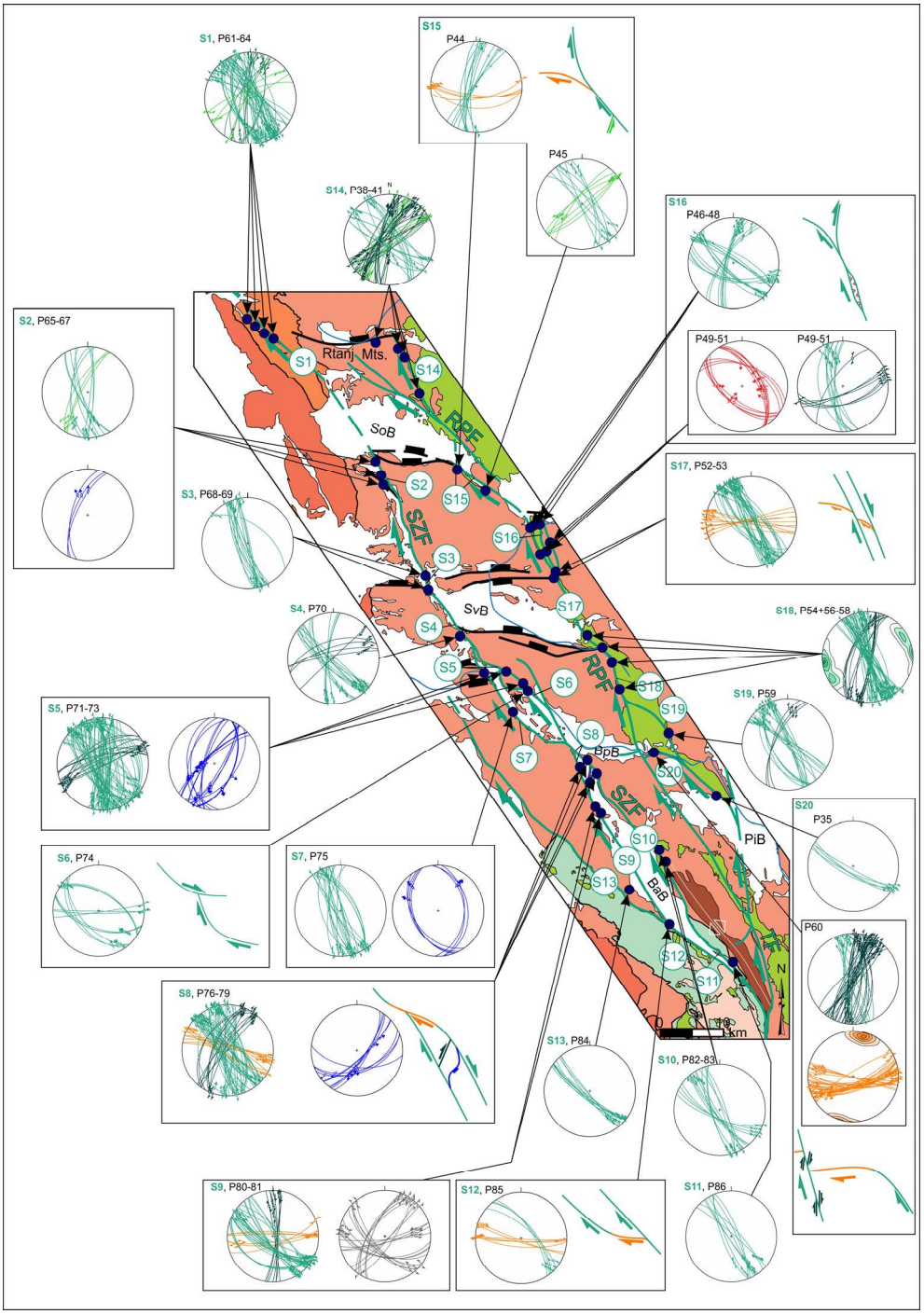

Figure 4.6 - Structural map and lower hemisphere stereographic projections of measured faults and foliations within fault gouge associated with the Sokobanja-Zvonce and Rtanj-

Pirot strike-slip faults. The location of the map is displayed in Fig. 4.2. Faults covered by Neogene sediments or faults with unclear prolongation are dashed. Numbered structures in stereonets correspond to map-scale structures with the same number. Each structure may combine multiple observation points. S - structure; P - observation point. Fault planes without a sense of shear are measured foliations within fault gouge. Faults measured in outcrops are located within or correlated with faults at map-scale with the same kinematics. Stereonet legend is the same as in Fig. 4.4. BaB - Babušnica Basin; BpB - Bela Palanka Basin; PiB - Pirot Basin; RPF - Rtanj-Pirot Fault; SoB - Sokobanja Basin; SvB - Svrljig Basin; SZF - Sokobanja-Zvonce Fault; TF - Timok Fault.

---

dragging during the formation of splays (e.g., S6, Figs. 4.6 and 4.7d). The Rtanj-Pirot Fault is generally transpressive (e.g., the positive flower structure of Fig. 4.7b), while the Sokobanja-Zvonce Fault is generally transtensive, documented by oblique dextral-normal faults (S2, S5, S7, S8, Figs. 4.6 and 4.7e). The SZF bounds and controls the deposition in NNW-SSE oriented corridors filled with middle Miocene sediments (S2-7, Fig. 4.6), while truncating the Eocene deposits in the similarly oriented Babušnica Basin (S8-12 in Figs. 4.6 and 4.7e). Rtanj-Pirot and Sokobanja-Zvonce faults are both connected with the Timok Fault to the SSE (Fig. 4.6).

Two strands of the Rtanj-Pirot Fault splay off of the Timok Fault in the SSE, while to the NNW they show secondary splays that are cross-cut by the western strand. The example of structure S20 (Fig. 4.6) shows that the eastern NNW-SSE oriented strand changes its orientation by splaying into an E-W oriented fault zone associated with ~15 metres thick foliated fault gouge (Fig. 4.7f). This E-W splay is truncated or terminated by the other NNW-SSE oriented strand located to the west. Similar truncated or terminated splays can be observed also to the NNW (e.g., S17 in Fig. 4.6). The Rtanj-Pirot Fault terminates to the NNE by splaying and the formation of a horse-tail structure in the area of the Rtanj Mountains (S14 - S16, Fig. 4.6).

The Sokobanja-Zvonce Fault shows a similar interaction by the formation of two main strands that are connected to the Timok Fault in the SSE. These strands show locally truncated splays (e.g., S12 in Fig. 4.6), which get connected or split again to the NNW (S8 in Fig. 4.6). Besides dragging effects (e.g., S6, Figs. 4.6, 4.7d), often oblique-slip dextral normal faulting can be observed in the field to be associated with regional faults (e.g., S2, S5, S7, S8, Figs. 4.6, 4.7e). To the NNW, the Sokobanja-Zvonce Fault can be interpreted to flank both or one of the margins of the Miocene strike-slip corridors, while our interpretation assumes a continuation in the same direction from beneath the middle Miocene cover of the Sokobanja Basin (S1 in Fig. 4.6)

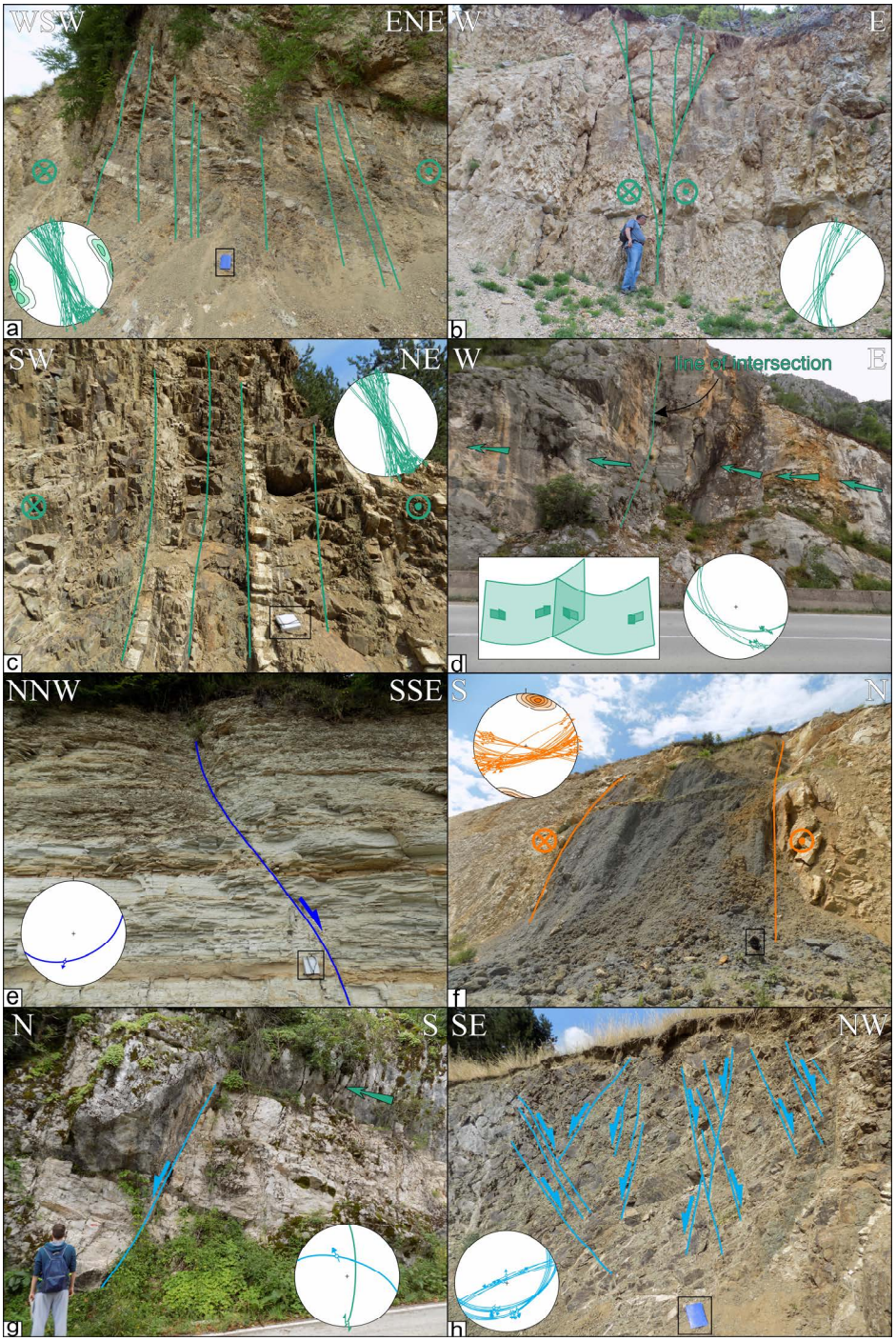

Figure 4.7 - Interpreted field photos of structures (and their stereographic projections) associated with the strike-slip and normal faulting. Locations of photos are displayed in

Figs. 4.6 and 4.8. The legend of colours in stereonets is the same as in Fig. 4.4. a) Sub-vertical pervasive dextral faulting affecting Paleogene clastics along the Rtanj-Pirot Fault at studied point P54. Note the blue notebook in the black rectangle for scale. b) Positive flower structure in Upper Cretaceous volcaniclastics along the Rtanj-Pirot Fault at studied point P44. The entire outcrop is affected by pervasive sub-vertical faulting. c) Tilted sub-vertical bedding in Upper Cretaceous volcaniclastics with bedding-parallel dextral shearing along the Rtanj-Pirot Fault at studied point P56. d) Decametre-scale curved dextral faults in Lower Cretaceous limestones in the Sokobanja-Zvonce Fault zone at studied point P74. The observed curvature of one fault is achieved by dragging along the adjacent sub-parallel fault with the same or similar kinematics. e) Normal fault with oblique-slip component truncating upper Eocene-Oligocene sediments of the Babušnica Basin along the Sokobanja-Zvonce Fault at studied point P79. f) Faulted Lower Cretaceous limestones illustrating deformation associated with the Rtanj-Pirot Fault at studied point P60. The outcrop exposes ~15 m thick dextral fault gouge, which is a splay within the Rtanj-Pirot Fault zone (see structure S20, Fig. 4.6). Note the black backpack (in the black rectangle) for scale. g) Dextral strike-slip fault intersecting with a top-N normal fault in Lower Cretaceous limestones along the Sokobanja-Zvonce Fault at studied point P66. h) Low-offset conjugated normal faults in Upper Cretaceous volcaniclastics along the Rtanj-Pirot Fault at studied point P56.

4.4.3 E-W oriented normal faults

Outside the main strike-slip fault zones, the Rtanj-Pirot and Sokobanja-Zvonce faults are connected by gradually rotating to E-W oriented top-N normal faults that are roughly perpendicular to the orogenic strike (Figs. 4.2, 4.6, 4.8). This is documented by a change in strike and kinematics of faults from dextral NNW-SSE oriented to normal E-W oriented. The normal faults control the sedimentation in the early middle Miocene Sokobanja and Svrljig basins, while the higher elevation of Paleozoic metasediments in their footwalls indicates exhumation and block-tilting (Figs. 4.8, 4.3g). At the outcrop scale, there is a large variability of the observed senses of shear, but in general, both N- and S-dipping conjugated sets of normal faults are observed (Fig. 4.8). Deformation along these normal faults is characterized by striated fault planes or fault gouges. Their offset increases westwards, closer to the Sokobanja-Zvonce Fault (e.g., Fig. 4.7g, S1 in Fig. 4.8), while towards their eastern connection with the Rtanj-Pirot Fault, the deformation is more distributed to a larger number lower offset, often conjugate normal faults (e.g., Fig. 4.7h, S7 in Fig. 4.8).

The normal faults often truncate E-W oriented splays of the Rtanj-Pirot and Sokobanja-Zvonce faults (e.g., S6 or S8 in Fig. 4.8), while they show a mutual cross-cutting relationship with NNW-SSE oriented dextral faults. For instance, normal faults truncate strike-slip faults (e.g., Fig. 4.7g, S2 in Fig. 4.6 and S1 in Fig. 4.8), but the opposite is also observed either by truncation or by a gradual clockwise rotation of normal faults when approaching a dextral strike-slip corridor (e.g., S2, Fig. 4.8). This mutual interplay between normal and dextral strike-slip faulting demonstrate that they formed during the same deformation event.

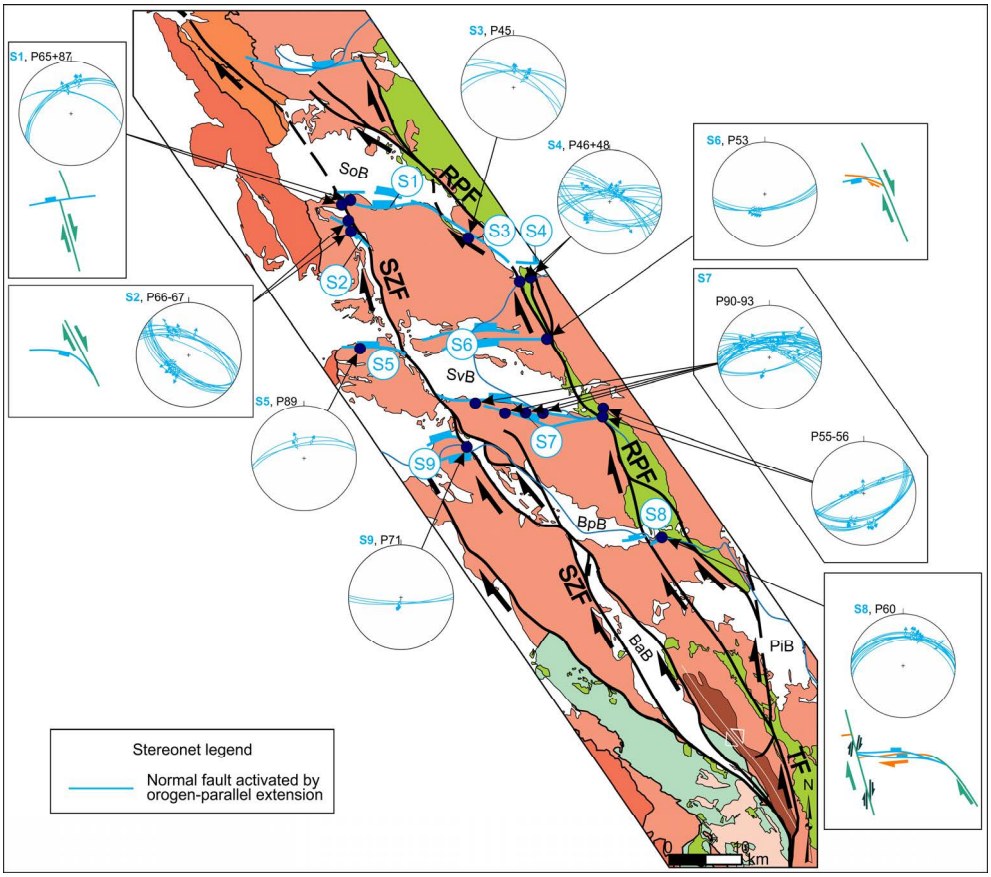

Figure 4.8 - Structural map and lower hemisphere stereographic projections of faults associated with orogen-parallel extension and Neogene basin formation. The location of the map is displayed in Fig. 4.2. Faults covered by Neogene sediments or faults with unclear prolongation are dashed. Numbered structures in stereonets correspond to map-scale structures with the same number. Each structure may combine multiple observation points. S - structure; P - observation point. Faults measured in the outcrops are located within or correlated with faults at map-scale with the same kinematics. BaB - Babušnica Basin; BpB - Bela Palanka Basin; PiB - Pirot Basin; RPF - Rtanj-Pirot Fault; SZF - Sokobanja-Zvonce Fault; SoB - Sokobanja Basin; SvB - Svrljig Basin; TF - Timok Fault.

4.5 Summary and integration of outcrop- and map-scale structures in the context of strain partitioning

The dominant strike-slip deformation observed on the outcrop scale is in agreement with the regional structure, which shows large offset dextral faults (Figs. 4.2 and 4.3). These faults include the previously known Cerna and Timok faults, but also the lower offset dextral, newly discovered Sokobanja-Zvonce and Rtanj-Pirot faults, as well as numerous other similarly oriented smaller faults (Figs. 4.4 and 4.6). All these structures cross-cut the Cretaceous nappe-stack of the Carpatho-Balkanides orocline, including the Danubian nappes, and part of the adjacent Balkanides (Figs. 4.2 and 4.3). Typically, these large strike-slip faults are composed of multiple fault strands (e.g., area of Iron Gates gorge, between the Timok and Knjaževac basins, NNW of the Pirot Basin or along the Babušnica Basin margins, Figs. 4.4, 4.6). Fault strands are often connected by splaying, branching or truncations.

In the north, transtensional deformation created large-scale negative flower structures along the Cerna and Timok faults (Figs. 4.3a, b), opening the middle Miocene Donji Milanovac and Orşova intramontane basins (along Cerna) and the early – middle Miocene Timok and Knjaževac basins (along the Timok Fault, Figs. 4.2, 4.4). In the latter, oblique normal faults likely root in the main Timok strike-slip strand in the subsurface (Figs. 4.2, 4.3c and 4.4). Subsidence in these basins reaches a maximum near the Timok Fault, where more than 1.5 km thick sediments are observed (Marović et al., 2007). Southwards, the NNW-SSE oriented segments of the Cerna and Timok faults (bounding the Deli Jovan and Zaglavak ophiolites, respectively, in Fig. 4.2) dip ENE-wards and have similar kinematics (Fig. 4.4, compare Cerna Fault in Fig. 4.3b with Timok Fault in Fig. 4.3d). This observation suggests that the Cerna Fault and the southern segment of the Timok Fault made up the same fault prior to the 65 km dextral offset of the Timok northern segment.

The decrease in dextral offset from 65 km in the area of the Zaglavak ophiolite to 8 km south of the Pirot Basin is partly accommodated by the transfer of Timok strike-slip deformation to thrusting in the Balkanides (Figs. 4.2 and 4.4). Outcrop-scale fault kinematics document this transfer immediately north of the Pirot Basin where dextral and reverse oblique faulting gradually changes to thrusting and internal folding of the frontal Getic nappe in the Balkanides, with cumulative shortening in the order of less than 10 km (Figs. 4.3e, f). The remaining dextral offset is too large to be accommodated by other dextral faults and the orogen-parallel extension (see below). Therefore, we follow previous interpretations (Schmid et al., 2020) and infer that a large part of the Timok dextral offset is transferred to thrusting and deformation inside the West Balkan unit, its frontal thrusting and internal deformation of the Forebalkan unit (Fig. 4.3c-f). Deformation along the main thrusts has often a dextral component, while their offset increases towards the Timok Fault, where the nappe-stack has a dextral drag-folding geometry, in agreement with outcrop observations (Figs. 4.2 and 4.4). A structural projection at the Permo-Triassic level indicates that the internal shortening and frontal thrusting of the West Balkan unit are in the order of up to 20 km, while probably less than 5 km in the Forebalkan unit (Fig. 4.3e, f). Part of this overall Getic and West Balkan

deformation must be late Early Cretaceous in age by the correlation with the Danubian nappes, which is constrained by post-tectonic Upper Cretaceous sediments covering thrust contacts in the vicinity of the basal (frontal) Getic thrusting (Ivanov, 1988; Vangelov et al., 2013; Schmid et al., 2020). However, such overprinting relations are unclear elsewhere in the West Balkan and Forebalkan units.

West of the Timok Fault, a part of the dextral offset is taken up by the dextral Rtanj-Pirot and Sokobanja-Zvonce faults (Fig. 4.3c-e), which splay off the Timok Fault in the south (Figs. 4.2 and 4.6). The Rtanj-Pirot Fault deforms Late Cretaceous and Paleocene sediments (Figs. 4.3c-e, 4.6, 4.7a-c) and has both transtensive and transpressive kinematics, observed by outcrop- and map-scale positive flower structures (Figs. 4.6, 4.7b). The transtensive kinematics is only locally observed at the connection with some of the basins (e.g., Knjaževac and Sokobanja, Figs. 4.3c and 4.6), while the transpressive kinematics is always associated with fault bends or with fault splaying and stranding into multiple structures (Fig. 4.3d, e). Although good map-scale regional offset markers are rare, we estimate the fault offset based on displaced slivers of Upper Cretaceous strata inside fault zones. These displacements accumulate ~10 km of dextral offset in the south (north of the Pirot Basin), which increases northwards to ~15 km in the area between Sokobanja and Svrljig basins (Figs. 4.2, 4.6).

Westwards, the Sokobanja-Zvonce Fault truncates upper Eocene – Oligocene sediments of the Babušnica Basin (Figs. 4.3e, 4.6 and 4.7e). Transtensive kinematics along the fault created along-strike accommodation space for the deposition of early middle Miocene sediments in a narrow corridor along its strike (Figs. 4.3c, d, and 4.5). Based on map-scale observations of dextral dragging in the Svrljig and Bela Palanka basins and associated E-W oriented normal faults, we infer that the Sokobanja-Zvonce Fault accumulates 15-20 km of dextral offset (Figs. 4.2, 4.6). To the NNW, offsets at both, the Rtanj-Pirot and the Sokobanja-Zvonce faults decrease where they terminate in horse-tail structures north of the E-W oriented Miocene basins (Fig. 4.2).

Regional E-W oriented normal faults correlate with the outcrop kinematics and can be observed only west of the Timok Fault (Fig. 4.8). These faults control the early middle Miocene subsidence and deposition in multiple intramontane basins, among which the largest are the Sokobanja and Svrljig basins (Figs. 4.3d, g, and 4.8). These faults often splay close to the surface into multiple sub-parallel faults that root likely into a larger partly listric-geometry normal fault at depth (Fig. 4.3g). While localized deformation along these normal faults leads to a total vertical offset of up to 2 km (Fig. 4.3g) in central and western segments, deformation is distributed over a higher number of low-offset faults farther to the east, resulting in the narrowing of basins in the same direction (Fig. 4.8). These E-W oriented normal faults connect with both the Rtanj-Pirot and Sokobanja-Zvonce faults in map view and outcrops by a gradual change in strike and kinematics from E-W normal to NNW-SSE dextral (Figs. 4.6, 4.8). Therefore, we have interpreted that the normal faults connect at depth with these dextral strike-slip faults (Fig. 4.3c, d). In more details, the normal faults splay from the Rtanj-Pirot Fault or otherwise reactivate its E-W oriented strike-slip splays (Figs. 4.6, 4.8) and show a mutual cross-cutting relationship with the Sokobanja-Zvonce Fault where they are also dragged in dextral strike-slip corridors (Figs. 4.6, 4.8). The regional E-W oriented normal faults have higher offsets westwards, and they are grouped in half-graben geometries (Sokobanja and

Svrljig basins, Fig. 4.3d, g, see also Marović et al., 2007). Similarly, this orogen-parallel extension controlled the opening of the Žagubica Basin north of the studied area (Fig. 4.2). However, normal faults controlling this basin do not demonstrate clear map-scale interaction with dextral strike-slip faults because to the north and northwest of our studied area strike-slip deformation is distributed and rarely localizes along large-offset structures (Krstekanić et al., 2020; see also Chapter 2).

4.6 Discussion

In summary, our detailed outcrop- and map- scale observations and correlations demonstrate that deformation is differently partitioned west and east of the Cerna-Timok Fault system by a gradual change in kinematics (Fig. 4.2). To the west, strain is partitioned between the Rtanj-Pirot and Sokobanja-Zvonce strike-slip faults and orogen-parallel extensional structures, where NNW-SSE to NW-SE oriented dextral faults are connected by E-W striking normal faults. Such a connection is counterintuitive for typical stress-inversion approaches when a regional homogenous stress field is applied to map-scale fault kinematics and evolution, and requires a more detailed strain partitioning explanation, detailed in the subsequent sections. To the east and southeast, the Cerna-Timok system transfers a large part of its offset to thrusting in the Balkanides. The timing of this deformation is constrained by cross-cutting relationships, deformation truncating Upper Cretaceous - Paleogene sediments, syn- to post- kinematic deposition observed in the early-middle Miocene sediments of the Timok and Knjaževac basins, middle Miocene of the Donji Milanovac, Orşova, Kučevo, Žagubica, Sokobanja, Svrljig basins and the narrow middle Miocene corridors along the Sokobanja-Zvonce Fault (Fig. 4.2). These timing constraints show that deformation was active during post-Eocene and pre-late middle Miocene times. Superposition criteria suggest that deformation started with a deformation transfer from strike-slip to thrusting east of the Cerna-Timok system while being coeval and followed by partitioning between strike-slip and orogen-parallel extension west of the same system.

4.6.1 The Circum-Moesian Fault System

The Circum-Moesian Fault System is related to the coeval formation of contrasting types of deformation that affected the orogens around the Moesian Platform. In our studied area of the Serbian Carpathians, this system experienced partitioning of the major dextral deformation into laterally continuous structures with different, orogen-parallel extension and thrusting kinematics. This type of strain partitioning can be correlated at a more regional area including the South Carpathians and Balkanides during the gradual Oligocene – middle Miocene formation of the backarc-convex orocline.

North of our studied area, the age of the prolongation of the Cerna Fault is constrained to late Oligocene by the formation of the Petroşani Basin in the South Carpathians (Fig. 4.1b, Berza and Drăgănescu, 1988; Moser et al., 2005) during the gradual oroclinal bending and dextral splaying demonstrated in the study by Ratschbacher et al. (1993). Our Timok Fault kinematic data and regional observations are also in agreement with

the northward early Miocene transtensional formation of the Getic Depression Basin in the South Carpathians foreland, repeatedly reactivated and truncated during the subsequent middle-late Miocene transpressional emplacement over the Moesian Platform (Figs. 4.1b, 4.2; Krézsek et al., 2013; Matenco et al., 2003; Rabăgia and Maţenco, 1999). The cessation of transtensional activity along the Timok Fault is demonstrated by middle Miocene sediments (i.e., ~13.4 Ma, middle Badenian in the Eastern Paratethys local stratigraphic division or late Badenian in the Central Paratethys domain) of the Getic Depression, which seal the fault (Matenco et al., 2016).

To the south, the curved geometry and the thrusting offset of the West Balkan unit decrease gradually to zero eastwards, away from the drag-folding effect of the Timok Fault (Fig. 4.1). At the Balkanides scale, the late Early Cretaceous and Eocene structuration can be demonstrated only for the Getic/Sredna Gora and Forebalkan thrusting, respectively, outside the area of the West Balkan unit (see also Schmid et al., 2020; Vangelov et al., 2013). Therefore, it is likely that the West Balkan unit was emplaced during the CMFS formation by partly transferring the Timok-Cerna dextral offset to thrusting (Fig. 4.9). There are no further geologic (or geochronologic) constraints available for more precise timing of emplacement of the West Balkans unit in the vicinity of the Timok Fault, but our superposition relationships indicate that the overall eastward transfer of dextral strike-slip to thrusting was initiated earlier than the westward transfer to normal faulting and intramontane basin formation. The remaining ~ 8 km Timok dextral offset left south of the Pirot Basin disappears southwards in a horse-tail structural geometry (Vangelov et al., 2016). Our data do not confirm the previously speculated south-eastwards connection between the Timok Fault and the Maritsa Fault of the northern Rhodope (details in Schmid et al., 2020), which is also not apparent in available geologic maps (see the 1:50.000 scale maps of the Bulgarian Geological Survey).

Figure 4.9 (next page) - Quantitative reconstruction with the Circum-Moesian Fault System (CMFS) overlying a detail of a Mediterranean quantitative paleogeographic and geodynamic reconstruction (modified after van Hinsbergen et al., 2020). This is the only reconstruction available where kinematic details of the Carpatho-Balkanides areas are implemented with sufficient details for a quantitative assessment. CF - Cerna Fault; DjO - Deli Jovan ophiolite; FT - Forebalkan Thrust; GD - Getic Depression Basin; GT - Getic Thrust; TF - Timok Fault; TiO - Tisovita-Iuti ophiolite; WT - West Balkan Thrust; ZaO - Zaglavak ophiolite. a) - d) Timesteps of the reconstruction at 30, 25, 20 and 15 Ma. The thickness of the grey arrow lines in a) indicates an increase in the amount of translation and clockwise rotation westwards.

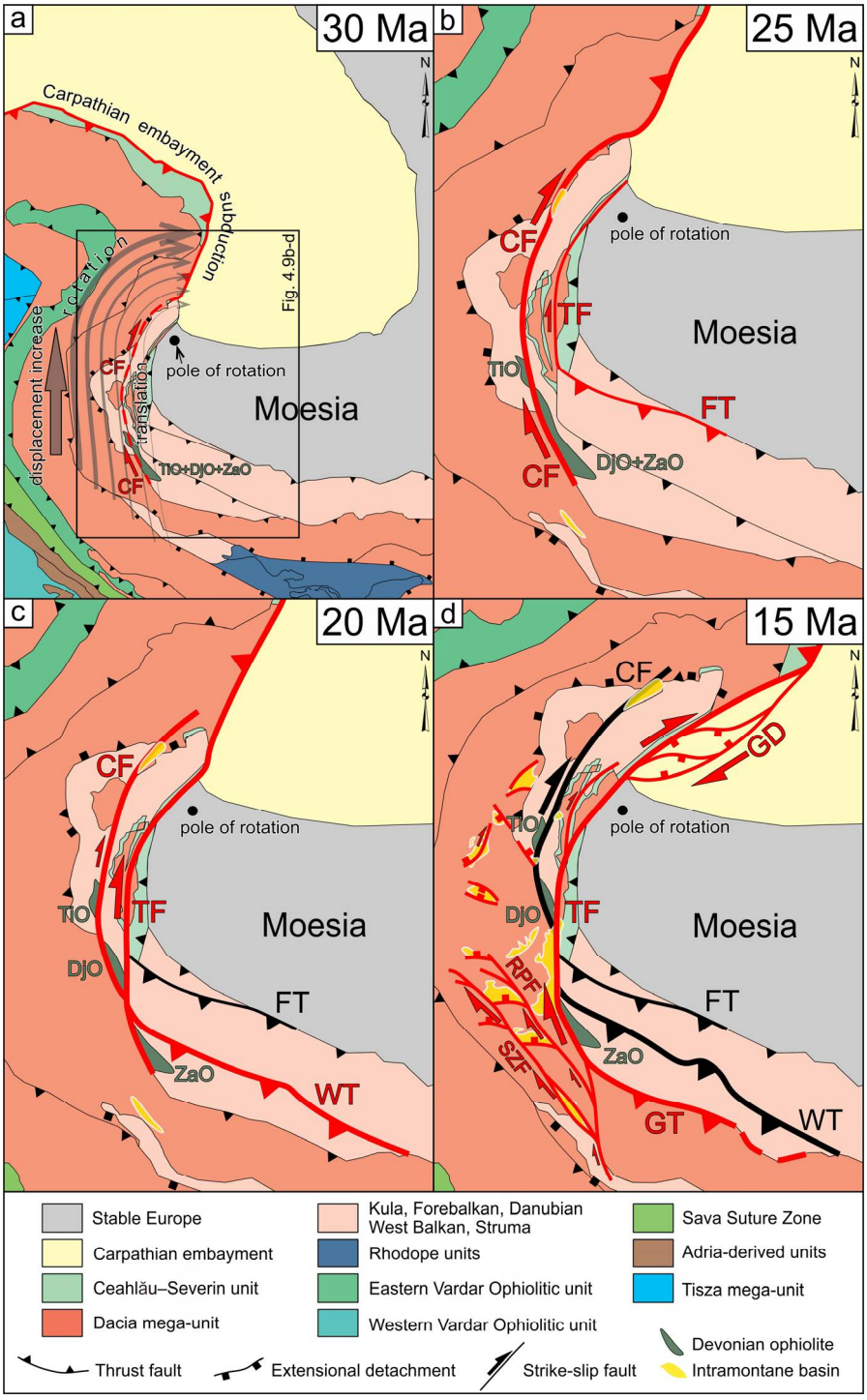
a
30 Ma
N
Carpathian embayment
subduction
rotation
displacement increase
translation
Fig. 4.9b-d
pole of rotation
Moesia
CF
TIO+DJO+ZaO
b
25 Ma
N
pole of rotation
CF
TF
TIO
Moesia
FT
DJO+ZaO
CF
c
20 Ma
N
CF
pole of rotation
TIO
TF
DJO
Moesia
FT
ZaO
WT
d
15 Ma
N
CF
GD
TIO
pole of rotation
DJO
TF
Moesia
RPF
FT
SZF
ZaO
GT
WT
Stable Europe
Carpathian embayment
Ceahlău–Severin unit
Dacia mega-unit
Kula, Forebalkan, Danubian
West Balkan, Struma
Rhodope units
Eastern Vardar Ophiolitic unit
Western Vardar Ophiolitic unit
Sava Suture Zone
Adria-derived units
Tisza mega-unit
Devonian ophiolite
Intramontane basin
Thrust fault
Extensional detachment
Strike-slip fault

4.6.2 Reconstruction and the influence of the geodynamic driver

Regional data infer that CMFS was active during a period of 15-17 Myr during the late Oligocene – middle Miocene (~30 - 13.4 Ma). By cumulating the offset of the Cerna, Timok, Rtanj-Pirot and Sokobanja-Zvonce faults, the total amount of dextral motions accommodating translations and rotations in the studied areas is in the order of 140 km. This allows for calculating an average deformation rate of ~8.23-9.33 mm/yr, which is similar to other large intracontinental strike-slip faults, such as the San Andreas Fault system (Mann et al., 2007). 140 km of dextral displacement correlates with the amount of shortening recorded by the external thin-skinned nappes of the SE Carpathians (e.g., Ellouz et al., 1994), which started in Oligocene times, as demonstrated by low-temperature thermochronology (Necea et al., 2021). This correlation suggests that the shortening associated with the Carpathians subduction has been directly transferred to the CMFS dextral strike-slip during the formation of the backarc-convex orocline. Note that the amount of shortening gradually increases in the Carpathians north of their SE corner to 180 and 220 km or more (see van Hinsbergen et al., 2020 and references therein), but such an increase is an effect of the clockwise rotation around a pole located in the western Moesian platform (Fig. 4.9a; the pole of rotation location is estimated after van Hinsbergen et al., 2020 and structural patterns of this study). The same rotational effect implies that deformation increases westwards in our studied area.

The CMFS postdates the Paleocene - Eocene orogen parallel extension recorded by the exhumation of the Danubian units and the coeval thrusting in the Balkanides (Fügenschuh and Schmid, 2005; Matenco and Schmid, 1999; Schmid et al., 1998, 2020; Vangelov et al., 2013). This extensional exhumation is an effect of the same general rotation and translation of the Dacia mega-unit, which was significantly rotated around the Moesian Platform already by the end of Eocene, as shown by large-scale tectonic reconstructions (e.g., Fügenschuh and Schmid, 2005; van Hinsbergen et al., 2020). This observation demonstrates that dextral strike-slip faulting, related to the Moesian indentation, started after the Eocene orogen-parallel extension and Balkanides thrusting, as previously inferred (Ratschbacher et al., 1993). However, the present dataset cannot preclude an earlier Eocene strike-slip precursor of the Cerna or Timok faults. The described variability in offsets along various segments of strike-slip faults and their transfer to thrusting and normal faulting demonstrate that the late Oligocene 35 km Cerna dextral offset (separating the Tisovita-Iuti from the combined Deli Jovan and Zaglavak ophiolite segments, Fig. 4.9b) was continued by a larger 65 km Timok offset by shortcutting deformation in an eastward splay (offsetting the Deli Jovan and Zaglavak ophiolite segments, Fig. 4.9c). In other words, the continuation to the south of the Cerna Fault is represented by the southern part of the Timok Fault, which transfers deformation to the West Balkan thrust system. Possibly, the Timok Fault was also activated during the late Oligocene, but such activation requires deformation transfer to relatively low thrusting offsets in the Balkanides (such as along the Forebalkan Thrust, as suggested in Fig. 4.9b). The subsequent Miocene Timok dextral offset was transferred mostly to the frontal Getic/Sredna Gora and West Balkan thrust systems and associated internal deformation in the latter (Fig. 4.9c). It is also clear that dextral dragging of these units (Fig. 4.1) was created by gradually eastwards decreasing the amount of post-Eocene thrusting.

The ~20 Ma onset of Carpathian slab retreat, recorded by the formation of the Pannonian backarc basin (e.g., Horvath et al., 2015), changed the situation by dramatically increasing the total amount and rates of CMFS dextral deformation during the formation of the backarc-convex orocline, from 35 km pre-roll-back Cerna Fault displacement (rate of ~3.5 mm/yr) to syn-roll-back 100 km offset of the combined Timok, Rtanj-Pirot and Sokobanja-Zvonce (rate of up to ~2 cm/yr). This process is also responsible for the rapid transtensional formation of the Getic Depression Basin in the frontal part of the South Carpathians in the prolongation of the Timok Fault (Krézsek et al., 2013; Rabăgia and Maţenco, 1999). As deformation progresses and increases northwards, older segments of the Cerna and Timok faults were bent by the rotation, while truncated by progressively younger NE-SW to E-W oriented dextral faults (such as structure S3, Fig. 4.4). This gradual rotation continued in the South Carpathians and its frontal Getic Depression, where is truncated by subsequent NW-SE to NNW-SSE oriented late Miocene strike-slip, which is the ultimate expression of dextral faulting accommodating the movement around the Moesian margin during rotation (Hippolyte et al., 1999; Maţenco et al., 1997; Rabăgia et al., 2013; Ratschbacher et al., 1993).

Correlating the observed structures with the coeval deformation observed to the south and southeast in the Rhodope Mountains is more difficult with data presented in our study, particularly because our mapped prolongation of the Timok Fault south of the Pirot Basin has a minor total offset and appears to terminate southwards in a horse-tail structure. Such a continuation is not required for the post-Cretaceous evolution because of the large-scale strain partitioning between the western Hellenides shortening and the post 42 Ma extension (Rhodope, southern Balkanides and Aegean) associated with the Aegean slab retreat, which has a pole of rotation somewhere near the termination of the Timok Fault (Fig. 4.1a, Brun and Sokoutis, 2007; Schmid et al., 2020, van Hinsbergen et al., 2020). A SE continuation of the Timok Fault is also prevented by the transfer of deformation to thrusting during indentation, as shown by recent analogue modelling applied to the study area (Krstekanić et al., 2021, see also Chapter 3).

4.6.3 Mechanism of strain partitioning and similar observations elsewhere

The post-20 Ma pull exerted by the retreating Carpathian slab and increasing the amount of deformation at farther distances from the pole of rotation was accommodated by orogen-parallel extension and formation of intramontane basins in the Serbian Carpathians (Fig. 4.9d). In our view, this is a clear expression of strain partitioning, because NW-SE dextral faults cannot form together with E-W oriented normal faults in isotropic materials and homogenous stress field (Fig. 4.10). Instead, the northward pull on the upper plate exerted by the Carpathian slab combined with the clockwise rotation and drag in respect to the Moesian Platform are creating higher displacements to the north and west (Fig. 4.10). This change in displacements is accommodated by splaying from the Timok Fault to E-W oriented normal faults accommodating the N-S oriented orogen-parallel extension. In more details, dextral faults terminating in horse-tails are activated successively at a farther distance from the Timok Fault, i.e. first the Rtanj-Pirot

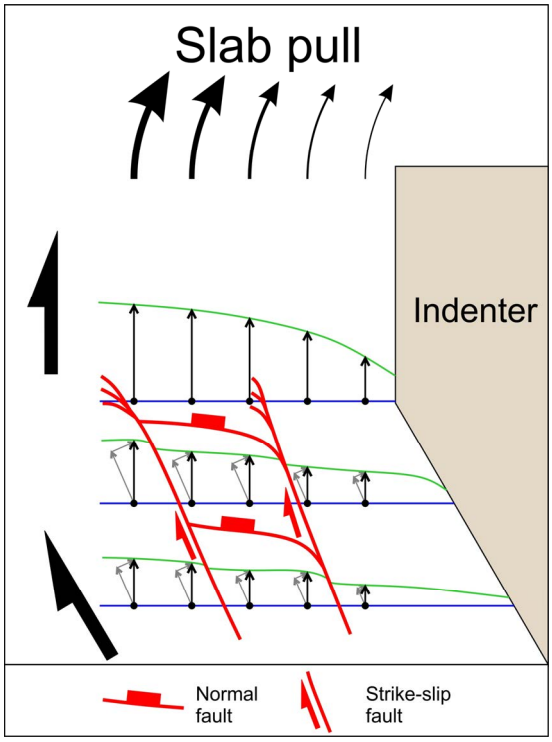

Figure 4.10 - Map-view sketch of strain partitioning in coupled NNW-SSE strike-slip and N-S (orogen-parallel) extension. Blue and green lines are marker lines, showing the situation before (blue) and after (green) the deformation. Black arrows show displacement variability due to the slab pull. Arrows' size indicates a relative difference in displacement magnitude. Note the increase in displacements westwards and northwards, created by slab pull. Grey arrows are indenter margin-parallel and perpendicular components of displacement. Half arrows indicate overall dextral drag against the indenter. Because displacements increase from south to north, there is an extension in the N-S direction creating E-W oriented normal faults. Strike-slip faults accommodate the abrupt change of indenter margin-parallel component of displacement. When there is a more gradual change in displacements (like along the N-S oriented indenter margin, northernmost marker line), there is no strike-slip faulting.

Fault, followed by the Sokobanja-Zvonce Fault. The latter truncates the earlier curved fault that shows a transfer of kinematics from NW-SE dextral to E-W normal faulting (Figs. 4.9d, 4.10).

The Carpatho-Balkanides backarc-convex orocline was ultimately controlled by the geometry of the Moesian indenter and the Carpathians subduction. Similar situations are observed elsewhere. For instance, the much larger indentation of India shows shortening in the Himalayas (Figs. 4.11a, b; e.g., Molnar and Tapponnier, 1975; Tapponier et al., 1986) being transferred to a strike-slip deformation that changes strike and ultimately becomes parallel with the margins of the indenter such as in the SE Asia (Morley, 2002, 2013; Morley and Arboit, 2019; Sloan et al., 2017; Vigny et al., 2003), during the coeval backarc-convex oroclinal bending around the Eastern Himalayan Syntaxis (e.g., van

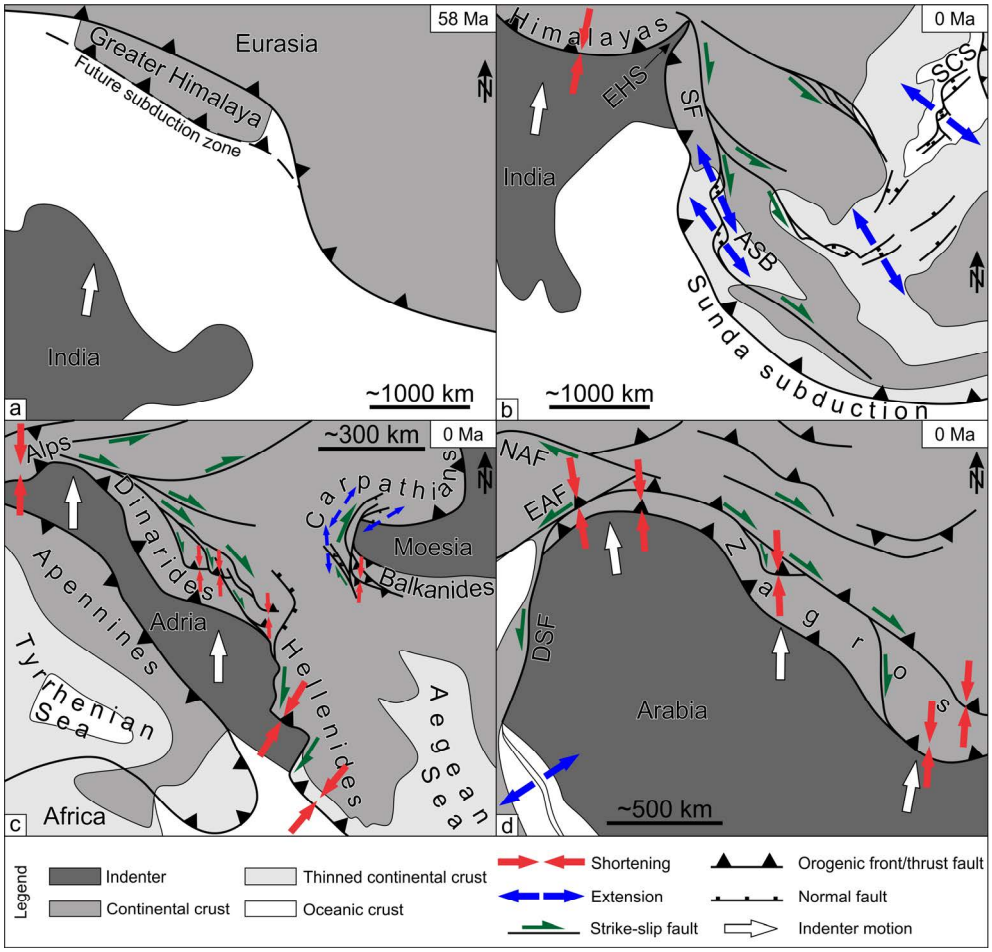

Figure 4.11 - Sketches of comparative cases of deformation transfer around indenters. a) India – Eurasia tectonic reconstruction in Paleocene (simplified after van Hinsbergen et al., 2019). b) Present-day structure of the India – Eurasia system showing the transfer of deformation around the Indian indenter during indentation and lateral slab roll-back (simplified after Tapponnier et al., 1986; Cullen, 2010; van Hinsbergen et al., 2019). ASB – Andaman Sea Basin; EHS – East Himalayan Syntax; SF – Sagaing Fault. c) Adriatic indentation and transfer of deformation along the Dinarides orogen (simplified after Ratschbacher et al., 1991a; van Unen et al., 2019a; van Hinsbergen et al., 2020). d) Arabian indentation and different styles of deformation transfer along its lateral margins (simplified after Authemayou et al., 2006). DSF – Dead Sea Fault; EAF – East Anatolian Fault; NAF – North Anatolian Fault.

Hinsbergen et al., 2019). Although the fault pattern is fairly more complex and is controlled by the inherited structures (Morley, 2007), the facilitators were the northward push by the lower plate Indian indenter and the retreating Sunda subduction pulling the upper plate, Sundaland, with higher velocities closer to the subduction zone (Sternai et al., 2016). The deformation during this gradual oroclinal bending of the initially less curved Eurasian margin (Fig. 4.11a) around the Indian indenter was partitioned along the large-scale dextral Sagaing Fault at the Indian eastern margin (Fig. 4.11b). The Sagaing Fault connects the thrusting in the Himalayas and the opening of the pull-apart Andaman Sea Basin above the Sunda subduction zone (Fig. 4.11b; Morley, 2002, 2013; Sloan et al., 2017), while it separates two regions of deformation transfer. West of the Sagaing Fault (i.e., towards the indenter) the strike-slip is transferred to transpression and thrusting (e.g., Maurin et al., 2010; Nielsen et al., 2004), while the strain is partitioned eastwards between strike-slip and normal faults (Morley, 2007). Therefore, although significantly larger, the mechanism of transfer from shortening in the Himalayas to complex strike-slip deformation along the Sagaing Fault during oroclinal bending around the Eastern Himalayan Syntaxis is comparable to the mechanism of the Balkanides shortening transfer to Cerna and Timok strike-slip deformation during oroclinal bending around the Moesia.

The relative plate motion in cases of the Moesian and Indian indentation and their associated Vrancea and SE Asia slab retreats are perpendicular to the frontal and parallel to the lateral indenter margins, which results in the large-scale transfer of shortening to strike-slip deformation, while differences in the resulting fault pattern are controlled by the geometry of the two indenters. In the case of India (Fig. 4.11a, b), the shortening is transferred more abruptly to strike-slip because of the relatively sharp corner in the Eastern Himalayan Syntaxis, while the deformation is transferred more gradually around the Moesian curved southwestern corner (Figs. 4.1b, 4.2, 4.9). In situations when the indenter geometry and relative plate motion are distributed in such a way that the lateral margin of the indenter is oblique to the plate motion, the deformation is transferred from frontal shortening to large-scale transpressive deformation along the oblique lateral indenter margin. Such cases are observed in the Alps transfer of deformation to the Dinarides - Hellenides(Fig. 4.11c) and in the Zagros (Fig, 4.11d) orogens along the Adriatic and Arabian oblique eastern margins. In these cases, deformation is partitioned between strike-slip faulting and thrusting in orogen-scale restraining bends or stepovers (e.g., Authemayou et al., 2006; van Unen et al., 2019a). The deformation along the western Arabian margin (Fig. 4.11d) is accommodated by transpressive East Anatolian Fault (margin oblique to plate motion) and strike-slip to transtensive Dead Sea Fault (margin parallel to plate motion; see Lyberis et al., 1992; Perinçek and Çemen, 1990; Smit et al., 2010).

4.7 Conclusions

To understand the transfer of deformation during backarc-convex oroclinal bending of the European Carpatho-Balkanides orogen around the Moesian indenter, we have performed a field structural and kinematic study of one of the largest, but poorly documented strike-slip systems known in continental Europe. The results demonstrate that the mechanics of deformation was accommodated by a likely unique situation of complex coeval strike-slip, thrust and normal faults (i.e. by the Circum-Moesian Fault System) that spans a regional area from the South Carpathians to the Balkanides mountains. In the studied region of the Serbian Carpathians, deformation is partitioned to multiple, kinematically different, high-offset faults, that accumulate an offset in the order of 140 km by dextral displacements along the previously known large curved Cerna - Timok system and the newly found Sokobanja-Zvonce and Rtanj-Pirot faults. These strike-slip faults transfer a significant part of their offset eastwards to thrusting in the Balkanides south of the Moesian indenter and to an orogen-parallel extension during the formation of intramontane basins westwards. Strike-slip faults often display multi-strand geometries that mutually connect by splaying, branching and truncations, while large faults demonstrate a change in kinematics from dominant transtension in the north to transpression in the south. To the west, the NNW-SSE oriented Sokobanja-Zvonce and Rtanj-Pirot faults accommodate deformation around the SW Moesian corner, by gradually changing their local strike and connecting or truncating the E-W oriented normal faults that control the formation of intramontane basins, which provide critical timing indicators. These observations demonstrate that the CMFS was active during the late Oligocene – middle Miocene, where dextral deformation progressed at average rates in the order of 9 mm/yr.

The correlation with paleogeographic and geodynamic reconstructions demonstrates that the overall formation of the CMFS system during the indentation of the Moesian Platform was driven by a gradual orogenic translation and rotation during the subduction of the Carpathian embayment. The rotation around the NW corner of the Moesia decreased southwards and was gradually replaced by translation along the Moesian western margin. The ~20 Ma onset of slab retreat and backarc extension has dramatically increased the rates of CMFS dextral deformation from ~3.5 mm/yr to ~2 cm/yr. The pull exerted by the retreating slab has facilitated the transfer of dextral deformation to orogen-parallel extension. The overall strain partitioning mechanics is similar to observations elsewhere, such as in the much larger India – Asia collision zone, but has specific mechanisms of strain partitioning linked to the geometry of the Moesian indenter. This specificity relates to shortcutting the dextral deformation along the margins towards the indenter and the interplay between the gradual activation of strike-slip and orogen-parallel extension.

The results of our study demonstrate that in most cases of indentation, a strain partitioning approach is required to understand the observed patterns of deformation, although is not a standardised methodology and requires adaptation to the specificity of kinematic observations and the mechanism of indentation.

4.8 Appendix

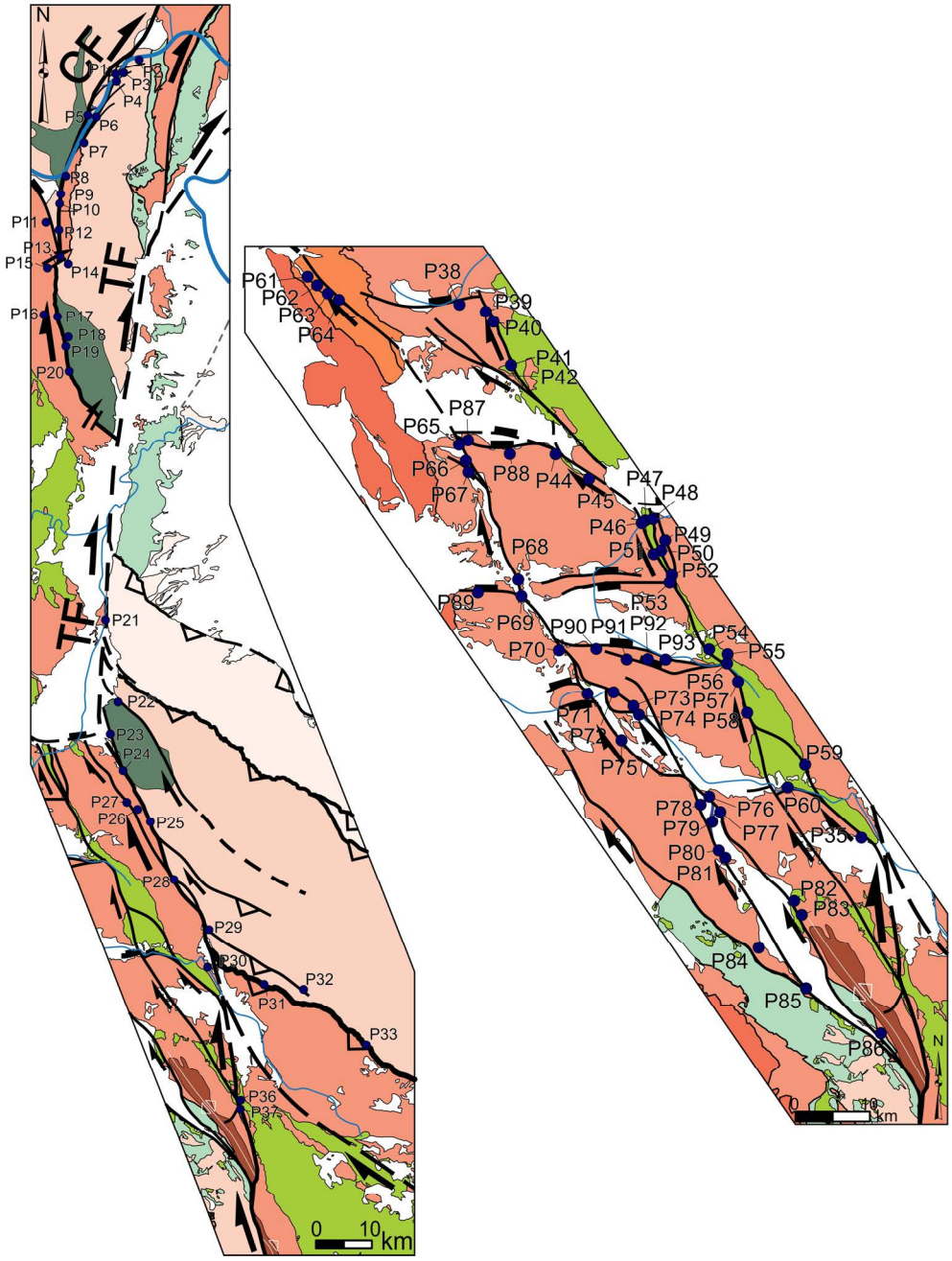

Figure 4.A1 - Field observation points. Locations of the left and right-hand side map are indicated by red and blue polygons (respectively) in Fig. 4.2. Legend is the same as in Fig. 4.2.

Chapter 5. The influence of back-arc extension direction on the strain partitioning associated with continental indentation: analogue modelling and implications for the Circum-Moesian Fault System of South-Eastern Europe[4]

[4]This chapter is based on Krstekanić, N., Willingshofer, E., Matenco, L., Toljić, M., Stojadinovic, U., 2021. The influence of back-arc extension direction on the strain partitioning associated with continental indentation: analogue modelling and implications for the Circum-Moesian Fault System of South-Eastern Europe, submitted to Journal of Structural Geology.

5.1 Introduction

Indentation is associated with a complex three-dimensional deformation transfer different fault kinematics and strain partitioning during frontal shortening and lateral strike-slip deformation. Deformation is often associated with extrusion of continental fragments, observed in situations like India-Eurasia collision and SE Asia extrusion (Fig. 5.1a; e.g., Molnar and Tapponier, 1975; Morley, 2002, 2013; Searle et al., 2011; Shen et al., 2001; Tapponier et al., 1986), Arabia-Anatolia system (Fig. 5.1b; e.g., Kaymakci et al., 2010; Lyberis et al., 1992; Mantovani et al., 2006; Martinod et al., 2000; Perinçek and Çemen, 1990; Smit et al., 2010) or Adria-Europe convergence (Fig. 5.1c; e.g., Frisch et al., 1998; Neubauer et al., 2000; Ratschbacher et al., 1991b; Rosenberg et al., 2004; van Gelder et al, 2020; van Unen et al., 2019a; Wölfler et al., 2011). In all these situations, indentation-induced deformation is affected by extension driven by the slab roll-back of another subduction zone (Fig. 5.1, see also Regard et al., 2005; Schellart et al., 2019; Sternai et al., 2016). This extension has a variable orientation (from parallel to perpendicular) with respect to the frontal shortening or the lateral strike-slip deformation taking place during indentation. The resulting multi-scale distribution of the bulk strain by connecting different kinematic types of deformation that cannot be explained by a uniform stress field is generally referred to as strain partitioning (e.g., Benesh et al., 2014; Cembrano et al., 2005; D'el-Rey Silva et al., 2011; De Vicente et al., 2009; Glen, 2004; Krézsek et al., 2013). Although it is known that slab-roll back can affect the large-scale deformation associated with indentation (e.g., Faccenna et al., 1996; Schellart et al., 2019), the mechanism of strain partitioning and deformation transfer between slab roll-back induced extension and indentation is not well understood. Previous research into indentation systems has demonstrated that the indenter geometry dominantly controls the strain partitioning and deformation transfer (Krstekanić et al., 2021; see also Chapter 3), which should be accounted for when studying the impact of the extension driven by slab-roll-back.

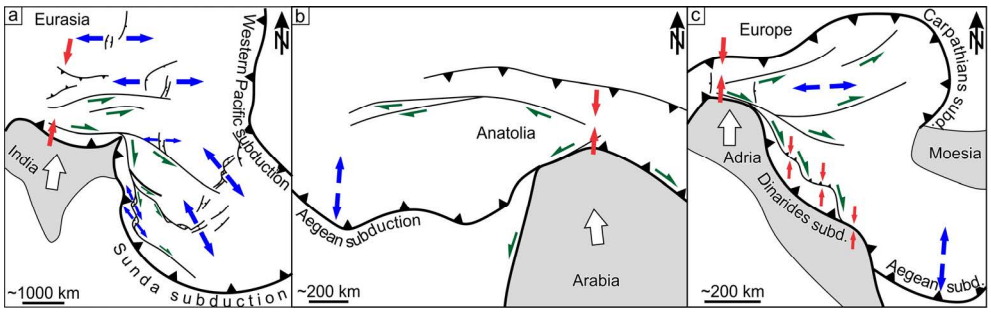

Figure 5.1 - Sketches of natural indentation systems. a) India – Eurasia collision. b) Arabia indentation and lateral extrusion of Anatolia. c) Adria – Europe collision. Indenters are grey areas. White arrow shows direction of indenter motion. Triangles along contractional zones are drawn in the upper plate/hanging wall of a subduction/thrust. Green half arrows indicate kinematics along strike-slip faults. Red arrows indicate shortening regions, while blue arrows indicate extension.

We aim to understand the interplay of extension driven by slab-roll back and indentation-driven deformation, together with a quantification of the associated strain partitioning and fault kinematics. To this aim we performed crustal-scale analogue modelling experiments designed to test the influence of the extension direction during indentation in terms of kinematics, distribution of deformation and the coeval formation and evolution of sedimentary basins. Image correlation methods were used to qualitatively and quantitatively analyse deformation patterns around the indenter. The analogue experiments were scaled and applied to the indentation of the Moesian Platform during the formation of the arcuate back-arc convex Carpatho-Balkanides orocline that was coeval with the back-arc extension driven by the Carpathians and Dinarides slabs (Fig. 5.2).

5.2 The Circum-Moesian Fault System of the Carpatho-Balkanides

The Carpatho-Balkanides orogenic system of south-eastern Europe (Fig. 5.2a) is a Cretaceous thick-skinned nappe stack whose formation was associated with the closure of the Alpine Tethys Ocean leading to the collision between the Dacia mega-unit and the Moesian Platform, a promontory of the stable pre-Alpine European continent (Fig. 5.2a, b; Săndulescu, 1988; Csontos and Vörös, 2004; Schmid et al., 2008, 2020). Subsequent Cenozoic subduction, slab retreat and closure of the Carpathians embayment created the oroclinal bending and the present-day double 180° curved geometry of the entire orogenic system (Fig. 5.2a; e.g., Csontos and Vörös, 2004; Fügenschuh and Schmid, 2005; Ustaszewski et al., 2008).

The southern of the two oroclines consists of the South Carpathians, the Serbian Carpathians and the Balkanides, has a backarc-convex geometry (Krstekanić et al., 2020; Chapter 2) and formed by oroclinal bending and dextral transcurrent motions of the Dacia mega-unit around the Moesian Platform (Fig. 5.2b; van Hinsbergen et al., 2020). This oroclinal bending was first accommodated by Paleocene – Eocene orogen-parallel extension in the South Carpathians (Matenco and Schmid, 1999; Fügenschuh and Schmid, 2005; Schmid et al., 1998), subsequently followed by Oligocene-middle Miocene deformation along the Circum-Moesian Fault System (thick black lines in Fig. 5.2b), one of the largest European intracontinental strike-slip fault systems, accumulating up to 140 km of dextral offset, associated with coeval thrusting and normal faulting (Krstekanić et al., 2022; see also Chapter 4). These faults have different orientations, connect and transfer the deformation along the entire orocline, from the South Carpathians in the north to the Balkanides in the south. The largest faults in the system are the Cerna and Timok curved strike- slip faults that have 35 km and 65 km of dextral offset, respectively, and connect with thrusting-dominated deformation in the frontal part of the South Carpathians and Balkanides Mountains (Fig. 5.2b; see also Berza and Drăganescu, 1988; Ratschbacher et al., 1993; Kräutner and Krstić, 2002).

The evolution of the Circum-Moesian Fault System was (partly) coeval with widespread extensional processes related to the roll back of the Carpathian and Dinaric slabs (Bennett et al., 2008; Matenco and Radivojević, 2012; Horváth et al., 2015, Andrić

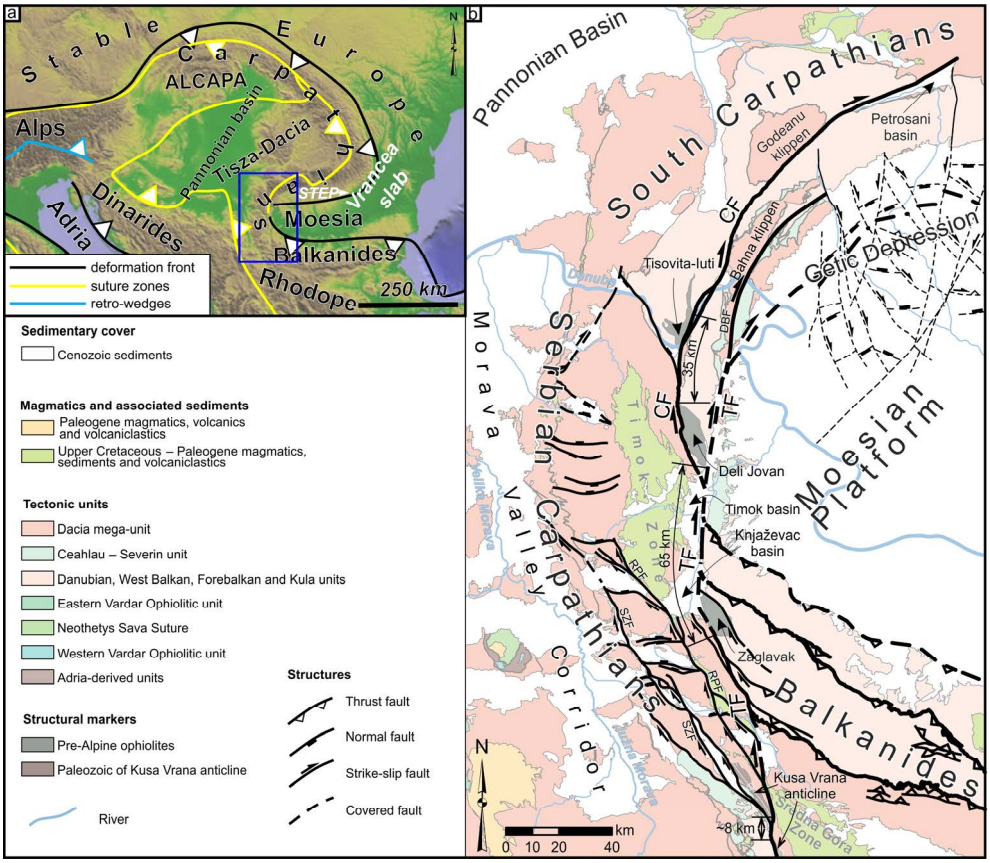

Figure 5.2 - a) First-order structures (orogenic fronts, suture zones and retro-shears) of the Mediterranean Alpine-age orogens in the South-Eastern Europe (modified from Krstekanić et al., 2020). Blue rectangle indicates the location of Fig. 2b. STEP – Subduction-Transform Edge Propagator system in the South Carpathians. White arrow indicates the direction of slab tearing. b) Tectonic map of the South Carpathians-Serbian Carpathians-Balkanides backarc-convex orocline around the Moesian Platform. Black lines are faults comprising the Circum-Moesian Fault System that accommodates oroclinal bending related deformation. CF – Cerna Fault; TF - Timok Fault. The map is compiled and modified after geological maps of Serbia, Romania and Bulgaria and Maţenco (2017). Fault pattern is modified after Maţenco (2017) and Krstekanić et al., 2022.

et al., 2018) where the latter probably controlled E-W extension in the Morava Valley Corridor, the southern prolongation of the Pannonian Basin, and affected the western margin of the Serbian Carpathians segment of the orocline, from Oligocene to middle Miocene times (Figs. 5.1c and 5.2a; Matenco and Radivojević, 2012; Erak et al., 2017; Sant et al., 2018; Krstekanić et al., 2020). Additionally, the oroclinal bending was complicated by one other extensional/transtensional deformation that affected the

Serbian and South Carpathians during their movement around the Moesian indenter and the formation of the Circum-Moesian Fault System, driven by the Carpathians slab roll-back kinematics (Figs. 5.1c and 5.2). In the prolongation of the Timok Fault (Fig. 5.2b), a late Oligocene – early Miocene period of transtension and extension led to the opening of the Getic Depression in the South Carpathians foreland, which was subsequently inverted and buried during of the middle to late Miocene docking of the South Carpathians against the Moesian indenter (e.g., Matenco et al., 2003; Răbăgia et al., 2011; Krézsek et al., 2013). This extension also created a number of presently E-W oriented intra-montane basins in the Serbian Carpathians (Krstekanić et al., 2020, 2022; see Chapters 2 and 4). These complex movements around the Moesian indenter are inferred to be driven by rotational kinematics of the retreating Carpathians slab and the formation of a STEP (subduction-transform edge propagator) system at high depths beneath the South Carpathians (Fig. 5.2a; Govers and Wortel, 2005; Maţenco, 2017).

5.3 Methodology

Starting from a published analogue modelling setup with a fixed indenter, around which a deformable material is translating and rotating (Krstekanić et al., 2021; see Chapter 3), we have performed crustal scale analogue experiments to simulate deformation in the upper to middle crust around a rigid indenter under the influence of variable extension direction. We note that the unusual high complexity of strain partitioning requires a correlation with this previously published study. Our experiments are designed (Fig. 5.3) to simulate the impact of variability in kinematic boundary conditions and provide the possibility of a direct analysis of deformation styles. Below we describe the modelling setup and results in a relative geographic framework where north is oriented upwards in top-view figures (e.g., Fig. 5.3), in analogy to the geographic framework of the Circum-Moesian Fault System (Fig. 5.2).

5.3.1 Modelling setup

5.3.1.1 Model geometry and kinematics

The indenter is made of a 2 cm thick rigid polyvinyl chloride plate with rounded corners (Fig. 5.3a) and 35° margin inclination (Fig. 5.3c), approximating the geometry of the base of the Cretaceous nappe-stack thrusted over the Moesian Platform (Fig. 5.2b; Maţenco, 2017 and references therein). The indenter upper width of 26 cm (Fig. 5.3a) correlates with the N-S dimension of the Moesian Platform (Fig. 5.2).

Similar to Krstekanić et al. (2021), the base of the deformable part of models is made of a mobile basal plastic plate and a fixed plastic sheet (Fig. 5.3). The 1 mm thick plastic plate (green in Fig. 5.3) underlies the entire model, including the rigid block. Though a bar and mechanical joints it is connected to a motor (Fig. 5.3a) that pulls it northward at a constant velocity of 2 cm/h. The other, fixed 0.1 mm thick plastic sheet (grey in Fig. 5.3) is placed on top of the moving plate north of the indenter, while it is below the moving plate to the north-west. This change is implemented at the N-S oriented cut in the middle of the moving plate (dashed green line in Fig. 5.3a). The purpose of this

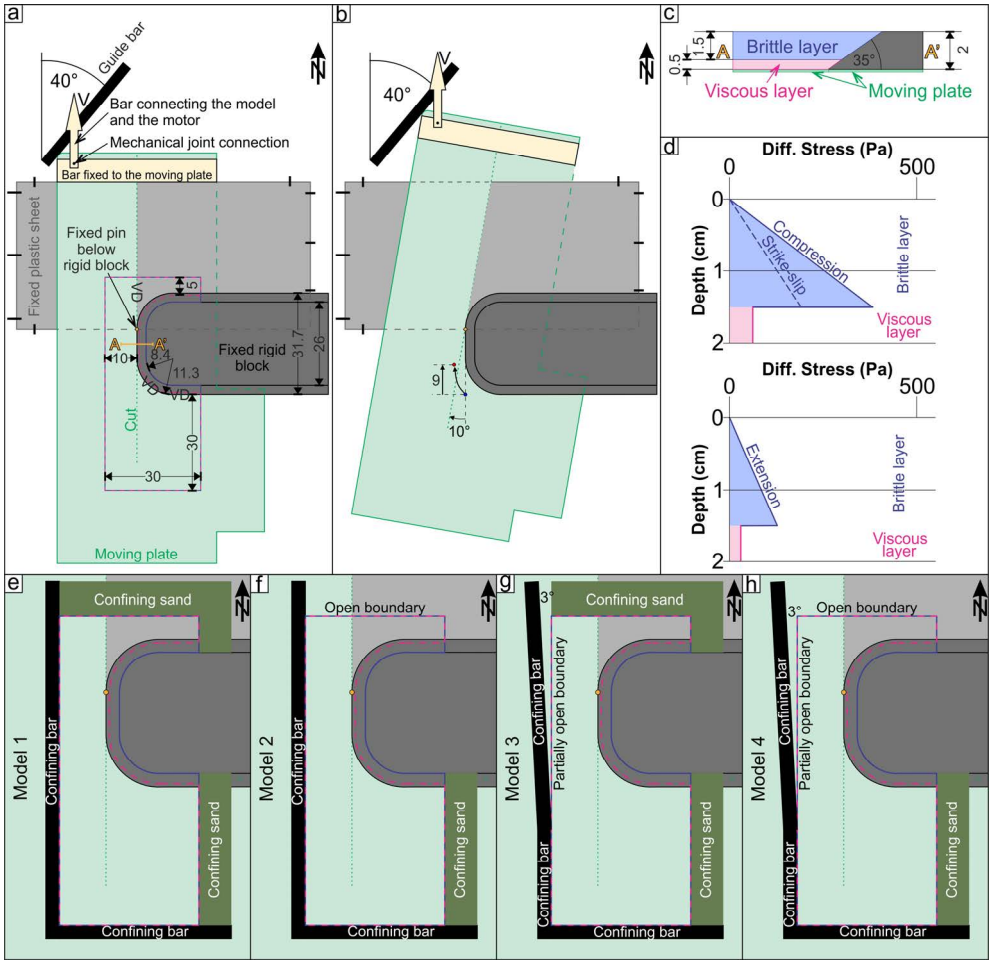

Figure 5.3 - Modelling setup. All numbers without units in Figs. 5.3a-c are in centimetres. a) Initial models' geometry setup and dimensions. b) Configuration of the basal plastic plate/sheet at the end of each experiment. Complex movement of the moving plate includes coupled northward translation and clockwise rotation that result in a total of 9 cm of northward translation and 10° of rotation (blue to red circle). c) Simplified sketch of setup cross-section. Cross-section location is indicated in Fig. 5.3a. d) Strengths profile for all models. For calculating strength of the viscous layer we used mean PDMS viscosity of 2.8 Pa·s at 20 °C measured by Rudolf et al. (2016). e-h) Kinematic boundary conditions applied to model boundaries for each of the four models presented in this study. The confined boundary indicates that any flow of the viscous layer is prevented at that boundary, while the open boundary allows gravity-driven flow of the viscous layer in a direction perpendicular to the boundary.

configuration is to prevent an E-W oriented velocity discontinuity along the northern margin of the indenter. This setup pre-defines velocity discontinuities (VD) in all models along the southern and western margins, as well as along the south-western corner of the indenter and along the cut in the moving plastic plate in the north (Fig. 5.3a).

The mobile plastic plate moves northwards in all models and its movement is controlled by the fixed guide bar in the north (Fig. 5.3a), which results in a coupled translational and rotational movement (Fig. 5.3b). The rotational component of motion is controlled by a stationary pin protruding from below the indenter (fixed pin in Fig. 5.3a), creating a pole of rotation. The cut in the moving plastic plate enables its sliding and rotation around the stationary pin. The coupled translation and rotation takes place during the entire period of each experiment, resulting in the total northward displacement of the mobile plate of 9 cm and 10° of clockwise rotation (Fig. 5.3b).

The difference between our models is the change in kinematic boundary conditions applied to the northern and western margins of the model, simulating different effects of extensional directions on the deformation transfer around the indenter. In model 1 (Fig. 5.3e) all model boundaries are confined, either by metal bars or sand, to prevent the silicone putty (see material properties below) flowing and creating extension. The effect of extension is simulated in models 2, 3 and 4 by (partially) opening lateral boundaries, which allows for extension of the model by gravity driven flow of the viscous, silicone putty layer in direction perpendicular to the open boundary. For loading conditions applied in this study, the gravity driven average velocity of the flow is ~9.6 mm/h (see also section 5.3.2). Model 2 (Fig. 5.3f) has open northern and north-eastern boundaries, which facilitates the flow of the viscous layer away from the indenter (i.e., to the north and north-east). Model 3 (Fig. 5.3g) has a partially open western boundary and allows the silicone putty to flow to the west until it reaches a confining bar, which is at larger distance in the north compared to the south (Fig. 5.3g) introducing a displacement gradient which simulates the limited extension of the southward narrowing Morava Valley Corridor. In model 4 (Fig. 5.3h) the northern boundary is fully open (as in model 2) and the western boundary is open partially (as in model 3).

5.3.1.2 Model materials

All four models consist of brittle and viscous layers with the same rheological properties (Fig. 5.3a-d). The 1.5 cm thick brittle layer is made of dry feldspar sand with a bulk density of ρ=1300 kg/m^3, a cohesion of 10-50 Pa and coefficients of friction of 0.68, 0.55 and 0.61, representing peak, dynamic and reactivation friction, respectively (Willingshofer et al., 2005, 2018). The sand has been sieved to grain size of 100-250 μm. Thin marker horizons of black feldspar sand mark vertical offsets along faults in cross-sections. Horizontal offsets are shown by passive maker lines of black and pink feldspar sand placed on the model's top surface. In Fig. 5.3a, the outline of the sand layer in the model is shown with a blue line and where it is in contact with the indenter it coincides with the upper edge of the inclined indenter margin (Figs. 5.3a, c)

Underlying the feldspar sand, the 0.5 cm thick viscous layer (pink dashed outline in Fig. 5.3a, see also Fig. 5.3c) is analogous to the ductile crust below the brittle-ductile transition. It is made of polydimethylsiloxane (PDMS silicon polymer) putty that has a Newtonian behaviour for strain rates below 10−1 s−1 (Rudolf et al., 2016), with a density

of ρ = 970 kg/m^3, no yield strength and an average viscosity of $2.8 \cdot 10^4$ Pa·s at room temperature (~20 °C; Rudolf et al., 2016).

5.3.2 Scaling

We scaled our models to nature according to principles of geometrical, rheological and kinematical similarities (Hubbert, 1937; Ramberg, 1981; Weijermars and Schmeling, 1986; Davy and Cobbold, 1991). When scaling lengths, we follow the previous analogue modelling study applied to the same natural case of the Carpatho-Balkanides by Krstekanić et al. (2021). This means that 1 cm in our models corresponds to 7 km in nature, which yields a length-scale ratio $L^* = 1.43 \cdot 10^{-6}$. With this length-scale ratio, 1.5 cm depth of the brittle-viscous transition in our models corresponds to ~10 km depth in nature, which is supported by the shallow seismicity and the crustal structure reported in the South and Serbian Carpathians (e.g., Dimitrijevic, 1994; Popa et al., 2018). Lithostatic stress at this depth in the experiments is 191 Pa, which corresponds to 280 MPa in nature, resulting in a stress-scale ratio of $6.82 \cdot 10^{-7}$. Such stress conditions at the base of the brittle layer lead to a threefold increase of flow velocity of silicone as determined by separate gravity driven flow test, performed under loaded (1,5 cm feldspar sand on top of the silicone layer) and not loaded conditions. Following Brun (2002) strength profiles (Fig. 5.3d) have been calculated which are representative for the initial model conditions. Externally imposed velocity, controlled by the engine, was used to calculate strength profiles for the strike-slip and compression regimes, whereas we used flow velocity of silicone putty under loaded conditions to calculate the strength of the viscous layer under gravity driven extension. Based on the flow properties of the viscous layer, we scaled velocity in our models for the strike-slip deformation, following Krstekanić et al. (2021), by calculating a time-scale ratio (Hubbert, 1937) $t^* = 5.3 \cdot 10^{-11}$, which yields a velocity ratio $V^* = 2.7 \cdot 10^4$. It follows that a velocity of 2 cm/h in our models scales to 0.65 cm/yr in nature. This corresponds well with the 60-65 km displacement along the Timok Fault during ~10 Myr (Kräutner and Krstić, 2003; Schmid et al., 2020). Though the velocity scaling is tied to the strike-slip deformation, we note that the displacement rates along normal faults in the Getic Depression (0.4-0.6 mm/y during the period of activity of the Timok Fault, estimated from normal fault offsets reported in Krézsek et al., 2013 and references therein) are significantly lower compared to the strike slip faults (e.g., Krézsek et al., 2013). This correlates well with gravity driven and engine driven flow velocities in our models, although the difference between the two velocities in our models is lower than the one in nature.

5.3.3 Experimental procedures, monitoring and analysis approach

All models are built and run in a normal gravity field and at room temperature (~20 °C). During the experiment, extensional deformation creates depressions in models. In order to track deformation in these depressions (i.e., basins), when they become ~1 mm deep, we fill them with alternating layers of differently coloured sand using a funnel. This sand represents, in simplified way syn-kinematic sedimentation. To preserve topography at the end of each experiment, two post-kinematic layers of black and white sand are sieved on top to cover the entire model. Subsequently, water is sprinkled on the

sand layers to increase cohesion in the sand allowing for sectioning of the experiments in order to obtain information on the geometry of deformation structures.

Top-view photographs perpendicular to the model surface are taken at regular time intervals of 3 minutes, which corresponds to 0.1 cm of motor-induced northward displacement between two photographs. We use particle image velocimetry on these top-view photographs (PIVlab, Thielicke and Stamhuis, 2014) to calculate incremental particle displacements for each pair of adjacent photographs in the time series. The obtained incremental displacement fields are inspected for the presence of very large displacements that represent data outliers. Such outliers form due to incorrect correlations and are removed by applying a magnitude threshold filter, followed by a visual inspection and manual removal. Displacements in basins for time frames when syn-kinematic sedimentation is added cannot be correlated automatically. Therefore, for these few time frames in each model, displacements in basin areas are interpolated from basin margins. Displacement fields are further analysed using the methodology and StrainMap software of Broerse et al. (2021) and Broerse (2021) to calculate 2D average strain type at the surface during evolution of our models. In the end, we combine our 2D strain analysis with visual interpretation of top-view photographs and vertical-cross sections to infer 3D deformation in our models.

5.3.4 Modelling limitations and simplifications

The laboratory time-scale of our experiments is 5 hours during which deformation is induced by horizontal motion of a mobile plate as described in section 3.1.1. This relatively fast deformation allows for adopting an inverse density gradient of the model layers without influencing the modelling outcome. This simplification is justified because buoyancy driven vertical motions typically occur on laboratory time-scales of days (e.g., Cobbold and Szatmari, 1991; Brun and Fort 2004, 2011; Krézsek et al., 2007; Warsitzka et al., 2015). We, therefore, consider that the buoyancy effect is negligible in our models and that no diapirism contributed to the overall deformation.

Furthermore, our models do not account for isostasy, surface erosion and sediment transport, creating exaggerated topography in the contractional area in front of the indenter. However, this area is not the main target of our study as we focus more on the interaction between strike-slip and extension behind the indenter and along its lateral margin. As our models do not account for vertical temperature gradients, the viscosity of the silicone putty simulating viscous behaviour is constant with depth, which is considered acceptable in analogue modelling studies (e.g., Davy and Cobbold, 1991). All other simplifications follow Krstekanić et al. (2021).

5.4 Results

The modelling results are presented as top-view photographs and average strain maps (Figs. 5.4 – 5.7) for key moments in the evolution of all 4 models (i.e., after 1 cm, 4 cm and 9 cm of northward displacement) and interpreted cross-sections (Figs. 5.4 – 5.7) portraying the final deep structure of each experiment. Furthermore, time-lapse map-

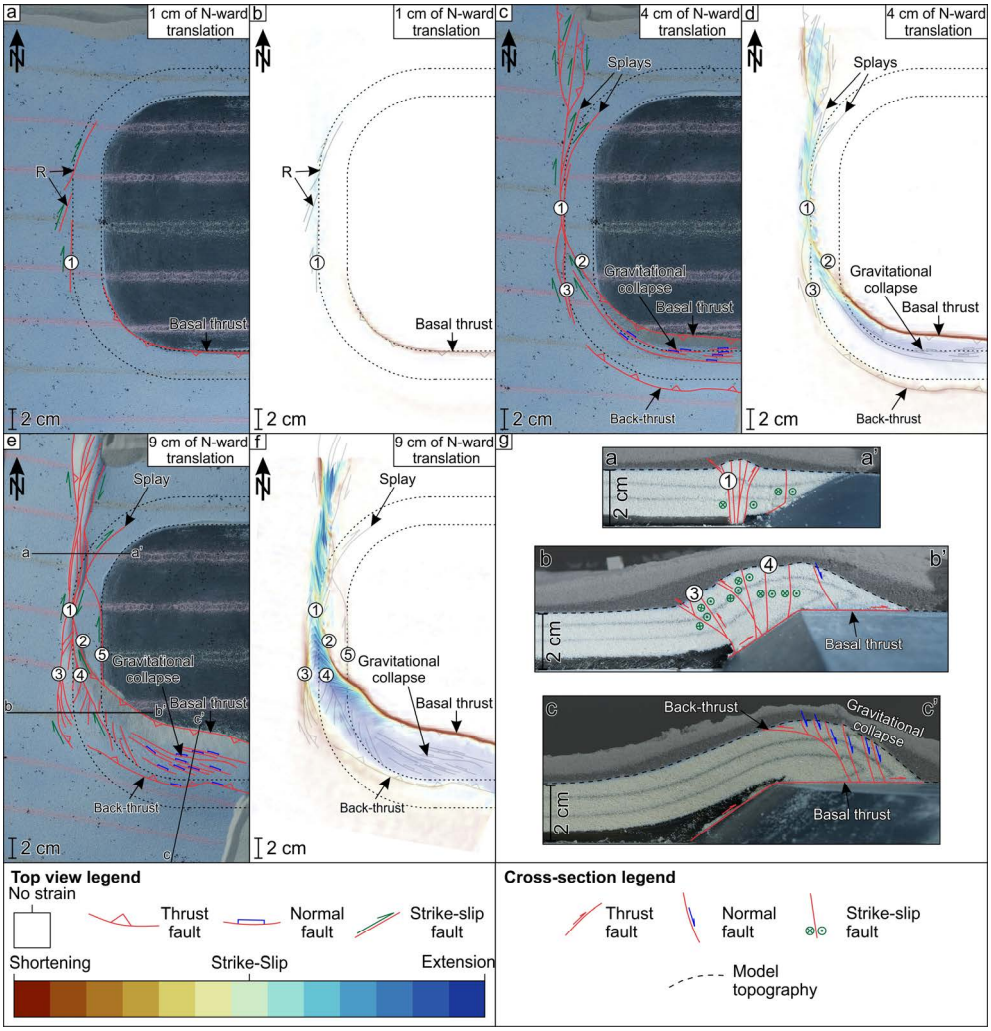

Figure 5.4 - Model 1 - closed boundaries. Dashed black lines mark the upper and lower edges of the indenter. R – Riedel shear. a) Interpreted top-view photo after 1 cm of northward translation. b) Cumulative average strain type map after 1 cm of northward translation. c) Interpreted top-view photo after 4 cm of northward translation. d) Cumulative average strain type map after 4 cm of northward translation. e) Interpreted top-view photo at the end of the experiment. f) Cumulative average strain type map at the end of the experiment. Strain plots in Figs. 5.4b, d, f overlay visually interpreted structures from Figs. 5.4a, c, e (grey lines). Strain colour legend corresponds to Figs. 5.4b, d, f. In order to supress areas without significant deformation, the transparency of areas with a strain magnitude below the 90 percentile is increased. g) Cross-sections of the reference model at the end of the experiment. Dashed line marks the model topography at the end of the experiment. Shaded area in the upper part of each cross-section marks post-kinematic sand cover. Cross-section locations are shown in Fig. 5.4e.

view videos of each model (see Supplementary material) were used to derive kinematics and temporal and spatial evolution of fault pattern during deformation.

5.4.1 Model 1: reference model with closed boundaries

In this experiment all sides are confined by metal bars or sand and the model shows a gradual transition from dextral strike-slip dominated deformation along the western indenter's margin through transpression around indenter's SW corner to shortening-dominated deformation along the southern margin (Fig. 5.4). The evolution of this deformation transfer and fault pattern is gradual and increases its complexity through time.

Early in the deformation history, lateral movement along the western indenter margin is accommodated by en-échelon NNE-SSW oriented Riedel shears (R in Figs. 5.4a, b) and a N-S oriented strike-slip fault, which develops above the lower edge of the indenter's margin (1 in Figs. 5.4a, b). At the same time shortening south of the indenter is accommodated along the top-N basal thrust (Figs. 5.4a, b), which has no clear connection to the strike-slip faults.

After approximately 4 cm of total northward translation (Figs. 5.4c, d), strike-slip fault segments connect to form a through-going N-S oriented fault system (1 in Figs. 5.4c, d). North of the pole of rotation, this strike-slip system partitions deformation in a positive flower structure with shortening to transpression being accommodated along the margins of the system (red and orange in Fig. 5.4d) and strike-slip to transtension (green and light blue in Fig. 5.4d) in the centre of the deformation zone. Remnants of Riedel shears form NNE oriented curved splays within the strike-slip system (Figs. 5.4c, d). The strike-slip system transfers part of its offset south-eastwards to a basal thrust via transpressional NW-SE oriented faults (2 in Figs. 5.4c, d), during its gradual southwards propagation (3 in Fig. 5.4c, d). Shortening in front of the indenter is also accommodated by a new back-thrust (Figs. 5.4c, d) and weak, distributed shortening farther to the south (pale red in Fig. 5.4d). In the area between the basal thrust and the back-thrust, minor extensional deformation (blue in Fig. 5.4d) accommodates the change from ramp to upper-flat surface of the indenter.

The first order style and kinematics of deformation remains similar until the end of experiment (i.e., after 9 cm of total northward translation; Figs. 5.4e, f), especially in the north, where the positive flower structure and north-eastward splay remain with a similar geometry and strain pattern (Figs. 5.4e, f and cross section a-a' in Fig. 5.4g). To the south, the connection between the main strike-slip fault (1 in Figs. 5.4e, f) and the basal thrust remains active and linked up with the NW-SE transpressional fault (2 in Figs. 5.4e, f). A new complex strike-slip fault (4 in Figs. 5.4e, f and cross-section b-b' in Fig. 5.4g) with numerous low-offset splays propagates southwards from the main strike-slip system and deforms the previously formed thrust wedge. South of the indenter, weak extensional deformation with numerous low-offset normal faults partially reactivate the back-thrust, while the bulk shortening is accommodated along the basal thrust (Figs. 5.4e, f, and cross-section c-c' in Fig. 5.4g).

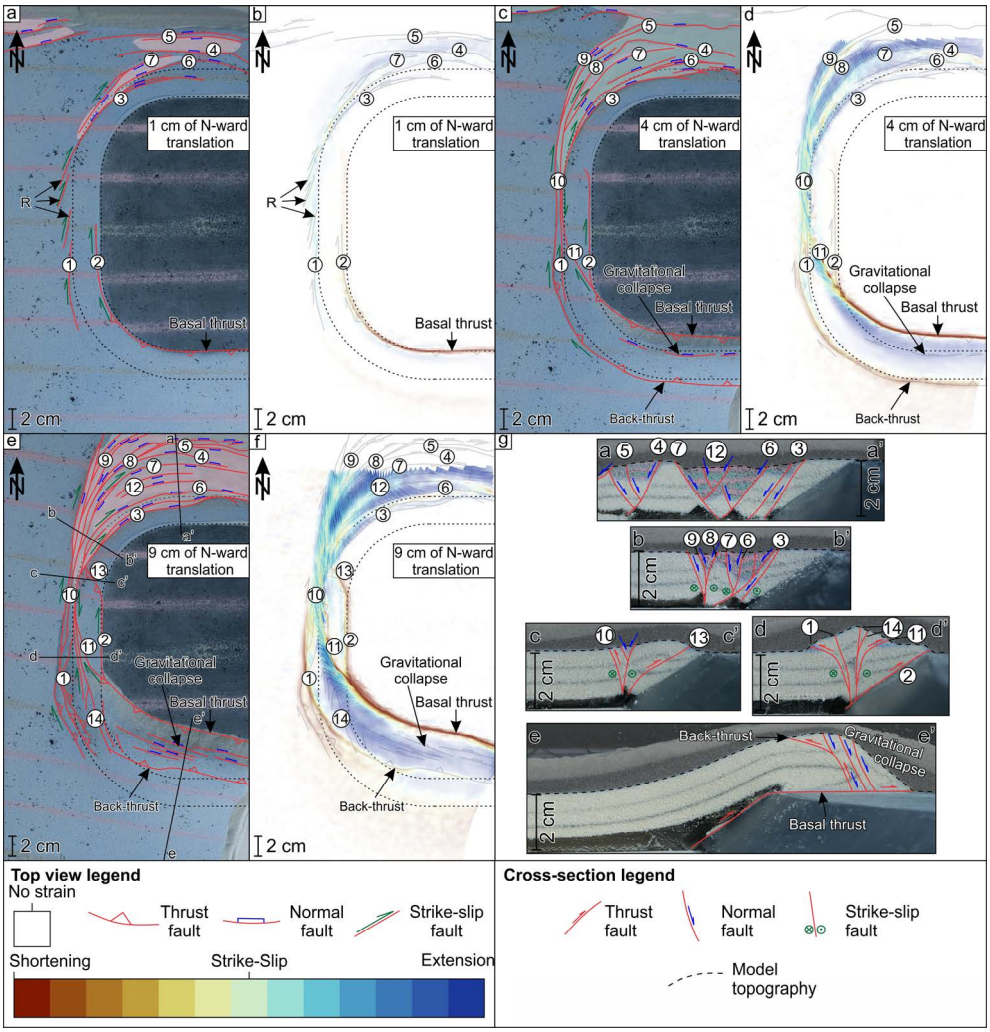

Figure 5.5 - Model 2 - open northern boundary. Dashed black lines mark the upper and lower edges of the indenter. R – Riedel shear. Highlighted semi-transparent white area marks the location of basin(s) with sedimentary infill. a) Interpreted top-view photo after 1 cm of northward translation. b) Cumulative average strain type map after 1 cm of northward translation. c) Interpreted top-view photo after 4 cm of northward translation. d) Cumulative average strain type map after 4 cm of northward translation. e) Interpreted top-view photo at the end of the experiment. f) Cumulative average strain type map at the end of the experiment. Strain plots in Figs. 5.5b, d, f overlay visually interpreted structures from Figs. 5.5a, c, e (grey lines). Strain colour legend corresponds to Figs. 5.5b, d, f. To supress areas without significant deformation, the transparency of areas with a strain magnitude below the 90 percentile is increased. g) Cross-sections of the reference model at the end of the experiment. Dashed line marks the model final topography. Shaded area in the upper part of each cross-section marks post-kinematic sand cover. Cross-section locations are shown in Fig. 5.5e.

5.4.2 Model 2: open northern boundary

The open northern boundary in model 2 creates extension, which results in the opening of a large fault controlled extensional basin north of the indenter (highlighted semi-transparent white area in Fig. 5.5). This basin reflects the interplay between extension and strike-slip deformation because the entire fault system north of the indenter connects towards SW to the N-S oriented dextral strike-slip deformation. This strike-slip system further transfers deformation to thrusting on top of the southern indenter's margin. The latter feature has the same evolution, geometry and kinematics as in the model 1 for the entire experiment duration. (Fig. 5.5).

The early strike-slip deformation along the western indenter's margin is accommodated by NNE-SSW oriented Riedel shears (R in Figs. 5.5a, b) and early N-S oriented strike-slip faults (1 and 2 in Figs. 5.5a, b). To the south, fault 2 connects to the basal thrust, while to the north, Riedel shears connect to numerous normal faults that accommodate extensional deformation (3-7 in Figs. 5.5a, b). These normal faults dip either to the north or south creating small and isolated basins (e.g., between faults 6 and 7 and 4 and 5 in Fig. 5.5a) separated by ridges (such as between faults 4 and 7 in Fig. 5.5a, cross-section a-a' in Fig. 5.5g). Closer to the indenter, these normal faults have curved geometries (3, 6 and 7 in Fig. 5.5a), controlled by the NW indenter corner, as they gradually transfer extension through transtension to strike-slip deformation (Fig. 5.5b).

After 4 cm of northward translation, the strike-slip system is fully connected into a continuous multi-strand structure (10 and 11 in Figs. 5.5c, d). In the north, the small, early basins connect into a single larger basin with intra-basinal highs and sub-basins, while new faults (e.g., 8 and 9 in Figs. 5.5c, d) form to connect normal faults with the strike-slip system along the western indenter's margin.

Towards the end of the experiment, the basin system in the north further enlarges with new smaller normal faults forming within its interior (e.g., 12 in Figs. 5.5e, f, cross-section a-a' in Fig. 5.5g). The overall strain pattern north of the indenter shows intercalating regions of extension-dominated and strike-slip to transtension-dominated deformation. The latter are more frequent around the NW indenter corner where the basin is narrower and extension connects with strike-slip system (Fig. 5.5f, cross-section b-b' in Fig. 5.5g). Along the western indenter's margin, fault 2 propagates to connect with the main strike-slip system along an oblique thrust (13, Figs. 5.5e, f, cross-section c-c' in Fig. 5.5g). To the south, the main strike-slip system (10 in Figs. 5.5e, f) completely inverts the narrow southern tip of the basin (cross-section c-c' in Fig. 5.5d), creating a positive topography (cross-section d-d' in Fig. 5.5d) during its southward propagation (14 in Figs. 5.5e, f).

5.4.3 Model 3: partially open western boundary

The ~E-W extension induced along the western model margin creates a distinctively different fault pattern along the western indenter margin compared to the previous two models (Fig. 5.6), where strain is partitioned into two sub-parallel ~N-S oriented zones of combined dextral strike-slip, transtension and extension. To the south, strike-slip

deformation is transferred to thrusting on top of the southern indenter's margin, which creates the same deformation pattern as in previous two models.

The early-stage deformation is localized in two closely spaced, sub-parallel dextral strike-slip faults (1 and 2 in Figs. 5.6a, b), also associated with a weak extensional strain (blue in Fig. 5.6b). Northwards, these two faults splay to form NE striking faults around the indenter's NW corner (Figs. 5.6a, b).

The evolution of both strike-slip and E-W oriented extension leads to a formation of two separate deformation zones, which connect where strike-slip deformation is gradually replaced by transpressive deformation at the southwestern indenter corner (Figs. 5.6c, d). The eastern of the two forms on top of the velocity discontinuity and is controlled by faults 1 and 2 (Figs. 5.6c, d), while the western deformation zone is slightly

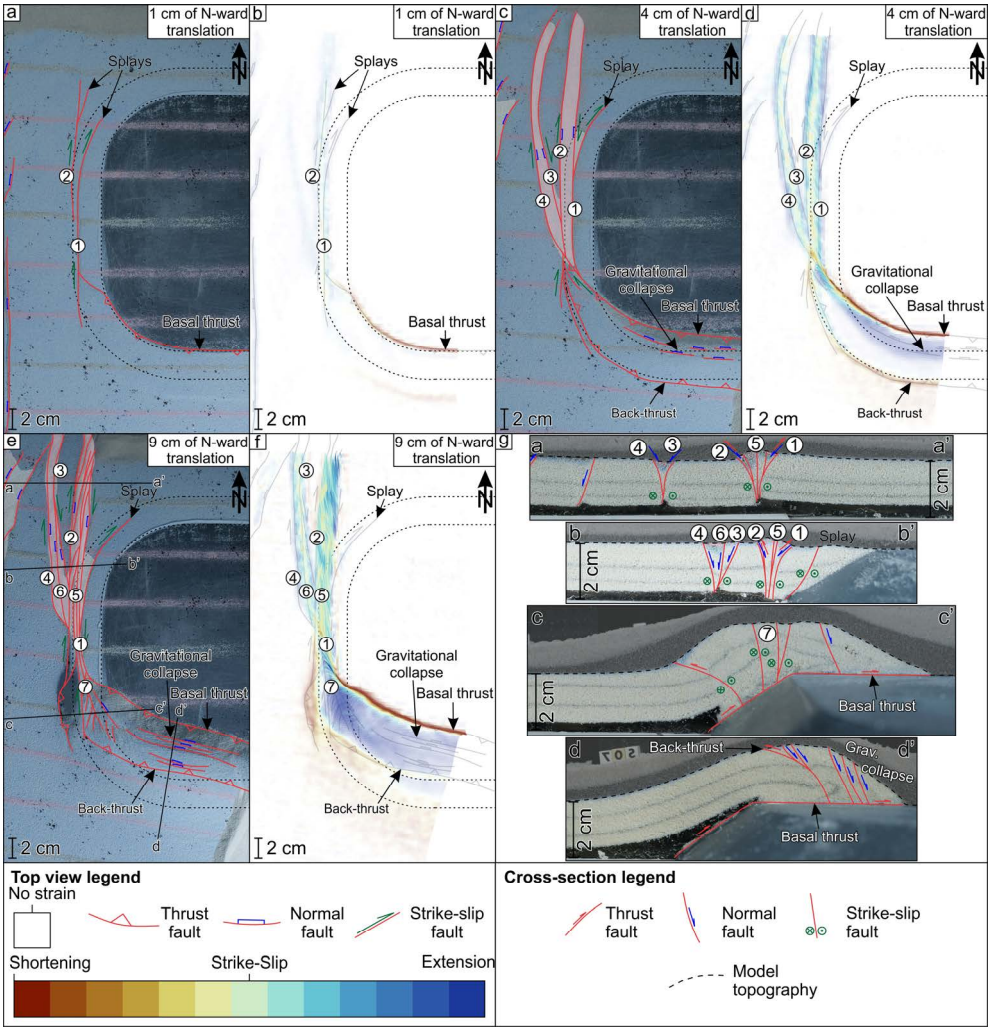

Figure 5.6 - Model 3 - partially open western boundary. Dashed black lines mark the upper and lower edges of the indenter. R – Riedel shear. Highlighted semi-transparent

white area marks the location of basin(s) with sedimentary infill. a) Interpreted top-view photo after 1 cm of northward translation. b) Cumulative average strain type map after 1 cm of northward translation. c) Interpreted top-view photo after 4 cm of northward translation. d) Cumulative average strain type map after 4 cm of northward translation. e) Interpreted top-view photo at the end of the experiment. f) Cumulative average strain type map at the end of the experiment. Strain plots in Figs. 5.6b, d, f overlay visually interpreted structures from Figs. 5.6a, c, e (grey lines). Strain colour legend corresponds to Figs. 5.6b, d, f. To supress areas without significant deformation, the transparency of areas with a strain magnitude below the 90 percentile is increased. g) Cross-sections of the reference model at the end of the experiment. Dashed line marks the model topography at the end of the experiment. Shaded area in the upper part of each cross-section marks post-kinematic sand cover. Cross-section locations are shown in Fig. 5.6e.

---

younger and is controlled by faults 3 and 4 (Figs. 5.6c, d). In both zones, subsidence in narrow basins (Fig. 5.6c) is controlled by dominant dip-slip faults, while strike-slip deformation affects central areas of the basins (Fig. 5.6d).

With progressing deformation, new faults with dominant strike-slip kinematics form within the two deformation zones (e.g., 5 and 6 in Figs. 5.6e, f). The gradual cessation of extension along the western model margin leads to basins inversion, mostly along the eastern shear zone. This is, for instance, observed in cross-sections a-a' and b-b' (Fig. 5.6g) where positive topography in the basin area (between faults 1 and 2), the offset at the base of the basin and deformed sedimentary infill indicate inversion of originally transtensive faults (1 and 2) and new strike-slip faulting (5). Strike-slip deformation becomes subsequently the dominant deformation along the western indenter's margin, where it propagates southwards and overprints the earlier thrust wedge (7 in Figs. 5.6e, f and cross-section c-c' in Fig. 5.6g).

5.4.4 Model 4: open northern and partially open western boundaries

The coevally evolving extensions along the northern and western model margins create a large extensional basin north of the indenter, which shows a combination of features observed in models 2 and 3. Extension is gradually transferred to dextral strike-slip and transtension that affects a wide area along the western margin of the indenter. Southwards, the strike-slip deformation is transferred to shortening like in all previous models (Fig. 5.7).

Early in the model evolution, the deformation along the western indenter's margin is accommodated by two N-S oriented dextral transtensional faults (1 and 2 in Figs. 5.7a, b), which control a narrow basin in between. Distributed subsidence affects a wider area west of these two faults (blue in Fig. 5.7b), with no evident normal faulting at the resolution of the model. Northwards, strike-slip to transtensional faults curve around the NW indenter's corner to connect to transtensional to normal faults north of the indenter (3 – 8 in Figs. 5.7a, b). These normal faults dip northwards or southwards, creating several isolated basins (Fig. 5.7a).

After ~4 cm of northward translation, the isolated basins and intervening highs are connected into one large basin (Figs. 5.7c, d, see also cross-section a-a' in Fig. 5.7g).

This basin enlargement and connection with strike-slip deformation takes place along previously and newly formed normal and strike-slip faults (8-12 in Figs. 5.7c, d). West of the indenter, new normal faults accommodate the extensional component of deformation which further contributes to basin enlargement (13 in Figs. 5.7c, d).

Towards the end of the experiment, the basin system expands, especially to the west of the main strike-slip zone where new faults (14 and 15 in Figs. 5.7e, f) accommodate subsidence at the transition from extension in the north to strike-slip and the extension in the west. North of the indenter, the structure of the basin is characterized by sub-basins separated by intra-basinal highs (cross-section a-a' in Fig. 5.7g). In the area around the

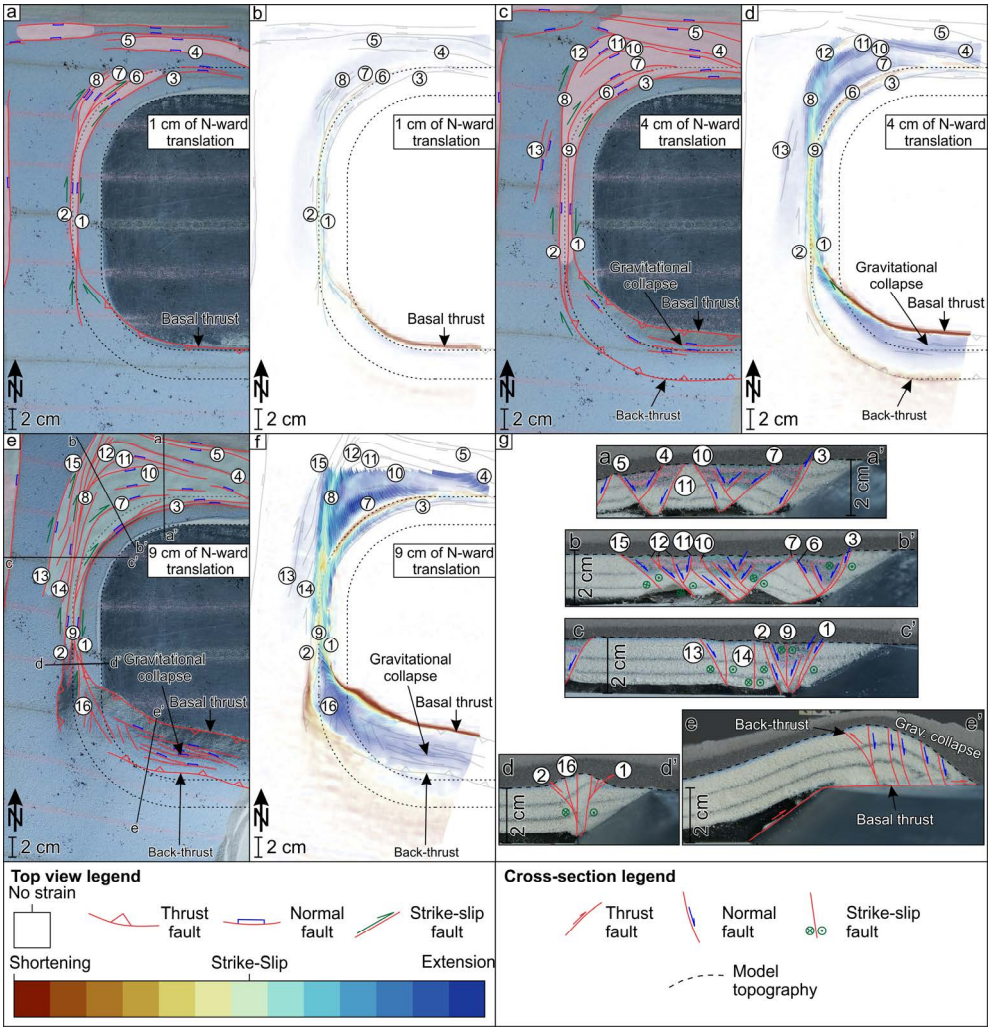

Figure 5.7 - Model 4 - open northern and partially open western boundaries. Dashed black lines mark the upper and lower edges of the indenter. R – Riedel shear. Highlighted semi-transparent white area marks the location of basin(s) with sedimentary infill. a) Interpreted top-view photo after 1 cm of northward translation. b) Cumulative average

strain type map after 1 cm of northward translation. c) Interpreted top-view photo after 4 cm of northward translation. d) Cumulative average strain type map after 4 cm of northward translation. e) Interpreted top-view photo at the end of the experiment. f) Cumulative average strain type map at the end of the experiment. Strain plots in Figs. 5.7b, d and f overlay visually interpreted structures from Figs. 5.7a, c and e (grey lines). Strain colour legend corresponds to Figs. 5.7b, d and f. Note that in order to supress areas without significant deformation, the transparency of areas with a strain magnitude below the 90 percentile is increased. g) Cross-sections of the reference model at the end of the experiment. Dashed line marks the model topography at the end of the experiment. Shaded area in the upper part of each cross-section marks post-kinematic sand cover. Cross-section locations are shown in Fig. 5.7e.

NW corner of the indenter where the two extension directions interfere, the structural pattern is more complex (Fig. 5.7e and cross-section b-b' in Fig. 5.7g). In this area, strain is partitioned into extension-dominated and strike-slip-dominated regions (areas of blue and green in Fig. 5.7f). A distinct feature is a narrow zone of shortening to transpressional deformation located in the hanging wall of fault 3 (Fig. 5.7f), which in our view is related to rotation of the hanging wall of fault 3 (or footwall of fault 7; see cross-sections a-a' and b-b' in Fig. 5.7g). This block rotates (clockwise in sections a-a' and b-b' in Fig. 5.7g) around a horizontal axis due to the listric geometry of fault 3. While the entire block moves away from the indenter due to extension, the rotation brings the segment of this block located away from fault 3 up and towards the indenter. In map view such displacement creates local apparent shortening. A similar, but less expressed, feature can be observed also in the model 2 above the fault 3 (Fig. 5.5). Towards the south, the basin narrows significantly (Fig. 5.7e and cross-section c-c' in Fig. 5.7g) until the strike-slip deformation starts its transfer to transpression and creates a positive topography (cross-section d-d' in Fig. 5.7g). The main strike-slip fault system (1, 2 and 9 in Figs. 5.7e, f) propagates southwards (16 in Figs. 5.7e, f and cross-section d-d' in Fig. 5.7g) and overprints the thrust wedge.

5.5 Effects of extension(s) on strain partitioning and deformation transfer around an indenter

The results of Chapter 3 (also Krstekanić et al., 2021) has shown that deformation transfer during indentation without an additional externally driven extension is controlled mainly by the geometry of the indenter. The new modelling results of this study exhibit similar features to Krstekanić et al. (2021) for similar modelling setups (model 1) but differ for areas which are affected by extensional boundary conditions (models 2-4). All models show similar deformation patterns with the formation of a thrust wedge with almost similar topographic height (4.4 cm, 4.3 cm, 4.1 cm and 4.3 cm for models 1 – 4, respectively) in the south and its transition to transpression and strike-slip south-west of the indenter (Figs. 5.4-5.7). This suggests that extension imposed on the north-western and northern model boundary did not affect the deformation at the

southern and south-western model areas. In contrast, significant subsidence associated with transtension and normal faulting creating isolated or connected basins is observed along the northern, north-western and western indenter's margins in models that allow extension at their margins (models 2 – 4, Figs 5.5-5.7).

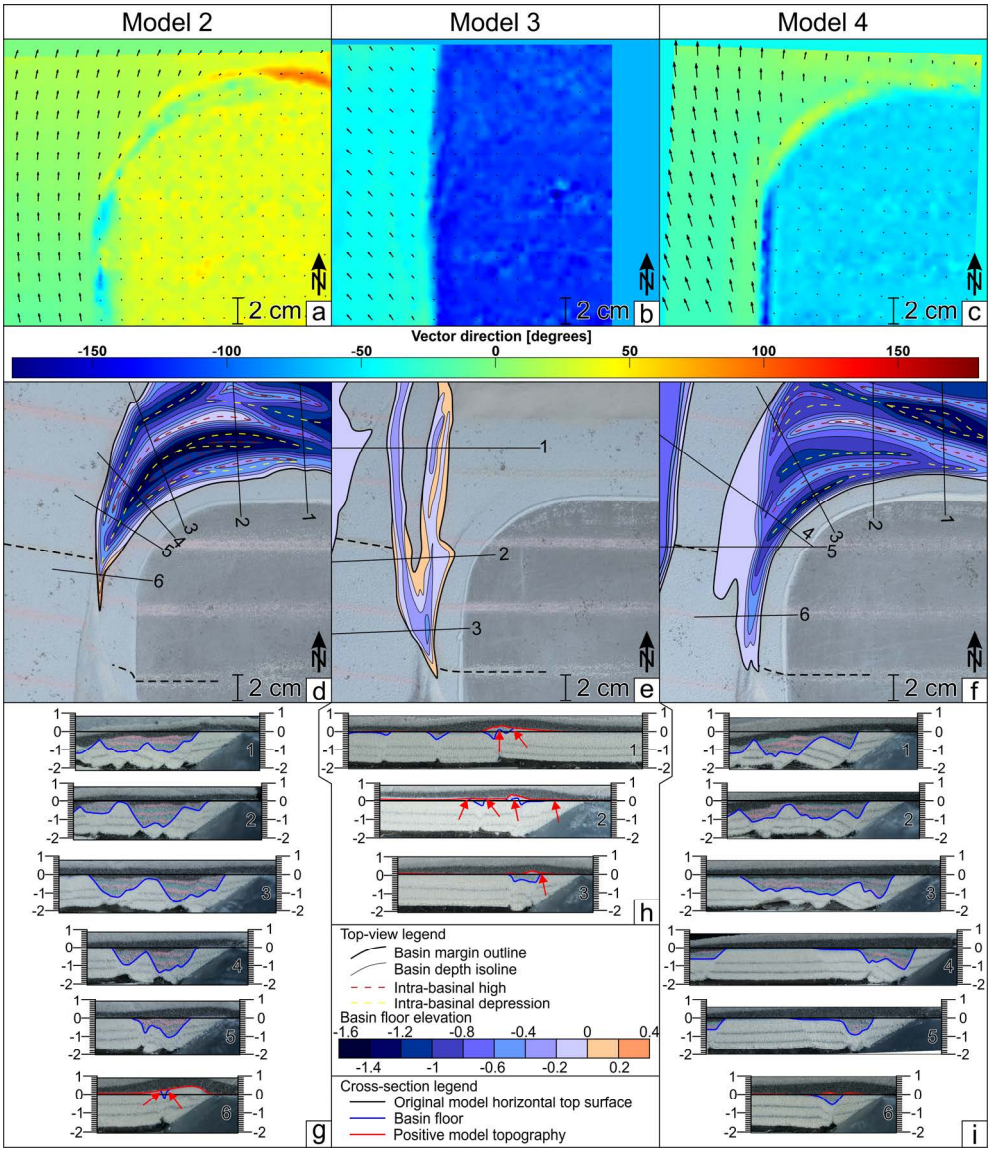

Figure 5.8 – a-c) Incremental displacement directions after 1 cm of total displacement in the northern parts of models 2, 3 and 4, respectively. Black arrow length indicates relative displacement magnitude. When there is no displacement (e.g., area of indenter) vector direction is randomly assigned by the software and is irrelevant in analysis. In the displacement vector direction legend, 0 is equivalent of north, -90 is west, while 90 is

east. d-f) Final top-view photographs of northern parts of models 2, 3 and 4, respectively, overlain by structural maps of the basin floor. Dashed black line indicate location of the central passive marker line on the model surface. Cross-sections locations are indicated by straight black lines and respective numbers. The maps are constructed by measuring elevation of basin floor in the cross-sections (g-i), projecting them in top-views along the respective cross-section lines and interpolating isolines in the areas between cross-sections. Isolines are drawn at 0.2 cm vertical distance. Red arrows in the cross-sections point to basin floor that is elevated to above the original flat surface of the model.

5.5.1 The influence of the northern extension

Extension along the northern boundary creates a NNE to ENE oriented displacement field in the area north of the indenter (Fig. 5.8a) resulting in a large basin with a curved southern margin, controlled by the geometry of the indenter's NW corner. Westwards, the basin is bound by a strike-slip to transtensional fault system (Figs. 5.5e, 5.8d) that has numerous splays curved to the east, along which the connection with normal faulting is ultimately established. The extension evolves gradually, which results in a segmented basin that has several elongated depo-centres (yellow dashed lines in Fig. 5.8d), separated by intra-basinal highs of different elevation (red dashed lines in Fig. 5.8d; see also cross-sections in Fig. 5.8g). The largest basin depth is observed in the vicinity of the NW indenter's corner, reaching 1.5 cm (cross-sections 2 and 3 in Fig. 5.8g). Southwards, the basin narrows and becomes less deep, as the influence of the northward extension decreases. The southern tip of the basin is located at the transition of the curved NW corner to the straight N-W oriented indenter's margin. This is the area where the main strike-slip deformation changes its kinematics, from transtension in the north to transpression in the south, while inverting the basin at the same time. This inversion results in the positive topography of the model and uplift of the basin floor (the elevation of the basin floor is, locally, higher than the original model surface in Fig. 5.8d; red arrows in cross-section 6 in Fig. 5.8g).

5.5.2 The influence of the western extension

Westward directed gravity spreading along the western model boundary combined with the northward motor-induced pull create a displacement field oriented towards NW (Fig. 5.8b), which distributes strike-slip deformation westwards and adds a transtensional component. Such coupled strike-slip and extension partition the deformation in two elongated ~N-S oriented transtensional corridors that control basin formation (Fig. 5.8e). These elongate basins merge southwards and reach up to the centre of the N-S oriented western margin of the indenter (marked by the dashed black marker line in Fig. 5.8e). With the cessation of the western extension, the strike-slip deformation takes over, inverting the basins, especially the one along the main eastern strike-slip corridor (Fig. 5.8e). This inversion is observed by uplift of the basin infill and its deformed floor (cross-sections in Fig. 5.8h), which implies that the relatively shallow basin system (less than 0.5 cm depth; see cross-section 3 in Fig. 5.8h) was deeper before inversion.

5.5.3 The influence of the coeval and coupled bi-directional extensions

When extension is bi-directional, the influence of extension along the northern boundary dominates over that along the western boundary, because more extension is applied along the former. The early model displacements are oriented to the NNW in the west, which changes to NE in the east (Fig. 5.8c). Similar to the model 2 (Fig. 5.8d), the northern extension creates a large basin with a curved southern margin and numerous elongated sub-basins and intra-basinal highs (Fig. 5.8f). These sub-basins are, in top-view, more often dissected, less continuous and wider towards the west when compared with model 2 (compare Fig. 5.8d with 5.8f). This is due to the north-westward flow of the silicone that distributes deformation over a wider area (compare Fig. 5.8a with 5.8c). The basin extents farther southwards where the tip of the basin reaches central regions of the western indenter's margin, similar to model 3 (compare Fig. 5.8e with 5.8f). The basin reaches 1.3 cm depth (cross-sections 1 and 3 in Fig. 5.8i), which is ~13% less when compared with model 2, which indicates an extension and associated subsidence distributed over a larger area. The southern tip of the basin was likely inverted, which is suggested by the associated uplift resulting in positive basin infill topography (cross-section 6 in Fig. 5.8i). Therefore, the northern extension controls the opening of a wider basin, the internal distribution of fault offsets, subsidence and the connection to the curved strike-slip faulting along western indenter's margin. The westward extension creates a transtensional deformation regime with subsidence along N-S oriented strike-slip faults, pulling and distributing the deformation towards the west, allowing for an additional, but relatively minor amount of subsidence west of the indenter.

5.5.4 Implications for the indentation processes

Existing modelling studies that investigate indentation and resulting shortening indicate that lateral extrusion during indentation requires a weaker crust and/or lithosphere rheology to be present laterally in the system (e.g., Ratschbacher et al., 1991a, Sokoutis et al., 2000; Rosenberg et al., 2004; van Gelder et al., 2017), associated or not with extension driven by slab roll-back (e.g., Faccenna et al., 1996; Philippon et al., 2014b; Schellart et al., 2019) and sometimes coupled with a collapse and spreading of orogenic wedges (Faccenna et al., 1996; Kydonakis et al., 2015). When the lateral margins are confined, there is no lateral extrusion and deformation is transferred only around the indenter and partitioned between shortening, transpression and strike-slip deformation depending on the indenter geometry (Zweigel 1998; Luth et al., 2013; Schellart et al., 2019; Krstekanić et al., 2021; see also Chapter 3). These results imply that a form of extension or gravity spreading at high angle to indentation shortening along one or multiple margins of the system is essential for lateral extrusion in indentation systems. Our models are in agreement with these previous inferences, but further imply that the amount of extension and thus space generated by this process is critical for lateral extrusion to occur. In cases of limited externally-driven extension, the structural complexity increases by adding an extensional component to indentation-induced deformation, but will not lead to large-scale extrusion of fault-bound crustal blocks.

5.6. Implications for the evolution of the Carpatho-Balkanides

The Circum-Moesian Fault System associated with the Carpatho-Balkanides backarc-convex oroclinal bending partitions the deformation around the Moesian Platform indenter in a similar way as in our analogue models, from transtension and strike-slip to transpression and shortening (Figs. 5.2 and 5.9; Krstekanić et al., 2021, 2022; see Chapters 3 and 4). This deformation was coeval with roll-back of the Carpathians and Dinarides slabs that together created the observed bimodal back-arc extension (Fig. 5.9; see also Matenco and Radivojević, 2012).

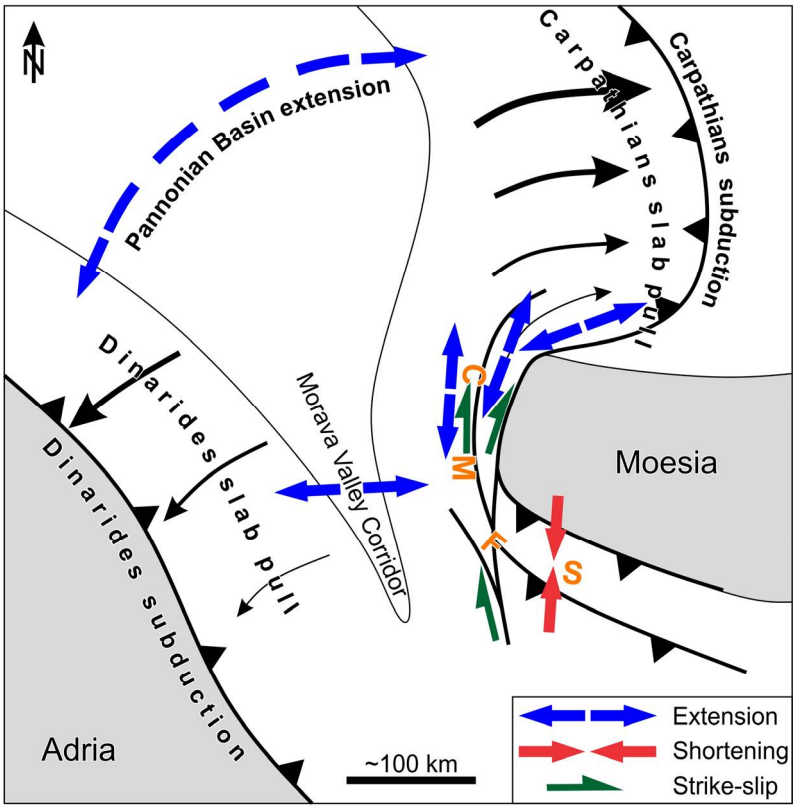

Figure 5.9 - Sketch of the influence of Carpathians and Dinarides slabs on the deformation around the Moesian Platform. Both slab roll-backs exert pull on the upper plate, which results in the extension in the Pannonian Basin. Additionally, Carpathians slab pull creates orogen-parallel extension along the Moesian indenter, which changes its orientation around the NW corner of Moesia and is, thus directed in ENE-WSW to N-W direction. To the west of the Moesia the extension in the Morava Valley Corridor is produced by the Dinarides slab pull and is perpendicular to the Moesian western margin. Both extensions affect the transfer of deformation in the Circum-Moesian Fault System (CMFS, orange letters) that is made of several thrusts south of Moesia and strike-slip deformation along the Moesian western margin.

Our models suggest that the extension and transtension north and north-west of the indenter can be indeed explained by the bimodal N-S and E-W oriented extension. The roll-back of the Carpathians slab pulled its upper plate creating the orogen-parallel N-S, NE-SW to ENE-WSW oriented extension in the Serbian and South Carpathians and their foreland due to the corner effect of the Moesia (e.g., Schmid et al., 1998; Matenco and Schmid, 1999; Ratschbacher et al., 1993; Krstekanić et al., 2020). Previous studies have shown 4-6 km of maximum Oligocene - early Miocene subsidence in various locations within the Getic Depression (e.g., Matenco et al., 2003; Răbăgia et al., 2011; Krézsek et al., 2013), which is smaller when compared with our models (1.3 – 1.5 cm in models scale to ~10 km in nature). Owing to the subsequent post- early Miocene basin inversion and burial to large depths (~10km) in the proximity of the South Carpathians, these studies were not able to establish a very precise internal geometry of the Oligocene - Early Miocene basin beyond a potential separation in northern and southern sub-basins by an intermediary high (e.g., Fig. 1b in Răbăgia et al., 2011 or Fig. 7 in Krézsek et al., 2013), which connect gradually to the west and SW in the present-day geometry. Our bi-modal extension results (Fig. 5.8f) predict a similar geometry and furthermore suggest that the Oligocene - early Miocene sediment thicknesses are similar in transects across sub-basins, but with higher northern values in the central Getic Depression. Although the detailed fault geometry and distribution is somewhat different, the deformation transfer and interplay between Timok Fault strike-slip offset to N- to NE- wards transtension and further E-wards normal faulting in the Getic Depression shows clear resemblance with our north and bi-modal extension models (see Răbăgia and Maţenco, 1999; Krézsek et al., 2013).

The geometry of the extension along the western model margin is very similar to the one of the orogen-perpendicular extension in the Morava Valley Corridor, which is probably driven by the Dinarides slab roll-back, affecting only the hinge area of the Carpatho-Balkanides back-arc convex orocline (Figs. 5.2 and 5.9, the westernmost side of the Serbian Carpathians bordering the Morava Valley Corridor, Matenco and Radivojević, 2012; Erak et al., 2017; Sant et al., 2018; Krstekanić et al., 2020). This Oligocene - Miocene orogen-perpendicular extension decreases gradually E- and S-wards (Krstekanić et al., 2020; see also Chapter 2), while extending with time during the middle Miocene to the SW into the external Dinarides (Andrić et al., 2018, van Unen et al., 2019a and references therein). Our modelling results show that the westward extension allows for the partitioning of strike-slip deformation into multiple sub-parallel strike-slip faults that merge into a single deformation zone along the western margin of the indenter. The connecting geometry and observed westward continuation of the orogen perpendicular extension is realistic in the model with bimodal extension when compared with the observed fault geometry and splaying characteristics (compare Fig. 5.2b with Figs. 5.7e and 5.8f, e.g., splaying the Timok offset along the Sokobanja-Zvonce and Rtanj-Pirot faults in Fig. 5.2b). These observations infer that the geometry of the Circum-Moesian Fault System requires the Morava Valley extension to be coupled with the oroclinal bending and orogen-parallel extension. The shallow (<1km) E-W oriented intra-montane basins of the Serbian Carpathians (Fig. 5.2) were not reproduced by our modelling, possibly because of the limited gravity spreading created at the

margins of our model, which does not completely reproduce the likely larger horizontal forces exerted by a slab roll-back, remaining a feature for further study.

5.7 Conclusions

We studied the effects of externally driven extension on strain partitioning and deformation transfer around an indenter by the means of analogue modelling. We have built four crustal scale analogue models where the deformable crust is translated and rotated around a stationary rigid indenter, while externally driven extension is simulated by allowing the viscous layer to flow in directions parallel and perpendicular to the indenter margins. This allowed a quantitative assessment of the effects of superposed extension on the evolution of a strike-slip dominated deformation zone during indentation.

Previous studies have shown that the indenter geometry controls the style of deformation and that strike-slip at the margin of the indenter is gradually connected to shortening in its frontal part. Our modelling results show that the additional extension with a direction parallel to the strike-slip zone is responsible for opening of a large sedimentary basin behind the indenter, characterised by sub-basins and intra-basinal highs, which are controlled by strain partitioning between the curved strike-slip, transtensional and normal faults. Furthermore, this extension stimulates an increase in the strike-slip faults curvature by connecting them with the basin-controlling normal faults. The extension perpendicular to the strike-slip system distributes deformation away from the indenter, creating a strike-slip system splaying into two zones of transtensional to strike-slip deformation that connect in the south and accommodate additional minor subsidence along N-S oriented transtensional faults. The modelling furthermore shows that bi-modal parallel and perpendicular extension controls the first-order structure and extent (westward and southward) of the subsidence in the basin.

The modelling results infer that the Circum-Moesian Fault System was affected by extensions in different directions driven by the Carpathians and Dinarides slab roll-backs. The extension in the north opened the Getic Depression, partitioned the strike-slip deformation and increased the curvature of the large Cerna and Timok faults and connected them with normal faults. The westward pull of the Dinarides slab added a component of transtensional deformation to the strike-slip system during the indentation by the Moesian Platform and contributed to splaying strike-slip deformation westwards.

Our modelling results demonstrate that the deformation transfer around rigid indenters can be significantly affected by far-field extension involving enhanced subsidence in newly formed basins, distributing deformation over a wider area and increasing in oblique kinematics along differently oriented faults, which create complex strain partitioning patterns.

Chapter 6. Synthesis and concluding remarks

The aim of this thesis is to constrain and better understand the tectonic processes associated with the formation of highly curved orogenic systems and the controlling mechanisms of strain partitioning and deformation transfer during coeval oroclinal bending and indentation. The research presented in the previous chapters combined field geological observations in the area of the Carpatho-Balkanides orocline, part of the larger Alpine-Mediterranean orogenic system, with process-oriented analogue modelling techniques.

The Carpatho-Balkanides orocline formed during the subduction of the Carpathians embayment and coeval indentation by the Moesian Platform. Its Serbian Carpathians segment is composed of the pre-Alpine metamorphic basement overlain by the Permian to Paleogene sedimentary cover and associated magmatism, as well as the sedimentary infill of Neogene intra-montane basins, which record the tectonic evolution and deformation history from the Cretaceous continental collision to the present-day backarc-convex oroclinal geometry connecting the Serbian with the South Carpathians and the Balkanides segments. Therefore, it is an excellent natural laboratory for studying the balance between orogen-building deformation and subsequent oroclinal bending processes. The analogue modelling presented in this thesis demonstrated that the spatial and temporal evolution of deformation in oroclines formed around indenters is often controlled by several overlapping processes associated with different, but coeval, tectonic regimes.

In this final chapter of the thesis, the results shown in the previous chapters will be summarised, combined and discussed in the context of the relevant mechanisms for the coupled oroclinal bending and indentation processes and the Carpatho-Balkanides tectonic evolution. At the end, perspectives for future research will be briefly discussed.

6.1 Interplay of indentation and subduction and kinematics of a backarc-convex oroclinal bending

The formation of a foreland-convex oroclinal geometry observed in many arcuate orogens in the upper plate above a subduction zone is often driven by a slab retreat, which results in opposite rotations of the oroclinal flanks (e.g., Weil and Sussman, 2004; Johnston et al., 2013). The Mediterranean Alpine-age orogens are well-documented examples where a foreland-convex oroclinal bending can be tied to the dynamics of the subduction system (e.g., Rosenbaum, 2014), which is different to the backarc-convex Carpatho-Balkanides orocline.

In this thesis, we demonstrate that a backarc-convex oroclinal formation is controlled by an indenter, which is bending an initially straight orogen (Chapter 2). As such, oroclinal bending occurs by buckling of a straight orogen between two stronger continental fragments, like the Mongolian, Cantabrian or Kazakhstan oroclines (Edel et al., 2014; Pastor-Galán et al, 2015; Li et al., 2018). In other cases, an oroclinal geometry forms progressively, driven by lateral variations of indentation and subduction processes along a zone of plate convergence. In these situations, the indenter may be part of an upper (Fig. 6.1a) or a lower plate (Fig. 6.1b-d), i.e., forms a hinterland or a foreland of a developing orogenic wedge. For instance, the subduction of the European below the

Adriatic plate and the subsequent Adriatic indentation into the European continent created the foreland-convex orocline of the Alps. The opposite situation was observed in the Carpatho-Balkanides Mountains, where the subduction of the Alpine Tethys led to the Moesian indentation. The strong Moesian Platform was in the lower plate position during the collision, which created a unique situation in the Mediterranean orogens, where a backarc-convex orocline formed around the indenter, driven by the slab retreat and pull in the lateral Carpathians subduction zone.

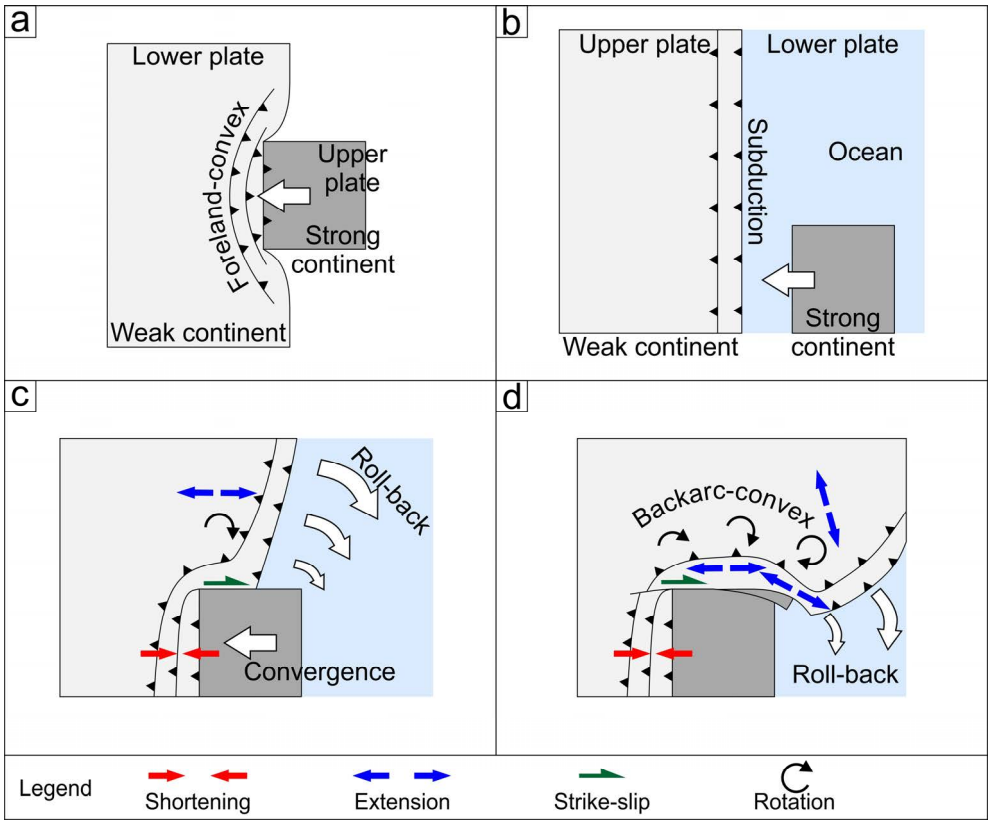

Figure 6.1 - a) Formation of a foreland-convex orocline during indentation when an indenter is located in the upper plate. b-d) Formation of the backarc-convex orocline around an indenter located in the lower plate surrounded by an ocean. b) Early stage before the onset of indentation. The ongoing subduction gradually closes the ocean between a strong and a weak continent with a straight fold-and-thrust belt. c) The collision between the two continents deforms additionally the weaker one. The lateral change from indentation to roll-back of the subducting slab imposes pull on the upper plate (i.e., the weak continent) with higher velocities away from the indenter. This results in the coupled drag along the indenter margin and the orogen-parallel extension in the upper plate. d) Late stage of oroclinal bending around the indenter. The trench retreated behind the strong continent, bending the entire weak upper plate around it and creating the backarc-convex orocline.

During the gradual formation of a backarc-convex orocline, most of the deformation transfer and strain partitioning are controlled by the geometry of the indenter (Chapter 3). Depending on the indenter corners geometry (sharp or curved), transfer of deformation from frontal shortening to strike-slip along the lateral indenter margin may be more abrupt or distributed over a larger area (Chapters 3 and 4). The rotations during oroclinal bending facilitate the opening of transtensional basins on top of large strike-slip faults, while the flow in the lower crust contributes to a more distributed deformation and its gradual transfer around the indenter (Chapter 3). The onset of the slab roll-back (Fig. 6.1c) imposes a pull on the upper plate, which creates a velocity gradient towards the subduction zone and an increase in strike-slip strain rate (Chapter 4). This velocity gradient in the upper plate further results in the orogen-parallel extension, roughly parallel to the strike-slip faults that accommodate increased drag, which may also offset the indenter margin (Fig. 6.1d). With the progress of the slab roll-back and the trench retreat, the upper plate is pulled behind the indenter and a full backarc-convex oroclinal curvature is achieved (Fig. 6.1d). This mechanism creates a large-scale strike-slip fault system in the hinge area of the orocline (Fig. 6.1d), a structural pattern that rarely exists in oroclines formed by different mechanisms. Furthermore, the deformation pattern can be more complex if an extension driven by an external force (e.g., another nearby subduction) overlaps with orocline formation (Chapter 5). In these situations, the deformation around the indenter is partitioned along multiple sub-parallel or splaying transtensional shear zones (Chapters 4 and 5).

6.2 Implications for the tectonic evolution of the Carpatho-Balkanides orocline

A new integrated structural model of the evolution of the backarc-convex southern Carpatho-Balkanides orocline and, in detail, its Serbian Carpathians segment was provided in this thesis (Fig. 6.2). Chapter 2 demonstrates that the orocline was structured during three major tectonic events: the Cretaceous orogen-building shortening, the Paleogene to middle Miocene oroclinal bending, and the late-stage thin-skinned thrusting during the final Carpathians docking against the Moesian Platform in the late Miocene. The Cretaceous thrusting was an orogen-building event associated with the closure of the Ceahlău-Severin branch of the Alpine Tethys Ocean, resulting in the Supragetic-Getic nappes emplacement, which was well documented in other segments of the orocline (e.g., Săndulescu, 1984, 1988; Dallmeyer et al., 1996; Bojar et al., 1998; Willingshofer et al., 1999; Fügenschuh and Schmid, 2005; Iancu et al., 2005a; Neubauer and Bojar, 2013) and further supported by the structural data of this thesis.

This initially relatively straight to slightly curved orogen was subsequently bent around the rigid Moesian Platform in post-Cretaceous times by gradually changing the amount of rotation from >90° in the South Carpathians to 30-40° in the Serbian Carpathians and 0° in the Balkanides (Chapter 1, van Hinsbergen et al., 2008; Panaiotu and Panaiotu, 2010; Lesić et al., 2019). This oroclinal bending resulted in a complex strain partitioning that includes overlapping and coupled strike-slip deformation, thrusting, orogen-parallel and orogen-perpendicular extensions (Chapters 2 and 4). The

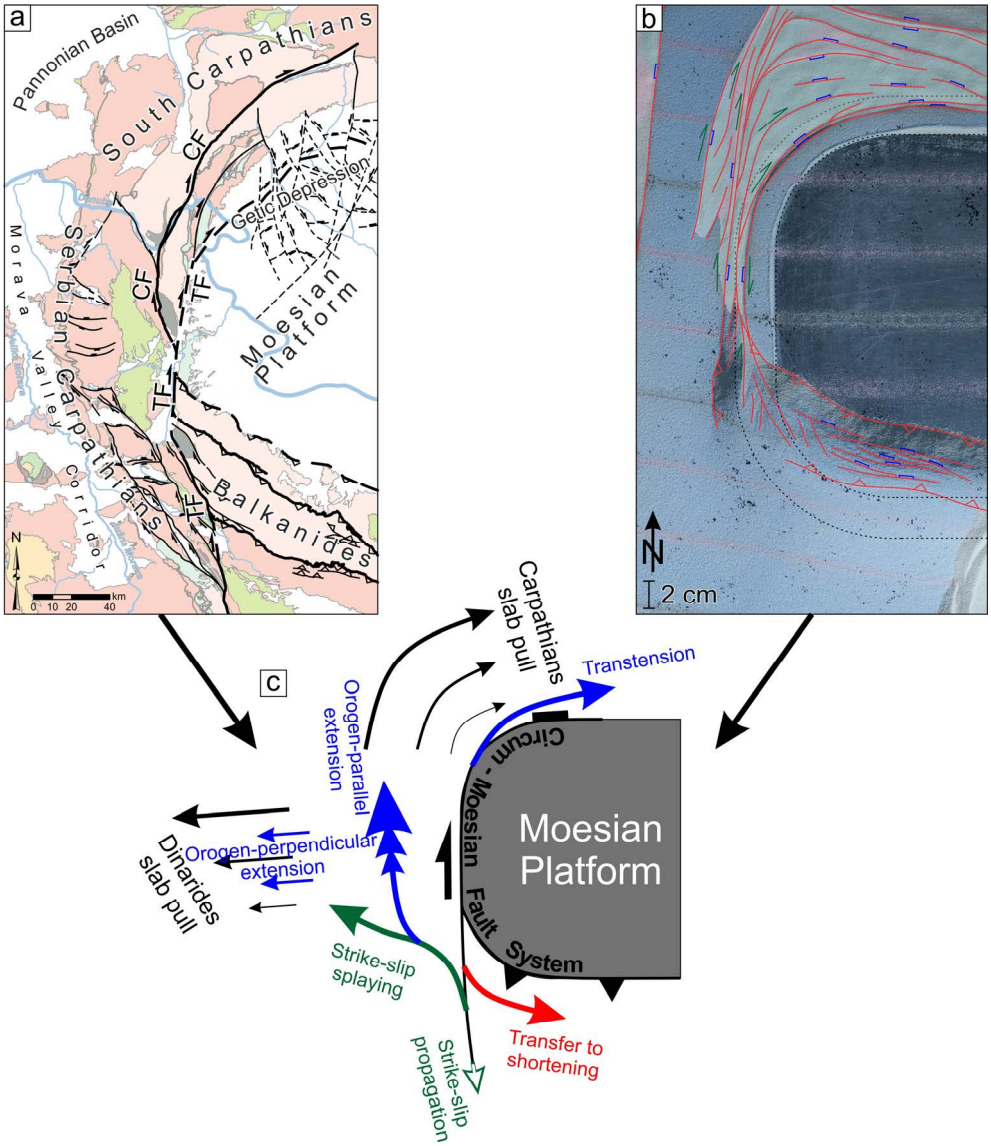

Figure 6.2 - a) Structural map of the Serbian Carpathians and connection with the South Carpathians and the Balkanides based on the results of Chapters 2 and 4. Structure of the Getic Depression is after Răbăgia et al. (2011). Legend is the same as in Fig. 5.2. CF – Cerna Fault; TF - Timok Fault. b) The interpreted final top-view photograph of the model simulating coeval northern and western extensions in Chapter 5. c) Simplified deformation transfer around the Moesian Platform based on the results of this thesis. The Carpathians slab is driving the northward increase in displacements, which results in orogen-parallel extension and facilitates the strike-slip splaying and connection with transtension towards the northeast. Strike-slip faulting propagates southwards while transferring part of its offset towards the shortening in the southeast and splaying towards

the west. This westward splaying and distributing of deformation is likely enhanced by an orogen-perpendicular extension driven by the Dinarides slab.

---

oroclinal bending was driven by the pull of the subducting Carpathians slab and the Moesian Platform indentation, and was accommodated by one of the largest European intra-continental fault systems, the Circum-Moesian Fault system, composed of coeval regional strike-slip, normal and thrust faults (Fig. 6.2). This fault system accommodates ~140 km of dextral offset while connecting deformation around the Moesian Platform, from the South Carpathians in the north to the Balkanides in the south. The variability of deformation partitioning within the orocline was documented by comparing the areas closer to the indenter, in the vicinity of its corners (Chapter 4) and farther away from Moesia, in the convex side of the oroclinal hinge (Chapter 2). The thesis shows that the deformation close to the Moesian margin was mostly localised along the curved, large-offset Cerna and Timok dextral strike-slip faults that link up with transtensional/extensional deformation in the South Carpathians and their foreland to the north. In the south, the strike-slip deformation was transferred eastwards to thrusting in the Balkanides and westwards to coupled strike-slip and orogen-parallel extension (Fig. 6.2). In contrast, the convex side of the oroclinal hinge was affected by the orogen-parallel extension coupled with a very distributed strike-slip deformation that was not localised along large-offset faults because of the greater distance to the strong Moesian indenter. Furthermore, it was affected by a (partially) coeval orogen-perpendicular extension imposed by the Dinarides slab (Fig. 6.2), which facilitated basin formation and strike-slip faults splaying. The hinge area was finally structured during the late Miocene top-E thrusting, which reactivated earlier normal faults. This last deformation phase was driven by the transfer of deformation from the East, South-East and South Carpathians in the final stages of the closure of the Carpathians embayment.

6.3 Future perspectives

This thesis focused on understanding the deformation around rigid indenters and the interaction between different fault orientations and kinematics on the crustal scale. Future studies using analogue and numerical modelling at a larger, lithospheric scale can contribute further to better containing the driving mechanisms of the deformation around indenters, such as the lateral slab roll-back. Such modelling can also test the effects of rheological coupling between the crust and lithospheric mantle or lithospheric flow on deformation transfer around indenters. Furthermore, modelling studies presented in this thesis assumed a rigid indenter. This approximation was necessary to directly observe deformation relative to the indenter. However, indenters are never completely rigid (e.g., Sokoutis et al., 2000; Willingshofer and Cloetingh, 2003; van Gelder et al., 2017) and, depending on their relative strength variation, can exhibit internal deformation during indentation (Sieberer et al., 2021). Future modelling studies may provide insights into the effects of the internal indenter deformation and rheology on the indentation-induced oroclinal bending.

To better constrain the deformation history and the evolution of the Circum-Moesian Fault System, a better understanding of the timing and temporal superposition of large fault zones is required. New syn-kinematic mineral dating within the key shear zones and thermo-chronological studies may further improve our understanding of the large-scale deformation transfer around the Moesian Platform and vertical offsets along the regional faults. In the larger context of the Alpine-Dinarides-Carpathians system, deformation was always driven by an interaction between two large indenters (i.e., Adria and Moesia) and four subduction zones (Alpine, Dinarides, Carpathians and Aegean) that led to the formations of arcuate orogens and orogenic segments often associated with significant rotations and strain partitioning. The results of this thesis demonstrate that a better understanding of the structural evolution of such curved orogens requires a strain partitioning approach and shear-zone analysis, adapted for every specific case, is needed in future regional studies based on geological field observations.

Acknowledgements

"Whilst this planet has gone circling on according to the fixed law of gravity, from so simple a beginning endless forms most beautiful and most wonderful have been, and are being, evolved." – Charles Darwin

Looking back now on the last four years of my life, I realised that this final sentence of Darwin's life's work does not have to apply only to biological species, but in a more conceptual way, to anything that strives to survive, grow and adapt, whether it is a thought, a person, an idea, knowledge, friendship, love or tectonic plates. In this case, from so simple a beginning a student fascinated by the mysteries of the Earth evolved into whatever I am today and this thesis. The journey that took me here, to this moment, was very eventful, intense and wonderful, but it wouldn't be possible without many people I met along the way that helped me evolve both professionally and personally.

First, I would like to thank my promoters Liviu Matenco and Marinko Toljić and co-promoter Ernst Willingshofer for providing me with the opportunity to have such an exciting PhD project.

Liviu, your critical guidance, enthusiasm, strict but fair requirements and challenges you set in front of me and the crucial encouragement and advice you provided made me a better geologist and person. I learned a lot from you, but most significantly to look at what is important process-wise. Thank you for everything. I promise, from now on I will communicate science directly.

Ernst, great thanks for giving me the opportunity to work in the TecLab and for introducing to me one of the most creative methods for studying tectonics. Thank you for all discussions and your excellent and very calm guidance during my modelling studies. That helped me a lot to regain focus and gave me confidence to continue when experiments didn't work as planned.

Marinko, thank you for introducing and recommending me to Liviu and the Tectonics group of Utrecht and for the confidence that I have what it takes to do PhD at Utrecht University. Thank you for all the support and discussions we had over the years. Also, I really appreciate the opportunity I got to work as a teaching assistant at the Chair of Dynamic Geology at the University of Belgrade.

I would like to thank the members of the reading committee: Prof. Michele Cooke, Prof. Djordje Grujic, Prof. Magdalena Scheck-Wenderoth, Prof. Guido Schreurs and Prof. Kamil Ustaszewski. Thank you for the time and effort you put into reading and evaluating my thesis.

My PhD research had significant benefits from collaboration with several people. Uroš, I want to thank you for all discussions, support and advice you gave me, especially during tough periods of my PhD life. You helped me see things more realistically. Also, I will always be grateful for the good times we had in the office and during fieldwork. Oleg, I really appreciate our discussions on the ages of numerous basins in the Carpatho-Balkanides, which became one of the key time constraints in this thesis. Taco, thank you for developing a novel and highly useful methodology to analyse deformation in analogue models. Your code has a very nice potential for future generations and I enjoyed working with you on its development.

When I first arrived in Utrecht, everything was new to me, and it took some time on getting used to the new country, new city, new university, new system. Great thanks to Attila, Nevena and Jon for helping me make my first steps in Utrecht and Utrecht

University, and especially, for introducing me to the Tectonics climbing group and the concept of the one last refreshment drink. It was great fun. Additionally, I want to thank Jon and Fred for translating my thesis summary to Dutch, I highly appreciate it.

Dear Tectos: Sierd, Fred, Ylona, Jan-Diederik, Fadi, Lukman, Fauzi, István, Jasper, Sjaak, Vince, Anna-Katharina, Vedad, Damien, Anouk, Noortje, Magdala, Manfred, Jeroen, Inge, Daan, Meng, Mohsen, thank you for creating a very positive working environment in the Tectonics group of Utrecht University and discussions that were always stimulating, productive and supportive, but also for great fun and nice time during coffee breaks. I will always have very fond memories of my time in Utrecht.

It was my pleasure to work in the TecLab. The great time I had there was thanks to the exceptional support and company of Job, Mike, Antoine, Taco, Pavlos and Dimitrios. Dimitrios, I really enjoyed spending time in the lab with you and having discussions on various topics about our beautiful Balkan Peninsula.

My time in Utrecht, both in and outside the office was much better because of the great company of Antoine, Kristóf, Eszter, Tracy, Simon, Jon and Marije. Thank you my friends for the wonderful time we had together and invaluable support during difficult periods. I also want to thank my paranymphs, Antoine and Kristóf, for being such great colleagues, office mates and friends.

In Utrecht, it is usually very difficult to find accommodation, especially if one is not staying long term. During my visits, I wasn't homeless thanks to Sacha, Simon and Antoine. I'll be indebted to you forever. Also, thank you, Tal, Puff, Benga and Coco for being great housemates.

Džoni, my dear friend and the fiercest pool opponent in the Netherlands, thank you for all the support, encouraging talks, walks, drinks, parties, sightseeing, pool games, helping me see the North Sea and for bringing a bit of Belgrade spirit to the Netherlands. Also a big thanks to all my friends in Belgrade for a great time we had for many years and thank you for pulling me and my thoughts away from work when I needed that.

During the times I was in Belgrade, I had great support and a nice working environment thanks to the members of the Chair of Dynamic Geology: Prof. Trivić, Uroš, Tamara, Nenad, Maja, Nikola and Dušan. Thank you for all discussions, coffees, laughs and the work we did together in teaching. Also, I want to thank all the other colleagues in Belgrade that I worked with throughout the last few years.

My field research took me to some wonderful and, sometimes, quite remote parts of the Carpatho-Balkanides Mountains. During the fieldwork, I had a lot of help and great company from Miloš, Timi and Nenad, for which I am very grateful.

Joana, I have a very special thanks for you and your immense support, which meant a lot to me. Nothing in the last years would be the same without you.

Finally, my dear family. Мама, бако и Тими, хвала вам за сву подршку и љубав овог света, и када сте се слагали и када нисте са мојим изборима. Ви сте моја највећа снага и вечно ћу вам бити захвалан.

References

Allen, M.B., Ghassemi, M.R., Shahrabi, M., Qorashi, M., 2003. Accommodation of late Cenozoic oblique shortening in the Alborz range, northern Iran. Journal of Structural Geology 25, 659–672.

Anđelković, J., Krstić, B., Bogdanović, P., Jadranin, D., Milenković, P., Milošaković, R., Urošević, D., Dimitrijević, D., Dolić, D., Rakić, M.O., Jovanović, Lj., Maslarević, Lj., Marković, B., Divljan, M., Đorđević, M., 1977. Explanatory book for sheets Pirot and Breznik, Basic geological map of SFRY 1:100.000. Savezni geološki zavod, Belgrade.

Anderson, D.L., 1971. The San Andreas fault. Scientific American 225 (5), 52-68.

Andrić, N., Sant, K., Matenco, L., Mandic, O., Tomljenović, B., Pavelić, B., Hrvatović, H., Demir, V., Ooms, J., 2017. The link between tectonics and sedimentation in asymmetric extensional basins: Inferences from the study of the Sarajevo–Zenica Basin. Marine and Petroleum Geology 83, 305–332.

Andrić, N., Vogt, K., Matenco, L., Cvetković, V., Cloetingh, S., Gerya, T., 2018. Variability of orogenic magmatism during Mediterranean-style continental collisions: A numerical modelling approach. Gondwana Research 56, 119–134.

Angelier, J., 1979. Determination of the mean principal directions of stresses for a given fault population. Tectonophysics 56, T17–T26.

Angelier, J., 1989. From orientation to magnitudes in paleostress determinations using fault slip data. Journal of Structural Geology 11 (1/2), 37–50.

Angelier, J., 1994. Fault slip analysis and paleostress reconstruction., in Hancock, P.L. (Ed.), Continental Deformation. Pergamon Press, Oxford, New York, Seoul, Tokyo, pp. 53–100.

Angelier, J., Mechler, P., 1977. Sur une méthode graphique de recherche des constraintes principales également utilisable en tectonique et en seismoligie: la méthode des dièdres droits. Bulletin de la Société Géologique de France 7 (19), 1309-1318.

Angelier, J., Goguel, J., 1979. Sur une méthode simple de détermination des axes principaux des constraintes pour une population de failles. Comptes rendus de l'Académie des Sciences, sér. D 288, 307–310.

Antić, M.D., Kounov, A., Trivić, B., Wetzel, A., Peytcheva, I., von Quadt, A., 2016a. Alpine thermal events in the central Serbo–Macedonian Massif (southeastern Serbia). International Journal of Earth Sciences 105, 1485–1505.

Antić, M., Peytcheva, I., von Quadt, A., Kounov, A., Trivić, B., Serafimovski, T., Tasev, G., Gerdjikov, I., Wetzel, A., 2016b. Pre-Alpine evolution of a segment of the North-Gondwanan margin: Geochronological and geochemical evidence from the central Serbo–Macedonian Massif. Gondwana Research 36, 523–544.

Antonijević, I., Veselinović, M., Đorđević, M., Kalenić, M., Krstić, B., Karajičić, Lj., 1970. Explanatory book for sheet Žagubica, Basic geological map of SFRY 1:100.000. Savezni geološki zavod, Belgrade.

Aramijo, R., Meyer, B., Hubert, A., Barka, A., 1999. Westward propagation of the North Anatolian fault into the northern Aegean: timing and kinematics. Geology 27, 267–270.

Argand, E., 1924. La tectonique de l'Asie. In: Conférence faite á Bruxelles., le 10 août 1922. Congrès géologique international (XIIIe session)- Belgique, Jun 1922, Belgique, 171-372.

Authemayou, C., Chardon, D., Bellier, O., Malekzadeh, Z., Shabanian, E., Abbassi, M.R., 2006. Late Cenozoic partitioning of oblique plate convergence in the Zagros fold-and-thrust belt (Iran). Tectonics 25, TC3002. doi:10.1029/2005TC001860

Bada, G., Horváth, F., Dövényi, P., Szafián, P., Windhoffer, G., Cloetingh, S., 2007. Present-day stress field and tectonic inversion in the Pannonian basin. Global and Planetary Change 58, 165–180.

Balázs, A., Matenco, L., Magyar, I., Horváth, F., Cloetingh, S., 2016. The link between tectonics and sedimentation in back-arc basins: New genetic constraints from the analysis of the Pannonian Basin. Tectonics 35, 1526–1559.

Balázs, A., Magyar, I., Matenco, L., Sztanó, O., Tőkés, L., Horváth, F., 2018. Morphology of a large paleo-lake: Analysis of compaction in the Miocene–Quaternary Pannonian Basin. Global and Planetary Change 171, 134-147.

Balla, Z. 1984: The Carpathian loop and the Pannonian Basin: a kinematic analysis. Geophysical Transactions 30/4, 313–353.

Balla, Z., 1987. Tertiary palaeomagnetic data for the Carpatho–Pannonian region in the light of Miocene rotation kinematics. Tectonophysics 139, 67–98.

Balla, Z. 1986: Paleotectonic reconstruction of the Central Alpine-Mediterranean belt for the Neogene. Tectonophysics 127, 213–243.

Balla, Z. 1988: On the Origin of the structural pattern of Hungary. Acta Geologica Hungarica 31/1-2, 53–63.

Banješević, M., 2006. Upper Cretaceous magmatism of the Timok Magmatic Complex. PhD Thesis, University of Belgrade, Belgrade. (in Serbian).

Basile, C., Brun, J.P., 1999. Transtensional faulting patterns ranging from pull-apart basin to transform continental margins: an experimental investigation. Journal of Structural Geology 21, 23–37.

Benesh, N.P., Plesch, A., Shaw, J.H., 2014. Geometry, kinematics, and displacement characteristics of tear-fault systems: An example from the deep-water Niger Delta. AAPG Bulletin 98/3, 465–482.

Bennett, R.A., Hreinsdóttir, S., Buble, G., Bašić, T., Bačić, Ž., Marjanović, M., Casale, G., Gendaszek, A., Cowan, D., 2008. Eocene to present subduction of southern Adria mantle lithosphere beneath the Dinarides. Geology 36 (1), 3–6.

Berryman, K.R., Beanland, S., Cooper, S., Cutten, H., Norris, R., Wood, P., 1992. The Alpien fault, New Zealand: variation in Quaternary structural style and geomorphic expression. Annalae Tectonicae 6, 126–163.

Berza, T., Kräutner, H.G., Dimitrescu, R., 1983. Nappe structure of the Danubian window of the central South Carpathians. An Inst. Geol. Geofiz. 60, 31–34.

Berza, T., Drăgănescu, A., 1988. The Cerna–Jiu fault system (South Carpathians, Romania), a major Tertiary transcurrent lineament. DS Inst. Geol. Geofiz. 72–73, 43–57.

Berza, T., Constantinescu, E., Vlad, S.N., 1998. Upper Cretaceous marmatic series and associated mineralisation in the Carpathian–Balkan orogen. Resour. Geol. 48 (4), 291–306.

Bogdanović, P., Rakić, M., 1980. Explanatory book for sheets Donji Milanovac, Oršova, Baja de Arama and Turnu Severin, Basic geological map of SFRY 1:100.000. Savezni geološki zavod, Belgrade.

Bojar, A.-V., Neubauer, F., Fritz, H., 1998. Cretaceous to Cenozoic thermal evolution of the southwestern South Carpathians: evidence from fission-track thermochronology. Tectonophysics 297, 229–249.

Bokelmann, G., Rodler, F.-A., 2014. Nature of the Vrancea seismic zone (Eastern Carpathians) – new constraints from dispersion of first-arriving P-waves. Earth and Planetary Science Letters 390, 59–68.

Bonini, M., Sokoutis, D., Mulugeta, G., Kantrivanos, E., 2000. Modelling hanging wall accommodation above rigid thrust ramps. Journal of Structural Geology 22, 1165–1179.

Boutelier, D., Schrank, C., Regenauer-Lieb, K., 2019. 2-D finite displacements and strain from particle imaging velocimetry (PIV) analysis of tectonic analogue models with TecPIV. Solid Earth 10 (4), 1123–1139.

Broerse, T. 2021. tacobroerse/strainmap: v1.0. Zenodo. https://doi.org/10.5281/zenodo.4529475

Broerse, T., Norder, B., Govers, R., Sokoutis, D., Willingshofer, E., Picken, S. J., 2019. New analogue materials for nonlinear lithosphere rheology, with an application to slab break-off. Tectonophysics 756, 73–96.

Broerse, T., Krstekanić, N., Kasbergen, C., Willingshofer, E., 2021. Mapping and classifying large deformation from digital imagery: application to analogue models of lithosphere deformation. Geophysical Journal International 226, 984–1017.

Brun, J-P., 2002. Deformation of the continental lithosphere: Insights from brittle-ductile models. Geological Society, London, Special Publications 200, 355–370.

Brun, J-P., Fort, X., 2004. Compressional salt tectonics (Angolan margin). Tectonophysics 382, 129–150.

Brun, J-P., Fort, X., 2011. Salt tectonics at passive margins: Geology versus models. Marine and Petroleum Geology 28, 1123–1145.

Brun, J.-P., Sokoutis, D., 2007. Kinematics of the Southern Rhodope Core Complex (North Greece). Int J Earth Sci (Geol Rundsch) 96, 1079–1099.

Brun, J.-P., Faccenna, C., Gueydan, F., Sokoutis, D., Philippon, M., Kydonakis, K., Gorini, C., 2016. The two-stage Aegean extension, from localized to distributed, a result of slab rollback acceleration. Canadian Journal of Earth Sciences 53 (11), 1142–1157. https://doi-org.proxy.library.uu.nl/10.1139/cjes-2015-0203

Burchfiel, B.C., Nakov, R., 2015. The multiply deformed foreland fold-thrust belt of the Balkan orogen, northern Bulgaria. Geosphere 11 (2), 463–490.

Burke, K., Sengör, C., 1986. Tectonic escape in the evolution of the continental crust, in: Barazangi, M., Brown, L., (Eds.), Reflection Seismology: The Continental Crust (vol. 14). American Geophysical Union, pp. 41–53.

Calignano, E., Sokoutis, D., Willingshofer, E., Brun, J.-P., Gueydan, F., Cloething, S., 2017. Oblique contractional reactivation of inherited heterogeneities: Cause for arcuate orogens. Tectonics 36, 542–558.

Carey, S.W., 1955. The orocline concept in geotectonics. Papers and Proceedings of the Royal Society of Tasmania 89, 255–288.

Carreras, J., Cosgrove, J.W., Druguet, E., 2013. Strain partitioning in banded and/or anisotropic rocks: Implications for inferring tectonic regimes. Journal of Structural Geology 50, 7–21.

Casas, A.M., Gapais, D., Nalpas, T., Besnard, K., Román-Berdiel, T., 2001. Analogue models of transpressive systems. Journal of Structural Geology 23, 733–743.

Célérier, B., Etchecopar, A., Bergerat, F., Vergely, P., Arthaud, F., Laurent, P., 2012. Inferring stress from faulting: From early concepts to inverse methods. Tectonophysics 581, 206–219.

Cembrano, J., González, G., Arancibia, G., Ahumada. I., Olivares, V., Herrera, V., 2005. Fault zone development and strain partitioning in an extensional strike-slip duplex: A case study from the Mesozoic Atacama fault system, Northern Chile. Tectonophysics 400, 105–125.

Chemenda, A.I., Cavalié, O., Vergnolle, M., Boissou, S., Delouis, B., 2016. Numerical model formation of a 3-D strike-slip fault system. Comptes Rendus Geoscience 348, 61–69.

Chen, Z., Burchfiel, B.C., Liu, Y., King, R.W., Royden, L.H., Tang, W., Wang, E., Zhao, J., Zhang, X., 2000. Global Positioning System measurements from eastern Tibet and their implications for India/Eurasia intercontinental deformation. Journal of Geophysical Research 105 (B7), 16215–16227.

Christie-Blick, N., Biddle, K.T., 1985. Deformation and basin formation along strike-slip faults, in: Biddle, K.T., Christie-Blick, N. (Eds.), Strike-Slip Deformation, Basin Formation, and Sedimentation. SEPM Spec. Publ. (No. 37). Society of Economic Paleontologists and Mineralogists, Tulsa, OK, pp. 1–34.

Cifelli, F., Mattei, M., Della Seta, M., 2008. Calabrian Arc oroclinal bending: The role of subduction. Tectonics 27, TC5001. doi:10.1029/2008TC002272

Ciulavu, M., Ferreiro Mählmann, R., Schmid, S.M., Hofmann, H., Seghedi, A., Frey, M., 2008. Metamorphic evolution of a very low- to low-grade metamorphic core complex (Danubian window) in the South Carpathians, in: Siegesmund, S., Fügenschuh, B., Froitzheim, N. (Eds.), Tectonic Aspects of the Alpine-Dinaride-Carpathian System. Geological Society, London, Special Publications 298, 281–315.

Cobbold, P.R., Szatmari, P., 1991. Radial gravitational gliding on passive margins. Tectonophysics 188, 249–289.

Codrea, V.A., 2001. Badenian insectivores from Bozovici Basin (Southern Carpathians, Caraş-Severin district). Acta Paleontologica Romaniae V (3), 67–75.

Costa, E., Speranza, F., 2003. Paleomagnetic analysis of curved thrust belts reproduced by physical models. Journal of Geodynamics 36, 633–654.

Crespo-Blanc, A., González-Sánchez, A., 2005. Influence of indenter geometry on arcuate fold-and-thrust wedge: preliminary results of analogue modelling. Geogaceta 37, 11–14.

Csontos, L., 1995. Cenozoic tectonic evolution of the Intra-Carpathian area: a review. Acta Vulcanologica 7, 1 –13.

Csontos, L., Vörös, A., 2004. Mesozoic plate tectonic reconstruction of the Carpathian region. Palaeogeography, Palaeoclimatology, Palaeoecology 210, 1–56.

Csontos, L., Nagymarosy, A., Horváth, F., Kovác, M., 1992. Tertiary evolution of the Intra-Carpathian area: a model. Tectonophysics 208, 221–241.

Cullen, A.B., 2010. Transverse segmentationof the Baram-Balabac Basin. NW Borneo: refining the model of Borneo's tectonic evolution. Petroleum Geoscience 16, 3–29.

Dahlen, F., Suppe, J., Davis, D., 1984. Mechanics of fold-and-thrust belts and accretionary wedges: Cohesive Coulomb theory. Journal of Geophysical Research 89 (B12), 10087–10101.

Dallmeyer, R.D., Neubauer, F., Handler, R., Fritz, H., Müller, W., Pana, D., Putis, M., 1996. Tectonothermal evolution of the internal Alps and Carpathians: evidence from 40Ar/39Ar mineral and whole-rock data. Eclogae Geol. Helv. 89/1, 203–227.

Dallmeyer, R.D., Neubauer, F., Fritz, H. & Mocanu, V., 1998. Variscan vs. Alpine tectonothermal evolution of the South Carpathian orogen: constraints from 40Ar/39Ar ages. Tectonophysics 290, 111–135.

Davis, D., Suppe, J., Dahlen, F.A., 1983. Mechanics of fold-and-thrust belts and accretionary wedges. Journal of Geophysical Research 88 (B2), 1153–1172.

Davy, P., Cobbold, P.R., 1988. Indentation tectonics in nature and experiment, 1. Experiments scaled for gravity. Bull. Geol. Inst. Univ. Uppsala, N.S., 14: 129-141.

Davy, P., Cobbold, P.R., 1991. Experiments on shortening of a 4-layer model of the continental lithosphere. Tectonophysics 188, 1–25.

de Bruijn, H., Marković, Z., Wessels, W., Milivojević, M., van de Weerd A.A., 2018. Rodent faunas from the Paleogene of south-east Serbia. Palaeobiodiversity and Palaeoenvironments 98 (3), 441–458.

de Leeuw, A., Filipescu, S., Maţenco, L., Krijgsman, W., Kuiper, K., Stoica, M., 2013. Paleomagnetic and chronostratigraphic constraints on the Middle to Late Miocene evolution of the Transylvanian Basin (Romania): Implications for Central Paratethys stratigraphy and emplacement of the Tisza–Dacia plate. Global and Planetary Change 103, 82–98.

De Vicente, G., Regas, R., Muñoz-Martín, A., Van Wees, J.D., Casas-Sáinz, A., Sopeña, A., Sánchez-Moya, P., Arche, A., López-Gómez, J., Oláiz, A., Fernandez Lozano, J., 2009. Oblique strain partitioning and transpression on an inverted rift: The Castilian Branch of the Iberian Chain. Tectonophysics 470, 224–242.

Del Castello, M., Pini, G.A., McClay, K.R., 2004. Effect of unbalanced topography and overloading on Coulomb wedge kinematics: Insights from sandbox modeling. Journal of Geophysical Research 109, B05405, doi:10.1029/2003JB002709.

D'el-Rey Silva, L.J.H., de Oliveira, Í.L., Pohren, C.B., Tanizaki, M.L.N., Carneiro, R.C., Fernandes, G.L. de F., Aragão, P.E., 2011. Coeval perpendicular shortenings in the Brasília belt: Collision of irregular plate margins leading to oroclinal bending in the Neoproterozoic of central Brazil. Journal of South American Earth Sciences 32, 1–13.

Delvaux, D., Sperner, B., 2003. New aspects of tectonic stress inversion with reference to the TENSOR program, in: Nieuwland, D.A. (Ed.), New Insights into Structural Interpretation and Modelling, Special Publications 212. Geological Society, London, pp. 75-100.

Dewey, J.F., 1980. Episodicity, sequence and style at convergent plate boundaries, in: Strangway, D.W., (Ed.), The Continental Crust and Its Mineral Deposits. Geol. Assoc. Canada, Waterloo, Ontario, pp. 553–573.

Dewey, J.F., Bird, J.M., 1970. Mountain belts and the new global tectonics. Journal of Geophysical Research 75 (14), 2625–2647.

Dewey, J.F., Holdsworth, R.E., Strachan, R.A., 1998. Transpression and transtension zones, in: Holdsworth, R.E., Strachan R.A., Dewey J.E. (Eds.), Continental Transpressional and Transtensional Tectonics, Special Publications 135. Geological Society, London, pp. 1–14.

Dimitrijevic, M.D. (Ed.), 1994. Geological atlas of Serbia 1:2.000.000. Seismotectonic and seismological map. Republical Foundation for Geological Investigations and Geological Institute GEMINI, Belgrade, 1994.

Dimitrijević, M.D., 1997. Geology of Yugoslavia. Geological Institute, Belgrade.

Djordjević-Milutinović, D., 2010. An overview of Paleozoic and Mesozoic sites with macroflora in Serbia. Bulletin of the Natural History Museum, 3, 27–46.

Djurović, P. & Živković, N. 2013. Morphological and hydrological characteristics of the Serbian border zone towards Bulgaria. Glasnik Srpskog geografskog društva 93/4, 51-69.

Doblas, M., 1998. Slickenside kinematic indicators. Tectonophysics, 295, 187–197.

Doglioni, C., Carminati, E., Cuffaro, M., Scrocca, D., 2007. Subduction kinematics and dynamic constraints. Earth-Science Reviews 83, 125–175.

Dooley, T.P., Schreurs, G., 2012. Analogue modelling of intraplate strike-slip tectonics: A review and new experimental results. Tectonophysics 574–575, 1–71.

Duarte, J.C., Rosas, F.M., Terrinha, P., Gutscher, M-A., Malavieille, J., Silva, S., Matias, L., 2011. Thrust–wrench interference tectonics in the Gulf of Cadiz (Africa–Iberia plate boundary in the North–East Atlantic): Insights from analog models. Marine Geology 289, 135–149.

Dufréchou, G., Odonne, F., Viola, G., 2011. Analogue models of second-order faults genetically linked to a circular strike-slip system. Journal of Structural Geology 33, 1193–1205.

Dupont-Nivet, G., Vasiliev, I., Langereis, C.G., Krijgsman, W., Panaiotu, C., 2005. Neogene tectonic evolution of the southern and eastern Carpathians constrained by paleomagnetism. Earth and Planetary Science Letters 236, 374–387.

Edel, J.B., Schulmann, K., Hanžl, P., Lexa, O., 2014. Palaeomagnetic and structural constraints on 90° anticlockwise rotation in SW Mongolia during the Permo–Triassic: Implications for Altaid oroclinal bending. Preliminary palaeomagnetic results. Journal of Asian Earth Sciences 94, 157–171.

Ellouz, N., Roure, F., Săndulescu, M., Badescu, D., 1994. Balanced cross sections in the Eastern Carpathians (Romania): a tool to quantify Neogene dynamics, in: Roure, F., Ellouz, N., Shein, V.S., Skvortsov, I. (Eds.), Geodynamic evolution of sedimentary basins, International symposium Moskow 1992 Proceedings. Technip, Paris, 305–325.

Erak, D., Matenco, L., Toljić, M., Stojadinović, U., Andriessen, P.A.M., Willingshofer, E., Ducea, M.N., 2017. From nappe stacking to extensional detachments at the contact between the Carpathians and Dinarides – The Jastrebac Mountains of Central Serbia. Tectonophysics 710–711, 162–183.

Faccenna, C., Davy, P., Brun, J.-P., Funiciello, R., Giardini, D., Mattei, M., Nalpas, T., 1996. The dynamics of back-arc extension: an experimental approach to the opening of the Tyrrhenian Sea. Geophysical Journal International 126, 781–795.

Faccenna, C., Piromallo, C., Crespo-Blanc, A., Jolivet, L., Rossetti, F., 2004. Lateral slab deformation and the origin of the western Mediterranean arcs. Tectonics 23, TC1012. DOI: 10.1029/2002TC001488

Faccenna, C., Becker, T.W., Auer, L., Billi, A., Boschi, L., Brun, J.P., Capitanio, F.A., Funiciello, F., Horvàth, F., Jolivet, L., Piromallo, C., Royden, L., Rossetti, F., Serpelloni, E., 2014. Mantle dynamics in the Mediterranean. Reviews of Geophysics 52, 283–332.

Farangitakis, G.-P., Sokoutis, D., McCaffrey, K.J.W., Willingshofer, E., Kalnins, L.M., Phethean, J.J.J., van Hunen, J., van Steen, V., 2019. Analogue Modeling of Plate Rotation Effects in Transform Margins and Rift-Transform Intersections. Tectonics 38, 823–841.

Farangitakis, G-P., McCaffrey, K.J., Willingshofer, E., Allen, M.B., Kalnins, L.M., van Hunen, J., Persaud, P., Sokoutis, D., 2021. The structural evolution of pull-apart basins in response to changes in plate motion. Basin Research 33 (2): 1603–1625. https://doi.org/10.1111/bre.12528

Farr, T.G., Rosen, P.A., Caro, E., Crippen, R., Duren, R., Hensley, S., Kobrick, M., Paller, M., Rodriguez, E., Roth, L., Seal, D., Shaffer, S., Shimada, J., Umland, J., Werner, M., Oskin, M., Burbank, D., Alsdorf, D., 2007. The shuttle radar topography mission. Reviews of Geophysics 45 (2), RG2004. doi:10.1029/2005RG000183.

Fedorik, J., Zwaan, F., Schreurs, G., Toscani, G., Bonini, L., Seno, S., 2019., The interaction between strike-slip dominated fault zones and thrust belt structures: Insights from 4D analogue models. Journal of Structural Geology 122, 89–105.

Finley, T., Morell, K., Leonard, L., Regalla, C., Johnston, S.T., Zhang, W., 2019. Ongoing oroclinal bending in the Cascadia forearc and its relation to concave-outboard plate margin geometry. Geology 47, 155–158.

Fitch, T.J., 1972. Plate convergence, transcurrent faults, and internal deformation adjacent to Southeast Asia and the western Pacific. Journal of Geophysical Research 77 (23), 4432– 4460.

Fodor, L., Bada, G., Csillag, G., Horváth, E., Ruszkiczay-Rüdiger, Z., Palotás, K., Síkhegyi, F., Timár, G., Cloetingh, S., Horváth, F., 2005. An outline of neotectonic structures and morphotectonics of the western and central Pannonian Basin. Tectonophysics, 410, 15–41.

Fossen, H., Tikoff, B., 1998. Extended models of transpression and transtension, and application to tectonic settings, in: Holdsworth, R.E., Strachan R.A., Dewey J.E. (Eds.), Continental Transpressional and Transtensional Tectonics, Special Publications 135. Geological Society, London, pp. 15–33.

Fossen, H., Tikoff, G., Teyssier, C., 1994. Strain modeling of transpressional and transtensional deformation. Norsk Geologisk Tidsskrift 74, 134–145.

Frisch, W., Kuhlemann, J., Dunkl, I., Brügel, A., 1998. Palinspastic reconstruction and topographic evolution of the Eastern Alps during late Tertiary tectonic extrusion. Tectonophysics 297, 1–15.

Fügenschuh, B., Schmid, S.M., 2005. Age and significance of core complex formation in a very curved orogen: Evidence from fission track studies in the South Carpathians (Romania). Tectonophysics 404, 33–53.

Gallhofer, D., von Quadt, A., Peytcheva, I., Schmid, S.M., Heinrich., C.A., 2015. Tectonic, magmatic, and metallogenic evolution of the Late Cretaceous arc in the Carpathian–Balkan orogen. Tectonics 34, 1813–1836.

Glen, J.M.G., 2004. A kinematic model for the southern Alaska orocline based on regional fault patterns, in: Sussman, A.J., Weil A.B. (Eds.), Orogenic Curvature: Integrating Paleomagnetic and Structural Analyses: Geological Society of America Special Paper 383. Geological Society of America, Boulder, CO, pp. 161–172.

González, D., Pinto, L., Peña, M., Arriagada, C., 2012. 3D deformation in strike-slip systems: Analogue modelling and num erical restoration. Andean Geology 39 (2), 295–316.

Govers, R., Wortel, M.J.R., 2005. Lithosphere tearing at STEP faults: Response to edges of subduction zones. Earth and Planetary Science Letters 236, 505–523.

Grădinaru, M., Lazar, I., Bucur, I.I., Grădinaru, E., Săsăran, E., Ducea, M.N., Andrăşanu et al., 2016. The Valanginian history of the eastern part of the Getic Carbonate Platform (Southern Carpathians, Romania): Evidence for emergence and drowning of the platform. Cretaceous Research 66, 11–42.

Gutiérrez-Alonso, G., Collins, A.S., Fernández-Suárez, J., Pastor-Galán, D., González-Clavijo, E., Jourdan, F., Weil, A.B., Johnston, S.T., 2015. Dating of lithospheric buckling: 40Ar/39Ar ages of syn-orocline strike-slip shear zones in northwestern Iberia. Tectonophysics 643, 44-54.

Hatem, A.E., Cooke, M.L., Toeneboehn, K., 2017. Strain localization and evolving kinematic efficiency of initiating strike-slip faults within wet kaolin experiments. Journal of Structural Geology 101, 96–108.

Henry, B., Naydenov, K., Dimov, D., Jordanova, D., Jordanova, N., 2012. Relations between the emplacement and fabric-forming conditions of the Kapitan-Dimitrievo pluton and the Maritsa shear zone (Central Bulgaria): magnetic and visible fabrics analysis. Int. J. Earth Sci. 101, 747–759.

Hippolyte, J.-C., Badescu, D., Constantin, P., 1999. Evolution of the transport direction of the Carpathian belt during its collision with the east European Platform. Tectonics 18, 6, 1120–1138.

Hippolyte, J.-C., Bergerat, F., Gordon, M.B., Bellier, O., Espurt, N., 2012. Keys and pitfalls in mesoscale fault analysis and paleostress reconstructions, the use of Angelier's methods. Tectonophysics 581, 144–162.

Hír, J., Venczel, M., Codrea, V., Angelone, C., van den Hoek Otende, L.W., Kirscher, U., Prieto, J., 2016. Badenian and Sarmatian s.str. from the Carpathian area: Overview and ongoing research on Hungarian and Romanian small vertebrate evolution. Comptes Rendus Palevol 15, 863–875.

Hirth, G., Teyssier, C., Dunlap, W.J., 2001. An evaluation of quartzite flow laws based on comparisons between experimentally and naturally deformed rocks. Int. J. Earth Sci. 90 (1),77–87.

Hollingsworth, J., Fattahi, M., Walker, R., Talebian, M., Bahroudi, A., Bolourchi, M. J., Jackson, J., Copley, A., 2010. Oroclinal bending, distributed thrust and strike-slip

faulting, and the accommodation of Arabia–Eurasia convergence in NE Iran since the Oligocene. Geophysical Journal International 181, 1214–1246.

Horváth, F., Bada, G., Szafián, P., Tari, G., Ádám, A., Cloetingh, S., 2006. Formation and deformation of the Pannonian Basin: Constraints from observational data. Geological Society of London Memoirs 32, 191–206.

Horváth, F., Musitz, B., Balázs, A., Végh, A., Uhrin, A., Nádor, A., Koroknai, B., Pap, N., Tóth, T., Wórum, G., 2015. Evolution of the Pannonian basin and its geothermal resources. Geothermics 53, 328–352.

Hubbert, M.K., 1937. Theory of scale models as applied to the study of geologic structures. GSA Bulletin 48 (10), 1459–1520.

Iancu, V., Berza, T., Seghedi, A., Gheuca, I., Hann, H-P., 2005a. Alpine polyphase tectono-metamorphic evolution of the South Carpathians: A new overview. Tectonophysics 410, 337–365.

Iancu, V., Berza, T., Seghedi, A., Marunţiu, M., 2005b. Paleozoic rock assemblages incorporated in the South Carpathian Alpine thrust belt (Romania and Serbia): A review. Geologica Belgica 8 (4), 48–68.

Isacks, B.L., 1988. Uplift of the Central Andean Plateau and Bending of the Bolivian Orocline. Journal of Geophysical Research 93, 3211–3231.

Iturrieta. P.C., Hurtado, D.E., Cembrano, J., Stanton-Yonge, A., 2017. States of stress and slip partitioning in a continental scale strike-slip duplex: Tectonic and magmatic implications by means of finite element modelling. Earth and Planetary Science Letters 473, 71–82.

Ivanov, Ž., 1988. Apercu general sur l`evolution geologique et structurale du massif des Rhodopes dans le cadre des Balkanides. Bulletin de la Societe Geologique de France, 4, 227–240.

Jiménez-Bonilla, A., Crespo-Blanc A., Balanyá, J.C., Expósito, I., Díaz-Azpiroz, M., 2020. Analog Models of Fold-and-Thrust Wedges in Progressive Arcs: A Comparison With the Gibraltar Arc External Wedge. Frontiers in Earth Science 8, 72. doi: 10.3389/feart.2020.00072

Johnson, M.R.W., 2002. Shortening budgets and the role of continental subduction during the India–Asia collision. Earth-Science Reviews 59, 101–123.

Johnston, S.T., Mazzoli, S., 2009. The Calabrian Orocline: buckling of a previously more linear orogen, in: Murphy, J.B., Keppie, J.D., Hynes, A.J. (Eds.), Ancient Orogens and Modern Analogues, Geological Society Special Publications 327. The Geological Society of London, London, pp. 113–125.

Johnston, S.T., Weil, A.B., Gutiérrez-Alonso, G., 2013. Oroclines: Thick and thin. GSA Bulletin 125 (5/6), 643–663.

Jolivet, L., Faccenna, C., Huet, B., Labrousse, L., Le Pourhiet, L., Lacombe, O., Lecomte, E., Burov, E., Denèle, Y., Brun, J.-P., Philippon, M., Paul, A., Salaün, G., Karabulut, H., Piromallo, C., Monié, P., Gueydan, F., Okay, A.I., Oberhänsli, R., Pourteau A., Augier, R., Gadenne, L., Driussi, O., 2013. Aegean tectonics: Strain localisation, slab tearing and trench retreat. Tectonophysics 597–598, 1–33.

Jolivet, L., Faccenna, C., Becker, T., Tesauro, M., Sternai, P., Bouilhol, P., 2018. Mantle Flow and Deforming Continents: From India-Asia Convergence to Pacific Subduction. Tectonics 37, 2887–2914.

Jones, R.R., Tanner, P.W.G., 1995. Strain partitioning in transpression zones. Journal of Structural Geology, 17 (6), 793–802.

Jovanović, D., Cvetković, V., Erić, S., Kostić, B., Peytcheva, I., Šarić, K., 2019. Variscan granitoids of the East Serbian Carpatho-Balkanides: new insight inferred from U–Pb zircon ages and geochemical data. Swiss Journal of Geosciences 112, 121–142.

Kalenić, M., Đorđević, M., Krstić, B., Bogdanović, P., Milošaković, R., Divljan, M., Čičulić, M., Džodžo, R., Rudolf, Lj., Jovanović, Lj., 1976; Explanatory book for sheet Bor, Basic geological map of SFRY 1:100.000. Savezni geološki zavod, Belgrade.

Kalenić, M., Hadži-Vuković, M., Dolić, D., Lončarević, Č., Rakić, M.O., 1980. Explanatory book for sheet Kučevo, Basic geological map of SFRY 1:100.000. Savezni geološki zavod, Belgrade.

Kaymakci, N., Inceöz, M., Ertepinar, P., Koç, A., 2010. Late Cretaceous to Recent kinematics of SE Anatolia (Turkey), in: Sosson, M., Kaymakci, N., Stephenson, R.A., Bergerat, F., Starostenko, V. (Eds), Sedimentary Basin Tectonics from the Black Sea and Caucasus to the Arabian Platform. Geological Society, London, Special Publications 340, 409–435.

Kerrich, R., Beckinsale, R.D., Durham, J.J., 1997. The transition between deformation regimes dominated by intercrystalline diffusion and intracrystalline creep evaluated by oxygen isotope thermometry. Tectonophysics 38, 241–257.

Klinkmüller, M., Schreurs, G., Rosenaub, M., Kemnitz, H., 2016. Properties of granular analogue model materials: A community wide survey. Tectonophysics 684, 23–38.

Knaak, M., Márton, I., Tosdal, R.M., van der Toorn, J., Davidović, D., Strmbanović, I., Zdravković, M., Živanović, J., Hasson, S., 2016. Geologic Setting and Tectonic Evolution of Porphyry Cu-Au, Polymetallic Replacement, and Sedimentary Rock-Hosted Au Deposits in the Northwestern Area of the Timok Magmatic Complex, Serbia. Society of Economic Geologists, Special Publication 19, 1–28.

Kolb, M., von Quadt, A., Peytcheva, I., Heinrich, C.A., Fowler, S.J., Cvetković, V., 2013. Adakite-like and Normal Arc Magmas: Distinct Fractionation Paths in the East Serbian Segment of the Balkan–Carpathian Arc. Journal of Petrology 54 (3), 421–451.

Kounov, A., Seward, D., Burg, J-.P., Bernoulli, D., Ivanov, Z., Handler, R., 2010. Geochronological and structural constraints on the Cretaceous thermotectonic evolution of the Kraishte zone (Western Bulgaria). Tectonics 29, TC2002. doi:10.1029/2009TC002509

Kounov, A., Burg, J.-P., Bernoulli, D., Seward, D., Ivanov, Z., Dimov, D., Gerdjikov, I., 2011. Paleostress analysis of Cenozoic faulting in the Kraishte area, SW Bulgaria. Journal of Structural Geology 33, 859–874.

Kounov, A., Gerdjikov, I., Vangelov, D., Balkanska, E., La¬zarova, A., Georgiev, S., Stockli, D., Blunt, E. 2018. First thermochronological constraints on the Cenozoic extension along the Balkan Fold-Thrust Belt (Central Stara Planina Mountain, Bulgaria). International Journal of Earth Sci¬ences 107 (4), 1515–1535.

Krantz, R.W., 1991. Measurements of friction coefficients and cohesion for faulting and fault reactivation in laboratory models using sand and sand mixtures. Tectonophysics 188, 203–207.

Kräutner, H.G., Krstić, B., 2002. Alpine and Pre-Alpine structural units within Southern Carpathians and the Eastern Balkanides. Proceedings of XVII Congress of Carpathian–Balkan Geological Association, Geologica Carpathica, 53, Special Issue.

Kräutner, H.G., Krstić, B., 2003. Geological map of the Carpatho–Balkanides between Mehadia, Oraviţa, Niš and Sofia. Geoinstitute, Belgrade.

Kreemer, C., Blewitt, G., Klein, E.C., 2014. A geodetic plate motion and global strain rate model. Geochemistry, Geophysics, Geosystems 15 (10), 3849–3889.

Krézsek, C., Adam, J., Grujic, D., 2007. Mechanics of fault and expulsion rollover systems developed on passive margins detached on salt: insights from analogue modelling and optical strain monitoring. Geological Society, London, Special Publications 292, 103–121.

Krézsek, C., Lăpădat, A., Maţenco, L., Arnberger, K., Barbu, V., Olaru, R., 2013. Strain partitioning at orogenic contacts during rotation, strike-slip and oblique convergence: Paleogene–Early Miocene evolution of the contact between the South Carpathians and Moesia. Global and Planetary Change 103, 63–81.

Krstekanić, N., Stojadinović, U., Kostić, B., Toljić, M., 2017. Internal structure of the Supragetic Unit basement in the Serbian Carpathians and its significance for the late Early Cretaceous nappe-stacking. Annalés Géologiques de la Péninsule Balkanique 78, 1–15.

Krstekanić, N., Matenco, L., Toljić, M., Mandic, O., Stojadinovic, U., Willingshofer, E., 2020. Understanding partitioning of deformation in highly arcuate orogenic systems: Inferences from the evolution of the Serbian Carpathians. Global and Planetary Change 195, 103361. https://doi.org/10.1016/j.gloplacha.2020.103361

Krstekanić, N., Willingshofer, E., Broerse, T., Matenco, L., Toljić, M., Stojadinovic, U., 2021. Analogue modelling of strain partitioning along a curved strike-slip fault system during backarc-convex orocline formation: Implications for the Cerna-Timok fault system of the Carpatho-Balkanides. Journal of Structural Geology 149, 104386. https://doi.org/10.1016/j.jsg.2021.104386

Krstekanić, N., Matenco, L., Stojadinovic, U., Willingshofer, E., Toljić, M., Tamminga, D., 2022. Strain partitioning in a large intracontinental strike-slip system accommodating backarc-convex orocline formation: the Circum-Moesian Fault System of the Carpatho-Balkanides. Global and Planetary Change, 208, 103714. https://doi.org/10.1016/j.gloplacha.2021.103714

Krstić, B., Kalenić, M., Divljan, M., Maslarević, Lj., Đorđević, M., Dolić, D., Antonijević, I., 1976. Explanatory book for sheets Knjaževac and Belogradčik, Basic geological map of SFRY 1:100.000. Savezni geološki zavod, Belgrade.

Krstić, N., Jovanović, G., Savić, Lj., Bodor, E., 2003. Lower Miocene lakes of the Balkan Land. Acta Geologica Hungarica 46 (3), 291–299.

Krstić, N., Savić, Lj., Jovanović, G., 2012. The Neogene Lakes on the Balkan Land. Geološki anali Balkanskog poluostrva, 37-60.

Krýza, O., Závada, P., Lexa, O., 2019. Advanced strain and mass transfer analysis in crustal-scale oroclinal buckling and detachment folding analoguemodels. Tectonophysics 764, 88–109.

Kydonakis, K., Brun, J.-P., Sokoutis, D., 2014. North Aegean core complexes, the gravity spreading of a thrust wedge. Journal of Geophysical Research: Solid Earth 120, 595–616.

Lacombe, O., 2012. Do fault slip data inversions actually yield ‘‘paleostresses’’ that can be compared with contemporary stresses? A critical discussion. Comptes Rendus Geoscience 344, 159–173.

Lazarević, Z., Milivojević, J., 2010. Early Miocene flora of the intramontane Žagubica Basin (Serbian Carpatho–Balkanides). Neues Jahrbuch für Geologie und Paläontologie – Abhandlungen 256 (2), 141–150.

Le Guerroué, E., Cobbold, P.R., 2006. Influence of erosion and sedimentation on strike-slip fault systems: insights from analogue models. Journal of Structural Geology 28, 421–430.

Leever, K.A., Matenco, L., Bertotti, G., Cloetingh, S., Drijkoningen, G.G., 2006. Late orogenic vertical movements in the Carpathian Bend Zone—seismic constraints on the transition zone from orogen to foredeep. Basin Research 18 (4), 521–545.

Leever, K.A., Gabrielsen, R.H., Sokoutis, D., Willingshofer, E., 2011. The effect of convergence angle on the kinematic evolution of strain partitioning in transpressional brittle wedges: Insight from analog modeling and high-resolution digital image analysis. Tectonics 30, TC2013. DOI: 10.1029/2010TC002823

Lesić, V., Márton, E., Gajić, V., Jovanović, D., Cvetkov, V., 2019. Clockwise vertical-axis rotation in the West Vardar zone of Serbia: tectonic implications. Swiss Journal of Geosciences 112, 199–215.

Li, P., Rosenbaum, G., 2014. Does the Manning Orocline exist? New structural evidence from the inner hinge of the Manning Orocline (eastern Australia). Gondwana Research 25, 1599–1613.

Li, P., Sun, M., Rosenbaum, G., Yuan, C., Safonova, I., Cai, K., Jiang, Y., Zhang, Y., 2018. Geometry, kinematics and tectonic models of the Kazakhstan Orocline, Central Asian Orogenic Belt. Journal of Asian Earth Sciences, 153, 42–56.

Lihoreau, F., Blondel, C., Barry, J., Brunet, M., 2004. A new species of the genus Microbunodon (Anthracotheriidae, Artiodactyla) from the Miocene of Pakistan: genus revision, phylogenetic relationships and palaeobiogeography. Zoologica Scripta 33 (2), 97–115.

Limberger, J., Calcagno, P., Manzella, A., Trumpy, E., Boxem, T., Pluymaekers, M.P.D., van Wees, J.–D., 2014. Assessing the prospective resource base for enhanced geothermal systems in Europe. Geoth. Energ. Sci. 2, 55–71.

Limberger, J., van Wees, J.–D., Tesauro, M., Smit, J., Bonté, D., Békési, E., Pluymaekers, M., Struijk, M., Vrijlandt, M., Beekman, F., Cloetingh, S., 2018. Refining the thermal structure of the European lithosphere by inversion of subsurface temperature data. Global and Planetary Change 171, 18–47.

Lisle, R.J., 2013. A critical look at the Wallace-Bott hypothesis in fault-slip analysis. Bull. Soc. géol. France 184 (4-5), 299–306.

Lister, G.S., Williams, P.F., 1983. The partitioning of deformation in flowing rock masses. Tectonophysics 92, 1–33.

Livani, M., Scrocca, D., Arecco, P., Doglioni, C., 2018. Structural and Stratigraphic Control on Salient and Recess Development along a Thrust Belt Front: The Northern

Apennines (Po Plain, Italy). Journal of Geophysical Research: Solid Earth 123, 4360–4387.

Lodolo E., Menichetti, M., Bartole, R., Ben-Avraham, Z., Tassone, A., Lippai, H., 2003. Magallanes – Fagnano continental transform fault (Tierra del Fuego, southernmost South America). Tectonics 22 (6), 1076.

Lonergan, L., White, N., 1997. Origin of the Betic-Rif mountain belt. Tectonics 16 (3), 504–522.

Luth, S., Willingshofer, E., ter Borgh, M., Sokoutis, D., van Otterloo, J., Versteeg, A., 2013. Kinematic and analogue modelling of the Passier- and Jaufen faults: implications for crustal indentation in the Eastern Alps. International Journal of Earth Sciences (Geol Rundsch) 102, 1071–1090.

Lyberis, N., Yurur, T., Chorowicz, J., Kasapoglu, E., Gundogdu, N., 1992. The East Anatolian Fault: an oblique collisional belt. Tectonophysics 204, 1–15.

Mai, D. H., 1995. Tertiäre Vegetationsgeschichte Europas. Methoden und Ergebnisse. Gustav Fischer Verlag, Jena, Stuttgart, New York.

Maksimović, B.B., 1956. Geological and tectonical relations of the coal bearing formations of the Senjsko–Resavski mines and the surrounding area. Special editions of the Geological institute "Jovan Žujević" 6, 1–104.

Malvern, L.E., 1969. Introduction to the mechanics of a continuous medium. pp. 713, Prentice-Hall, Inc., Englewood Cliffs, NJ.

Mann, P., 2007. Global catalogue, classification and tectonic origins of restraining and releasing bends on active and ancient strike-slip fault systems. Geological Scociety, London, Special Publications 290, 13–142.

Mantovani, E., Viti, M., Babbucci, D., Tamburelli, C., Albarello, D., 2006. Geodynamic connection between the indentation of Arabia and the Neogene tectonics of the central–eastern Mediterranean region, in: Dilek, Y., Pavlides, S. (Eds.), Postcollisional tectonics and magmatism in the Mediterranean region and Asia: Geological Society of America Special Paper 409, 15–41.

Marković, Z., 2003. The Miocene small mammals of Serbia, a review. Deinsea, 10, 393–398.

Marković, Z., Wessels, W., van de Weerd, A.A., de Bruijn, H., 2017. On a new diatomyid (Rodentia, Mammalia) from the Paleogene of south-east Serbia, the first record of the family in Europe. Palaeobiodiversity and Palaeoenvironments 98 (3), 459–469.

Marović, M., Djoković, I., Milićević, V., Toljić, M., Gerzina, N., 2002. Paleomagnetism of the late Paleogene and Neogene rocks of the Serbian Carpatho-Balkanides: Tectonic implications. Annales Géologiques de la Péninsule Balkanique 64, 1–12.

Marović, M., Toljić, M., Rundić, Lj., Milivojević, J., 2007. Neoalpine Tectonics of Serbia. Serbian Geological Society, Belgrade.

Marshak, S., 1988. Kinematics of orocline and arc formation in thin-skinned orogens. Tectonics 7, 73–86.

Marshak S., Wilkerson, M.S., Hsui, A.T., 1992. Generation of curved fold-thrust belts: Insights from simple physical and analytical models, in McClay, K.R. (Ed.), Thrust Tectonics, Chapman & Hall, pp. 83–92.

Martínez-García, P., Comas, M., Soto, J.I., Lonergan, L., Watts, A. B., 2013. Strike-slip tectonics and basin inversion in the Western Mediterranean: the Post-Messinian evolution of the Alboran Sea. Basin Research 25, 361–387.

Martinod, J., Hatzfeld, D., Brun, J.P., Davy, P., Gautier, P., 2000. Continental collision, gravity spreading, and kinematics of Aegea and Anatolia. Tectonics 19 (2), 290–299.

Márton, E., 2000. The Tisza megatectonic unit in the light of paleomagnetic data. Acta Geologica Hungarica 43 (3), 329–343.

Márton, E., Tischler, M., Csontos, L., Fügenschuh, B., Schmid, S.M., 2007. The contact zone between the ALCAPA and Tisza–Dacia mega-tectonic units of Northern Romania in the light of new paleomagnetic data. Swiss Journal of Geosciences, 100 (1), 109–124.

Maţenco, L., 2017. Tectonics and Exhumation of Romanian Carpathians: Inferences from Kinematic and Thermochronological Studies, in: Rădoane, M., Vespremeanu-Stroe, A. (Eds.), Landform Dynamics and Evolution in Romania, Springer Geography. Springer, pp. 15–56.

Matenco, L., Schmid, S., 1999. Exhumation of the Danubian nappes system (South Carpathians) during the Early Tertiary: inferences from kinematic and paleostress analysis at the Getic/Danubian nappes contact. Tectonophysics 314, 401–422.

Matenco, L., Radivojević, D., 2012. On the formation and evolution of the Pannonian Basin: Constraints derived from the structure of the junction area between the Carpathians and Dinarides. Tectonics 31, TC6007. DOI: 10.1029/2012TC003206

Maţenco, L., Bertotti, G., Dinu, C., Cloetingh, S., 1997. Tertiary tectonic evolution of the external South Carpathians and the adjacent Moesian platform (Romania). Tectonics 16 (6), 896–911.

Matenco, L., Bertotti, G., Cloetingh, S., Dinu, C., 2003. Subsidence analysis and tectonic evolution of the external Carpathian–Moesian Platform region during Neogene times. Sedimentary Geology 156, 71–94.

Matenco, L., Munteanu, I., ter Borgh, M., Stanica, A., Tilita, M., Lericolais, G., Dinu, C., Oaie, G., 2016. The interplay between tectonics, sediment dynamics and gateways evolution in the Danube system from the Pannonian Basin to the western Black Sea. Science of the Total Environment 543, 807–827.

Mattei, M., Cifelli, F., Alimohammadian, H., Rashid, H., Winkler, A., Sagnotti, L., 2017. Oroclinal bending in the Alborz Mountains (Northern Iran): New constraints on the age of South Caspian subduction and extrusion tectonics. Gondwana Research 42, 13–28.

Maurin, T., Masson, F., Rangin, C., Min, U.T., Collard, P., 2010. First global positioning system results in northern Myanmar: Constant and localized slip rate along the Sagaing fault. Geology 38 (7), 591–594.

McClay, K., Bonora, M., 2001. Analog models of restraining stepovers in strike-slip fault systems. AAPG Bulletin 85 (2), 233–260.

McKenzie, D., 1972. Active Tectonics of the Mediterranean Region. Geophys. J. R. 30, 109–185.

Meijers, M.J.M., Kaymakci, N., van Hinsbergen, D.J.J., Langereis, C.G., Stephenson, R.A., Hippolyte, J.-C., 2010. Late Cretaceous to Paleocene oroclinal bending in the central Pontides (Turkey). Tectonics 29, TC4016. DOI: 10.1029/2009TC002620

Melinte-Dobrinescu, M.-C., Jipa, D.C., 2007. Stratigraphy of the Lower Cretaceous Sediments from the Carpathian Bend Area, Romania. Acta Geologica Sinica 81 (6), 949–956.

Menant, A., Jolivet, L., Vrielynck, B., 2016a. Kinematic reconstructions and magmatic evolution illuminating crustal and mantle dynamics of the eastern Mediterranean region since the late Cretaceous. Tectonophysics 675, 103–140.

Menant, A., Sternai, P., Jolivet, L., Guillou-Frottier, L., Gerya, T., 2016b. 3D numerical modeling of mantle flow, crustal dynamics and magma genesis associated with slab roll-back and tearing: The eastern Mediterranean case. Earth and Planetary Science Letters 442, 93–107.

Miser, H.D., 1932. Oklahoma structural salient of the Ouachita Mountains. Geological Society of America Bulletin 43, 138.

Mladenović, A., Trivić, B., and Cvetković, V., 2015. How tectonics controlled post-collisional magmatism within the Dinarides: Inferences based on study of tectono-magmatic events in the Kopaonik Mts. (Southern Serbia). Tectonophysics 646, 36–49.

Mladenović, A., Antić, M.D., Trivić, B., Cvetković, V., 2019. Investigating distant effects of the Moesian promontory: brittle tectonics along the western boundary of the Getic unit (East Serbia). Swiss Journal of Geosciences 112, 143–161.

Molnar, P., Tapponnier, P., 1975. Cenozoic Tectonics of Asia: Effects of a Continental Collision. Science 189 (4201), 419–426.

Molnar, N.E., Cruden, A.R., Betts, P.G., 2017. Interactions between propagating rotational rifts and linear rheological heterogeneities: insights from three dimensional laboratory experiments. Tectonics 36, 420–443. https://doi.org/10.1002/2016TC004447

Molnar, N.E., Cruden, A.R., Betts, P.G., 2019. Interactions between propagating rifts and linear weaknesses in the lower crust. Geosphere 15, 1617–1640. https://doi.org/10.1130/GES02119.1

Moores, E.M., Twiss, R.J., 1995. Tectonics. W. H. Freeman and Company, New York, USA.

Morley, C.K., 2002. A tectonic model for the Tertiary evolution of strike–slip faults and rift basins in SE Asia. Tectonophysics 347, 189– 215.

Morley, C.K., 2007. Variations in Late Cenozoic–Recent strike-slip and oblique-extensional geometries, within Indochina: The influence of pre-existing fabrics. Journal of Structural Geology 29, 36–58.

Morley, C.K., 2013. Discussion of tectonic models for Cenozoic strike-slip fault-affected continental margins of mainland SE Asia. Journal of Asian Earth Sciences 76, 137–151.

Morley, C.K., Arboit, F., 2019. Dating the onset of motion on the Sagaing fault: Evidence from detrital zircon and titanite U-Pb geochronology from the North Minwun Basin, Myanmar. Geology 47, 581–585.

Mortimer, N., 2014. The oroclinal bend in the South Island, New Zealand. Journal of Structural Geology 64, 32–38.

Moser, F., Hann, H.P., Dunkl, I., Frisch, W., 2005. Exhumation and relief history of the Southern Carpathians (Romania) as evaluated from apatite fission track chronology

in crystalline basement and intramontane sedimentary rocks. International Journal of Earth Sciences 94, 218–230.

Nabavi, S.T., Alavi, S.A., Mohammadi, S., Ghassemi, M.R., 2018. Mechanical evolution of transpression zones affected by fault interactions: Insights from 3D elasto-plastic finite element models. Journal of Structural Geology 106, 19–40.

Naydenov, K., von Quadt, A., Peytcheva, I., Sarov, S., Dimov, D., 2009. U-Pb zircon dating of metamorphic rocks in the region of Kostenets-Kozarsko villages: constraints on the tectonic evolution of the Maritsa strike-slip shear zone. Review of the Bulgarian Geological Society 70/1–3, 5–21.

Naydenov, K., Peytcheva, I., von Quadt, A., Saro, S., Kolcheva, K., Dimov, D., 2013. The Maritsa strike-slip shear zone between Kostenets and Krichim towns, South Bulgaria d structural, petrographic and isotope geochronology study. Tectonophysics 595–596, 69–89.

Necea, D., Juez-Larré, J., Matenco, L., Andriessen P.A.M., Dinu, C., 2021. Foreland migration of orogenic exhumation during nappe stacking: Inferences from a high-resolution thermochronological profile over the Southeast Carpathians. Global and Planetary Change 200, 103457.

Neubauer, F., 2015. Cretaceous tectonics in Eastern Alps, Carpathians and Dinarides: two step microplate collision and Andean-type magmatic arc associated with orogenic collapse. Rend. Online Soc. Geol. Ital. 37, 40–43.

Neubauer, F., Bojar, A.-V., 2013. Origin of sediments during Cretaceous continent—continent collision in the Romanian Southern Carpathians: preliminary constraints from 40Ar/39Ar single-grain dating of detrital white mica. Geologica Carpathica 64 (5), 375–382.

Neubauer, F., Fritz, H., Genser, J., Kurz, W., Nemes, F., Wallbrecher, E., Wang, X., Willingshofer, E., 2000. Structural evolution within an extruding wedge: model and application to the Alpine-Pannonian system. In: Lehner, F.K., Urai, J.L. (Eds.), Aspects of Tectonic Faulting (Festschrift in Honour of Georg Mandl). Springer-Verlag, Berlin – Heidelberg – New York, pp. 141–153.

Neugebauer, J., 1994. Closing-up structures, alternatives to pull-apart basins: the effect of bends in the North Anatolian fault, Turkey. Terra Nova 6, 359–365.

Nielsen, C., Chamot-Rooke, N., Rangin, C., the ANDAMAN Cruise Team, 2004. From partial to full strain partitioning along the Indo-Burmese hyper-oblique subduction. Marine Geology 209, 303–327.

Obradović, J., Vasić, N., 2007. Jezerski baseni u neogenu Srbije. Special Issues (Vol. 662). Serbian Academy of Sciences and Arts, Belgrade.

Orife, T., Lisle, R.J., 2003. Numerical processing of palaeostress results. Journal of Structural Geology 25, 949–957.

Pamić, J.J., 1984. Triassic magmatism of the Dinarides in Yugoslavia. Tectonophysics 109, 273–307.

Pamić, J., 2002. The Sava-Vardar Zone of the Dinarides and Hellenides versus the Vardar Ocean. Eclogae Geologicae Helvetiae 95, 99–113.

Panaiotu, C.G., Panaiotu, C.E., 2010. Palaeomagnetism of the Upper Cretaceous Sânpetru Formation (Haţeg Basin, South Carpathians). Palaeogeography, Palaeoclimatology, Palaeoecology 293, 343–352.

Pastor-Galán, D., Gutiérrez-Alonso, G., Weil, A.B., 2011. Orocline timing through joint analysis: Insights from the Ibero-Armorican Arc. Tectonophysics 507, 31–46.

Pastor-Galán, D., Gutiérrez-Alonso, G., Zulauf, G., Zanella, F., 2012. Analogue modeling of lithospheric-scale orocline buckling: Constraints on the evolution of the Iberian-Armorican Arc. GSA Bulletin 124 (7-8), 1293–1309.

Pastor-Galán, D., Ursem, B., Meere, P., Lanereis, C.G. 2015. Extending the Cantabrian Orocline to two continents (Gondwana and Laurussia). Paleomagnetism from South Ireland. Earth and Planetary Science Letters 432, 223–231.

Pătraşcu, S., Bleahu, M., Panaiotu, C., 1990. Tectonic implications of paleomagnetic research into Upper Cretaceous magmatic rocks in the Apuseni Mountains, Romania. Tectonophysics 180, 309–322.

Pătraşcu, S., Bleahu, M., Panaiotu, C., Panaiotu, C.E., 1992. The paleomagnetism of the Upper Cretaceous magmatic rocks in the Banat area of the South Carpathians: tectonic implications. Tectonophysics 213, 341–352.

Pătraşcu, S., Şeclăman, M., Panaiotu, C., 1993. Tectonic implications of paleomagnetism in Upper Cretaceous deposits in the Haţeg and Rusca Montană basins (South Carpathians, Romania). Cretaceous Research 14, 255–264.

Pătraşcu, S., Panaiotu, C., Şeclăman, M., Panaiotu, C.E., 1994. Timing of rotational motion of Apuseni Mountains (Romania): paleomagnetic data from Tertiary magmatic rocks. Tectonophysics 233, 163–176.

Pavlović, M.B., 1997. Anthracotherium iz Bogovine (istočna Srbija). Annalés Géologiques de la Péninsule Balkanique 61, 153–160.

Peltzer, G., Tapponnier, P., 1988. Formation and evolution of strike-slip faults, rifts, and basins during the India-Asia collision: an experimental approach. Journal of Geophysical Research 93 (B12), 15085–15117.

Perinçek, D., Çemen, İ., 1990. The structural relationship between the East Anatolian and Dead Sea fault zones in southeastern Turkey. Tectonophysics 172, 331–340.

Petković, K. (Ed.), 1975a. Geologija Srbije: Stratigrafija – prekambrijum i paleozoik. Faculty of Mining and Geology, Belgrade.

Petković, K. (Ed.), 1975b. Geologija Srbije: Stratigrafija – mezozoik. Faculty of Mining and Geology, Belgrade.

Petrović, B., Dimitrijević, M., Karamata, S., 1973. Explanatory book for sheet Vlasotince, Basic geological map of SFRY 1:100.000. Savezni geološki zavod, Belgrade.

Philippon, M., Corti, G., Sani, F., Bonini, M., Balestrieri, M.-L., Molin, P., Willingshofer, E., Sokoutis, D., Cloetingh, S., 2014a. Evolution, distribution and characteristics of rifting in southern Ethiopia. Tectonics 33, 485–508, doi:10.1002/2013TC003430

Philippon, M., Brun, J.-P., Gueydan, F., Sokoutis, D., 2014b. The interaction between Aegean back-arc extension and Anatolia escape since Middle Miocene. Tectonophysics 631, 176–188.

Pinter, N., Grenerczy, G., Weber, J., Stein, S., Medak, D. (Eds.), 2005. The Adria Microplate: GPS Geodesy, Tectonics and Hazards (Nato Science Series: IV: Earth and Environmental Sciences). Springer, Dodrecht, the Netherlands.

Platt, J.P., 1986. Dynamics of orogenic wedges and the uplift of high-pressure metamorphic rocks. Geological Society of America Bulletin 97, 1037–1053.

Platt, J.P., 1993. Mechanics of oblique convergence. Journal of Geophysical Research 98 (B9), 16239– 16256.

Platt, J.P., Allerton, S., Kirker, A., Mandeville, C., Mayfield, A., Platzman, E.S., Rimi, A., 2003. The ultimate arc: Differential displacement, oroclinal bending, and vertical axis rotation in the External Betic-Rif arc. Tectonics 22/3, 1017. doi:10.1029/2001TC001321

Platt, J.P., Behr, W.M., Johanesen, K., Williams, J.R., 2013. The Betic-Rif Arc and Its Orogenic Hinterland: A Review. Annual Review of Earth and Planetary Sciences 41, 313–357.

Plissart, G., Monnier, C., Diot, H., Mărunţiu, M., Berger, J., Triantafyllou, A., 2017. Petrology, geochemistry and Sm-Nd analyses on the Balkan-Carpathian Ophiolite (BCO − Romania, Serbia, Bulgaria): remnants of a Devonian back-arc basin in the easternmost part of the Variscan domain. Journal of Geodynamics 105, 27–50.

Popa, M., Munteanu, I., Borleanu, F., Oros, E., Radulian, M., Dinu, C., 2018. Active tectonic deformation and associated earthquakes: a case study – South West Carpathians Bend zone. Acta Geodaetica et Geophysica 53, 395–413.

Porkoláb, K., Kövér, S., Benkó, Z., Héja, G.H., Fialowski, M., Soós, B., Gerzina Spajić, N., Đerić, N., Fodor, L., 2019. Structural and geochronological constraints from the Drina-Ivanjica thrust sheet (Western Serbia): implications for the Cretaceous–Paleogene tectonics of the Internal Dinarides. Swiss Journal of Geosciences 112, 217–234.

Rabăgia, T., Maţenco, L., 1999. Tertiary tectonic and sedimentological evolution of the South Carpathians foredeep: tectonic vs eustatic control. Marine and Petroleum Geology 16, 719–740.

Răbăgia, T., Matenco, L., Cloetingh, S., 2011. The interplay between eustacy, tectonics and surface processes during the growth of a fault-related structure as derived from sequence stratigraphy: The Govora–Ocnele Mari antiform, South Carpathians. Tectonophysics 502, 196–220.

Ramberg, H., 1981. Gravity, deformation, and the Earth's crust: in theory, experiments, and geological application. Academic Press, London, New York.

Ratschbacher, L., Merle, O., Davy, P., Cobbold, P., 1991a. Lateral extrusion in the eastern Alps, Part 1: Boundary conditions and experiments scaled for gravity. Tectonics, 10 (2), 245–256.

Ratschbacher, L., Frisch, W., Linzer, H.-G., Merle, O., 1991b. Lateral extrusion in the eastern Alps, Part 2: Structural analysis. Tectonics, 10 (2), 257–271.

Ratschbacher, L., Linzer, H.G., Moser F., Strusievicz, R.O., Bedelean, H., Har, N., Mogos, P.A., 1993. Cretaceous to Miocene thrusting and wrenching along the central South Carpathians due to a corner effect during collision and orocline formation. Tectonics 12, 855–873.

Regard, V., Faccenna, C., Martinod, J., Bellier, O., 2005. Slab pull and indentation tectonics: insights from 3D laboratory experiments. Physics of the Earth and Planetary Interiors 149, 99–113.

Ries, A.C., Shackleton, R.M., 1976. Patterns of strain variation in arcuate fold belts. Philosophical Transactions of the Royal Society of London Series A, 283, 281–288.

Roldán, F.J., Galindo-Zaldívar, J., Ruano, P., Chalouan, A., Pedrera, A., Ahmamou, M., Ruiz-Costán, A., Sanz de Galdeano, C., Benmakhlouf, M., López-Garrido, A.C., Anahnah, F., González-Castillo, L., 2014. Basin evolution associated to curved thrusts: The Prerif Ridges in the Volubilis area (Rif Cordillera, Morocco). Journal of Geodynamics 77, 56–69.

Rosas, F.M., Duarte, J.C., Neves, M.C., Terrinha, P., Silva, S., Matias, L., Gràcia, E., Bartolome, R., 2012. Thrust-wrench interference between major active faults in the Gulf of Cadiz (Africa-Eurasia plate boundary, offshore SW Iberia): Tectonic implications from coupled analog and numerical modelling. Tectonophysics 548–549, 1–21.

Rosas, F.M., Duarte, J.C., Schellart, W.P., Tomás, R., Grigorova, V., Terrinha, P., 2015. Analogue modelling of different angle thrust-wrench fault interference in a brittle medium. Journal of Structural Geology 74, 81–104.

Rosas, F.M., Duarte, J.C., Almeida, P., Schellart, W.P., Riel, N., Terrinha, P., 2017. Analogue modelling of thrust systems: Passive vs. active hanging wall strain accommodation and sharp vs. smooth fault-ramp geometries. Journal of Structural Geology 99, 45–69.

Rosenbaum, G., 2012. Oroclines of the southern New England Orogen, eastern Australia. Episodes, 35 (1), 187–194.

Rosenbaum, G., 2014. Geodynamics of oroclinal bending: Insights from the Mediterranean. Journal of Geodynamics 82, 5–15.

Rosenberg, C.L., Brun, J.-P., Gapais, D., 2004. Indentation model of the Eastern Alps and the origin of the Tauern Window. Geology 32 (11), 997–1000.

Rosenberg, C.L., Schneider, S., Scharf, A., Bertrand, A., Hammerschmidt, K., Rabaute, A., Brun, J.-P., 2018. Relating collisional kinematics to exhumation processes in the Eastern Alps. Earth-Science Reviews 176, 311–344.

Royden, L.H., 1993a. Evolution of retreating subduction boundaries formed during continental collision. Tectonics, 12 (3). 629–638.

Royden, L.H., 1993b. The tectonic expression slab pull at continental convergent boundaries. Tectonics 12 (2) 303– 325.

Royden L., Burchfiel, B.C., 1989. Are systematic variations in thrust belt style related to plate boundary processes? (The Western Alps versus the Carpathians). Tectonics 8 (1), 51–61.

Rudolf, M., Boutelier, D., Rosenau, M., Schreurs, G., Oncken, O., 2016. Rheological benchmark of silicone oils used for analog modling of short- and longterm lithospheric deformation. Tectonophysics 684, 12–22.

Rundić, Lj., Vasić, N., Banješević, M., Prelević, D., Gajić, V., Kostić, B., Stefanović, J., 2019. Facies analyses, biostratigraphy and radiometric dating of the Lower-Middle Miocene succession near Zaječar (Dacian basin, eastern Serbia). Annalés Géologiques de la Péninsule Balkanique 80 (2), 13–37.

Săndulescu, M. (Ed.), 1984. Geotectonica României (translated title: Geotectonics of Romania). Tehnică, Bucharest.

Săndulescu, M., 1988. Cenozoic Tectonic History of the Carpathians, in: Royden, L.H., Horvath, F. (Eds.), The Pannonian basin, a study in basin evolution, AAPG Memoir (Vol. 45). American Association of Petroleum Geologists, Tulsa, OK., pp. 17–25.

Sant, K., Mandic, O., Rundić, Lj., Kuiper, K.F., Krijgsman, W., 2018. Age and evolution of the Serbian Lake System: integrated results from Middle Miocene Lake Popovac. Newsletters on Stratigraphy 51 (1), 117–143.

Savu, H., Udrescu, C., Neacsu, V., Bratosin, I., Stoian, M., 1985. Origin, geochemistry and tectonic position of the Alpine ophiolites in the Severin nappe (Mehedinti Plateau, Romania). Ofioliti 10 (2/3), 423–440.

Schefer, S. C., 2012. Tectono-metamorphic and magmatic evolution of the Internal Dinarides (Kopaonik area, southern Serbia) and its significance for the geodynamic evolution of the Balkan Peninsula, (Doctoral dissertation). Retrieved from edoc (http://edoc.unibas.ch/diss/DissB_9908). University of Basel, Basel, Switzerland.

Schellart, W.P., Strak, V., 2016. A review of analogue modelling of geodynamic processes: Approaches, scaling, materials and quantification, with an application to subduction experiments. Journal of Geodynamics 100, 7–32.

Schellart, W.P., Chen, Z., Strak, V., Duarte, J.C., Rosas, F.M., 2019. Pacific subduction control on Asian continental deformation including Tibetan extension and eastward extrusion tectonics. Nature Communications 10, 4480. https://doi.org/10.1038/s41467-019-12337-9

Schmid, S.M., Berza, T., Diaconescu, V., Froitzheim, N., Fügenschuh, B., 1998. Orogen-parallel extension in the Southern Carpathians. Tectonophysics 297, 209–228.

Schmid, S.M., Bernoulli, D., Fügenschuh, B., Matenco, L., Schefer, S., Schuster, R., Tischler, M., Ustaszewski, K., 2008. The Alpine–Carpathian–Dinaridic orogenic system: correlation and evolution of tectonic units. Swiss Journal of Geosciences 101, 139–183.

Schmid, S.M., Fügenschuh, B., Kounov, A., Matenco, L., Nievergelt, P., Oberhänsli, R., Pleuger, J., Schefer, S., Schuster, R., Tomljenović, B., Ustaszewski, K., van Hinsbergen, D.J.J., 2020. Tectonic units of the Alpine collision zone between Eastern Alps and western Turkey. Gondwana Research 78, 308–374.

Searle, M.P., Elliot, J.R., Phillips, R.J., Chung, S.-L., 2011. Crustal–lithospheric structure and continental extrusion of Tibet. Journal of the Geological Society 168, 633–672.

Seghedi, A., Berza, T., Iancu, V., Mărunţiu, M., Oaie, G., 2005. Neoproterozoic terranes in the Moesian basement and in the Alpine Danubian nappes of the South Carpathians. Geologica Belgica 8 (4), 4–19.

Senatore, C., Wulfmeier, M., Vlahinić, I., Andrade, J., Iagnemma, K., 2013. Design and implementation of a particle image velocimetry method for analysis of running, gear–soil interaction. Journal of Terramechanics 50, 311–326.

Shen, F., Royden, L.H., Burchfiel, B.C., 2001. Large-scale crustal deformation of the Tibetan Plateau. Journal of Geophysical Research 106 (B4), 6793–6816.

Sieberer, A.-K., Klotz, T., Pomella, H., Ortner, H., Fügenschuh, B., Willingshofer, E., 2021. Internal deformation of the Dolomites Indenter, eastern Southern Alps: An integrated field, thermochronology and physical analogue modelling approach.

EGU21-13598, EGU General Assembly 2021, https://doi.org/10.5194/egusphere-egu21-13598

Simpson, C., Schmid, S.M., 1983. An evaluation of criteria to deduce the sense of movement in sheared rocks. Geological Society of America Bulletin 94, 1281–1288.

Sloan, R.A., Elliot, J.R., Searke, M.P., Morley, C.K., 2017. Active tectonics of Myanmar and the Andaman Sea, in: Barber, A., Khin Zaw, J., Crow, M.J. (Eds.), Myanmar: Geology, Resources and Tectonics. Geological Society, London, Memoirs 48, 19–52.

Smit, J., Brun, J.-P., Cloetingh, S., Ben-Avraham, Z., 2008. Pull-apart basin formation and development in narrow transform zones with application to the Dead Sea Basin. Tectonics 27, TC6018. DOI:10.1029/2007TC002119

Smit, J., Brun, J.-P., Cloetingh, S., Ben-Avraham, Z., 2010. The rift-like structure and asymmetry of the Dead Sea Fault. Earth and Planetary Science Letters 290, 74–82.

Sokoutis D., Bonini, M., Medvedev, S., Boccaletti, M., Talbot, C.J., Koyi, H., 2000. Indentation of a continent with a built-in thickness change: experiment and nature. Tectonophysics 320, 243–270.

Sperner, B., Zweigel, P., 2010. A plea for more cauton in fault-slip analysis. Tectonophysics 482, 29–41.

Stampfli, G.M., Borel, G.D., 2002. A plate tectonic model for the Paleozoic and Mesozoic constrained by dynamic plate boundaries and restored synthetic oceanic isochrons. Earth and Planetary Science Letters 196, 17–33.

Stanier, S.A., Blaber, J., Take, W.A., White, D., 2016. Improved image-based deformation measurement for geotechnical applications. Canadian Geotechnical Journal 53 (5), 727–739.

Stefanov, Y.P., Bakeev, R.A., 2014. Deformation and fracture structures in strike-slip faulting. Engineering Fracture Mechanics 129, 102–111.

Sternai, P., Avouac, J.–P., Jolivet, L., Faccenna, C., Gerya, T., Becker, T.W., Menant, A., 2016. On the influence of the asthenospheric flow on the tectonics andtopography at a collision-subduction transition zones:Comparison with the eastern Tibetan margin. Journal of Geodynamics 100, 184–197.

Stojadinovic, U., Matenco, L., Andriessen, P.A.M., Toljić, M., Foeken, J.P.T., 2013. The balance between orogenic building and subsequent extension during the Tertiary evolution of the NE Dinarides: Constraints from low-temperature thermochronology. Global and Planetary Change 103, 19–38.

Stojadinovic, U., Matenco, L., Andriessen, P., Toljić, M., Rundić, Lj., Ducea, M.N., 2017. Structure and provenance of Late Cretaceous–Miocene sediments located near the NE Dinarides margin: Inferences from kinematics of orogenic building and subsequent extensional collapse. Tectonophysics 710–711, 184–204.

Tapponnier, P., Peltzer, G., Le Dain, A., Aramijo, R., Cobbold, P., 1982. Propagating extrusion tectonics in Asia: new insights from simple experiments with plasticine. Geology 10 (12), 611–612.

Tapponnier, P., Peltzer, G., Aramijo, R., 1986. On the mechanics of the collision between India and Asia. In Coward, M.P., Ries, A.C., (Eds.). Collision Tectonics, Geological Society Special Publication 19., 115–157.

ter Borgh, M., Vasiliev, I., Stoica, M., Knežević, S., Matenco, L., Krijgsman, W., Rundić, Lj., Cloetingh, S., 2013. The isolation of the Pannonian basin (Central Paratethys): New constraints from magnetostratigraphy and biostratigraphy. Global and Planetary Change 103, 99–118.

Thielicke, W., Stamhuis, E.J., 2014. PIVlab – Towards User-friendly, Affordable and Accurate Digital Particle Image Velocimetry in MATLAB. Journal of Open Research Software, 2: e30. doi: http://dx.doi.org/10.5334/jors.bl

Tikoff, B., Wojtal, S.F., 1999. Displacement control of geologic structures. Journal of Structural Geology 21, 959–967.

Toljić, M., Matenco, L., Ducea, M.N., Stojadinović, U., Milivojević, J., Đerić, N., 2013. The evolution of a key segment in the Europe–Adria collision: The Fruška Gora of northern Serbia. Global and Planetary Change 103, 39–62.

Toljić, M., Matenco, L., Stojadinović, U., Willingshofer, E., Ljubović-Obradović, D., 2018. Understanding fossil fore-arc basins: Inferences from the Cretaceous Adria-Europe convergence in the NE Dinarides. Global and Planetary Change 171, 167-184.

Tomljenović, B., Csontos, L., Márton, E., Márton, P., 2008. Tectonic evolution of the northwestern Internal Dinarides as constrained by structures and rotation of Medvednica Mountains, North Croatia, in: Siegesmund, S., Fügenschuh, B., Froitzheim, N. (Eds.), Tectonic Aspects of the Alpine–Dinaride–Carpathian System, Special Publications. Geological Society, London, pp. 145–167.

Torres Carbonell, P.J., Guzmán, C., Yagupsky, D., Dimieri, L.V., 2016. Tectonic models for the Patagonian orogenic curve (southernmost Andes): An appraisal based on analog experiments from the Fuegian thrust–fold belt. Tectonophysics 671, 76–94.

Turcotte, D.L., Schubert, G., 2014. Geodynamics, Third edition. pp. 636, Cambridge University Press, Cambridge, United Kingdom.

Twiss, R.J., Unruh, J.R., 1998. Analysis of fault slip inversions: Do they constrain stress or strain rate? Journal of Geophysical Research 103 (B6), 12205–12222.

Ustaszewski, K., Schmid, S. M., Fügenschuh, B., Tischler, M., Kissling, E., Spakman, W., 2008. A map-view restoration of the Alpine–Carpathian–Dinaridic system for the Early Miocene. Swiss Journal of Geosciences 101, 273–294.

Ustaszewski, K., Schmid, S.M., Lugović, B., Schuster, R., Schaltegger, U., Bernoulli, D., Hottinger, L., Kounov, A., Fügenschuh, B., Schefer, S., 2009. Late Cretaceous intra-oceanic magmatism in the internal Dinarides (northern Bosnia and Herzegovina): Implications for the collision of the Adriatic and European plates. Lithos 108, 106–125.

Ustaszewski, K., Kounov, A., Schmid, S. M., Schaltegger, U., Krenn, E., Frank, W., Fügenschuh, B. 2010. Evolution of the Adria-Europe plate boundary in the northern Dinarides: From continent-continent collision to back-arc extension. Tectonics 29, TC6017. DOI: 10.1029/2010TC002668

van der Pluijm, B.A., Marshak, S., 2004. Earth Structure: an introduction to structural geology and tectonics, Second edition. pp. 656, W. W. Norton & Company, Inc., New York.

van Gelder, I.E., Matenco, L., Willingshofer, E., Tomljenović, B., Andriessen, P.A.M., Ducea, M.N., Beniest, A., Gruić, A., 2015., The tectonic evolution of a critical

segment of the Dinarides-Alps connection: Kinematic and geochronological inferences from the Medvednica Mountains, NE Croatia. Tectonics 34, 1952–1978,

van Gelder, I.E., Willingshofer, E., Sokoutis, D., Cloetingh, S.A.P.L., 2017. The interplay between subduction and lateral extrusion: A case study for the European Eastern Alps based on analogue models. Earth and Planetary Science Letters 472, 82–94.

van Gelder, I.E., Willingshofer, E., Andriessen, P.A.M., Schuster, R., Sokoutis, D., 2020. Cooling and Vertical Motions of Crustal Wedges Prior to, During, and After Lateral Extrusion in the Eastern Alps: New Field Kinematic and Fission Track Data from the Mur-Mürz Fault System. Tectonics 39, e2019TC005754.

van Hinsbergen, D.J.J., Dupont-Nivet, G., Nakov, R., Oud, K., Panaiotu, C., 2008. No significant post-Eocene rotation of the Moesian Platform and Rhodope (Bulgaria): implications for the kinematic evolution of the Carpathian and Aegean arcs. Earth and Planetary Science Letters 273, 345–358.

van Hinsbergen, D.J.J., Lippert, P.C., Li, S., Huang, W., Advokaat, E.L., Spakman, W., 2019. Reconstructing Greater India: Paleogeographic, kinematic, and geodynamic perspectives. Tectonophysics 760, 69–94.

van Hinsbergen, D.J.J., Torsvik, T.H., Schmid, S.M., Maţenco, L.C., Maffione, M., Vissers, R.L.M., Gürer, D. and Spakman, W., 2020. Orogenic architecture of the Mediterranean region and kinematic reconstruction of its tectonic evolution since the Triassic. Gondwana Research, 81, 79-229.

van Unen, M., Matenco, L., Demir, V., Nader, F.H., Darnault, R., Mandic, O., 2019a. Transfer of deformation during indentation: Inferences from the post-middle Miocene evolution of the Dinarides. Global and Planetary Change 182, 103027.

van Unen, M., Matenco, L., Nader, F.H., Darnault, R., Mandic, O., Demir, V., 2019b. Kinematics of Foreland-Vergent Crustal Accretion: Inferences From the Dinarides Evolution. Tectonics 38, 49–76.

Vangelov, D., Gerdjikov, Y., Kounov, A., Lazarova, A., 2013. The Balkan Fold-Thrust Belt: an overview of the main features. Geologica Balcanica 42 (1–3), 29–47.

Vangelov, D., Pavlova, M., Gerdjikov, I., Kounov, A., 2016. Timok fault and Tertiary strike-slip tectonics in part of western Bulgaria. Annual of the University of Mining and Geology “St. Ivan Rilski” 59 (1), 112–117.

Vergés, J., Fernàndez, M., 2012. Tethys–Atlantic interaction along the Iberia–Africa plate boundary: The Betic–Rif orogenic system. Tectonophysics 579, 144–172.

Veselinović, M., Antonijević, I., Milošaković, R., Mićić, I., Krstić, B., Čićulić, M., Divljan, M., Maslarević, Lj., 1970. Explanatory book for sheet Boljevac, Basic geological map of SFRY 1:100.000. Savezni geološki zavod, Belgrade.

Veselinović, M., Divljan, M., Đorđević, M., Kalenić, M., Milošaković, R., Rajčević, D., Popović, R., Rudolf, Lj., 1975. Explanatory book for sheet Zaječar, Basic geological map of SFRY 1:100.000. Savezni geološki zavod, Belgrade.

Vigny, C., Socquet, A., Rangin, C., Chamot-Rooke,N., Pubellier, M., Bouin, M.-N., Bertrand, G., Becker, M., 2003. Present-day crustal deformation around Sagaing fault, Myanmar. Journal of Geophysical Research 108 (B11), 2533, doi:10.1029/2002JB001999.

Visarion, M., Săndulescu, M., Stănică, D., Veliciu, S., 1988. Contributions á la connaissance de la structure profonde de la plate-forme Moésienne en Roumanie. St. Tehn. Econ. Geofiz. 15, 68–92.

von Quadt, A., Moritz, R., Peytcheva, I., Heinrich, C.A., 2005. 3:Geochronology and geodynamics of Late Cretaceous magmatism and Cu-Au mineralization in the Panagyurishte region of the Apuseni–Banat–Timok–Srednogorie belt, Bulgaria. Ore Geology Reviews 27, 95–126.

Vujisić, T., Navala, M., Kalenić, M., Krstić, B., Maslarević, Lj., Marković, B., Buković, J., 1980. Explanatory book for sheet Bela Palanka, Basic geological map of SFRY 1:100.000. Savezni geološki zavod, Belgrade.

Vujisić, T., Kalenić, M., Navala, M., Lončarević, Č., 1981. Explanatory book for sheet Lapovo, Basic geological map of SFRY 1:100.000. Savezni geološki zavod, Belgrade.

Wallace, R.E., (Ed.), 1990. The San Andreas Fault System, California. USGS Professional Paper 1515. US Geologiocal Survey, California

Wang, H., Liu, M., Ye, J., Cao, J., Jing, Y., 2017. Strain partitioning and stress perturbation around stepovers and bends of strike-slip faults: Numerical results. Tectonophysics 721, 211–226.

Warsitzka, M., Kley, J., Kukowski, N., 2015. Analogue experiments of salt flow and pillow growth due to basement faulting and differential loading. Solid Earth 6, 9–31.

Weijermars, R., Schmeling, H., 1986. Scaling of Newtonian and non-Newtonian fluid dynamics without inertia for quantitative modelling of rock flow due to gravity (including the concept of rheological similarity). Physics of the Earth and Planetary Interiors 43, 316–330.

Weil, A.B., Sussman, A.J., 2004. Classifying curved orogens based on timing relationships between structural development and vertical-axis rotations, in: Sussman, A.J., Weil, A.B. (Eds.), Orogenic Curvature: Integrating Paleomagnetic and Structural Analysis: Geological Society of America Special Paper 383, pp. 1–15.

Whipp, D.M., 2008. Quantitative thermochronology and interpretation of exhumation in the central Nepalese Himalaya. PhD thesis, The University of Michigan. pp. 255.

Willingshofer, E., Cloetingh, S., 2003. Present-day lithospheric strength of the Eastern Alps and its relationship to neotectonics. Tectonics 22 (6), 1075. doi:10.1029/2002TC001463

Willingshofer, E., Neubauer, F., Cloetingh, S., 1999. The Significance of Gosau–Type Basins for the Late Cretaceous Tectonic History of the Alpine–Carpathian Belt. Physics and Chemistry of the Earth (A) 24 (8), 687–695.

Willingshofer, E., Sokoutis, D., Burg, J.-P., 2005. Lithospheric-scale analogue modelling of collision zones with a pre-existing weak zone, in Gapais, D., Brun, J. P., Cobbold, P. R., (Eds.), Deformation Mechanisms, Rheology and Tectonics: from Minerals to the Lithosphere, Volume 243, Geological Society, London, Special Publications 243, 277–294.

Willingshofer, E., Sokoutis, D., Beekman, F., Schönebeck, J.-M., Warsitzka, M., Rosenau, M., 2018. Ring shear test data of feldspar sand and quartz sand used in the

Tectonic Laboratory (TecLab) at Utrecht University for experimental Earth Science applications. GFZ Data Services, http://doi.org/10.5880/fidgeo.2018.072

Wölfler, A., Kurz, W., Fritz, H., Stüwe, K., 2011. Lateral extrusion in the Eastern Alps revisited: Refining the model by thermochronological, sedimentary, and seismic data. Tectonics 30, TC4006, doi:10.1029/2010TC002782

Xiao, W., Windley, B.F., Han, C., Liu, W., Wan, B., Zhang, J., Ao, S., Zhang, Z., Song, D., 2018. Late Paleozoic to early Triassic multiple roll-back and oroclinal bending of the Mongolia collage in Central Asia. Earth-Science Reviews 186, 94–128.

Xiao, Y., Wu, G., Lei, Y., Chen, T., 2017. Analogue modeling of through-going process and development pattern of strike-slip fault zone. Petroleum Exploration and Development 44 (3), 368–376.

Yamaji, A., 2003. Are the solutions of stress inversion correct? Visualisation of their reliability and the separation of stresses from heterogeneous fault-slip data. Journal of Structural Geology 25, 241–252.

Yonkee, A., Weil, A.B., 2010. Reconstructing the kinematic evolution of curved mountain belts: Internal strain patterns in the Wyoming salient, Sevier thrust belt, U.S.A. GSA Bulletin 122 (1/2), 24–49.

Zakariadze, G., Karamata, S., Korokovsky, S., Ariskin, A., Adamia, S., Chkhouta, T., Sergeev, S., Solov'eva, N., 2012. The Early-Middle Palaeozoic Oceanic Events Along the Southern European Margin: the Deli Jovan Ophiolite Massif (NE Serbia) and Palaeo-oceanic Zones of the Great Caucasus. Turkish Journal of Earth Sciences 21, 635–668.

Žujović, J.M., 1886. Geologische Uebersicht des Königreiches Serbien. Jahrbuch der Geologischen Bundesanstalt 36, 71–126.

Zwaan, F., Schreurs, G., 2020. Rift segment interaction in orthogonal and rotational extension experiments: Implications for the large-scale development of rift systems. Journal of Structural Geology 140, 104119. https://doi.org/10.1016/j.jsg.2020.104119

Zwaan, F., Schreurs, G., Rosenau, M., 2020. Rift propagation in rotational versus orthogonal extension: Insights from 4D analogue models. Journal of Structural Geology 135, 103946. https://doi.org/10.1016/j.jsg.2019.103946

Zweigel, P., 1998. Arcuate accretionary wedge formation at convex plate margin corners: results of sandbox analogue experiments. Journal of Structural Geology 20 (12), 1597–1609.

Zweigel, P., Ratschbacher, L., Frisch, W., 1998. Kinematics of an arcuate fold-thrust belt: the southern Eastern Carpathians (Romania). Tectonophysics 297, 177–207.

About the author

Nemanja Krstekanić was born on September 4, 1991 in Belgrade, Serbia. In 2014 he earned his Bachelor's degree (with honours) in Geology, and in 2016 his Master's degree (with honours) in Regional Geology, both at the University of Belgrade, Faculty of Mining and Geology, Belgrade, Serbia. During and following the master studies he worked as a teaching assistant at the Department of Regional Geology, Faculty of Mining and Geology, University of Belgrade, Serbia. In January 2018, he started his PhD project in the Tectonics Group, Department of Earth Sciences, Utrecht University. His PhD project was funded by the Netherlands Research Centre for Integrated Solid Earth Science (ISES).